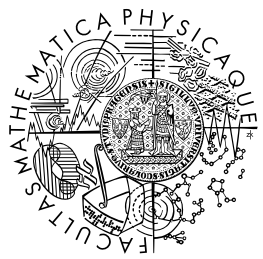


FACULTY
OF MATHEMATICS
AND PHYSICS
Charles University

**DOCTORAL THESIS**

Jakub Rozehnal

# Orbital and collisional dynamics of small bodies

Astronomical Institute, Charles University, Prague

Supervisor of the doctoral thesis: doc. Mgr. Miroslav Brož, Ph.D.

Study programme: Physics

Study branch: Theoretical Physics, Astronomy and Astrophysics

Prague 2021

I declare that I carried out this doctoral thesis independently, and only with the cited sources, literature and other professional sources. It has not been used to obtain another or the same degree.

I understand that my work relates to the rights and obligations under the Act No. 121/2000 Sb., the Copyright Act, as amended, in particular the fact that the Charles University has the right to conclude a license agreement on the use of this work as a school work pursuant to Section 60 subsection 1 of the Copyright Act.

In ..... date .....  .....

Author's signature

At this point, I would like to thank my supervisor Miroslav Brož for his immense efforts and careful supervision of my work. His enthusiasm for science has inspired me a lot all along.

My thanks also go to my colleagues from Planetum, who supported me in my work, especially to Petr Kulhánek, who taught me to love astronomy and physics.

I would like to dedicate this work to my loved ones: my parents, my daughter Veronica and my beloved Lenka. Without their support, I would find it difficult to complete this work.

Title: Orbital and collisional dynamics of small bodies

Author: Jakub Rozehnal

Institute: Astronomical Institute, Charles University, Prague

Supervisor: doc. Mgr. Miroslav Brož, Ph.D.

Abstract: This work is devoted to a study of dynamical and collisional processes, governing populations of small bodies in the Solar System. It pays special attention to asteroid families and Jupiter Trojans. Librating around $L_4$ and $L_5$ Lagrangian points of the Sun–Jupiter––asteroid system, these asteroids are believed to be captured from the trans-Neptunian region during a giant planet system instability about 4 Gy ago. We discovered (back in 2011) there is only one significant collisional family among Trojans, associated with C-type asteroid (3548) Eurybates, i.e., one of the targets for the upcoming 'Lucy' mission. Detailed analysis of new proper resonant orbital elements, colours and albedos, together with statistical significance computations, allowed us to find five more collisional families: Hektor, (9799), Arkesilaos, Ennomos, and (247341). The discovery of the first D-type family associated with (624) Hektor was the most surprising, because it is the most primitive taxonomic type. Using long-term dynamical simulations of synthetic families, evolving by chaotic diffusion, we estimated the ages of the Eurybates and Hektor families, approximately $(2.5 \pm 1.5)$ Gy for both. We also studied impact processes by means of the smoothed-particle hydrodynamics (SPH). We simulated cratering events on (624) Hektor, the origin of its family and its moonlet. The bi-lobed shape of the body, which affects the shock wave propagation, was also taken into account. The same method was applied to a formation of main-belt families during the late heavy bombardment ($\sim 3.85$ Gy ago). If asteroids were bombarded by comets, as predicted by the Nice model, hundreds of families (catastrophic disruptions of $D \geq 100$ km bodies) should be created, but the observed number is only 20. Therefore we computed 125 simulations of collisions between representative asteroids and high-speed icy projectiles (comets) and derived parametric relations for statistical collisional models, which can be used to better understand this early evolution.

Keywords: asteroids – Solar System – Trojans – orbital dynamics – collisional dynamics

# Contents


**1 Introduction** **3**
- 1.1 Trojans as a key to understand the Solar System . . . 3
- 1.2 Citations and implications of our works . . . 7

**2 Hektor — an exceptional D-type family among Jovian Trojans** **15**
- 2.1 Introduction . . . 15
- 2.2 New observational data . . . 16
  - 2.2.1 Resonant elements . . . 16
  - 2.2.2 WISE and AKARI albedos and diameters . . . 16
- 2.3 Physical characterisation of Trojan populations . . . 17
  - 2.3.1 Albedo distribution and taxonomy . . . 17
  - 2.3.2 Size-frequency distributions . . . 17
- 2.4 Families detection methods . . . 18
  - 2.4.1 Randombox method . . . 22
  - 2.4.2 Hierarchical clustering method . . . 22
- 2.5 Properties of statistically significant families . . . 24
  - 2.5.1 Eurybates . . . 24
  - 2.5.2 Hektor — the first D–type family . . . 24
  - 2.5.3 1996 RJ — extremely compact family . . . 26
  - 2.5.4 Arkesilaos . . . 26
  - 2.5.5 Ennomos . . . 31
  - 2.5.6 2001 $UV_{209}$ . . . 31
- 2.6 Collisional models of the Trojan population . . . 31
  - 2.6.1 Initial conditions . . . 31
  - 2.6.2 Long-term collisional evolution . . . 32
  - 2.6.3 An estimate of the number of observable families . . . 34
- 2.7 SPH simulations of Hektor family . . . 34
  - 2.7.1 Methods and initial conditions . . . 35
  - 2.7.2 Resulting size-frequency distributions . . . 36
  - 2.7.3 Resulting velocity fields . . . 37
  - 2.7.4 Synthetic moons . . . 40
- 2.8 Conclusions . . . 40

**3 Eurybates — the 'only' asteroid family among Trojans?** **43**
- 3.1 Introduction . . . 43
- 3.2 Methods . . . 44
  - 3.2.1 Resonant elements . . . 44
  - 3.2.2 Hierarchical clustering . . . 44
  - 3.2.3 Size-frequency distribution . . . 48
  - 3.2.4 Colour and spectral data . . . 49
  - 3.2.5 Impact disruption model . . . 52

3.2.6 Planetary migration . . . 52
3.2.7 Inefficient Yarkovsky/YORP effect . . . 52
3.3 Asteroid families and insignificant groups . . . 54
3.3.1 Eurybates family . . . 54
3.3.2 Ennomos group . . . 54
3.3.3 Group denoted Aneas . . . 55
3.3.4 Group denoted 1988 $RG_{10}$ . . . 55
3.4 Long-term evolution of Trojan families . . . 56
3.4.1 Evolution due to chaotic diffusion . . . 56
3.4.2 Stability during planetary migration . . . 56
3.4.3 Families lost by the ejection of fragment outside the resonance . . . 58
3.4.4 Collisional rates . . . 60
3.5 Conclusions . . . 61

**4 SPH simulations of high-speed collisions** **63**
4.1 Introduction . . . 63
4.2 Methods . . . 64
4.3 Results . . . 65
4.4 Comparison with low-speed collisions . . . 71
4.5 Conclusions . . . 73
4.6 Supplementary figures . . . 73

**5 Conclusions** **93**

**A Reprint of Rozehnal et al. (2016)** **95**

**B Reprint of Brož and Rozehnal (2011)** **111**

**C Reprint of Brož et al. (2013)** **123**

**References** **141**

**List of publications** **151**

# Chapter 1

# Introduction

Small bodies of the Solar System are influenced not only by gravity of the Sun, but also by gravitational perturbations of planets, most massive asteroids (incl. Ceres, Pallas, Juno, Vesta, ...; Park et al. 2021), tidal perturbations, the non-gravitational Yarkovsky effect, the YORP effect, the Poynting–Robertson effect, radiation pressure, solar wind, cometary outgassing, mutual collisions, mass shedding, etc. The character of small-body populations is highly influenced by gravity of planets, if perturbations are *resonant*. Their stability can be studied with the secular theory. This, however, does not solve the question of their origin. The very existence of resonant asteroids (e.g., orbiting in 1:1, 3:2, 2:1 mean-motion resonances; see Figs. 1.1, 1.2) and their other orbital properties also imply that significant changes to the orbits of planets had to occur (e.g. Malhotra, 1995; Gomes et al., 2005; Nesvorný, 2018).

## 1.1 Trojans as a key to understand the Solar System

Trojan asteroids are small bodies that oscillate around two lagrangian points $L_4$ and $L_5$ of the Sun–Jupiter–asteroid system (Lagrange, 1772), leading and trailing Jupiter by approximately 60°. In literature, the leading group is sometimes called "Greeks" and the trailing group "Trojans". The mean longitudal libration amplitude of Trojan asteroids is $\approx 14°$ with the period of $\approx 150$ y (Bertotti et al. 2003; Fig. 1.3). To this date (Jun 2021), there is over 10 000 Jovian Trojans in the Minor Planet Center database (MPCORB), but given the observational bias, the estimated number Trojans larger than 1 km in diameter is $\approx 5 \cdot 10^5$ (cf. Fig. 1.4).

Given the generality of the three-body problem, it is probably not surprising there are other 'triples'. So far, Mars Trojans were observed (Christou, 2013; Ćuk et al., 2015), as well as Neptune Trojans (Sheppard and Trujillo, 2006, 2010), Uranus Trojans (Alexandersen et al., 2013; Zhou et al., 2020); even one Trojan of Earth (Connors et al., 2011), Venus (de la Fuente Marcos and de la Fuente Marcos, 2014), and temporary ones for Ceres and Vesta (Christou and Wiegert, 2012). Interestingly, there are no Saturn Trojans (cf. stability; Hou et al. 2014).

According to dynamical studies (e.g. Marzari and Scholl, 1998), the vicinity of Jupiter's Lagrangian points is very stable in the current configuration of planets and it is virtually impossible for a body to enter (or leave) it and eventually become a Trojan with a small libration amplitude (Bertotti et al., 2003). Consequently, when searching for the origin of Jovian Trojans, several scenarios must have been considered.

1. **Jupiter's accretion.** A "classical" theory suggests that Trojans are former planetesimals formed close to the current orbit of Jupiter (5.2 au). They were captured on tadpole orbits around the equilibrium $L_4$ and $L_5$ Lagrangian points when Jupiter's gravity rather abruptly increased as it accreted its massive gaseous envelope. According to numerical simulations (Marzari and Scholl, 1998), the capture could be very efficient,

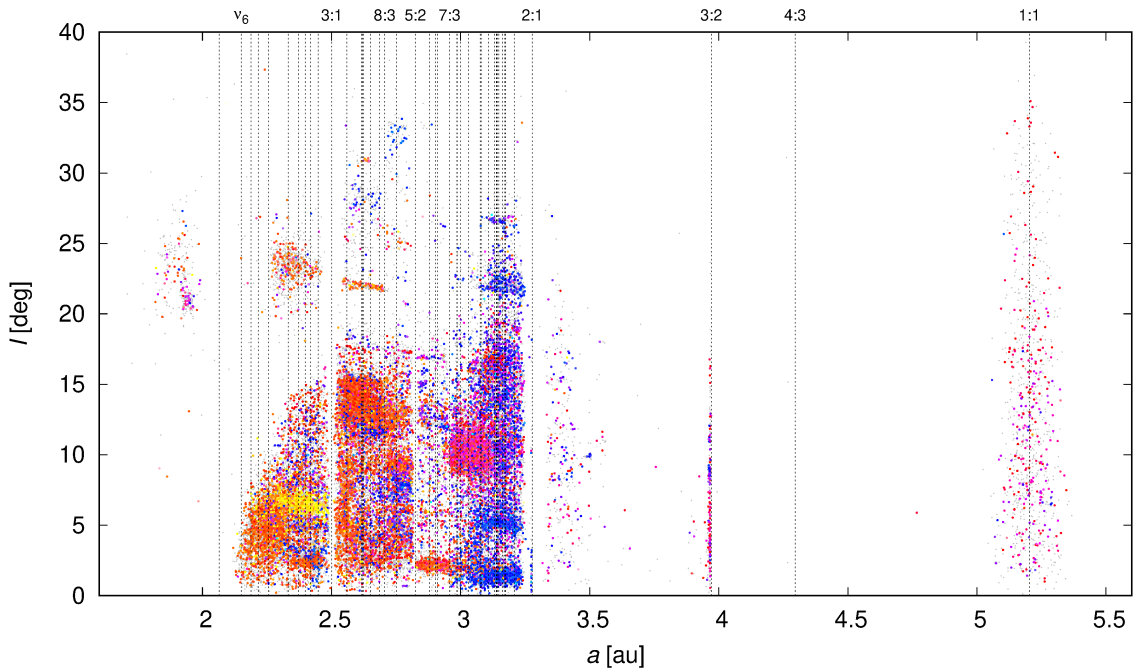


Figure 1.1: Semimajor axis $a$ vs. eccentricity $e$ for asteroids brighter than $H < 15$ mag. Colours correspond to the Sloan Digital Sky Survey colour indices (Parker et al., 2008), with orange corresponding to S-types and blue to C-types. Apart from the main belt (2.1 to 3.27 au), Trojan (1:1), Hilda (3:2), other resonant (2:1), Hungaria, Phocaea, Cybele, high-inclination populations are visible. Major asteroid families are the prominent concentration of bodies with similar orbits and colours. (Minor families are to small to be visible.) Unlike the main belt, Trojans asteroid have distinct colours (pink/magenta), similar to the trans-Neptunian (TNO) population, or D- and P-types.

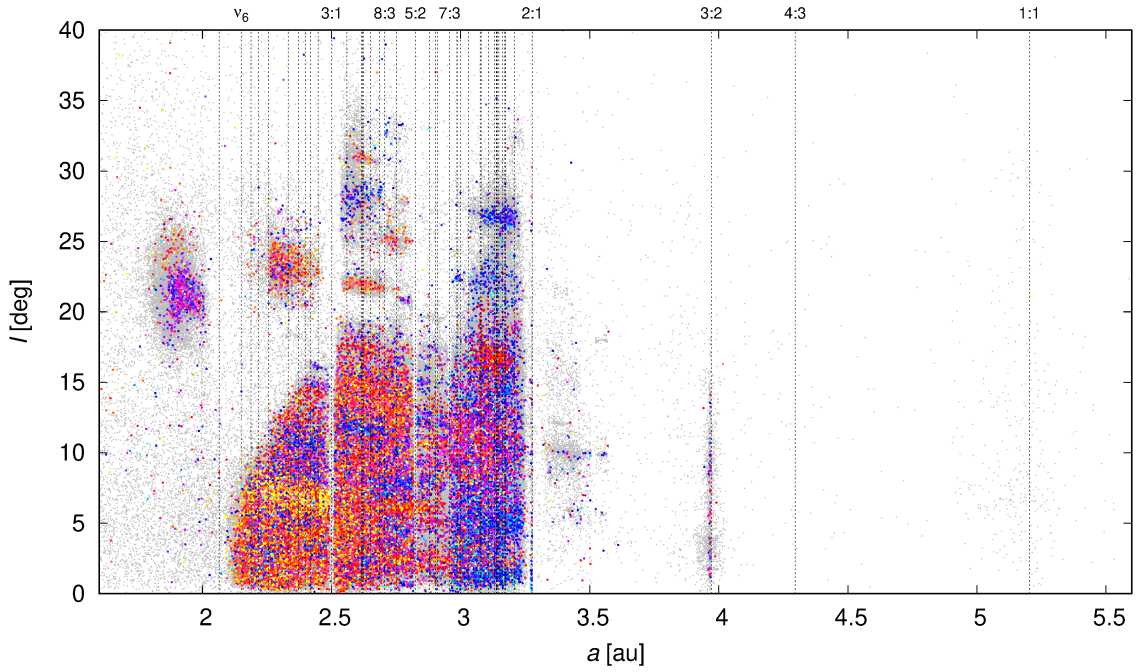


Figure 1.2: Same as Fig. 1.1, but for asteroids with $H \geq 15$ mag.

over 40 % of planetesimals orbiting in the ring spanning up to 0.4 au from Jupiter's orbit can be eventually captured as Trojans.

However, this simple model has several drawbacks. Trojans captured in this scenario have much larger libration amplitudes than observed ones (Dones et al., 2004). This problem can be partially solved by taking into account subsequent collisional evolution and ballistic transport. Also Trojans with high libration amplitudes usually leave tadpole orbits within several Gy due to chaotic diffusion, as was shown also in our long-term dynamical simulations (Brož and Rozehnal, 2011; Rozehnal et al., 2016). An even more serious problem is related to the inclinations of their orbits. Trojans captured from a planetesimal disk should have a similar distribution of eccentricities and inclination as the disk itself. Of course, planetesimals near Jupiter were dynamically stirred by Jupiter, but on its own it cannot explain inclinations up to 40° (cf. Pirani et al. 2019).

2. **Chaotic capture.** A different model is related to the *migration* of planets (Fernandez and Ip, 1984). After the Solar System lost primordial gas, mutual interactions between trans-Neptunian (TNO) planetesimals and the giant planets led to systematic changes of their semimajor axes. Planetesimals were dynamically excited during close approaches to Neptune (or Uranus). Several per cent of these planetesimals had reached distances of the order of $10^4$ to $10^5$ au from the Sun, where they eventually formed the Oort cloud (Dones et al., 2004). The disk mass decreased from $10^1$ Earth's masses ($M_\mathrm{E}$) to less than 0.1 $M_\mathrm{E}$, corresponding to the current Kuiper Belt. After interacting with Neptune, Uranus, Saturn and Jupiter, planetesimals were scattered on hyperbolic orbits. In this way, Jupiter was forced to migrate inwards, while Saturn, Uranus and Neptune migrated outwards. The so-called "Nice model" (Gomes et al., 2005; Tsiganis et al., 2005; Morbidelli et al., 2005) was developed to explain the observed values of eccentricity and inclination of the giant planets, the origin of the late heavy bombardment (LHB), as well as the existence of Jupiter Trojans on high-inclination orbits.

   This model suggests that during the phase, when Jupiter and Saturn were close to their mutual 1:2 mean-motion resonance, the *secondary* resonances 3:1 and 2:1 occurred between the libration frequency (or -ies) of Trojans and the $(1\mathrm{J} - 2\mathrm{S})$ frequency, where J and S denote the orbital frequencies of Jupiter and Saturn, respectively. During these secondary resonances, surroundings of the libration points are dynamically destabilised and small bodies can thus enter and leave these regions. After the secondary resonances ceased, the regions became stable again, so that scattered TNO bodies present there remained captured (Morbidelli et al., 2005).

   Although the original Nice model simulations matched the observed planetary semiaxes, eccentricities and inclinations (and it was also able to explain the LHB, Trojans, TNOs), the slow migration of Jupiter and Saturn past the 2:1 resonance — which is the basic assumption of the Nice model — seems to be in contradiction with other observational constrains, namely the angular momentum of the terrestrial planets (Brasser et al., 2009), the orbital structure of the asteroid belt (Morbidelli et al., 2010), or the observed amplitudes of secular variations in eccentricities of giant planets (Nesvorný et al., 2013; Nesvorný, 2018).

3. **Jump capture.** Some of the Nice model problems could be treated, if assuming the "Jumping Jupiter" scenario (Morbidelli et al., 2010) for the planetesimal-disk phase. In this case, a close encounter of Jupiter with an ice giant caused an abrupt jump of Jupiter (by approximately 0.2 au); because the ice giant orbit was so eccentric, the trans-Neptunian planetesimal population had been already scattered at that time. Nesvorný et al. (2013) found that a majority of Trojans were captured from the scattered TNOs

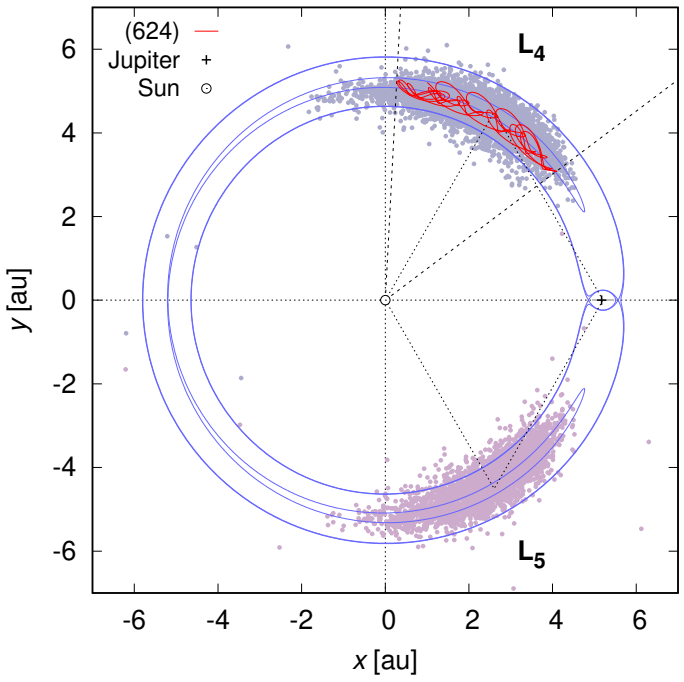


Figure 1.3: Positions of $L_4$ and $L_5$ Trojans with respect to the Sun and Jupiter projected to the ecliptic $(x, y)$ plane (as of Apr 2020). The trajectory of (624) Hektor in the frame corotating with Jupiter is plotted in red. Its time span 150 yr corresponds to the mean libration period of Trojans. Critical equipotentials of the restricted 3-body problem (RTPB) are overplotted in blue; Jupiter's orbits is eccentric ($e = 0.022$) and perturbed though.

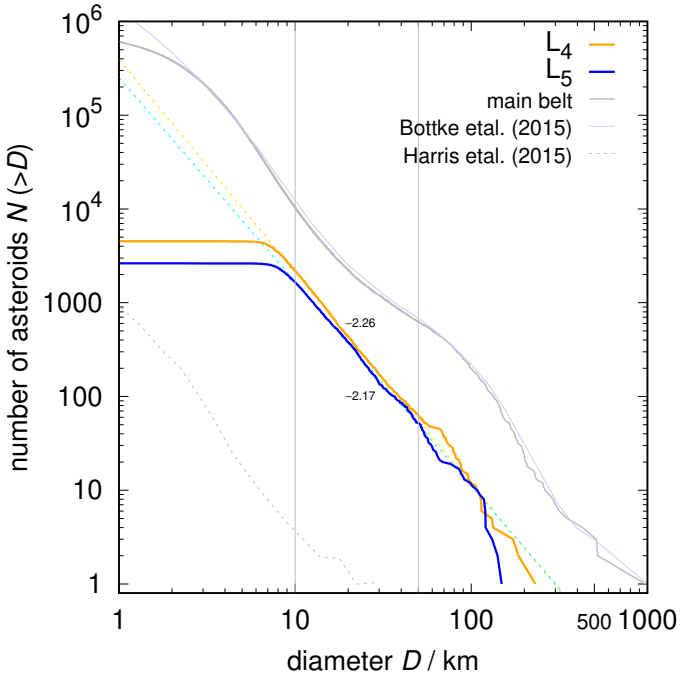


Figure 1.4: Size-frequency distribution (SFD) $N(>D)$ of $L_4$ and $L_5$ Trojans. Its extrapolation to $D = 1$ km is plotted by a dashed line. For comparison, the main belt and the near-Earth asteroids SFDs are plotted (Bottke et al., 2015; Harris et al., 2015).

immediately after the closest encounter. A related process, an overlap of the planetary Hill spheres during close encounters leads also to a capture of irregular moons (Nesvorný et al., 2014).

Because there is statistically low probability that the ice giant would remain in the planetary system after the encounter, Nesvorný and Morbidelli (2012) proposed an alternative scenario with a fifth ice giant (see also Nesvorný, 2018)). If true, a substantial population of free-floating exoplanets may be present in our galaxy (Mróz et al., 2020; McDonald et al., 2021).

4. **Gas-assited concentration.** Yet another possibility is that Trojans come into existence earlier than previously thought, in the gas-disk phase, provided that the planetesimal-disk phase was much less violent. A gas-assisted capture of dust, pebbles, and their concentration by vortices is possible due to aerodynamic drag and a partial coupling of solids to gas (Montesinos et al., 2020). A growth of solids may be facilitated by the streaming instability (Li et al., 2018; Nesvorný et al., 2019). In this framework, the eccentric and inclined orbits of planets must be explained by radiative hydrodynamic interactions of protoplanets with gas (Chrenko et al., 2017; Eklund and Masset, 2017) and the terrestrial planets also must have formed early (Brož et al., 2021). Details of all these processes are yet to be explored...

There is certainly a relation to other populations, especially the Kuiper Belt (Morbidelli and Nesvorný, 2020), with which Trojans share similar physical properties and similar inclination distribution. Hildas located in the 3:2 mean-motion resonance with Jupiter (Levison et al., 2009; Brož et al., 2011) were probably captured in a similar way as Trojans. Last but not least, Centaurs on orbits crossing the giant planets, which correspond to the scattered TNOs of today, were the same dynamical population as Trojans were captured from in the past.

Jupiter Trojans clearly represent the key to understand the formation and evolution of the early Solar System. Their basic characteristics, such as the asymmetric $L_4/L_5$ ratio (Szabó et al. 2007; Fig. 1.4), the peculiar inclination distribution (Morbidelli et al., 2005), or the predominance of D- and P-type (over S- and C-type) asteroids (Grav et al. 2012; Fig. 1.1), etc. must be all explained by any viable theory. In the following, we explore even more detailed characteristics of Trojans. The existence of families with similar orbits (Brož and Rozehnal 2011; Rozehnal et al. 2016; Figs. 1.5, 1.6) is one of them, especially if they were indeed created by mutual collisions (cratering, reaccumulative, or catastrophic impacts) of Trojan asteroids, or other impactor populations.

## 1.2 Citations and implications of our works

Given the fact that our works were published a few years ago, it is a good opportunity to review their citations. While the motivation is described at the beginning of the respective papers, as usual (see Secs. 2, 3, 4), this "retrospective" view is very useful to explain implications of our past works and it also serves as a motivation for future works.

In particular, there are 11 citations to Rozehnal et al. (2016), 25 to Brož and Rozehnal (2011), and 72 to Brož et al. (2013). They include, e.g., Nesvorný et al. (2013), Christou (2013), Di Sisto et al. (2014), Wong et al. (2014), Wong and Brown (2016), Wong and Brown (2017), Ćuk et al. (2015), Vinogradova (2015), Vernazza et al. (2017), Ryan et al. (2017), Milani et al. (2017), Jiang et al. (2018), Perna et al. (2018), Nesvorný (2018), Sugiura et al. (2018), Vokrouhlický et al. (2019), Lin et al. (2019), Souza-Feliciano et al. (2020), Holt et al. (2020a), Holt et al. (2020b), Holt et al. (2021), Noll et al. (2020), Brown et al. (2021), Brown and Schemel (2021), McNeill et al. (2021), ... Some of these citations are reviewed in detail in the following text.

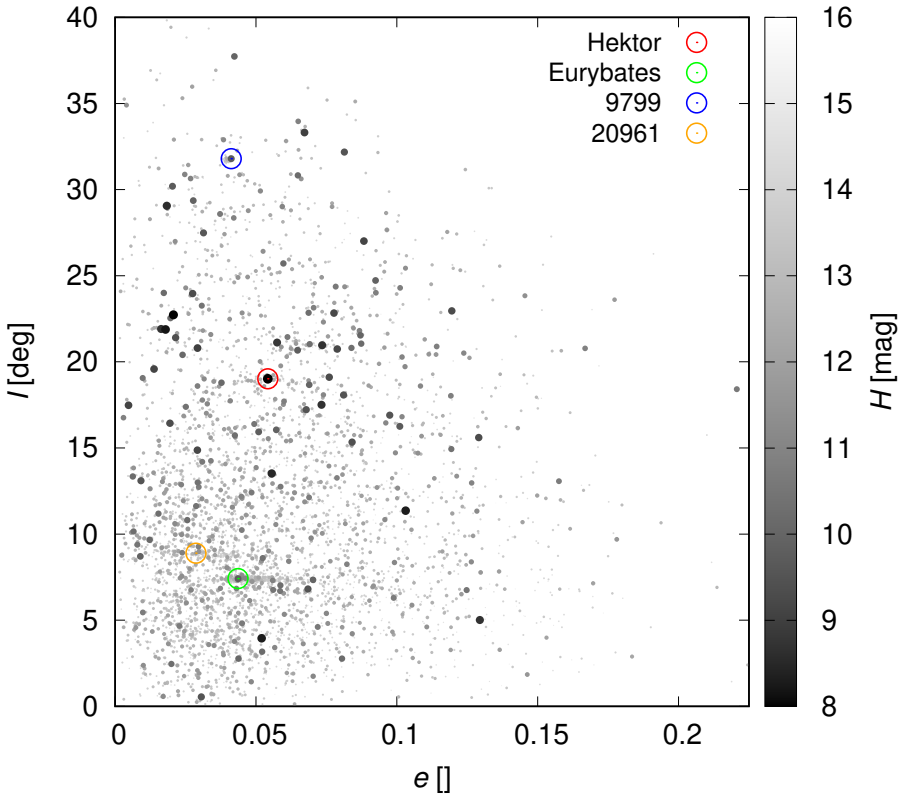


Figure 1.5: Resonant eccentricity $e$ vs. resonant inclination $I$ for $L_4$ Trojans, computed using recent catalogues (Apr 2020). Gray scale and sizes correspond to the absolute magnitude $H$. The principal bodies of asteroid families identified by Rozehnal et al. (2016) are indicated by colour.

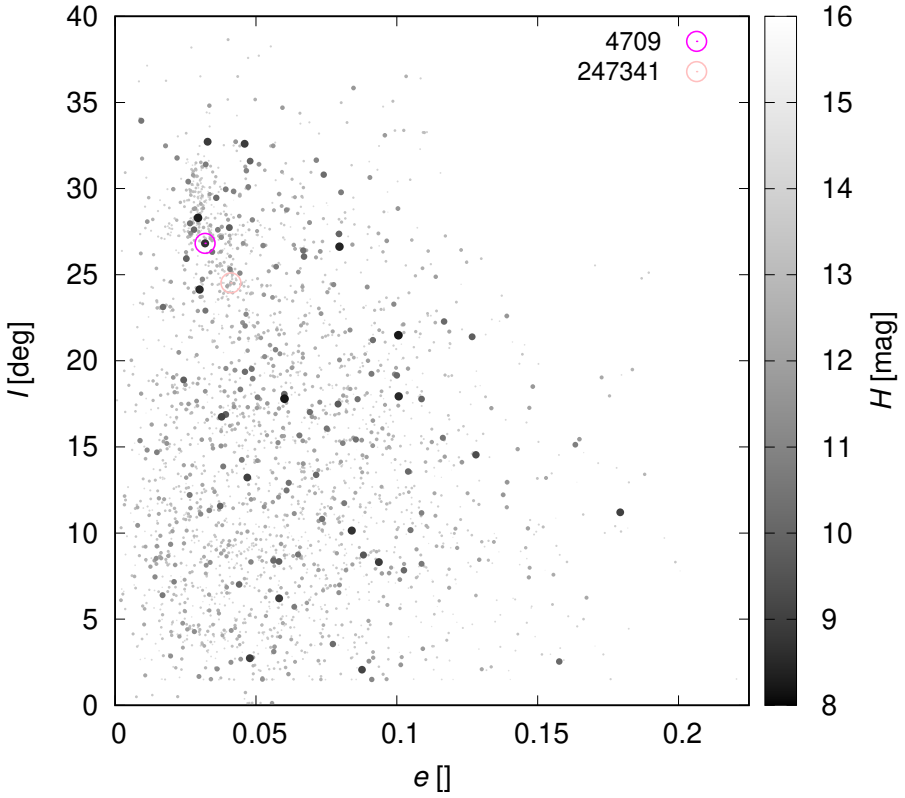


Figure 1.6: Same as Fig. 1.5 for $L_5$ Trojans.

**Selected citations to Rozehnal et al. (2016):**

**The orbit and density of the Jupiter Trojan satellite system Eurybates – Queta (Brown et al., 2021).** Detailed studies of Trojans, particularly of the respective collisional families, allow to identify interesting targets for future explorations. In our seminal work Brož and Rozehnal (2011) we showed that there is just one large collisional family — Eurybates, named after its largest remnant (3548) Eurybates. In our later work Rozehnal et al. (2016), we identified another family associated to asteroid (624) Hektor. We demonstrated this family was likely created by a cratering event and we showed that the same event could create Hektor's moonlet, described by Marchis et al. (2014). This is not a rare case, because Brown et al. (2021) determined orbital parameters of Queta — the satellite of (3548) Eurybates: $a = (2350 \pm 11)$ km, $e = 0.125 \pm 0.009$, $P = (82.46 \pm 0.06)$ days. These parameters determine the mass of Eurybates $m = (1.51 \pm 0.03) \cdot 10^{17}$ kg. As one can see, further studies of families among Trojans are still important; especially because (3548) Eurybates is the principal target of the "Lucy" spacecraft (Levison and Lucy Science Team, 2016), which is scheduled to arrive on 12 Aug 2027.

**Stability of Jovian Trojans and their collisional families (Holt et al., 2020a).** Our works could be considered as one of the starting points of Holt et al. (2020a). Their work is devoted to a study of the escape rate from the Trojan swarms. They show that bodies escape at a linear rate (23 % escape from L4 and 25 % escape from L5 over the past 4 Gy), so the population size was likely 1.31 and 1.35 times larger than today. Upon leaving the Trojan population, escaped objects move on orbits that resemble Centaurs and the short-period comet population.

Holt et al. (2020a) also found that minor families 1996 RJ and 2001 UV209, identified in our work Rozehnal et al. (2016), are dynamically stable over the lifetime of the Solar System, but Hektor, Arkesilos and Ennomos families exhibit various degrees of instability. Regarding the Eurybates family, they found 19 per cent escape. The escape rate tends to increase in the course of time, what allowed them to determine the age of the family $(1.0 \pm 0.3)$ Gy. This value is consistent with our previous estimate, based on the orbital distribution of family members, within a 1-$\sigma$ uncertainty.

**A pair of Jovian Trojans at the L4 Lagrange point (Holt et al., 2020b).** Both our works Brož and Rozehnal (2011) and Rozehnal et al. (2016), namely the so-called "randombox" method for clustering identification as well as the method for computation of resonant elements, are mentioned in the work of Holt et al. (2020b). It reports on a discovery of the first asteroid *pair*, (258656) 2002 ES76 and 2013 CC41, among Jovian Trojans. They propose that the formation mechanism of the pair is a dissociation of an ancient binary system, which was triggered by a sub-catastrophic impact, although they can not rule out a rotation fission of a single object, which was driven by the YORP torque.

**Astrocladistics of the Jovian Trojan swarms (Holt et al., 2021).** Our Randombox method, together with the list of families identified in Rozehnal et al. (2016), are mentioned in the work of Holt et al. (2021), concerned with the 'cladistics' (known from biology) of Trojans with distinctive characteristics, using colour data from the WISE, SDSS, Gaia DR2 and MOVIS surveys, including also their orbital elements. However, the number of so-called clans is larger than the number of (our) collisional families, because even a random distribution would be classified to clans.

**Colours of Jupiter Trojan dynamical families as measured by the Zwicky Transient Facility (Brown and Schemel, 2021).** Brown and Schemel (2021) used colour data from the Zwicky Transient Facility to analyze colours of proposed Trojan families. They found that the average

colours of the Eurybates family are less red than for typical Trojans, what is consistent with our work Brož and Rozehnal (2011), where the Sloan Digital Sky Survey data were analyzed, as well as Rozehnal et al. (2016), where we used albedos from the WISE infrared satellite derived by Grav et al. (2011).

**On the ages of resonant, eroded and fossil asteroid families (Milani et al., 2017).** Our methods from Rozehnal et al. (2016), namely the cutoff velocities we used to determine the number of family members, are discussed in the work of Milani et al. (2017), where they present a new classification, which identifies a number of Trojan families by using synthetic proper elements and a full hierarchical clustering method (HCM). Their results also indicate that families have a distinct structure, what is consistent with our results. Milani et al. (2017) confirmed that "Yarkovsky perturbations are ineffective in determining secular changes in all proper elements, what implies that all Trojan families are fossil families, frozen with the original field of relative velocities, possibly augmented by slow chaotic diffusion", so they have no way to estimate the upper limit of dynamical age. This is why we tried to estimate the age by comparing their distribution in the space of proper elements with long-term simulations of chaotic diffusion (see Brož et al. 2011; Rozehnal et al. 2016).

**Orbital stability close to asteroid (624) Hektor using the polyhedral model (Jiang et al., 2018).** Another part of our latter work, where we used the smoothed particle hydrodynamics (SPH) method and demonstrated that the moonlet of (624) Hektor can be created by a single impact event, is cited by Jiang et al. (2018), who calculated periodic orbits near (624) Hektor. Their results show that unstable periodic orbits exist near the surface of this largest Trojan asteroid.

**Rotationally resolved spectroscopy of Jupiter Trojans (624) Hektor and (911) Agamemnon (Perna et al., 2018).** Contrarily to what spectral observations in the literature could suggest, Perna et al. (2018) found hints of extremely homogeneous surfaces of the two largest Trojan asteroids. They did not find any water-related absorption features, nor signs of coma/outgassing, according to the analysis of complementary photometric data they acquired (with upper limits of the order of 10 kg/s for the dust production rate). Their best-fit models include amorphous carbon, magnesium-rich pyroxene and kerogen, and they put an upper limit of a few percent to the amount of surface water ice. To explain all these features, they propose several scenarios. Besides space weathering and past cometary activity, they suggest that the lack of surface heterogeneity on Hektor can be connected with the collisional event that formed the Hektor family. As they state, "the collisional dynamical family associated with Hektor has been recently attributed by Rozehnal et al. (2016) to a cratering event happened 1 to 4 Gy ago".

**Dynamical evolution of the early Solar System (Nesvorný, 2018).** This review paper compares observational constraints with models of the early evolution of the Solar System. Beside other, it underlines the importance of Trojans in the context of understanding the outer planetesimal disk and its decay during planetary migration. As Trojans could serve as a 'snapshot' of the primordial disk, it is important to know every collisional and dynamical processes that occurred during the past 4 Gy. The families identified in Brož and Rozehnal (2011) and Rozehnal et al. (2016) serve as an evidence of the ongoing collisional evolution of Trojans.

**Toward understanding the origin of asteroid geometries. Variety in shapes produced by equal-mass impacts (Sugiura et al., 2018).** The work of Sugiura et al. (2018) suggests that "irregular shapes, especially flat shapes, of asteroids with diameters larger than 80 km are

likely to be formed through similar-mass and low-velocity impacts, which are likely to occur in the primordial environment prior to the formation of Jupiter". They argue that among 20 irregularly shaped asteroids with $D > 80$ km they found in the DAMIT database (Durech et al., 2010), only three of them ((20) Massalia, (63) Ausonia, (624) Hektor) are associated to asteroid families, according to the AstDyS-2 database. Indeed, (624) Hektor is the largest remnant of a family that formed by a cratering impact, as described by Rozehnal et al. (2016).

**Origin and evolution of long-period comets (Vokrouhlický et al., 2019).** This work deals with a development of an evolutionary model of the long-period comet population, starting from their birthplace in a massive trans-Neptunian disk that was dispersed by migrating giant planets. They use the Trojan population to quantitatively calibrate the original planetesimal disk population. The key assumption in this case is that Trojans underwent only little collisional evolution after their capture, at least for the observed size range, as concluded by Rozehnal et al. (2016).

### Selected citations to Brož and Rozehnal (2011):

**Capture of Trojans by jumping Jupiter (Nesvorný and Morbidelli, 2012).** Nesvorný and Morbidelli (2012) tested a possibility that Trojans were captured during a fast dynamical instability of the outer planets. Their numerical simulations satisfactorily reproduce the orbital distribution of Trojans and their total mass and suggest that the jump capture is potentially capable of explaining the observed *asymmetry* in the number of leading and trailing Trojans. To determine the original size-frequency distribution and the original number of captured asteroids, they had to remove the Eurybates family members, as identified in our work Brož and Rozehnal (2011). On the other hand, they note that at the faint end the sample is incomplete, and the ratio of $L_4$ vs. $L_5$ bodies can be influenced by a few large collisions that generated a lot of small debris, as also suggested by Brož and Rozehnal (2011).

**Orbital clustering of Martian Trojans: An asteroid family in the inner Solar System? (Christou, 2013).** This work reports on the discovery of new Martian Trojans in the Minor Planet Center orbital catalogue. Their orbital evolution over $10^8$ y shows characteristic signatures of dynamical longevity while their average orbits resemble that of the largest known Martian Trojan, (5261) Eureka. The group is located within the region where the most stable Trojans should reside. Our work Brož and Rozehnal (2011) is mentioned in the context of rarity of local concentrations among Trojans and of the inefficient Yarkovsky effect for orbits captured in 1:1 mean-motion resonances. However, the Yarkovsky effect may be more important in Mars' case, at 1.5 au (Christou, 2013).

**Yarkovsky-driven spreading of the Eureka family of Mars Trojans (Ćuk et al., 2015).** In their paper, Ćuk et al. (2015) found that the dispersal of the Eureka cluster in eccentricity is primarily due to dynamical chaos, while the inclinations and libration amplitudes are primarily changed by the Yarkovsky effect. They conclude the cluster is a genetic family formed either by a collision or by multiple rotational fissions and they estimate the age of the family of the order of 1 Gy. They also proposed its long-term orbital evolution is likely dominated by the seasonal, rather than diurnal, Yarkovsky effect. If confirmed, Gy-scale dominance of the seasonal drift may indicate a suppression of the diurnal drift by the related YORP effect. They compare their results with our Eurybates family study (Brož and Rozehnal, 2011), where the Yarkovsky effect is present, but ineffective in secular evolution.

**Giga-year evolution of Jupiter Trojans and the asymmetry problem (Di Sisto et al., 2014).** The work of Di Sisto et al. (2014) is devoted to a study of long-term stability of Jovian

Trojans, with respect to the asymmetry of the leading and trailing clouds. The method for calculation of the proper (resonant) elements we used in Brož and Rozehnal (2011) is compared with a semi-analytical approach of Beaugé and Roig (2001). Di Sisto et al. (2014) found that both methods yield very similar results (although significant differences can be found for bodies that were not numbered in 2011, which is not so surprising). Regarding the asymmetry, authors confirm it cannot be explained by differences in chaotic diffusion between $L_4$ and $L_5$.

**The colour-magnitude distribution of Hilda asteroids: Comparison with Jupiter Trojans (Wong and Brown, 2017).** In this work, colour-magnitude distribution of the Hilda (3:2) asteroids was studied. Using photometric data listed in the SDSS catalogue, Wong and Brown (2017) confirm the previously reported bimodality of the spectral slope (in visible), indicative of two sub-populations with differing surface composition. Regarding the comparison with Jovian Trojans, the colour distributions are so similar that a common origin (and common emplacement) of Hildas and Trojans is supported. This is in accord with a dynamical instability of the outer Solar System. They also found both the Hilda and Schubart families are exclusively comprised of less red objects and note a similarity with the Eurybates family members, whose colours were analyzed in our work (Brož and Rozehnal, 2011).

**A hypothesis for the colour bimodality of Jupiter Trojans (Wong and Brown, 2016).** In their work, Wong and Brown (2016) propose a hypothesis for the origin and evolution of the Trojan population, based on the existence of two markedly different colour populations among Trojans: the 'red' (R) one and the 'less red' (LR) one. They suggest that R and LR Trojans formed in different locations, from objects which were originally 'very red' (VR) and 'red'. These primordial colours were created by the $H_2S$ sublimation boundary, when bodies closer to the Sun were depleted in $H_2S$ (on the time scale of 100 My) and bodies farther away retained $H_2S$. While primordial VR and R objects became VR and R Kuiper-belt objects (and Centaurs), Trojans captured in the vicinity of the libration points during a dynamical instability experienced a surface colour evolution, which however maintained their colour bimodality: VR $\rightarrow$ R, and R $\rightarrow$ LR. In the context of our work Brož and Rozehnal (2011), they showed the Eurybates family members belong to the class of LR objects. Wong and Brown (2016) propose that it is the result of the family-forming collision, which depleted fragments in (all) volatile ice compounds. Alternatively, if the taxonomy is closer to C-types (Fornasier et al., 2007; De Luise et al., 2010), (3458) may have been captured from the outer main belt.

**Identification of asteroid families in Trojans and Hildas (Vinogradova, 2015).** Vinogradova (2015) was partly concerned with the same goal we dealt in Brož et al. (2013) and Rozehnal et al. (2016) — the identification of families among Jupiter Trojans. Four families were found in $L_4$: (3548) Eurybates, (2148) Epeios, (624) Hektor, and (9799) $1996_{\mathrm{RJ}}$. Regarding $L_5$, no reliable families have been identified. This seems to be (partly) at odds with our conclusions, because we found four families in $L_4$, associated with asteroids (3548) Eurybates, (624) Hektor, (9799) $1996_{\mathrm{RJ}}$ and (20961) Arkesilaos; but in $L_5$, we identified two families: (4709) Ennomos (actually more associated with asteroid (17492) Hippasos), and (247341) 2001 $\mathrm{UV}_{209}$. In $L_4$, the Epeios family described in Vinogradova (2015) and the Arkesilaos family described in Rozehnal et al. (2016) are the same clusters indeed. We identified (20961) Arkesilaos as the largest remnant, because it is the only larger asteroid ($H < 12$ mag), for which the associated family has a reasonable number of members even for small values of the cutoff velocity; it is also the only larger body located near the center in the proper-element space. Regarding $L_5$, we worked with more than twice larger sample, so the clustering of small bodies was much better visible than in the sample of Vinogradova (2015).

**Different origins or different evolutions? Decoding the spectral diversity among C-type asteroids (Vernazza et al., 2017).** In this work, devoted to observations of C-type asteroids (1) Ceres and (45) Eugenia, authors discuss CM, CI, or Tagish Lake meteorites and their analogue asteroids. While CM-like are commonly observed, it is not the case for CI-like, Tagish-Lake-like, which is paradoxical, especially when the latter material is more fragile and often does not survive an atmospheric entry. Vernazza et al. (2017) suggest an explanation that CI and Tagish Lake meteorites actually represent former *interiors* of C-, P-, or D-type asteroids, which were excavated by catastrophic disruptions. They explicitly mention the Eurybates family (and cite Brož and Rozehnal, 2011) as an example of spectrally heterogeneous (C- and P-type) family. Because most of Trojans are P- and D-type, it may indicate a genetic relation similar as core/mantle/crust. However, it would be also useful to estimate the number of interlopers, which are (inevitably) expected within the proper-element-space volume occupied by the Eurybates family, and take into account the capture probability from the primordial main belt population, during the giant planet instability, which is non-zero.

# Chapter 2

# Hektor — an exceptional D-type family among Jovian Trojans

## 2.1 Introduction

Jovian Trojans are actually large populations of minor bodies in the 1:1 mean motion resonance (MMR) with Jupiter, librating around $L_4$ and $L_5$ Lagrangian points. In general, there are two classes of theories explaining their origin: i) a theory in the framework of accretion model (e.g. Goldreich et al., 2004; Lyra et al., 2009) and ii) a capture of bodies located in libration zones during a migration of giant planets (Morbidelli et al., 2005, 2010; Nesvorný et al., 2013), which is preferred in our solar system. Since the librating regions are very stable in the current configuration of planets and they are surrounded by strongly chaotic separatrices, bodies from other source regions (e.g. Main belt, Centaurs, Jupiter family comets) cannot otherwise enter the libration zones and Jupiter Trojans thus represent a rather primitive and isolated population.

Several recent analyses confirmed the presence of several families among Trojans (e.g. Nesvorný et al., 2015; Vinogradova, 2015). The Trojan region as such is very favourable for dynamical studies of asteroid families, because there is no significant systematic Yarkovsky drift in semimajor axis due to the resonant dynamics. On the other hand, we have to be aware of boundaries of the libration zone, because ballistic transport can cause a partial depletion of family members. At the same time, as we have already shown in Brož and Rozehnal (2011), no family can survive either late phases of a slow migration of Jupiter, or Jupiter "jump", that results from relevant scenarios of the Nice model (Morbidelli et al., 2010). We thus focus on post-migration phase in this paper.

We feel the need to evaluate again our previous conclusions on even larger datasets, that should also allow us to reveal as-of-yet unknown structures in the space of proper elements or unveil possible relations between orbital and physical properties (e.g. albedos, colours, diameters) of Jovian Trojans.

In Section 2.2 we use new observational data to compute appropriate resonant elements. In Section 2.3 we use albedos obtained by Grav et al. (2012) to derive size-frequency distributions and distribution of albedos, which seem to be slightly dependent on the proper inclination $I_\mathrm{p}$. In Section 2.4 we identify families among Trojans with our new "randombox" method. We discuss properties of statistically significant families in Section 2.5. Then we focus mainly on the Hektor family because of its unique D–type taxonomical classification, which is the first of its kind. We also discuss its long-term dynamical evolution. In Section 2.6 we simulate collisional evolution of Trojans and we estimate the number of observable families among Trojans. Finally, in Section 2.7 we simulate an origin of the Hektor family using smoothed-particle hydrodynamics and we compare results for single and bilobed targets. Section 2.8 is devoted to Conclusions.

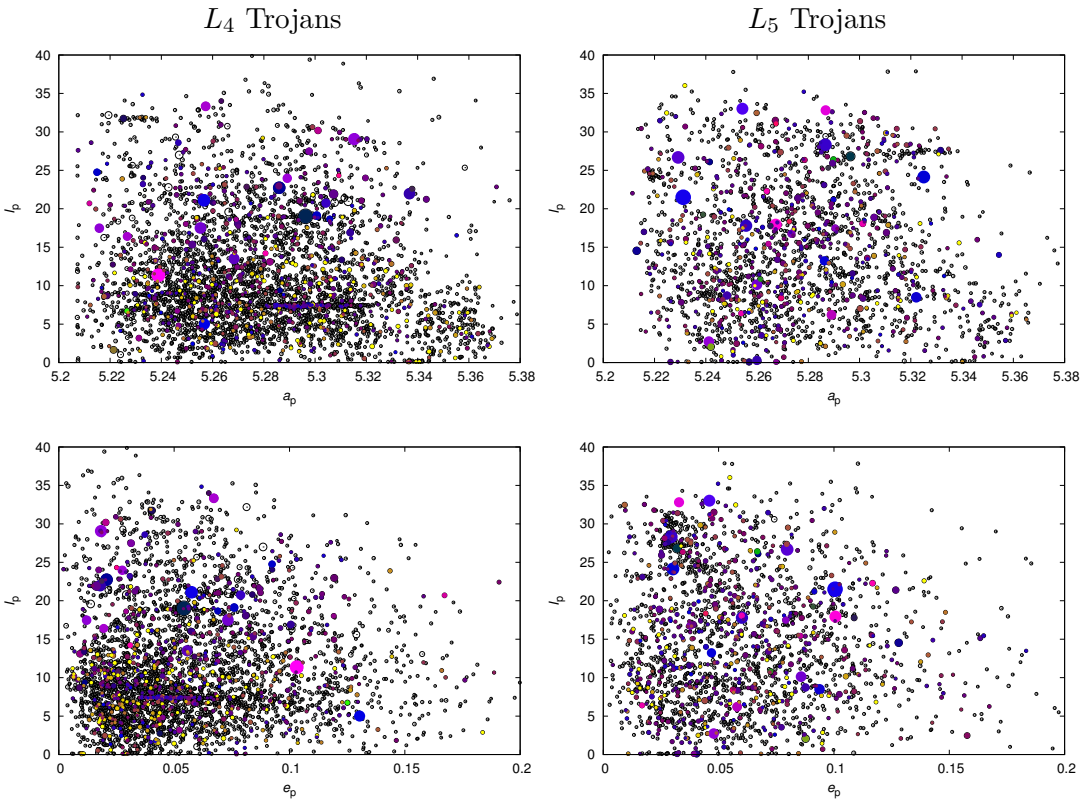


Figure 2.1: The resonant semi-major axis vs inclination $(a_\mathrm{p}, I_\mathrm{p})$ (top) and eccentricity vs inclination $(e_\mathrm{p}, I_\mathrm{p})$ (bottom) for $L_4$ (left) and $L_5$ Trojans (right). The circles indicate relative diameters of bodies, as determined by WISE (Grav et al. 2011), or when unavailable, computed from the absolute magnitude $H$ and geometric albedo $p_\mathrm{V}$, which we assumed to be $p_\mathrm{V} = 0.07$ for both the $L_4$ and $L_5$ Trojans (WISE median value is $p_\mathrm{V} = 0.072$ for $L_4$ and $p_\mathrm{V} = 0.069$ for $L_5$ Trojans). Colours correspond to the values of $p_\mathrm{V}$, blue are dark ($p_\mathrm{V} \simeq 0.05$) and yellow are bright ($p_\mathrm{V} \simeq 0.25$). One can see clearly all asteroid families on this plot, especially in $(a_\mathrm{p}, I_\mathrm{p})$, because they tend to be confined in inclinations.

## 2.2 New observational data

### 2.2.1 Resonant elements

We computed resonant elements, i.e. the averaged semimajor axis $\bar{a}$, libration amplitude $\Delta a_\mathrm{p}$, eccentricity $e_\mathrm{p}$ and inclination $I_\mathrm{p}$ of 3907 Trojans in $L_4$ cloud and 1945 Trojans in $L_5$ cloud. As an input, we used osculating elements listed in AstOrb catalogue (Bowell et al., 2002), released in July 2014. A detailed description of the resonant elements computation can be found in Brož & Rozehnal (2011). Positions of Trojans in the space of proper elements $(a_\mathrm{p},\ I_\mathrm{p})$, where $a_\mathrm{p} = \bar{a} + \Delta a_\mathrm{p}$, and $(e_\mathrm{p},\ I_\mathrm{p})$, calculated with a suitably modified version of the SWIFT integrator (Levison and Duncan, 1994), are presented graphically in Figure 2.1, together with their sizes and albedos. [1]

### 2.2.2 WISE and AKARI albedos and diameters

To construct size-frequency distributions of the whole $L_4$ and $L_5$ Trojan populations and later of individual families, we mostly used WISE albedos and diameters derived by Grav et

[1] The table of resonant elements is listed online at `http://sirrah.troja.mff.cuni.cz/~mira/mp/trojans/`.

al. (2012). We also compared the respective values to AKARI (Usui et al., 2011).[2]

We used albedo values of 1609 Trojans in both $L_4$ and $L_5$ clouds obtained by WISE; about one third of these albedos were obtained during cryo-phase, the rest were measured in post-cryo-phase (see Grav et al., 2011).

## 2.3 Physical characterisation of Trojan populations

### 2.3.1 Albedo distribution and taxonomy

The values of visible albedos $p_{\rm V}$ of Trojans derived by Grav et al. (2012) vary in the range from $p_{\rm V} = 0.025$ to $p_{\rm V} \simeq 0.2$. Distributions of albedos are qualitatively the same for both $L_4$ and $L_5$ populations. The median albedo of WISE sample is $\widetilde{p}_{\rm v} = 0.072 \pm 0.017$ for $L_4$ and $\widetilde{p}_{\rm v} = 0.069 \pm 0.015$ for $L_5$. These values of visible albedos mostly correspond to C or D taxonomical classes in Tholen taxonomic classification scheme (Mainzer et al., 2011). However, there is a significant presence of small asteroids ($D < 15\,$km) with apparently high albedo — almost 20 % of asteroids in $L_4$ and 13 % of asteroids in $L_5$ have albedo $p_{\rm V} > 0.10$. As stated in Grav et al. (2012), this is probably not a physical phenomenon, it is rather due to the fact that for small diameters the photon noise contribution becomes too significant.

When we compute the median albedo from AKARI data, we realize that its value is slightly lower ($\widetilde{p}_{\rm v} = 0.054 \pm 0.005$) than that from WISE, but when we compute the median from WISE values for the same asteroids which are listed in AKARI catalogue, we obtain a similar value ($\widetilde{p}_{\rm v} = 0.061 \pm 0.012$). What is more serious, AKARI and WISE data differ considerably for large asteroids with $D > 100\,$km — the average difference between albedos is $|p_{\rm V_{AKARI}} - p_{\rm V_{WISE}}| = 0.02$. The same difference we see in derived diameters. These discrepancies may be caused for example by limitations of the thermal model (cf. spheres in NEATM models). Hereinafter, we prefer to use the WISE data when available, because they represent orders of magnitude larger sample than AKARI.

When we split Trojan asteroids according to their albedo into two rather artificial subpopulations with $p_{\rm V} < 0.08$ and $p_{\rm V} > 0.08$ respectively, and then we compute distributions of these subpopulations with respect to the resonant inclination $I_{\rm p}$, we get two different pictures. As can be seen in Figure 2.2, most bodies have resonant inclinations $I_{\rm p} < 15°$, but there are 77 % of bodies with higher albedo with $I_{\rm p} < 15°$, while only 55 % of the population with lower albedo is located in the same range of inclinations. This is a similar phenomenon as described by Vinogradova (2015), who reported different upper limits in inclinations for different taxonomical types obtained mostly from SDSS colour data.

### 2.3.2 Size-frequency distributions

The WISE data (Grav et al. 2011, 2012) provide very useful source of information on diameters we need to construct size-frequency distributions (SFDs) of Trojan populations in $L_4$ and $L_5$. However, the sample measured by WISE is not complete. In our previous work (Brož and Rozehnal, 2011), we constructed the SFDs assuming a constant albedo which we set to be equal to the median albedo of Trojans that was measured back then. Since the number of measurements was very low (several tens), this was the only reasonable way. Now we choose another method to construct more reliable SFDs. As we calculated resonant elements for more than 5800 Trojans and we have more than one quarter of appropriate albedos, we constructed the SFDs by assigning albedos randomly from the observed WISE distribution to the remaining Trojans, whose albedo was not measured. To avoid a bias, we compared different SFDs constructed with different random generator seeds and we realized that the

[2]While there are some differences between individual values even at $3\sigma$ level, they do not seem to be important for population studies like ours.

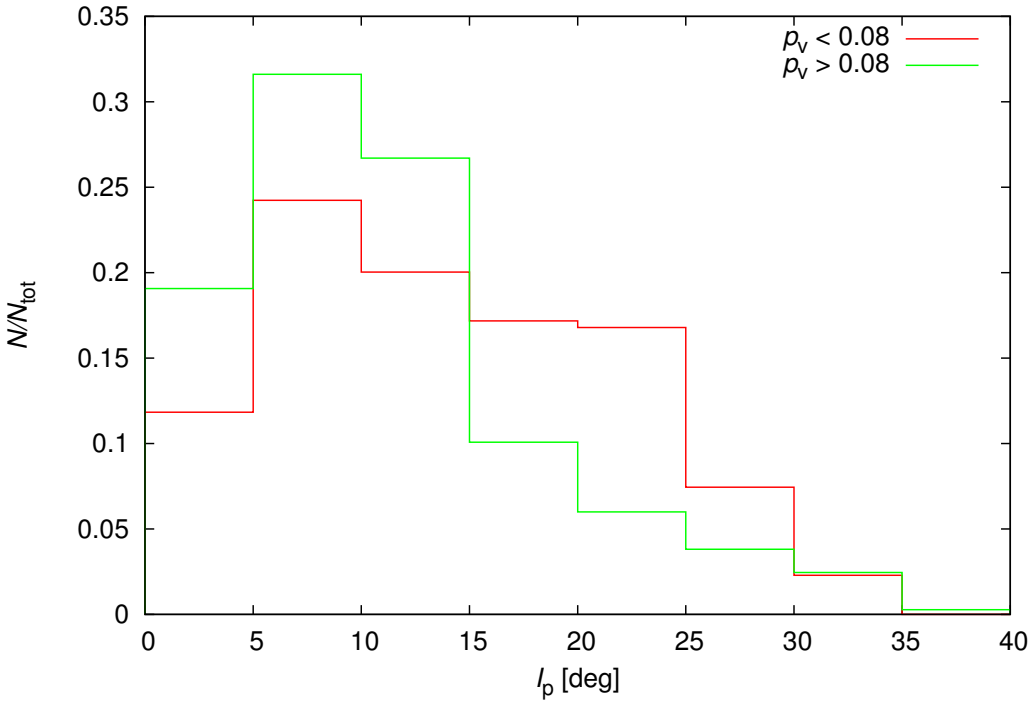


Figure 2.2: The differential histogram of the resonant inclination $I_\mathrm{p}$ for $L_4$ Trojans with a lower albedo ($p_\mathrm{V} < 0.08$, red) and a higher one ($p_\mathrm{V} > 0.08$, green). Eurybates family was removed from the dataset.

overall shape of SFDs does not change noticeably, the slope $\gamma$ varies in the range of $\pm 0.1$ at most. The SFDs we constructed this way are shown in Figure 2.3.

The SFDs for the $L_4$ and $L_5$ clouds look slightly different, especially in the size range from 60 km to 100 km. This part of the SFD is not influenced by the Eurybates family, the largest family among Trojans, because all its members have diameters $D < 50$ km. We used these SFDs to determine the ratio of the number of asteroids in $L_4$ and $L_5$ clouds. There are 2746 asteroids with diameter $D > 8$ km in $L_4$ and 1518 asteroids in $L_5$. When we remove all family members with diameters $D > 8$ km, we have 2436 asteroids in $L_4$ and 1399 in $L_5$. However, this sample may be still influenced by debris produced by catastrophic disruptions of small bodies ($D \geq 50$ km), which need not to be seen as families. Counting only asteroids with diameter $D > 20$ km, which corresponds to the absolute magnitude $H \simeq 12$, and removing family members, we get the ratio $N_{L_4}/N_{L_5} = 1.3 \pm 0.1$. As this is entirely consistent with value of Nesvorný et al. (2013), which was derived for Trojans with $H > 12$, and with Grav et al. (2012), whose estimate is $N_{L_4}/N_{L_5} = 1.4 \pm 0.2$, we can confirm a persisting asymmetry between the number of $L_4$ and $L_5$ Trojans in new data. Although for bodies with diameter $D > 100$ km, the $L_5$ cloud has more asteroids than $L_4$, the total number of these bodies is of the order of 10, so this is just an effect of small-number statistics and does not affect the $N_{L_4}/N_{L_5}$ ratio much.

## 2.4 Families detection methods

A brief inspection of the resonant-element space ($a_\mathrm{p}$, $e_\mathrm{p}$, $I_\mathrm{p}$) (see Figure 2.1), reveals several locations with higher concentrations of bodies. These could be collisional families, created by a disruption of a parent body during a random collision, but they could also originate randomly by chaotic diffusion and due to effects of secular and high-order resonances. To

$L_4$ Trojans

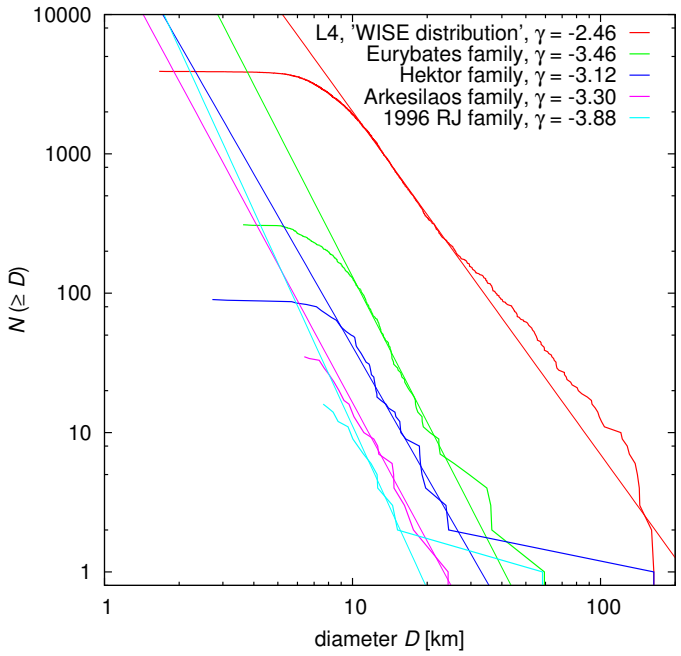


$L_5$ Trojans

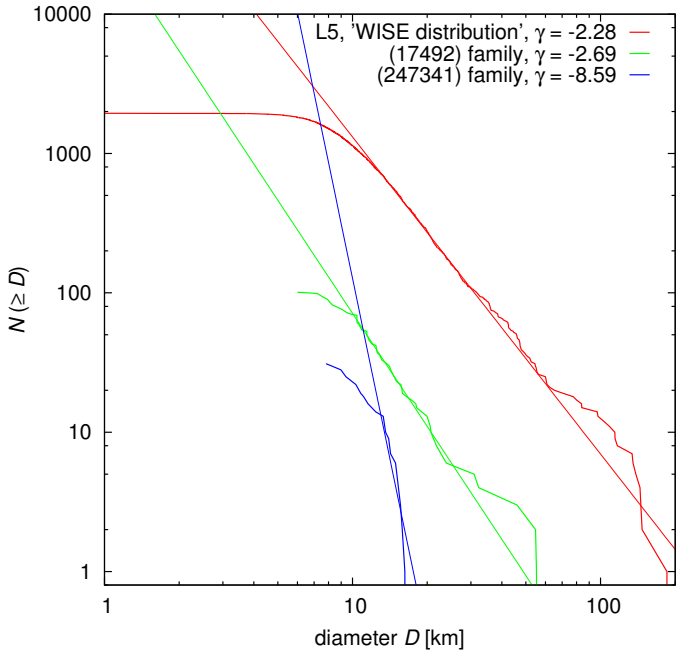


Figure 2.3: Size-frequency distributions for both $L4$ and $L_5$ Trojans, constructed using the albedos measured by WISE satellite (Grav et al. 2012). Since WISE data cover just about 18 % of $L_4$ and 29 % of $L_5$ Trojans known today, we assigned albedos randomly from the WISE distribution to the remaining Trojans. We also present SFDs of individual asteroid families discussed in the main text. There are also our fits of each SFD in the range $D = 12$ to 30 km by the power law $N(> D) = CD^{\gamma}$. As we can see, both clouds seem to be near the collisional equilibrium ($\gamma \simeq -2.5$, Dohnanyi 1969), while most families have slope $\gamma$ significantly steeper. Of course, we can expect the slopes of the SFDs become shallower for smaller $D$ due to observational incompleteness.

Table 2.1: Physical properties of Trojan families identified by both the "randombox" and the HCM methods. We list Family Identification Number (FIN, as in Nesvorný et al., 2015), the designation of the family, the designation of the asteroid with which the family is associated (i.e. usually the largest remnant of the parent body), the cutoff velocity $v_{\mathrm{cutoff}}$, for which family is still clearly detached from the background, and the number of members of the family $N_{\mathrm{memb}}$ corresponding to the respective $v_{\mathrm{cutoff}}$. Next we list optical albedos $p_{\mathrm{V}}$ of associated bodies determined by Grav et al. (2012) from WISE observations, and their taxonomical classification.

| FIN | family designation | cloud | asteroid designation | $v_{\mathrm{cutoff}}[\mathrm{m\,s^{-1}}]$ | $N_{\mathrm{memb}}$ | $p_{\mathrm{V}}$(WISE) | tax. type |
|---|---|---|---|---|---|---|---|
| 004 | Hektor | $L_4$ | (624) Hektor | 110 | 90 | $0.087 \pm 0.016$ | D |
| 005 | Eurybates | $L_4$ | (3548) Eurybates | 60 | 310 | $0.060 \pm 0.016$ | C/P |
| 006 | 1996 RJ | $L_4$ | (9799) 1996 RJ | 140 | 17 | $0.082 \pm 0.014$ | – |
| 008 | Arkesilaos | $L_4$ | (20961) Arkesilaos | 55 | 35 | n/a | – |
| 009 | Ennomos | $L_5$ | (17492) Hippasos | 100 | 104 | $0.064 \pm 0.012$ | – |
| 010 | 2001 $\mathrm{UV}_{209}$ | $L_5$ | (247341) 2001 $\mathrm{UV}_{209}$ | 120 | 30 | $0.088 \pm 0.023$ | – |

→ 20 →

Table 2.2: Derived properties of Trojan families. We list here the family designation, the diameter of the largest remnant $D_{\rm LR}$, the minimal diameter of the parent body min $D_{\rm PB}$, obtained as the sum of all observed family members, the diameter of the parent body $D_{\rm PB(SPH)}$ and the mass ratio $M_{\rm LR}/M_{\rm PB}$ of the largest fragment and the parent body, both derived from our fits by scaled SPH simulations performed by Durda et al. (2007). We use this ratio to distinguish between the catastrophic disruption ($M_{\rm LR}/M_{\rm PB} < 0.5$) and the cratering ($M_{\rm LR}/M_{\rm PB} > 0.5$). Finally, there is the escape velocity $v_{\rm esc}$ from the parent body and estimated age of the family derived in this and our previous work (Brož and Rozehnal, 2011).

→ 21 ←

| family desig. | $D_{\rm LR}$ [km] | min $D_{\rm PB}$ | $D_{\rm PB(SPH)}$ | $M_{\rm LR}/M_{\rm PB}$ | $v_{\rm esc}[{\rm m\,s^{-1}}]$ | age [Gyr] | notes, references |
|---|---|---|---|---|---|---|---|
| Hektor | $250 \pm 26$ | 250 | 257 | 0.92 | 73 | 0.3 or 3 | 1, 3 |
| Eurybates | $59.4 \pm 1.5$ | 100 | 155 | 0.06 | 46 | 1.0 to 3.8 | 2 |
| 1996 RJ | $58.3 \pm 0.9$ | 61 | 88 | 0.29 | 26 | – | 2,4 |
| Arkesilaos | $24 \pm 5$ | 37 | 87 | 0.02 | 16 | – | 2 |
| Ennomos | $55.2 \pm 0.9$ | 67 to 154 | 95 to 168 | 0.04 to 0.19 | 29 to 66 | 1 to 2 | 2, 5 |
| 2001 $UV_{209}$ | $16.3 \pm 1.1$ | 32 | 80 | 0.01 | 14 | – | 2 |

[1] $D_{\rm LR}$ derived by Marchis et al. (2014), [2] $D_{\rm LR}$ derived by Grav et al. (2012), [3] bilobe, satellite (Marchis et al. 2014), [4] very compact, Brož and Rozehnal (2011), [5] $D_{\rm PB}$ strongly influenced by interlopers, [6] The largest fragment of Ennomos family is (17492) Hippasos.

be regarded as a family, the cluster must comply with, inter alia, the following criteria: i) it must be concentrated in the space of proper elements; ii) the cluster must have the SFD different from that of the whole $L_4$ and $L_5$ population; iii) the last criterion is usually spectral, or at least, albedo homogeneity of family members, but so far, there are not enough sufficiently accurate data for Trojans, especially for bodies with diameters $D < 50\,\mathrm{km}$, which usually form a substantial part of Trojan families. Therefore we cannot perform any detailed spectral analysis in this work.

We analyzed the space of resonant elements both in terms of mutual distances among bodies and in terms of statistical probability that clusters are *not* random.

### 2.4.1 Randombox method

Besides the commonly used hierarchical clustering method (HCM, Zappala et al., 1990) (HCM, Zappalà et al., 1990), we applied a "randombox" method, based on numerical Monte-Carlo simulations. This method allows us to compute the statistical significance of the clusters, i.e. the probability that the cluster is a random concentration of bodies in the space of proper elements $(a_\mathrm{p}, e_\mathrm{p}, \sin I_\mathrm{p})$.

We divided the space of proper elements into equally sized "boxes" with dimensions $\Delta a_\mathrm{p} = 0.025\,\mathrm{au}$, $\Delta e_\mathrm{p} = 0.2$ and $\Delta \sin I_\mathrm{p} = 0.025$. Then we created $N = 100,000$ random distributions of the same number of bodies which are observed together in the given box and two adjacent boxes (in the direction of the $y$-axis, cf. Figure 2.4), and we counted number of positive trials $N^+$, for which the randomly generated number of bodies in the central box was larger than the observed one. From here we can calculate the probability $P_\mathrm{rnd}$, that the observed number of bodies in the box is random: $P_\mathrm{rnd} = N^+/N$.

Alternatively, one can also use our analytical formula:

$$p_\mathrm{rnd} = \frac{\sum_{k=n_2}^{n} C(n,k) V'(n_\mathrm{box}-1, n-k)}{V'(n_\mathrm{box}, n)}\,, \tag{2.1}$$

where $n$ denotes the total number of bodies, $n_\mathrm{box}$ is the total number of boxes (3 in our case), $n_2$ is the observed number of bodies in the middle box, $k$ is the number of observed bodies in the current box, $C(n,k)$ are combinations without repetitions, i.e. the total number of trials to select $k$ bodies observed in the current box from the total number of $n$ bodies; $V'(n_\mathrm{box}-1, n-k)$ are variations with repetitions, i.e. the total number of trials to distribute the remaining bodies into the remaining boxes; and $V'(n_\mathrm{box}, n)$ are also variations with repetitions, i.e. the total number of trials to distribute all $n$ bodies into all $n_\mathrm{box}$ boxes. We verified the results of the analytical formula (2.1) by the MC method.

We plot the results in Figure 2.4 for both the $L_4$ and $L_5$ clouds. In comparison with Figure 2.1, one can see that for all clusters we identified as families the probability $P_\mathrm{rnd}$ varies between $2 \cdot 10^{-3}$ and $5 \cdot 10^{-5}$, i.e. the probability that clusters are random fluctuations is indeed very low.

We also re-evaluated all families identified by the hierarchical clustering method using the "randombox" method, which makes our decision whether the cluster is a real family much more quantitative.

### 2.4.2 Hierarchical clustering method

We also used the HCM independently to extract significant clusters. Families identified by both the "randombox" and HCM methods are listed in Table 2.1. For each family, we constructed a dependence of the number of members of the cluster $N_\mathrm{memb}$ on the cutoff velocity $v_\mathrm{cutoff}$. Because the number of members of a real collisional family rises first slowly with rising $v_\mathrm{cutoff}$ (Brož and Rozehnal, 2011) — in contrast with random clusters which are merging very quickly with the background — the constructed dependence allows us to guess

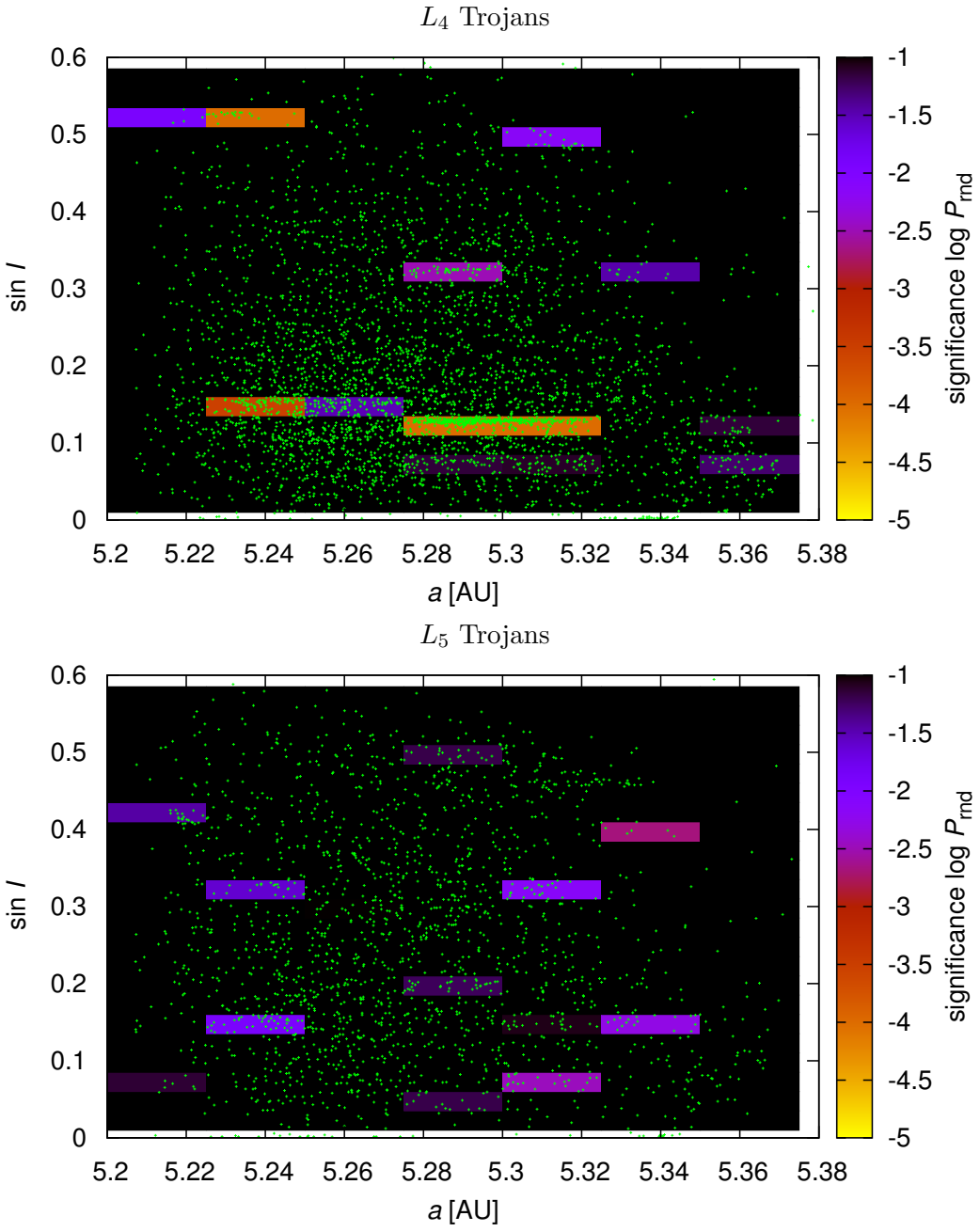


Figure 2.4: The statistical significance $p$ expressed as colour on the logarithmic scale for observed asteroids in the proper semi-major axis vs proper inclination plane $(a_{\rm p}, \sin I_{\rm p})$ (i.e. the same data as in Figure 2.1). $L_4$ Trojans are on the top, $L_5$ Trojans on the bottom. We computed the values of $p$ for 7 times 18 boxes using our "randombox" method The range in proper eccentricity is 0.00 to 0.20. Statistically significant groups appear as orange boxes and they correspond to the families reported in Table 2.1.

a realistic number of family members $N_{\rm memb}$. For all families listed in Table 2.1 we were convinced that they fulfill this criterion. However, we cannot distinguish possible interlopers this way, and it is also possible that some fraction of family members with high $v_{\rm cutoff}$ (so called halo, as in Brož and Morbidelli, 2013) remains unidentified in the surrounding background.

## 2.5 Properties of statistically significant families

### 2.5.1 Eurybates

As we have already demonstrated in Brož and Rozehnal (2011), the family associated with asteroid (3548) Eurybates is the largest collisional family, and it is the only family among Trojans with the parent body size $D_{\rm PB} > 100\,{\rm km}$, which originated by a catastrophic disruption (this means that the mass ratio of the largest remnant to the parent body $M_{\rm LR}/M_{\rm PB} < 0.5$).

Using new albedos derived by Grav et al. (2012), we recalculated the overall SFD slope of the family to be $\gamma = -3.4 \pm 0.1$. As the WISE sample provides albedos for only about 1/5 of the family members, we calculated two values of $\gamma$: the first one assuming that remaining asteroids have a constant albedo $p_{\rm V} = 0.06$, the second one by assigning albedos randomly from the WISE distribution, as described in Section 2.3.2. Both values are equal within their errorbars. The new slope $\gamma$ is significantly steeper than our previous calculation ($\gamma = -2.5 \pm 0.1$), derived with the assumption of a constant albedo of all members of the family. The lower value was most likely caused by a significant observational incompleteness in the size range from $D = 12\,{\rm km}$ to $D = 30\,{\rm km}$.

We also derived the new value of the parent body diameter, which is still above the limit of 100 km. An extrapolation of the SFD by a power law gives the value $D_{\rm PB} \simeq 140\,{\rm km}$. By fitting the synthetic SFDs from SPH simulations (Durda et al., 2007), we obtained the value $D_{\rm PB(SPH)} \simeq 155\,{\rm km}$.

### 2.5.2 Hektor — the first D–type family

Since asteroid (624) Hektor is a close binary with a satellite (Marchis et al., 2014), i.e. an exceptional object, we want to address its association with the family. The cluster around the largest Trojan asteroid appears in the space of proper elements as a relatively compact group, which is limited particularly in proper inclinations, $I_{\rm p} \in \langle 18.13^\circ; 19.77^\circ \rangle$, and with resonant semimajor axes located in the interval $a_{\rm p} \in \langle 5.234; 5.336 \rangle$ au. The number of members of this group slowly increases with increasing cutoff velocity up to $v_{\rm cutoff} \simeq 110\,{\rm m\,s^{-1}}$, above which it quickly joins the background. With our randombox method, we estimated the probability that the family is just a random fluke to be as low as $P_{\rm rnd} \simeq 2 \cdot 10^{-3}$.

The nominal diameter of asteroid (624) Hektor derived from its albedo is 164 km (Grav et al., 2012), but the albedo measured by AKARI $p_V = 0.034 \pm 0.001$ (Usui et al., 2011) totally differs from that measured by WISE, $p_V = 0.087 \pm 0.016$. and these values do not match even within the error limits. This may be caused by applying a thermal model assuming spheres to the bilobed shape of the asteroid (Marchis et al., 2014). We hence do not determine Hektor's diameter from its albedo, but from fits of Marchis et al. (2014), which effective value $D = (250 \pm 26)\,{\rm km}$ is suitable within its uncertainty for all possible geometries (convex, bilobe and binary). For other bodies in family we use a nominal value $p_{\rm V} = 0.072$, which is the median of WISE measurements.

Asteroid (624) Hektor is often classified as D-type (e.g. Cruikshank et al., 2001; Emery et al., 2006, 2011). We tried to evaluate taxonomical classification of other family members and we have found colours for two more expected family members in SDSS-MOC version 4 (Ivezic et al., 2002): asteroids (65000) 2002 AV63 and (163702) 2003 FR72. Even though the photometric noise in individual bands is not negligible ($\sigma_i = 0.02\,{\rm mag}$ up to $\sigma_u = 0.12\,{\rm mag}$)

both of them are D-types, with principal components (aka slopes) $PC_1 > 0.3$. This seems to support the D-type classification of the whole family.

We also tried to constrain the taxonomic classification of the family members by comparing their infrared albedos $p_{IR}$ and visual albedos $p_V$ as described in Mainzer et al. (2011), but there are no data for family members in the W1 or W2 band of the WISE sample, which are dominated by reflected radiation.

The fact that we observe a collisional family associated with a D–type asteroid is the main reason we use word "exceptional" in connection with the Hektor family. As we claimed in Brož et al. (2013), in all regions containing a mixture of C–type and D–type asteroids (e.g. Trojans, Hildas, Cybeles), there have been only C–type families observed so far, which could indicate that disruptions of D–type asteroids leave no family behind, as suggested by Levison et al. (2009). Nevertheless, our classification of the Hektor family as D–type is not in direct contradiction with this conclusion, because Levison et al. (2009) were concerned with catastrophic disruptions, while we conclude below that the Hektor family originated from a cratering event, i.e. by an impactor with kinetic energy too small to disrupt the parent body.

**Simulations of long-term dynamical evolution**

To get an upper limit of the age of the Hektor family, we simulated a long-term evolution of *seven synthetic families* created for different breakup geometries. Our model included four giant planets on current orbits, integrated by the symplectic integrator SWIFT (Levison and Duncan, 1994), modified according to Laskar and Robutel (2001), with the time step of $\Delta t = 91$ days and time span 4 Gyr.

We also accounted for the Yarkovsky effect in our simulations. Although in a first-order theory, it is not effective in zero-order resonances (it could just shift libration centre, but there is no systematic drift in semimajor axis) and the observed evolution of proper elements is mainly due to chaotic diffusion, in higher-order theories the Yarkovsky effect can play some role. In our model, we assumed a random distribution of spins and rotation periods (typically several hours), the bulk and surface density $\rho_{bulk} = \rho_{surf} = 1.3\ \mathrm{g\,cm^{-3}}$, the thermal conductivity $K = 0.01\ \mathrm{W\,m^{-1}\,K^{-1}}$, the specific heat capacity $C = 680\ \mathrm{J\,kg^{-1}\,K^{-1}}$, the Bond albedo $A_B = 0.02$ and the IR emissivity $\epsilon = 0.95$.

We created each synthetic family by assigning random velocities to 234 bodies (i.e. 3 times more than the number of the observed family members), assuming an isotropic velocity field with a typical velocity of $70\ \mathrm{m\,s^{-1}}$, corresponding to the escape velocity from parent body (Farinella et al., 1993). Here we assumed the velocity of fragments to be size independent. Possible trends in the ejection velocity field cannot be easily revealed in the $(a, H)$ space in the case of the Hektor family, because of its origin by a cratering event – there is a large gap in the range between absolute magnitude of (624) Hektor ($H = 7.20$) and other bodies ($H > 11.9$), so we are not able to distinguish a simple Gaussian dispersion from the physical dependence (cf. Carruba and Nesvorný, 2016). Either way, we are interested in the orbital distribution of *mostly* small bodies. Our assumption of size-independent ejection velocity is also in good agreement with results of SPH models (see Subsection 2.7.3 and Figure 2.13).

To create a synthetic family in the same position as occupied by the observed Hektor family, we integrated the orbit of asteroid (624) Hektor with osculating elements taken from AstOrb catalogue (Bowell et al., 2002), until we got appropriate values of the true anomaly $f$ and the argument of pericentre $\omega$. We tried values of $f$ ranging from 0° to 180° with the step of 30° and $\omega$ always satisfying the condition $f + \omega = 60°$, i.e. we fixed the angular distance from the node to ensure a comparably large perturbations in inclinations.

Initial positions of synthetic families members just after the disruption, compared to the observed Hektor family, are shown in Figure 2.5. To make a quantitative comparison of the distribution in the space of proper elements, we used a two-dimensional Kolmogorov–Smirnov test to compute KS distance of the synthetic family to the observed one with the

output timestep of 1 Myr. The results for different initial geometries are shown in Figure 2.6.

Our two best fits corresponding to the lowest KS distance are displayed in Figure 2.7. As we can see from the image of the whole Trojan L4 population, Hektor seems to be near the outskirts of the librating region (cf. Figure 2.1). In Figure 2.5, we can note, that there are almost no observed asteroids in the shaded area with $a_\mathrm{p} > 5.32\,\mathrm{au}$, but we can see some synthetic family members in the left panel of Figure 2.7 (initial geometry $f = 0°$, $\omega = 60°$).

On the other hand, when we look at right panel of Figure 2.7 (initial geometry $f = 150°$, $\omega = 270°$), we can see that there are many fewer bodies in the proximity of the border of the stable librating region. One can also see the initial "fibre-like" structure is still visible on the left, but is almost dispersed on the right.

Hence, we conclude that the geometry at which the disruption occurred is rather $f = 150°$, $\omega = 270°$ and the corresponding age is between 1 and 4 Gyr. The second but less likely possibility is that the disruption could have occured more recently (0.1 to 2.5 Gyr) at $f = 0°$, $\omega = 60°$.

#### Parent body size from SPH simulations

We tried to estimate the parent body size of Hektor family and other families by the method described in Durda et al. (2007). To this point, we calculated a pseudo$-\chi^2$ for the whole set of synthetic size-frequency distributions as given by the SPH simulations results (see Figure 2.8).

Parent body sizes $D_{\mathrm{PB(SPH)}}$ and mass ratios of the largest fragment and parent body $M_\mathrm{LF}/M_\mathrm{PB}$ estimated by this method are listed in Table 2.2. The parent body size for Hektor family we derived from SPH simulations is $D_{\mathrm{PB(SPH)}} = (260 \pm 10)\,\mathrm{km}$, the impactor diameter $D_\mathrm{imp} = (24 \pm 2)\,\mathrm{km}$, the impactor velocity $v_\mathrm{imp} = (4 \pm 1)\,\mathrm{km\,s^{-1}}$ and the impact angle $\varphi_\mathrm{imp} = (60° \pm 15°)$. We will use these values as initial conditions for simulations of collisional evolution below.

### 2.5.3 1996 RJ — extremely compact family

In our previous work, we mentioned a small cluster associated with asteroid (9799) 1996 RJ, which consisted of just 9 bodies. With the contemporary sample of resonant elements we can confirm that this cluster is indeed visible. It is composed of 18 bodies situated near the edge of the librating zone on high inclinations, within the ranges $I_\mathrm{p} \in \langle 31.38°; 32.27° \rangle$ and $a_\mathrm{p} \in \langle 5.225\,;\, 5.238 \rangle$ au. As it is detached from the background in the space of proper elements, it remains isolated even at high cutoff velocity $v_\mathrm{cutoff} = 160\,\mathrm{m\,s^{-1}}$.

Unfortunately, we have albedos measured by WISE for just 4 members of this family. These albedos are not much dispersed. They range from $p_\mathrm{V} = 0.079 \pm 0.019$ to $p_\mathrm{V} = 0.109 \pm 0.029$ and, compared to the median albedo of the whole $L_4$ population $\widetilde{p_\mathrm{V}} = 0.072 \pm 0.017$, they seem to be a bit brighter, but this statement is a bit inconclusive.

### 2.5.4 Arkesilaos

This family is located on low inclinations $I_\mathrm{p} \in \langle 8.52°; 9.20° \rangle$, in the range of major semi-axes $a_\mathrm{p} \in \langle 5.230\,;\, 5.304 \rangle$ au. It is clearly visible in the space of proper elements, although this area of $L_4$ cloud is very dense.

Still, it is difficult to find the largest remnant of the parent body, because this region is populated mainly by small asteroids with absolute magnitudes $H > 12$. The only four asteroids with $H < 12$ are (2148) Epeios with $H = 10.7$, (19725) $1999\,\mathrm{WT_4}$ with $H = 10.7$, (38600) $1999\,\mathrm{XR_{213}}$ with $H = 11.7$ and (20961) Arkesilaos with $H = 11.8$. The only diameter derived from measured albedo is that of (2148) Epeios, which is $D = (39.02 \pm 0.65)\,\mathrm{km}$. Diameters of remaining bodies were calculated from their absolute magnitude

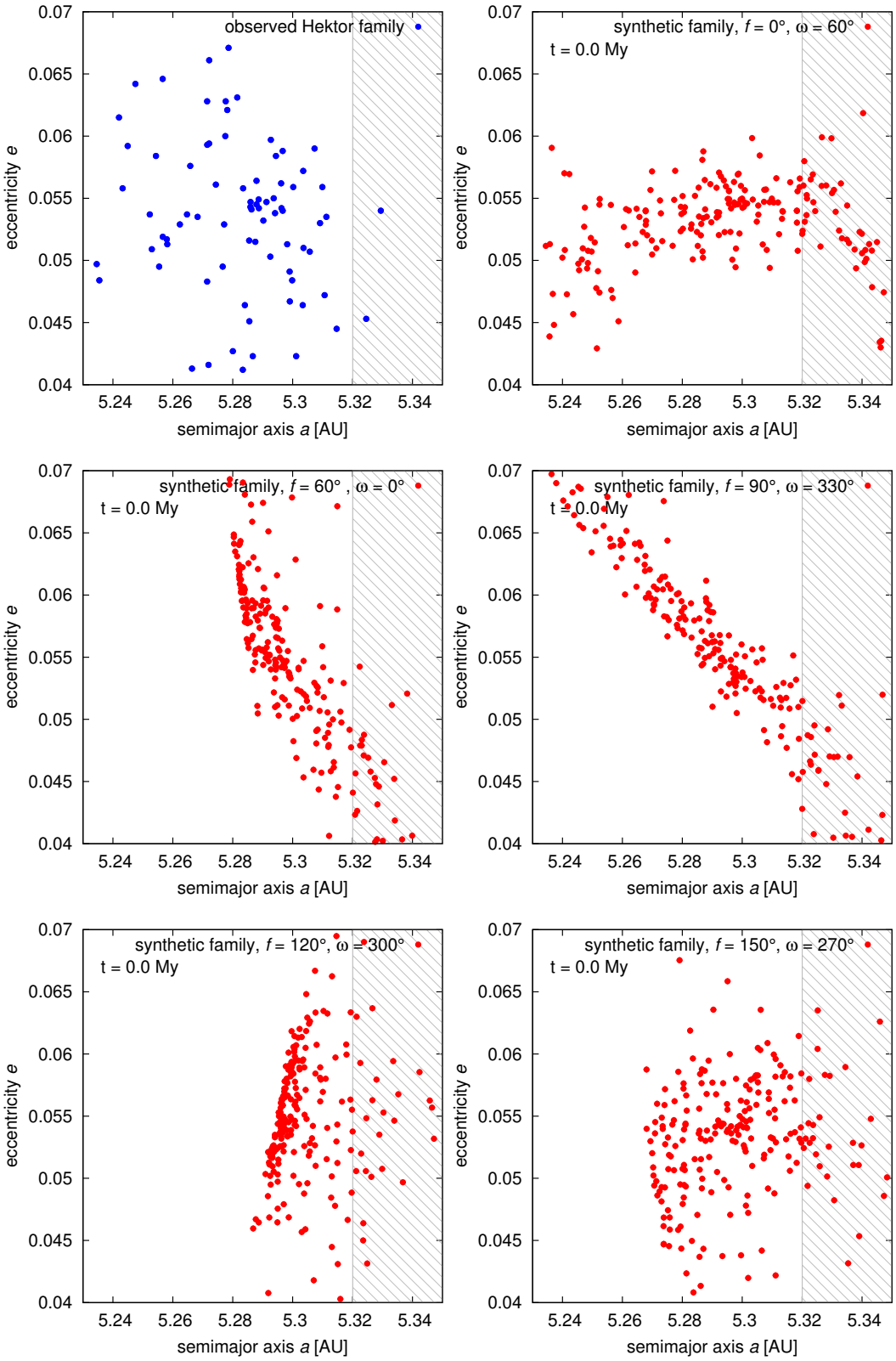


Figure 2.5: Initial conditions for simulations of long-term evolution of synthetic families (red), compared to the observed Hektor family (blue) in the space of proper elements $(a_\mathrm{p}, e_\mathrm{p})$. Each figure shows a different disruption geometry with different values of the true anomaly $f$ and the argument of pericentre $\omega$. Note the shaded area in the top left figure – there are only two observed asteroids with $a_\mathrm{p} > 5.32\,\mathrm{au}$. This is due to the proximity to the border of the stable librating region. As there are many more synthetic asteroids in this region in all cases of initial distributions, we need to simulate a dynamical evolution of the family.

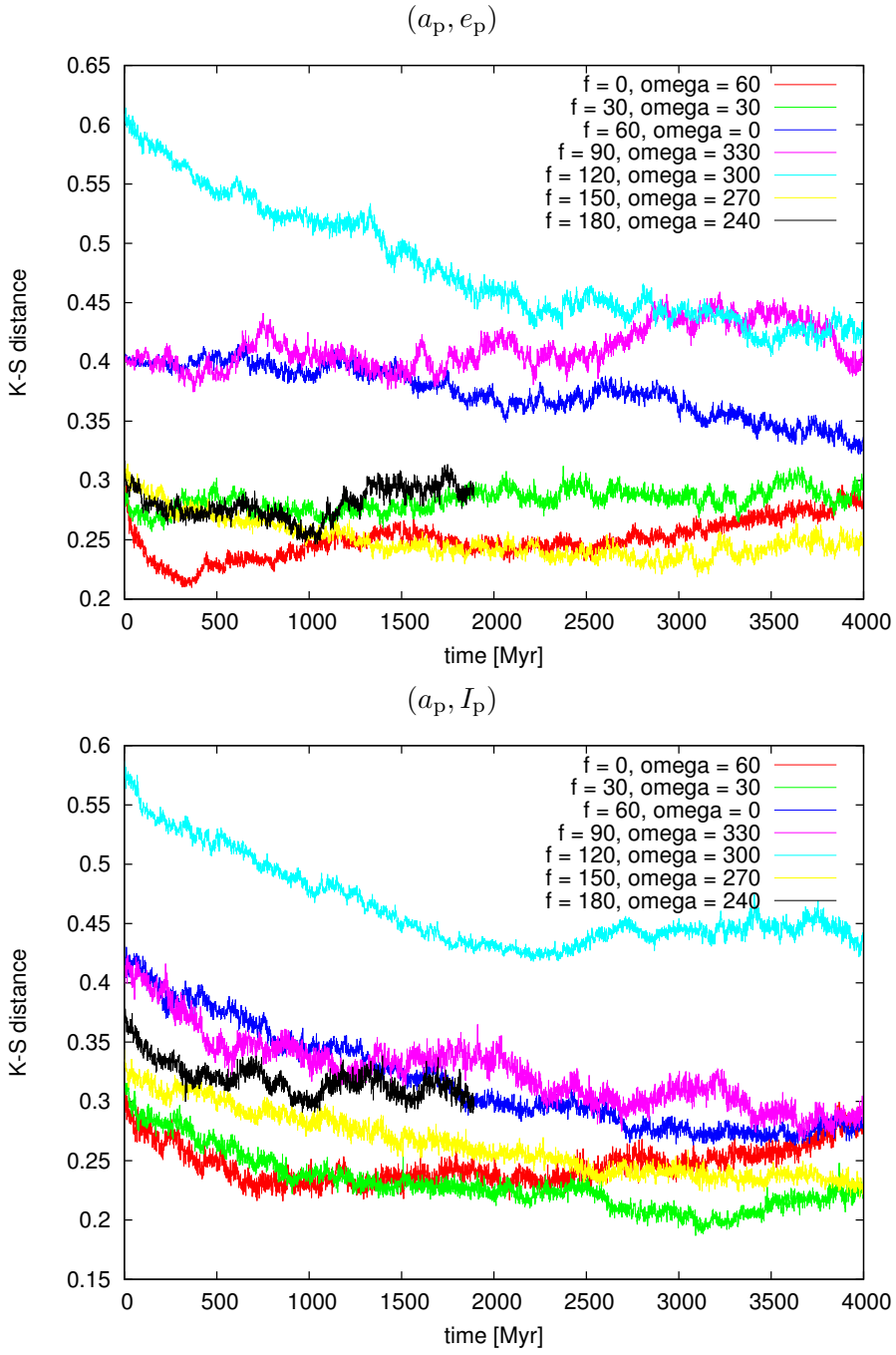


Figure 2.6: Kolmogorov–Smirnov distance $D_\mathrm{KS}$ vs time for 7 different synthetic families compared with the observed Hektor family. Two-dimensional KS test was computed for the distributions of synthetic and observed families in the space of proper elements $(a_\mathrm{p}, e_\mathrm{p})$ (top) and $(a_\mathrm{p}, I_\mathrm{p})$ (bottom). The synthetic families were created assuming different impact geometries, namely the true anomaly $f = 0°, 30°, 60°, 90°, 120°, 150°, 180°$ and the argument of pericenter $\omega = 60°, 30°, 0°, 330°, 300°, 270°, 240°$, which were combined so that the sum $f + \omega = 60°$. The averaged distance $D_\mathrm{KS}$ changes in the course of dynamical evolution and we can see two minima: for $f = 0°$ and $\omega = 60°$ (red curve) it is at about $(350 \pm 100)$ Myr; for $f = 150°$ and $\omega = 270°$ (yellow curve) there is a flat minimum at $(2800 \pm 1500)$ Myr. Since the red and yellow curves are overlapping in the range from 1800 Myr to 2500 Myr, we adopt the values of possible ages as 100 to 2500 Myr for the $f = 0°$ and $\omega = 60°$ geometry (red curve) and 1000 to 4000 Myr for the $f = 150°$ and $\omega = 270°$ geometry (yellow curve).

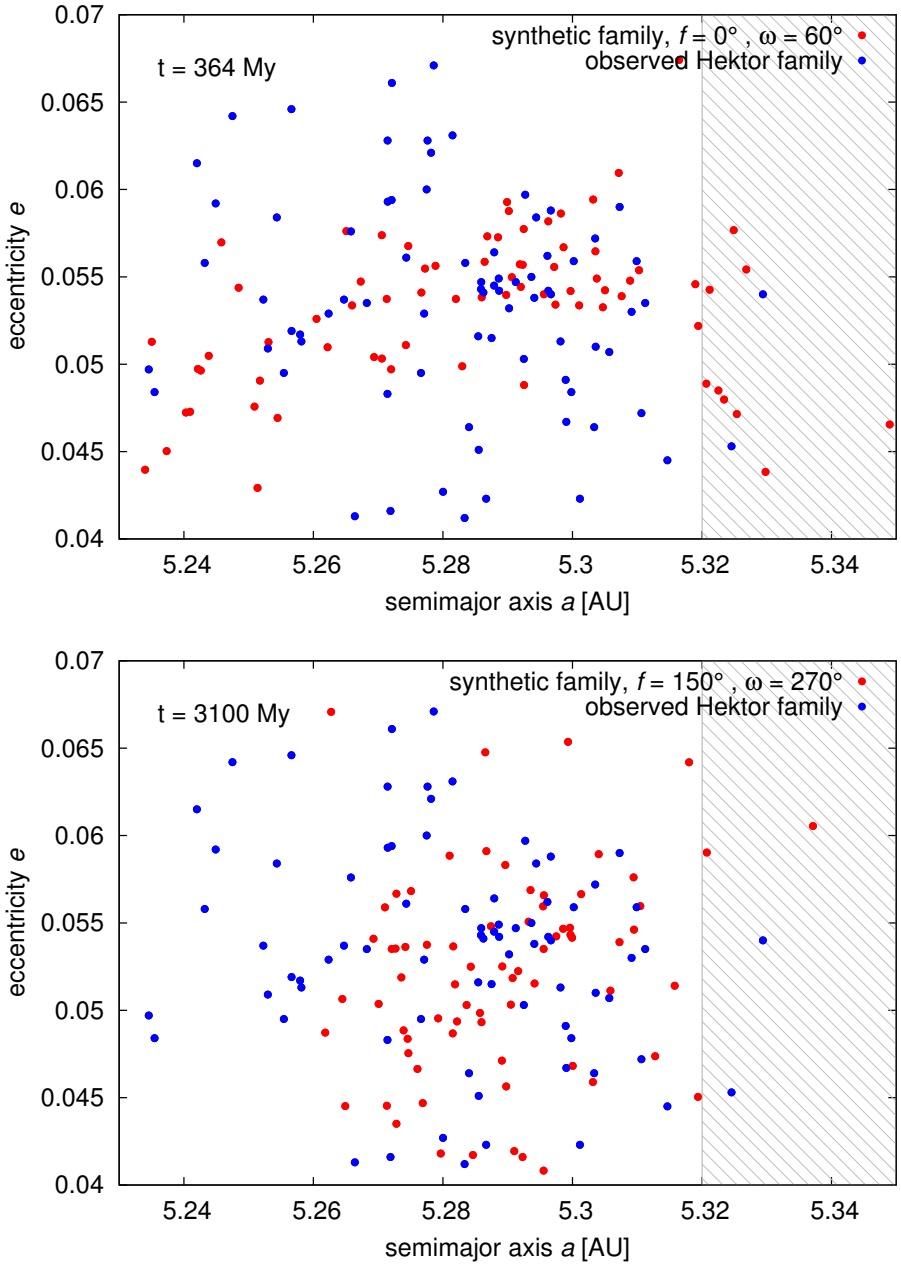


Figure 2.7: Two evolved synthetic families in the space of proper elements $(a_{\mathrm{p}}, e_{\mathrm{p}})$, which correspond to the minima of KS distance in Figure 2.6. Upper picture shows the synthetic family (red) with $f = 0°$ and $\omega = 60°$ after 364 Myr of evolution in comparison with the observed Hektor family (blue). Lower picture corresponds to the synthetic family with $f = 150°$ and $\omega = 270°$ after 3100 Myr of evolution. These two pictures differ in fine details, which cannot be accounted for in the KS statistics: i) the "fibre-like" structure of the relatively young family is still visible in the left picture; ii) there are many fewer synthetic bodies in the shaded area of the right picture ($a_{\mathrm{p}} > 5.32\,\mathrm{au}$) than on the left, which is closer to the observed reality.

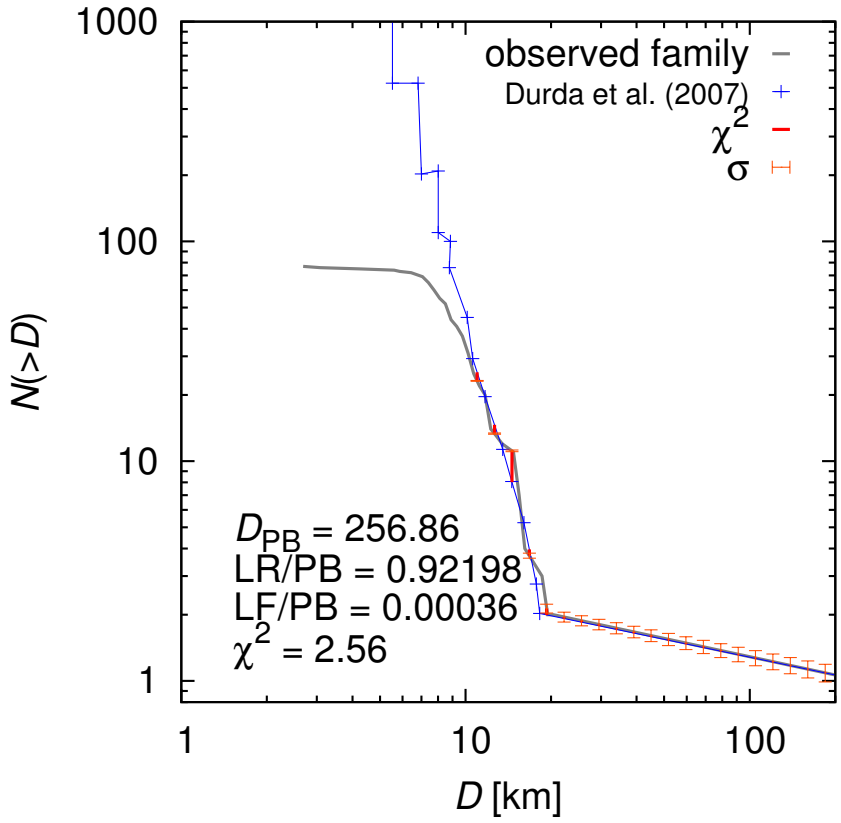


Figure 2.8: Our best-fit size-frequency distribution of Hektor family by scaled SFDs from SPH simulations of Durda et al. (2007). In this particular case $D_{\mathrm{PB(SPH)}} = 257\,\mathrm{km}$, impactor diameter $D_{\mathrm{imp}} = 48\,\mathrm{km}$, impactor velocity $v_{\mathrm{imp}} = 4\,\mathrm{km\,s^{-1}}$ and impact angle $\varphi_{\mathrm{imp}} = 60°$. However, other fits with similar pseudo-$\chi^2$ suggest the uncertainties are as follows: $\Delta D_{\mathrm{PB(SPH)}} = 10\,\mathrm{km}$, $\Delta D_{\mathrm{imp}} = 2\,\mathrm{km}$, $\Delta v_{\mathrm{imp}} = 1\,\mathrm{km\,s^{-1}}$ and $\Delta\varphi_{\mathrm{imp}} = 15°$. SFD shape seems to be more dependent on impact geometry than on impact velocity.

assuming albedo $p_V = 0.072$, which is the median of $L_4$ Trojans. Although (20961) Arkesilaos has the diameter only $D = (24 \pm 5)$ km, it is the only asteroid with $H < 12$, for which the associated family has a reasonable number of members $N_{\rm memb}$ even for small values of the cutoff velocity $v_{\rm cutoff}$ (see Section 2.4.2). As this is also the only larger body located near the center of the family in the space of proper elements, we treat (20961) Arkesilaos as the largest remnant of the parent body, whose diameter we estimate to be $D_{\rm PB(SPH)} \simeq 87$ km. Given that the mass ratio of the largest remnant and the parent body, as derived from SPH simulations of Durda et al. (2007), is $M_{\rm LR}/M_{\rm PB} \simeq 0.02$ only, it seems this family inevitably originated from a catastrophic disruption.

### 2.5.5 Ennomos

In our previous work, we reported a discovery of a possible family associated with asteroid (4709) Ennomos. With new data, we can still confirm that there is a significant cluster near this body, but when we take into account our "$N_{\rm memb}(v_{\rm cutoff})$" criterion described above, it turns out that the family is rather associated with asteroid (17492) Hippasos. It is a relatively numerous group composed of almost 100 bodies, situated near the border of the stable librating zone $L_5$ at high inclinations, ranging from $I_{\rm p} \in \langle 26.86°; 30.97° \rangle$, and $a_{\rm p} \in \langle 5.225; 5.338 \rangle$ au.

### 2.5.6 2001 $UV_{209}$

Using new data, we discovered a "new" family around asteroid (247341) 2001 $UV_{209}$, which is the second and apparently the last observable family in our sample. Similar to the Ennomos family, it is located near the border of the $L_5$ zone on high inclinations $I_{\rm p} \in \langle 24.02°; 26.56° \rangle$ and $a_{\rm p} \in \langle 5.218; 5.320 \rangle$ au. This family has an exceptionally steep slope of the SFD, with $\gamma = -8.6 \pm 0.9$, which may indicate a recent collisional origin or a disruption at the boundary of the libration zone, which may be indeed size-selective as explained in Chrenko et al. (2015).

## 2.6 Collisional models of the Trojan population

In order to estimate the number of collisional families among $L_4$ Trojans, we performed a set of 100 simulations of the collisional evolution of Trojans with the Boulder code (Morbidelli et al., 2009) with the same initial conditions, but with different values of the random seed.

### 2.6.1 Initial conditions

We set our initial conditions of the simulations such that 4 Gyr of collisional evolution leads to the observed cumulative SFD of $L_4$ Trojans (red curve in Figure 2.9). We constructed the initial synthetic SFD as three power laws with the slopes $\gamma_{\rm a} = -6.60$ in the size range from $D_1 = 117$ km to $D_{\rm max} = 250$ km, $\gamma_{\rm b} = -3.05$ from $D_2 = 25$ km to $D_1$ and $\gamma_{\rm c} = -3.70$ from $D_{\rm min} = 0.05$ km to $D_2$. The synthetic initial population was normalized to contain $N_{\rm norm} = 11$ asteroids with diameters $D \geq D_1$.

To calculate the target strength $Q^*_D$, we used a parametric formula of Benz and Asphaug (1999):

$$Q^*_D = Q_0 R^a_{\rm PB} + B \rho_{\rm bulk} R^b_{\rm PB}, \tag{2.2}$$

where $R_{\rm PB}$ is the parent body radius in centimetres, $\rho_{\rm bulk}$ its bulk density, which we set to be $\rho_{\rm bulk} = 1.3$ g cm$^{-3}$ for synthetic Trojans (cf. Marchis et al., 2014). As of constants $a$, $b$, $B$ and $Q_0$ we used the values determined by Benz and Asphaug (1999) for ice at the impact velocity $v_{\rm imp} = 3$ km s$^{-1}$, which are: $a = -0.39$, $b = 1.26$, $B = 1.2$ erg cm$^3$ g$^{-2}$ and $Q_0 = 1.6 \cdot 10^7$ erg g$^{-1}$.

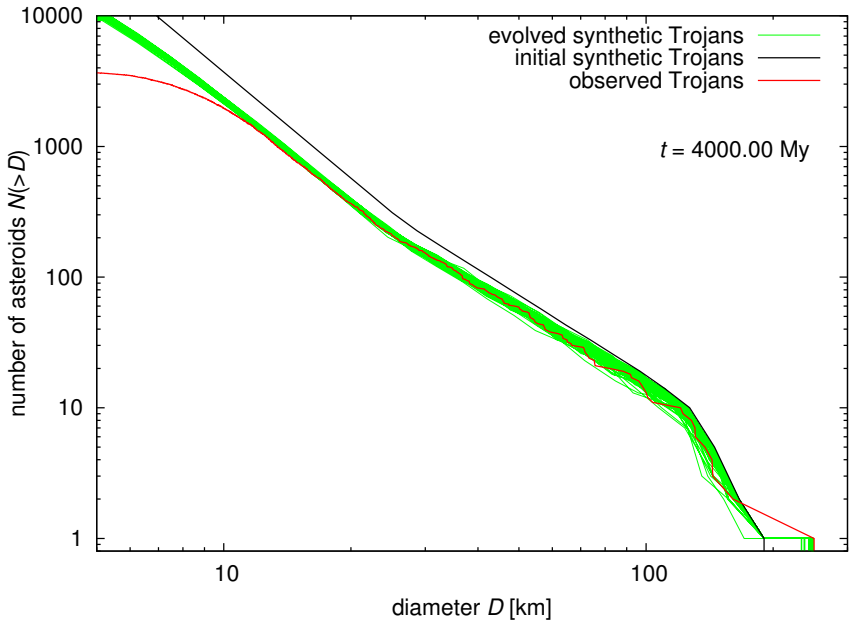


Figure 2.9: Simulations of the collisional evolution of $L_4$ Trojans with the Boulder code (Morbidelli et al., 2009). Shown here is the initial cumulative SFD of a synthetic population (black) and the SFD of the observed one (red). Green are the final SFDs of 100 synthetic populations with the same initial SFD but with different random seeds, after 4 Gyr of a collisional evolution. The evolution of bodies larger than $D > 50\,\mathrm{km}$ is very slow, hence we can consider this part of the SFD as captured population.

In our model, we take into account only Trojan vs Trojan collisions, as the Trojan region is practically detached from the main belt. Anyway, main-belt asteroids with eccentricities large enough to reach the Trojan region are usually scattered by Jupiter on a time scale significantly shorter than the average time needed to collide with a relatively large Trojan asteroid. We thus assumed the values of collisional probability $P_\mathrm{i} = 7.80 \cdot 10^{-18}\ \mathrm{km^{-2}\,yr^{-1}}$ and the impact velocity $v_\mathrm{imp} = 4.66\ \mathrm{km\,s^{-1}}$ (dell'Oro et al., 1998). Unfortunately, Benz and Asphaug (1999) do not provide parameters for ice at the impact velocities $v_\mathrm{imp} > 3\,\mathrm{km\,s^{-1}}$.

We also ran several simulations with appropriate values for basalt at impact velocity $v_\mathrm{imp} = 5\,\mathrm{km\,s^{-1}}$ ($a = -0.36$, $b = 1.36$, $B = 0.5\ \mathrm{erg\,cm^3\,g^{-2}}$ and $Q_0 = 9 \cdot 10^7\ \mathrm{erg\,g^{-1}}$).

Both models qualitatively exhibit the same evolution of SFD and they give approximately the same total numbers of disruptions and craterings occured, but for basalt the model gives three times fewer *observable* families originated by cratering than for ice. The results for the ice match the observation better, so we will further discuss the results for ice only.

### 2.6.2 Long-term collisional evolution

The results of our simulations of the collisional evolution are shown in Figure 2.9. Our collisional model shows only little changes above $D > 50\,\mathrm{km}$ over the last 3.85 Gyr (i.e. post-LHB phase only). Slopes of the initial synthetic population and the observed $L_4$ population differ by $\Delta\gamma < 0.1$ in the size range from 50 km to 100 km, while a relative decrease of the number of asteroids after 3.85 Gyr of collisional evolution is only about 12 % in the same size range. Hence, we can consider this part of the Trojan population as a representative sample of the source population, which is not much affected by collisional evolution. Therefore, these Trojans provide very useful information about the source population, from which they were captured (as modeled in Nesvorný et al., 2013).

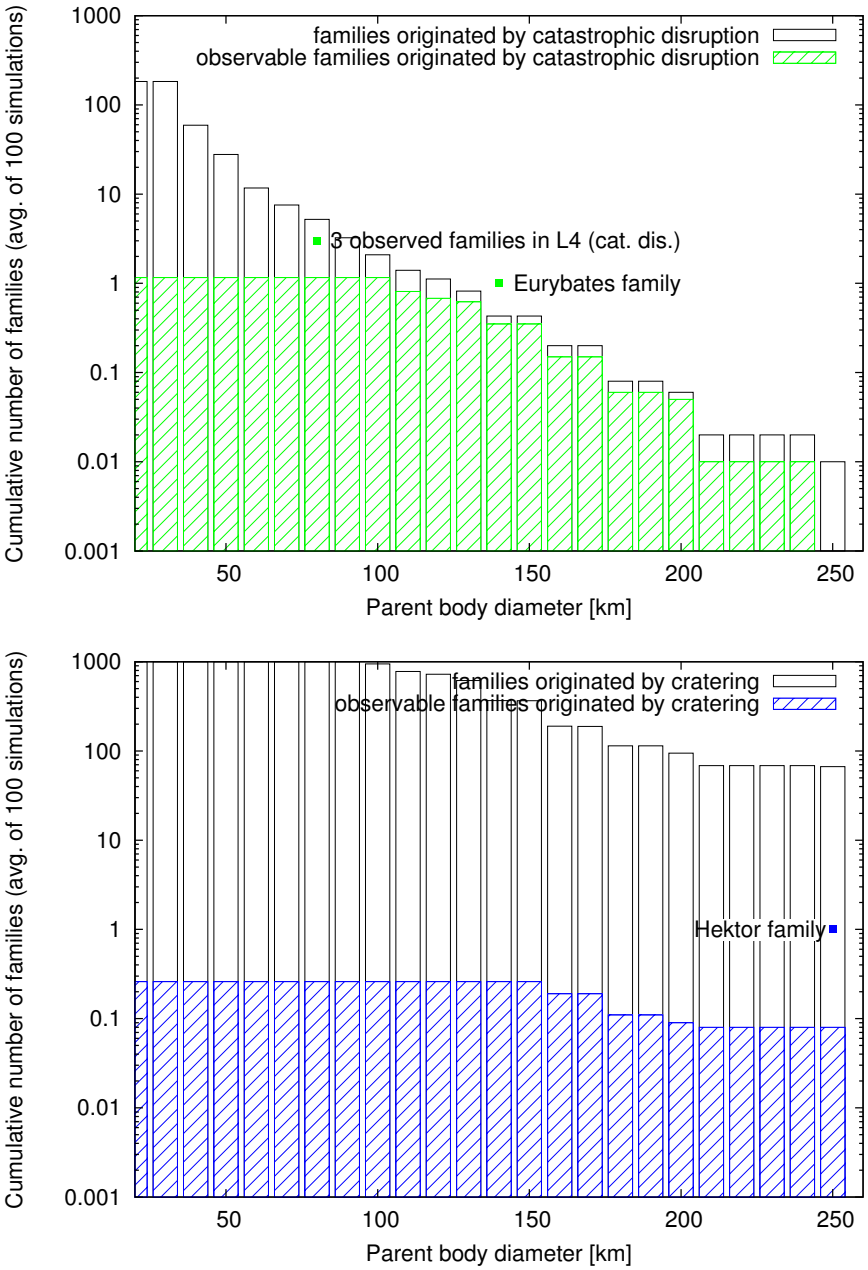


Figure 2.10: The dependence of the cumulative number (an average over 100 simulations) of catastrophic disruptions among Trojans (upper panel) and cratering events (lower panel) on the target diameter $D_{\mathrm{PB}}$ (black boxes), and a subset of those Trojan families, which should be detected in contemporary observational data, i.e. with the number of fragments $N(D > 10\,\mathrm{km}) > 10$ (green boxes for disruptions and blue boxes for craterings). In other words, colour boxes represent simulated detections of families based on the expected effectiveness of our detection methods. This is the reason, why the cumulative number of the observable families does not strictly increase with the decreasing parent body size, but is rather constant under the limit of about 95 km in the case of catastrophic disruptions and 145 km in the case of craterings. There are also observed families marked for a comparison. Three of the four observed families in $L_4$ cloud originated by catastrophic disruption, while only one (Hektor) originated by cratering event (cf. Table 2.1).

### 2.6.3 An estimate of the number of observable families

From our set of simulations, we also obtained the number of collisions leading to collisional families among $L_4$ Trojans, namely catastrophic disruptions, where the mass ratio of the largest remnant and the parent body $M_{\mathrm{LR}}/M_{\mathrm{PB}} < 0.5$, and cratering events, where $M_{\mathrm{LR}}/M_{\mathrm{PB}} > 0.5$. As one can verify in Figure 2.10, these numbers are dependent on the diameter of the parent body $D_{\mathrm{PB}}$.

However, not all of these collisions produce families which are in fact observable (detectable). There are generally two possible obstacles in the detection of a family in the space of proper elements: i) somewhat more concentrated background population, due to which our detection methods (both "randombox" and HCM, see Chapter 2.4) may fail, if the number of observed fragments is too low in comparison with the background, and ii) an observational incompleteness, which means that in the case of Trojans, a substantial part of fragments with sizes $D < 10\,\mathrm{km}$ is still unknown, what again reduces a chance of a family detection.

For these reasons, we constructed a criterion of observability that a synthetic family must fulfill in order to be detectable in the current conditions (i.e. we simulated a detection of synthetic families by the same methods we used to detect the real ones). The simplest criterion could be that a family must contain at least $N_{\mathrm{min}} = 10$ fragments with diameter $D \geq 10\,\mathrm{km}$.

Within 100 simulations, there were 93 catastrophic disruptions of bodies with diameters $D_{\mathrm{PB}} > 100\,\mathrm{km}$, but only 50 of them produced more than 10 fragments with $D \geq 10\,\mathrm{km}$, see Figure 2.10. Hence, the probability that we would observe a collisional family originated by a catastrophic disruption of a parent body with $D_{\mathrm{PB}} > 100\,\mathrm{km}$ is *only* 0.50, which matches the observations (namely Eurybates family with $D_{\mathrm{PB(SPH)}} \simeq 155$ km, see Table 2.2). This value is also roughly consistent with our previous estimate based on the stationary model (Brož and Rozehnal, 2011), which gives the value 0.32 with new observational data.

As one can also see in Figure 2.10, the number of cratering events is about one to two orders higher than the number of catastrophic disruptions, however, they do not produce enough fragments larger than $D \geq 10\,\mathrm{km}$. For the parent body size $D_{\mathrm{PB}} > 100\,\mathrm{km}$ there occurred almost 45,000 cratering events within 100 simulations which produced the largest fragment with $D_{\mathrm{LF}} \geq 1\,\mathrm{km}$, but only 10 of them fulfill our criterion of observability. Hence, the probability that we can observe a family originated by a cratering of a parent body with $D_{\mathrm{PB}} > 100\,\mathrm{km}$ is only 0.10, at least with contemporary data. From a statistical point of view, this can actually correspond to the Hektor family.

As we have already demonstrated in Brož and Rozehnal (2011), the number of families is not significantly affected by chaotic diffusion or by a ballistic transport outside the libration zone.

## 2.7 SPH simulations of Hektor family

As we have already mentioned in Section 2.5.2, (624) Hektor is very interesting Trojan asteroid with possibly bilobed shape and a small moon. Diameters of (624) Hektor stated in Marchis et al. (2014) are as follows: equivalent diameter $D_{\mathrm{eq}} = (250 \pm 26)$ km for a convex model, the individual diameters of the lobes $D_{\mathrm{A}} = (220 \pm 22)$ km, $D_{\mathrm{B}} = (183 \pm 18)$ km for a bilobed version. Estimated parameters of the moon are: the diameter $D_{\mathrm{m}} = (12 \pm 3)$ km, the semimajor axis $a_{\mathrm{m}} = (623 \pm 10)$ km, the eccentricity $e_{\mathrm{m}} = (0.31 \pm 0.03)$ and the inclination (with respect to the primary equator) $I_{\mathrm{m}} = (50 \pm 1)^\circ$.

As we associate (624) Hektor with the collisional family, we would like to know, how the properties of the family are influenced by the shape of target body. We therefore performed a series of SPH simulations aiming to explain the origin of the Hektor family, for both cases of convex and bilobed shape of its parent body.

Table 2.3: Material constants used in our SPH simulations for basalt and silicated ice (30 % of silicates). Listed here are: the zero-pressure density $\rho_0$, bulk modulus $A$, non-linear compressive term $B$, sublimation energy $E_0$, Tillotson parameters $a$, $b$, $\alpha$ and $\beta$, specific energy of incipient vaporization $E_{\rm iv}$, complete vaporization $E_{\rm cv}$, shear modulus $\mu$, plastic yielding $Y$, melt energy $E_{\rm melt}$ and Weibull fracture parameters $k$ and $m$. Values we used for silicated ice are identical to those of pure ice, except density $\rho_0$, bulk modulus $A$ and Weibull parameters $k$ and $m$. All values were adopted from Benz and Asphaug (1999).

| quantity | basalt | silicated ice | unit |
|---|---|---|---|
| $\rho_0$ | 2.7 | 1.1 | $\mathrm{g\,cm^{-3}}$ |
| $A$ | $2.67 \cdot 10^{11}$ | $8.44 \cdot 10^{10}$ | $\mathrm{erg\,cm^{-3}}$ |
| $B$ | $2.67 \cdot 10^{11}$ | $1.33 \cdot 10^{11}$ | $\mathrm{erg\,cm^{-3}}$ |
| $E_0$ | $4.87 \cdot 10^{12}$ | $1.00 \cdot 10^{11}$ | $\mathrm{erg\,g^{-1}}$ |
| $a$ | 0.5 | 0.3 | – |
| $b$ | 1.5 | 0.1 | – |
| $\alpha$ | 5.0 | 10.0 | – |
| $\beta$ | 5.0 | 5.0 | – |
| $E_{\rm iv}$ | $4.72 \cdot 10^{10}$ | $7.73 \cdot 10^{9}$ | $\mathrm{erg\,g^{-1}}$ |
| $E_{\rm cv}$ | $1.82 \cdot 10^{11}$ | $3.04 \cdot 10^{10}$ | $\mathrm{erg\,g^{-1}}$ |
| $\mu$ | $2.27 \cdot 10^{11}$ | $2.80 \cdot 10^{10}$ | $\mathrm{erg\,cm^{-3}}$ |
| $Y$ | $3.5 \cdot 10^{10}$ | $1.0 \cdot 10^{10}$ | $\mathrm{erg\,g^{-1}}$ |
| $E_{\rm melt}$ | $3.4 \cdot 10^{10}$ | $7.0 \cdot 10^{9}$ | $\mathrm{erg\,g^{-1}}$ |
| $k$ | $4.0 \cdot 10^{29}$ | $5.6 \cdot 10^{38}$ | $\mathrm{cm^{-3}}$ |
| $m$ | 9.0 | 9.4 | – |

### 2.7.1 Methods and initial conditions

We simulated a collisional disruption using the smoothed-particle hydrodynamic code SPH5 (Benz and Asphaug, 1994). We performed two sets of simulations. In the first one, we simulated an impact on a single spherical asteroid. In the second, on a bilobed asteroid represented by two spheres positioned next to each other. The two touching spheres have a narrow interface, so that the SPH quantities do not easily propagate between them. In this setup, we are likely to see differences between sinlge/bilobed cases as clearly as possible.

As for the main input parameters (target/impactor sizes, the impact velocity and the impact angle) we took the parameters of our best-fit SFDs, obtained by Durda et al. (2007) scaling method, see Section 2.5.2 and Figure 2.8.

To simulate a collision between the parent body and the impactor we performed a limited set of simulations: i) a single spherical basalt target with diameter $D_{\rm PB} = 260$ km vs a basalt impactor with diameter $D_{\rm imp} = 48$ km; ii) the single basalt target $D_{\rm PB} = 260$ km vs an ice impactor (a mixture of ice and 30 % of silicates) with $D_{\rm imp} = 64$ km (impactor diameter was scaled to get the same kinetic energy); iii) a bilobed basalt target approximated by two spheres with diameters $D_{\rm PB} = 200$ km each (the total mass is approximately the same) vs a basalt impactor with $D_{\rm imp} = 48$ km; iv) a single spherical ice target $D_{\rm PB} = 260$ km vs an ice impactor $D_{\rm imp} = 38$ km (impactor diameter was scaled to get the same ratio of the specific kinetic energy $Q$ to the target strength $Q^*_{\rm D}$).

The integration was controlled by the Courant number $C = 1.0$, a typical time step thus was $\Delta t \simeq 10^{-5}$ s, and the time span was $t_{\rm stop} = 100$ s. The Courant condition was the same in different materials, using always the maximum sound speed $c_{\rm s}$ among all SPH particles, as usually.

We used $N_{\rm SPH,st} = 10^5$ SPH particles for the single spherical target and $N_{\rm SPH,bt} = 2 \cdot 10^5$ for the bilobed one. For impactor $N_{\rm SPH,i} = 10^3$ SPH particles. We assumed the Tillotson equation of state (Tillotson, 1962) and material properties, which are listed in Table 2.3.

We terminated SPH simulations after 100 s from the impact. This time interval is needed to establish a velocity field of fragments and to complete the fragmentation. Then we handed

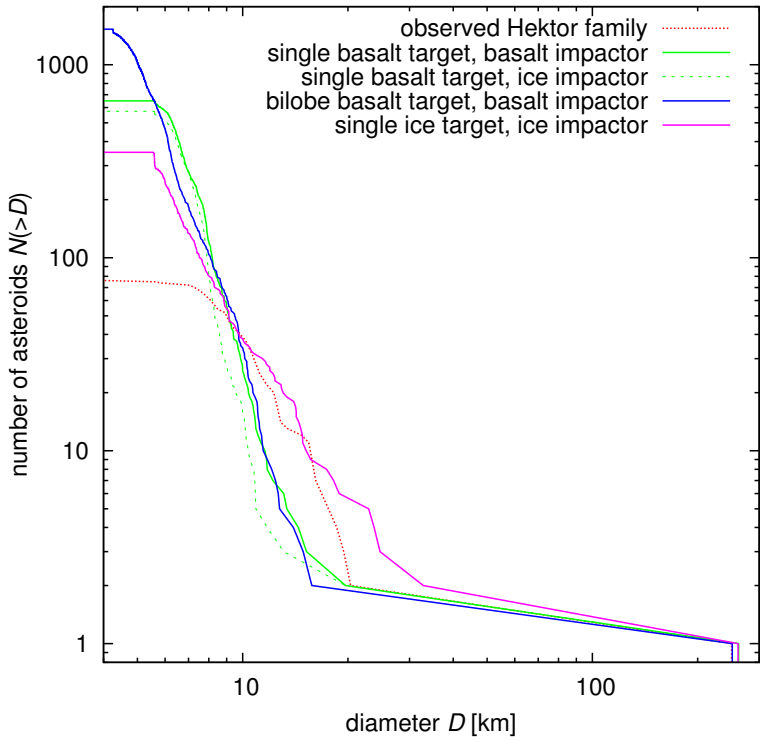


Figure 2.11: A comparison of size-frequency distributions of the observed Hektor family (red dotted) and SFDs of synthetic families created by different SPH simulations, always assuming the impactor velocity $v_{\mathrm{imp}} = 4\ \mathrm{km\,s^{-1}}$ and the impact angle $\varphi_{\mathrm{imp}} = 60°$. For a single spherical target (green lines) we assumed the diameter $D_{\mathrm{PB}} = 260$ km, for a bilobe target (blue line) we approximated the lobes as spheres with diameters $D_{\mathrm{PB}} = 200$ km each. The impactor size was assumed to be $D_{\mathrm{imp}} = 48$ km in the case of basalt, $D_{\mathrm{imp}} = 64$ km in the case of silicate ice impacting on basalt target (scaled to the same $E_{\mathrm{imp}}$) and $D_{\mathrm{imp}} = 38$ km in the case of silicate ice impacting on ice target (scaled to the same $Q/Q^*_{\mathrm{D}}$). Fragments of the impactor were purposely removed from this plot, as they do not remain in the libration zone for our particular impact orbital geometry.

the output of the SPH simulation as initial conditions to the N–body gravitational code Pkdgrav (Richardson et al., 2000), a parallel tree code used to simulate a gravitational reaccumulation of fragments. Unlike Durda et al. (2007), who calculated radii of fragments $R$ from the smoothing length $h$ as $R = h/3$, we calculated fragments radii from their masses $m$ and densities $\rho$ as $R = (m/(4\pi\rho))^{1/3}$.

We ran Pkdgrav with the time step $\Delta t = 5.0$ s and we terminated this simulation after $t_{\mathrm{evol}} = 3$ days of evolution. To ensure this is sufficiently long, we also ran several simulations with $t_{\mathrm{evol}} = 5$ days, but we had seen no significant differences between final results.

We used the nominal value for the tree opening angle, $\mathrm{d}\theta = 0.5$ rad, even though for the evolution of eventual moons it would be worth to use even smaller value, e.g. $\mathrm{d}\theta = 0.2$ rad.

### 2.7.2 Resulting size-frequency distributions

From the output of our simulations we constructed size-frequency distributions of synthetic families, which we compare to the observed one, as demonstrated in Figure 2.11. As one can see, there are only minor differences between SFDs of families created by the impacts on the single and bilobed target, except the number of fragments with diameter $D < 5$ km, but this is mostly due to different numbers of SPH particles. However, there are differences between

ice and basalt targets. Basalt targets provide generally steeper SFDs with smaller largest remnants than the ice target.

To make the comparison of these synthetic initial SFDs to each other more realistic, we removed the fragments of the impactor from our synthetic families. This is because fragments of the impactor often do not remain in the libration zone. Note that this procedure does not subtitute for a full simulation of further evolution; it serves just for a quick comparison of the SFDs.

To match the observed SFD of the Hektor family more accurately, we should perform a much larger set of simulations with different sizes of projectiles and also different compositions (mixtures of ice and basalt). However, material parameters of these mixtures are generally not known. Regarding the material constants of pure ice, we have them for the impact velocity $v_{\mathrm{imp}} = 3\,\mathrm{km\,s^{-1}}$ only (Benz and Aspaugh, 1999). There are also some differences between SFDs of single and bilobe targets, so we should perform these simulations for each target geometry. However, we postpone these detailed simulations for future work; in this work we further analyse results of simulations with basalt targets and we focus on the evolution of the SFDs.

It should be emphasized that the SFDs presented here correspond to very young synthetic families, hence they are not affected by any dynamical and collisional evolution yet. To reveal possible trends of the evolution by a ballistic transport and chaotic diffusion, we prepared initial conditions for the SWIFT integrator, similarly as described in Section 2.5.2, let the simulation run and monitored the corresponding evolution of the SFD. The results can be seen in Figure 2.12. The biggest difference between $t = 0$ and $t = 1$ Myr is caused by a ballistic transport outside the libration zone — fragments (especially of the impactor) missing from the SFD at $t = 1$ Myr were perturbed too much to remain in the libration zone, at least for a given impact geometry. We actually tested two impact geometries: in the direction tangential and perpendicular to the orbit.

This may be important for the method we used in Section 2.5.2 to derive a preliminary parent body size and other properties of the family. The SFDs obtained by Durda et al. (2007) were directly compared in their work to the main-belt families, however, there is a part of fragments among Trojans (in our case even the largest ones, see Figure 2.12), which cannot be seen in the space of resonant elements, because they do not belong to Trojans any more. Fortunately, values of pseudo-$\chi^2$ we computed in Section 2.5.2 depend rather weakly on the distribution of a few largest bodies. Even so, we plan to analyze SFDs of synthetic families more carefully in future works.

### 2.7.3 Resulting velocity fields

In our $N$-body simulations, we used the model of isotropic disruption (Farinella et al., 1994). As we compared the synthetic family with the observed one (see Section 2.5.2), we simulated only the evolution of bodies with relatively low ejection velocities ($v < 200\,\mathrm{m\,s^{-1}}$), because the observed family is confined by the cutoff velocity $v_{\mathrm{cutoff}} = 110\,\mathrm{m\,s^{-1}}$. Very small fragments with higher velocities may be still hidden in the background.

Here, we compare Farinella's model to the velocity fields of fragments from SPH simulations, see Figure 2.13. We realized that Farinella's model is not offset substantially with respect to other velocity histograms, especially at lower velocities, $v < 200\,\mathrm{m\,s^{-1}}$. On the other side, there remained some fragments of the impactor with velocities $v > 2\,\mathrm{km\,s^{-1}}$ in our SPH simulations, which are not produced in the isotropic model. It does not affect a comparison of the synthetic and observed families in the space of proper elements, as these high-velocity fragments leaved the Trojan region in our case, but it does affect the SFD of the synthetic family. As a consequence, one should always analyse SFDs and velocity fields together.

We also simulated a further evolution of the velocity field. After just 1 Myr of evolution,

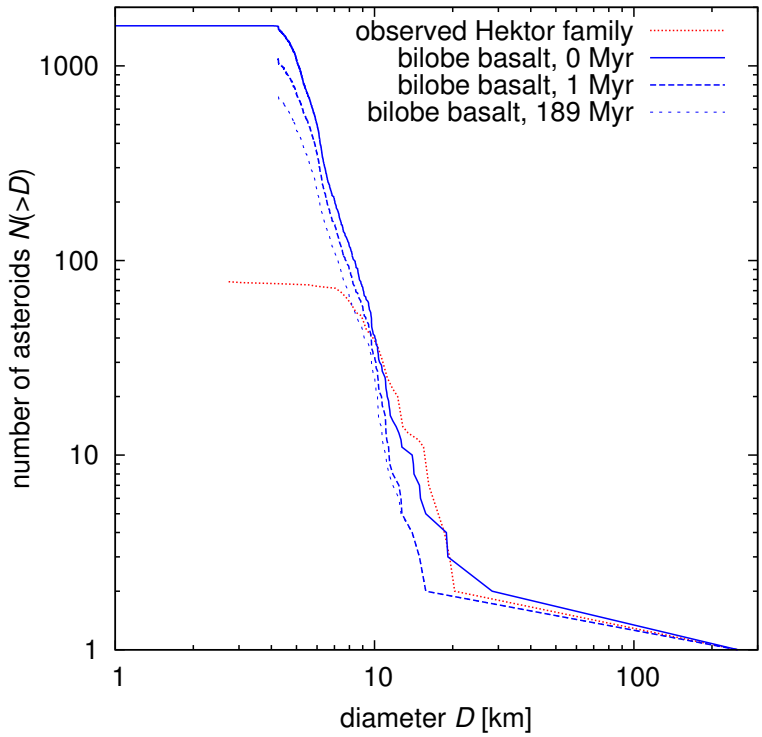


Figure 2.12: A simulation of evolution of the SFD of a synthetic Hektor family due to a ballistic transport and chaotic diffusion. One can see here a rapid change of SFD within the first 1 Myr after the breakup as the fragments of the impactor leaved the libration zone in our impact geometry. This ballistic transport resulted in a reduction of the number of particularly larger bodies in our case. Further evolution due to the chaotic diffusion seems to cause the reduction of mostly smaller bodies. Note that the initial SFD (0 Myr) contains some fragments of the impactor, so the blue solid curve looks different than the curve in Figure 2.11, where the fragments of the impactor were removed.

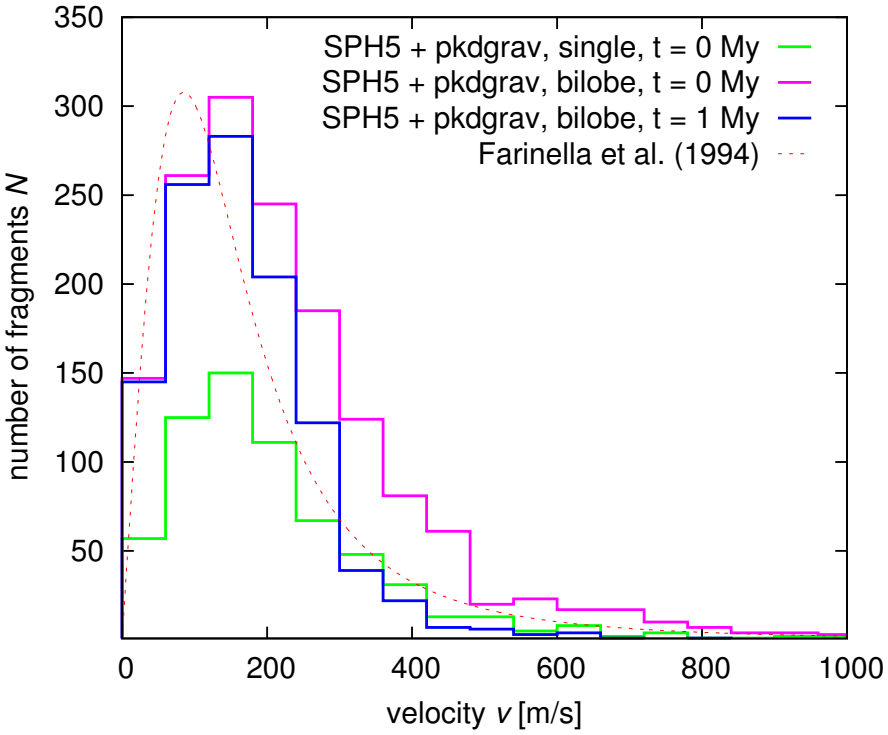


Figure 2.13: Velocity distributions of fragments originated in various SPH simulations (green, violet) in comparison with the model of Farinella et al. (1994) we used in our $N$-body simulations of isotropic disruption and dynamical evolution (see Section 2.5.2). Shown here is also the distribution of velocities after 1 Myr of evolution, i.e. of fragments that remained in libration zones.

Table 2.4: A comparison of the sizes and the orbital parameters (i.e. semimajor axis $a$, eccentricity $e$ and period $P$) of the observed moon of (624) Hektor as listed in Marchis et al. (2014), with the parameters of synthetic moons SPH I and SPH II captured in our SPH simulation of impact on the bilobed target.

| desig. | diam. [km] | $a$ [km] | $e$ | $P$ [days] |
|---|---|---|---|---|
| observed | $12 \pm 3$ | $623.5 \pm 10$ | $0.31 \pm 0.03$ | $2.9651 \pm 0.0003$ |
| SPH I | 2.2 | 715 | 0.82 | 1.2 |
| SPH II | 2.7 | 370 | 0.64 | 0.4 |

there remained no bodies with $v > 1.5\,\mathrm{km\,s^{-1}}$ in our impact geometries, and as one can see in Figure 2.13, there was a rapid decrease in the number of fragments with initial $v > 300\,\mathrm{m\,s^{-1}}$. The resulting histogram is again similar to that of the simple isotropic model.

### 2.7.4 Synthetic moons

In our simulation of the impact of basalt projectile on the bilobe-shape basalt target, we spotted two low-velocity fragments with original velocities $130\,\mathrm{m\,s^{-1}}$ and $125\,\mathrm{m\,s^{-1}}$, which were consequently captured as moons of the largest remnant. Their sizes and orbital parameters are listed in Table 2.4.

These satellites were captured on orbits with high eccentricities ($e = 0.82$ and 0.64 respectively), which are much higher than the eccentricity of the observed moon determined by Marchis et al. (2014) ($e = 0.31 \pm 0.03$). However, this could be partly caused by the fact, that we handed the output of (gravity free) SPH simulations to the gravitational N-body code after first 100 s. Hence, fragments leaving the parent body could move freely without slowing down by gravity. More importantly, we do not account for any long-term dynamical evolution of the moons (e.g. by tides or binary YORP).

When compared to the observed satellite, the diameters of the synthetic moons are several times smaller. This is not too surprising, given that the results for satellite formation are at the small end of what can be estimated with our techniques (median smoothing length $h = 2.3\,\mathrm{km}$; satellite radius $r \simeq 1.2\,\mathrm{km}$). The size of captured fragments could also be dependent on impact conditions as different impact angles, impactor velocities and sizes (as is the case for scenarios of Moon formation) which we will analyze in detail in the future and study with more focused simulations.

## 2.8 Conclusions

In this paper, we updated the list of Trojans and their proper elements, what allowed us to update parameters of Trojan families and to discover a new one (namely $2001\,\mathrm{UV}_{209}$ in $L_5$ population). We focused on the Hektor family, which seems the most interesting due to the bilobed shape of the largest remnant with a small moon and also its D-type taxonomical classification, which is unique among the collisional families observed so far.

At the current stage of knowledge, it seems to us there are no major inconsistencies among the observed number of Trojan families and their dynamical and collisional evolution, at least in the current environment.

As usual, we "desperately" need new observational data, namely in the size range from 5 to 10 km, which would enable us to constrain the ages of asteroid families on the basis of collisional modeling and to decide between two proposed ages of Hektor family, 1 to 4 Gyr or 0.1 to 2.5 Gyr.

As expected, there are qualitative differences in impacts on single and bilobed targets. In our setup, the shockwave does not propagate easily into the secondary, so that only one half

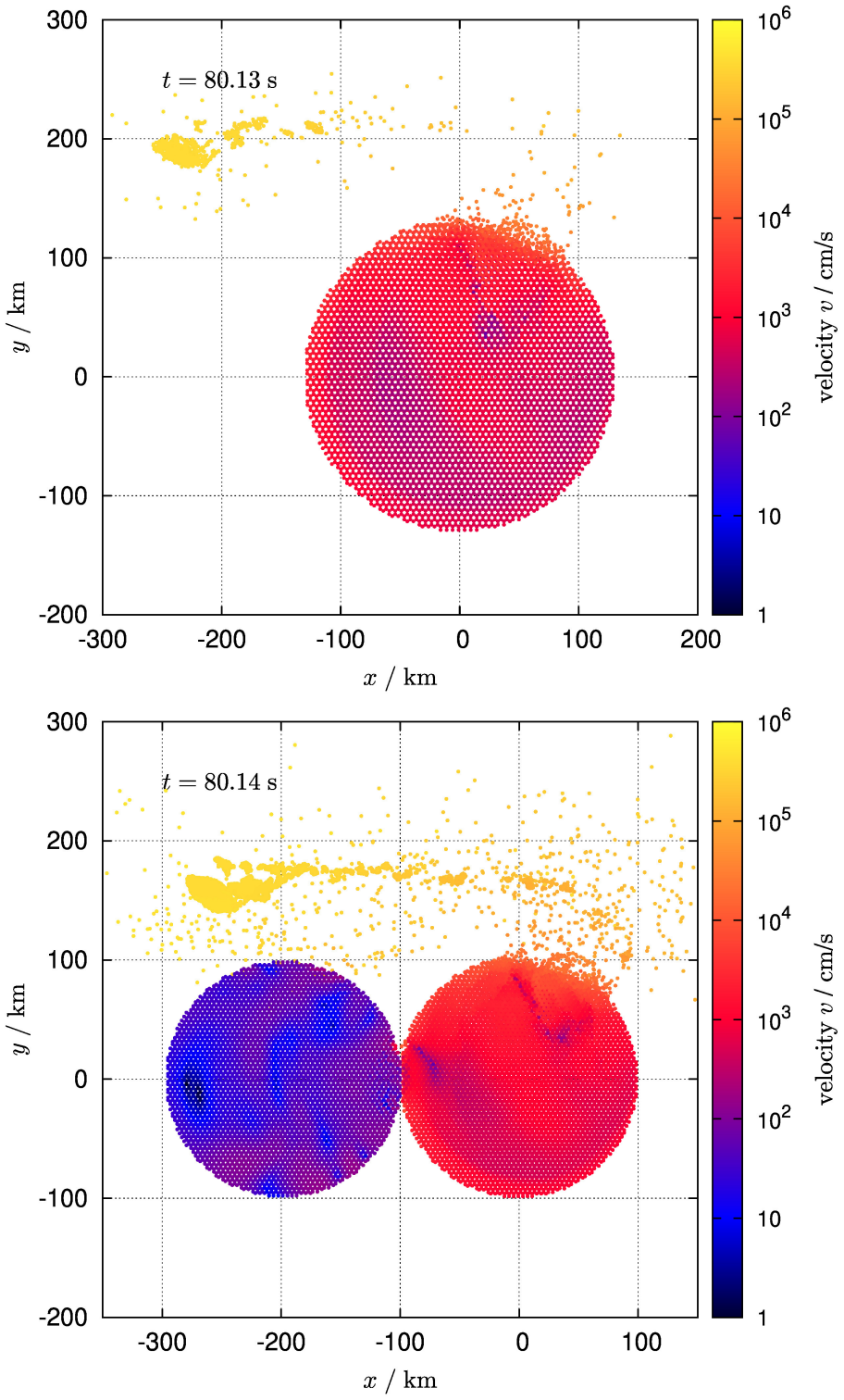


Figure 2.14: A comparison of SPH simulations of a disruption of a single body (basalt) with diameter $D_{\text{target}} = 250\,\text{km}$, by an impactor with the diameter $D_{\text{imp}} = 48\,\text{km}$ (silicate ice) (*top*) and a disruption of a bilobe basalt target, with $D_{\text{target}} = 198\,\text{km}$ for each sphere, by an impactor with $D_{\text{imp}} = 46\,\text{km}$ (silicate ice) (*bottom*). Time elapsed is $t = 80.1\,\text{s}$ in both cases. There are notable physical differences between the two simulations, especially in the propagation of the shock wave, which is reflected from free surfaces, the number of secondary impacts, or the fragmentation (damage) of the target. Nevertheless, the amount of ejected material and the resulting size-frequency distributions do not differ that much (cf. Figure 2.11).

the mass is totally damaged as one can see in Figure 2.14. On the other hand, the resulting SFDs are not that different, as we would expect.

Even so, there is a large parameter space, which is still not investigated (i.e. the impact geometry with respect to the secondary, secondary impacts, the position in the orbit). SPH simulations of impacts on bilobed or binary targets thus seem very worthy for future research.

Our work is also a strong motivation for research of disruptions of weak bodies (e.g. comets), better understanding the cometary disruption scaling law and also for experimental determination of material constants, which appear in the respective equation of state.

As a curiosity, we can also think of searching for the remaining projectile, which could be still present among Trojans on a trajectory substantially different from that of family. A substantial part of projectile momentum is preserved in our simulations, so we may turn the logic and we may assume the projectile most likely came from the Trojan region and then it should remain in this region too.

## Acknowledgements

We thank Alessandro Morbidelli for his review which helped to improve the final version of the paper.

The work of MB was supported by the grant no. P209/13/01308S and that of JR by P209/15/04816S of the Czech Science Foundation (GA CR). We acknowledge the usage of computers of the Stefanik Observatory, Prague.

# Chapter 3

# Eurybates — the 'only' asteroid family among Trojans?

## 3.1 Introduction

Trojans of Jupiter, which reside in the neighbourhood of $L_4$ and $L_5$ Lagrangian points, serve as an important test of the planetary migration theory (Morbidelli et al. 2005). Their inclination distribution, namely the large spread of $I$, can be explained as a result of chaotic capture during a brief period when Jupiter and Saturn encountered a 1:2 mean-motion resonance. Moreover, the Late Heavy Bombardment provides the timing of this resonant encounter $\simeq$3.8 Gyr ago (Gomes et al. 2005). It is thus important to understand the population of Trojans accurately.

There are several unresolved problems regarding Trojans, however, for example the number of families, which is a stringent constraint for collisional models. Roig et al. (2008) studied as many as ten suggested families, using relatively sparse SLOAN data and spectra. They noted most families seem to be heterogeneous from the spectroscopic point of view, with one exception — the C-type Eurybates family. As we argue in this paper, the number of families (with parent-body size $D \gtrsim 100$ km) is indeed as low as one.

Another strange fact is the ratio of $L_4$ and $L_5$ Trojans. Szabó et al. (2007) used SLOAN colour data to reach fainter than orbital catalogues and estimated the ratio to $N(L_4)/N(L_5) = 1.6 \pm 0.1$. There is no clear explanation for this, since the chaotic capture as a gravitational interaction should be independent of size or $L_4/L_5$ membership. Any hypothesis involving collisions would require a relatively recent disruption of a huge parent body, which is highly unlikely (O'Brien and Morbidelli, 2008, D. O'Brien, personal communication). This is again related to the actual observed number of Trojan families.

Brož and Vokrouhlický (2008) studied another resonant population, the so called Hilda group in the 3/2 mean-motion resonance with Jupiter, and reported only two families: Hilda and Schubart with approximately 200 and 100 km parent bodies. This number might be in accord with low collisional probabilities, assuming the Hilda family is very old and experienced the Late Heavy Bombardment (Brož et al. 2011).

Levison et al. (2009) compared the observed distribution of D-type asteroids and the model of their delivery from transneptunian region. They found a good match assuming the D-types (presumably of cometary origin) are easy-to-disrupt objects (with the strength more than 5 times lower than that of solid ice). Note that Trojan asteroids are a mixture of C- and D-type objects and we have to discriminate between them with respect to collisional behaviour.

All of the works mentioned above are a good motivation for us to focus on asteroid families in the Trojan population. The paper is organised as follows. First, we describe our data sources and methods in Section 3.2. A detailed study of orbital and physical properties

of families (and other 'false' groupings) is a matter of Section 3.3. Section 3.4 is devoted to the modelling of long-term dynamical evolution. Finally, there are concluding remarks in Section 3.5.

## 3.2 Methods

### 3.2.1 Resonant elements

We use the symplectic SWIFT integrator (Levison & Duncan 1994) for orbital calculations. Our modifications include a second order scheme of Laskar & Robutel (2001) and on-line digital filters, which enable us to compute suitable resonant proper elements: libration amplitude $d$ of the $a - a'$ oscillations, where $a$ is the osculating semimajor axis of an asteroid and $a'$ that of Jupiter, eccentricity $e$ and inclination $\sin I$. (In figures, we usually plot a mean value $\bar{a}$ of semimajor axis plus the libration amplitude $d$.) We employ their definition from Milani (1993). The source of initial osculating elements is the AstOrb catalogue, version JD = 2455500.5 (Oct 31st 2010).

There are actually two independent filters running in parallel: in the first one, we sample osculating elements every 1 yr, compute mean elements using the filter sequence B, B with decimation factors 3, 3 (refer to Quinn et al., 1991) a store this data in a buffer spanning 1 kyr. We then estimate the libration frequency $f$ by a linear fit of $\phi(t) = \lambda - \lambda' - \chi$, where $\lambda$, $\lambda'$ are the mean longitudes of an asteroid and Jupiter and $\chi = \pm 60^\circ$ for $L_4$ or $L_5$ respectively. The revolution of angle $\phi(t)$ must not be confined to the interval $[0, 360^\circ)$, of course. The amplitude of $d$ is computed for the already known $f$ by a discrete Fourier transform. Finally, an off-line running-average filter with a window 1 Myr is used to smooth the data.[1]

In the second filter, we compute proper eccentricity $e$ and proper inclination $\sin I$ by sampling osculating elements (1 yr step), computing mean elements using a filter sequence A, A, B and decimation factors 10, 10, 3, and then we apply a frequency modified Fourier transform (Sidlichovský and Nervorný, 1997), which gives us the relevant proper amplitudes.

The values of the resonant elements agree very well with those listed in the AstDyS catalogue by Knežević & Milani (see Figure 3.1). There are only few outliers, probably due to a different time span of integration. We computed proper elements for 2647 $L_4$ and 1496 $L_5$ Trojan asteroids.[2] This sample is roughly twice larger than previously analysed. The ratio of populations valid for $H \lesssim 15$ mag asteroids is thus $N(L_4)/N(L_5) \simeq 1.8$.

The overall distribution of Trojans in the $(d, e, \sin I)$ space is shown in Figure 3.2. Note there is only one cluster visible immediately in the bottom-left panel — around (3548) Eurybates. The reason is its tight confinement in inclinations ($\sin I = 0.125$ to 0.135).

### 3.2.2 Hierarchical clustering

In order to detect clusters in the resonant element space we use a hierarchical clustering method (Zappalá et al. 1994) with a standard metric $d_1$, with $\delta a$ substituted by $d$. We run the HCM code many times with various starting bodies and different cut–off velocities $v_{\rm cutoff}$ and determine the number of bodies $N$ in the given cluster. We find the $N(v_{\rm cutoff})$ dependence a very useful diagnostic tool. We can see these dependences for $L_4$ and $L_5$ Trojans in Figure 3.3.

It is easy to recognise, if a cluster has a concentration towards the centre — even at low $v_{\rm cutoff}$ it must have more than one member ($N \gg 1$). It is also instructive to compare clusters

[1] Equivalently, we may compute the amplitude $D$ of mean longitudes $\lambda - \lambda'$. Anyway, there is a linear relation between $d$ and $D$.

[2] The data are available on our web site `http://sirrah.troja.mff.cuni.cz/~mira/mp/`. We use also one-apparition orbits for the purposes of physical studies. Of course, orbital studies require more precise multi-apparition data.

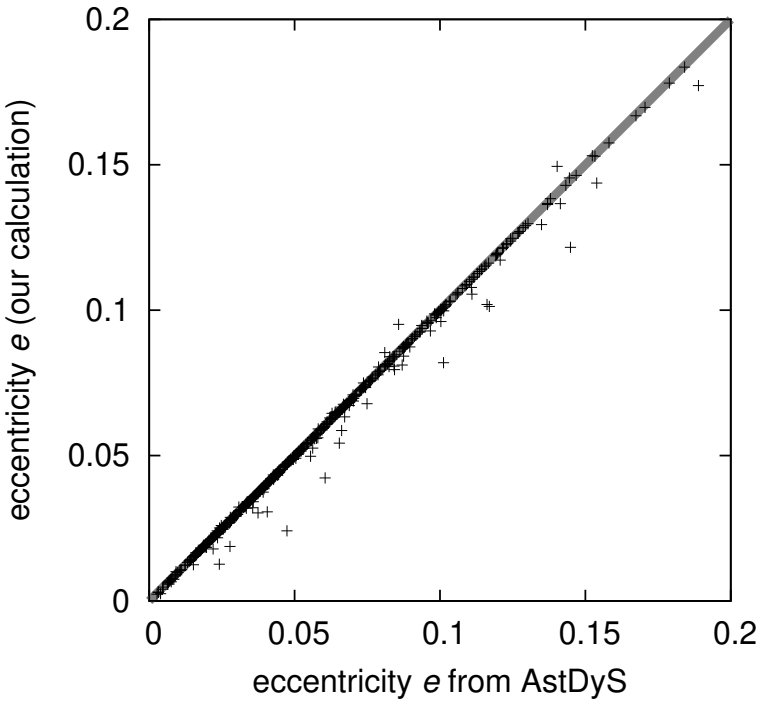


Figure 3.1: Comparison of the resonant eccentricity calculated by our code to that of Knežević & Milani (AstDyS catalogue). There is a line $x = y$ to aid a comparison.

with a random background (thin lines), which we generated artificially by a random-number generator in the same volume of the $(d, e, I)$ space. Insignificant (random) clusters usually exhibit an abrupt increase of $N$ at a high cut–off velocity.

As starting bodies we selected those listed in Roig et al. (2008). Only three clusters, namely the Eurybates, Aneas, 1988 $RG_{10}$ seem to be somewhat concentrated, i.e., denser than the background. The Hektor cluster is also concentrated but it contains only a relatively low number of members (20 to 70) before it merges with the background. In other words, smaller asteroids do not seem concentrated around (624) Hektor. Remaining clusters are more or less comparable to the background.

Nevertheless, we report a detection of a previously unknown cluster around (4709) Ennomos in $L_5$. It is relatively compact, since the minimum cut-off velocity is 70 m/s only. The cluster contains mostly small bodies which were discovered only recently.

Finally, let us point out a very tight cluster around (9799) 1996 RJ, associated already at $v_{\rm cutoff} = 20\,{\rm m/s}$. It is located at high inclinations and contains 9 bodies, three of them having short arcs. The cluster seems peculiar in the osculating element space too since it exhibits a non-random distribution of nodes and perihelia (see Table 3.1). This is similar to very young families like the Datura (Nesvorny et al., 2006) and it makes the 1996 RJ cluster a particularly interesting case with respect to collisional dynamics. Because one has to use slightly different methods for studies of such young families we postpone a detailed analysis to a next paper.

Let us compare Trojan clusters to the well known asteroid families in the outer Main Belt (Figure 3.4). Most families (e.g., Themis, Koronis, Eos) exhibit a steady increase of $N$ until they merge with another families or the entire outer Main Belt. Eurybates, Aneas and 1988 $RG_{10}$ are the only Trojan clusters which behave in a similar fashion. The Veritas family (dynamically young, Nesvorný et al. 2003) exhibits a different behaviour — for a large interval of $v_{\rm cutoff}$ the number of members $N$ remains almost the same, which indicates a clear separation from the background population. With respect to the $N(v_{\rm cutoff})$ dependence, the Ennomos cluster is similar to Veritas.

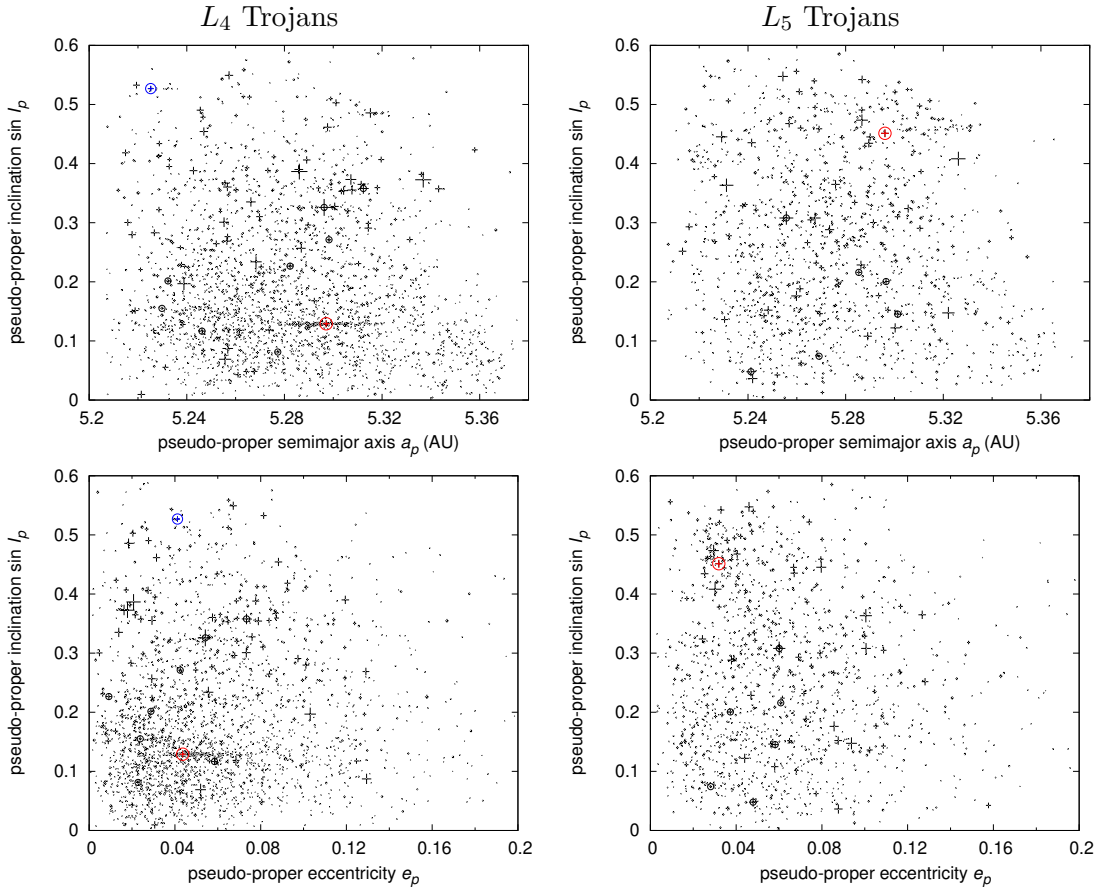


Figure 3.2: The resonant elements $(a \equiv \bar{a} + d, \sin I)$ and $(e, \sin I)$ for $L_4$ and $L_5$ Trojans. The crosses indicate relative sizes of bodies, taken either from the AstOrb catalogue or computed from absolute magnitude $H$ and geometric albedo $p_V$. In this plot, we assumed $p_V = 0.058$ for $L_4$ Trojans and 0.045 for those in $L_5$ (it corresponds to medians of known $p_V$'s). The asteroids (3548) Eurybates in $L_4$ and (4709) Ennomos in $L_5$, around which significant clusters are visible, are shown in red. Moreover, the asteroid (9799) 1996 RJ in $L_4$, which is surrounded by a small cluster, is denoted by a blue circle. (This cluster is so tight, that its members are located inside the circle on the $(e, \sin I)$ plot.)

Table 3.1: List of nine members of the (9799) 1996 RJ cluster and their proper $(a, e, \sin I)$ and osculating $(\Omega_{\rm osc}, \varpi_{\rm osc})$ elements and absolute magnitude $H$. Note the distribution of nodes and perihelia is not entirely uniform. Asteroids with short-arc orbits (<60 days) are denoted by a * symbol.

| number | designation | | $a$ | $e$ | $\sin I$ | $\Omega_{\rm osc}$ | $\varpi_{\rm osc}$ | $H$/mag |
|---|---|---|---|---|---|---|---|---|
| 9799 | 1996 RJ | | 5.2252 | 0.0412 | 0.5269 | 115.4 | 259.6 | 9.9 |
| 89938 | 2002 $FR_4$ | | 5.2324 | 0.0394 | 0.5274 | 70.0 | 23.1 | 12.5 |
| 226027 | 2002 $EK_{127}$ | | 5.2316 | 0.0399 | 0.5263 | 62.8 | 352.9 | 12.6 |
| 243316 | 2008 $RL_{32}$ | | 5.2340 | 0.0398 | 0.5268 | 27.3 | 358.2 | 12.8 |
| | 2005 $MG_{24}$ | | 5.2275 | 0.0404 | 0.5252 | 172.3 | 236.5 | 13.1 |
| | 2008 $OW_{22}$ | * | 5.2276 | 0.0401 | 0.5274 | 53.7 | 340.9 | 13.9 |
| | 2009 $RA_{17}$ | * | 5.2258 | 0.0409 | 0.5272 | 257.7 | 194.5 | 13.7 |
| | 2009 $RK_{63}$ | * | 5.2305 | 0.0407 | 0.5260 | 56.4 | 5.6 | 12.8 |
| | 2009 $SR_{30}$ | | 5.2362 | 0.0409 | 0.5258 | 103.6 | 22.0 | 13.3 |

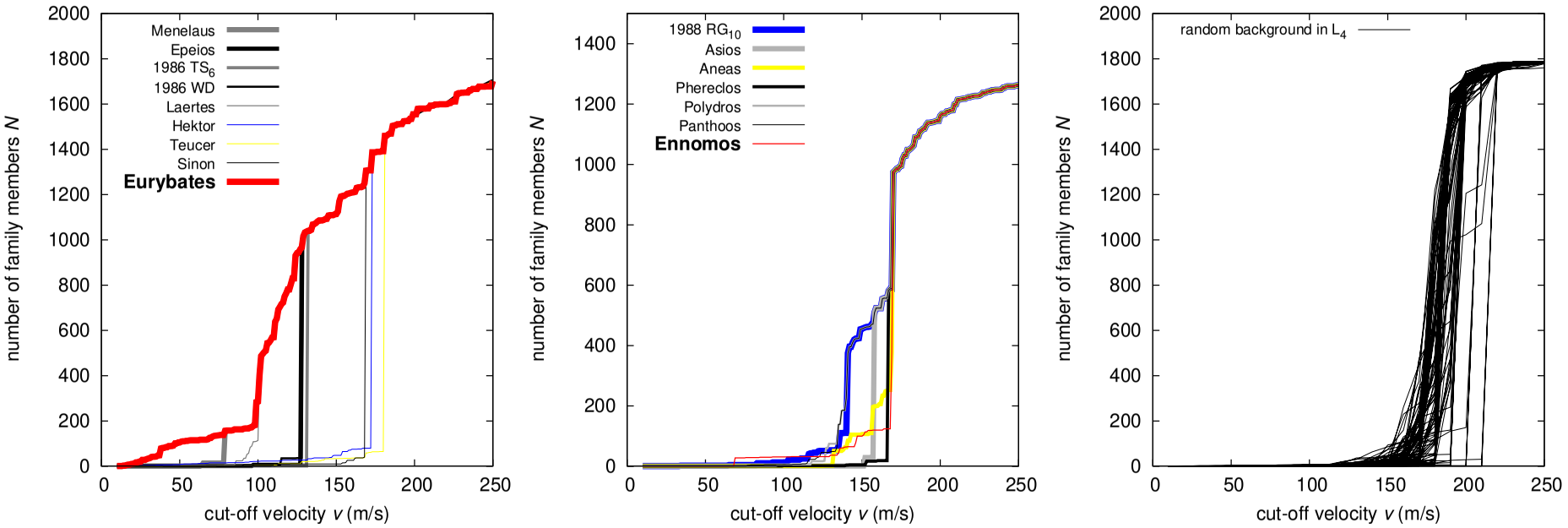


Figure 3.3: Left panel: The dependence of the number of family members $N$ on the cut–off velocity $v_{\rm cutoff}$ computed by the hierarchical clustering method. Only clusters among $L_4$ Trojans are included in this plot. Middle panel: The same $N(v_{\rm cutoff})$ dependence for $L_5$ Trojans. Right panel: Artificial clusters selected from *random* distribution of asteroids generated in the same volume of the $(d, e, \sin I)$ space.

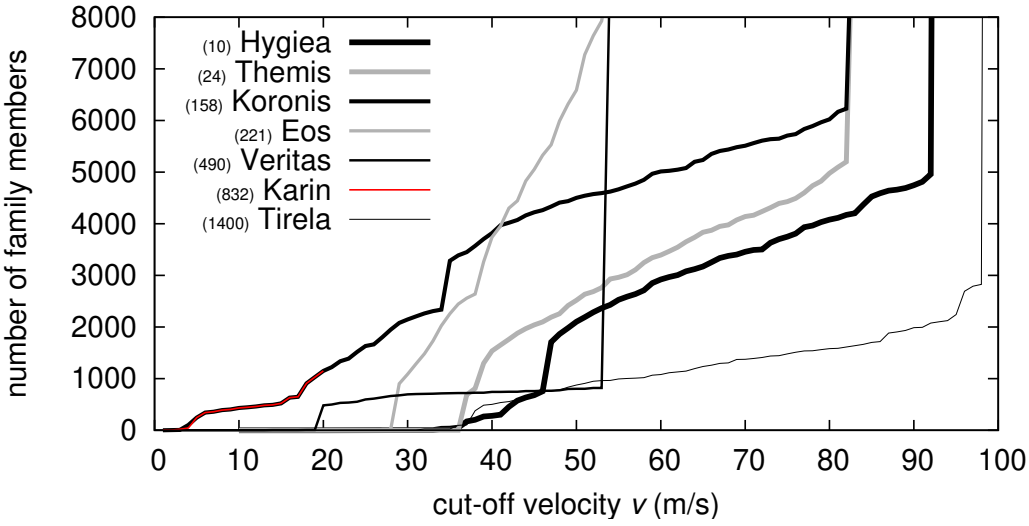


Figure 3.4: The $N(v_{\rm cutoff})$ dependence for seven outer main-belt families. If we would consider only a subset of asteroids brighter than $H = 15$ mag, which is an approximate observational limit for Trojans, the $N(v_{\rm cutoff})$ dependencies would be qualitatively the same, only slightly shifted to larger cut–off velocities.

### 3.2.3 Size-frequency distribution

At first, let us assume a single value of albedo for all family members. It is a reasonable assumption if the family is of collisional origin. We can then calculate sizes from absolute magnitudes and construct size-frequency distributions. Figure 3.5 shows a comparison of SFD's for the clusters detected by the HCM[3] and for the whole population of $L_4$ and $L_5$ Trojans.

A slope $\gamma$ of the cumulative distribution $N(>D) \propto D^{\gamma}$ is an indicative parameter. For $L_4$ and $L_5$ Trojans it equals to $-2.0 \pm 0.1$ and $-1.9 \pm 0.1$ in the intermediate size range 15 to 60 km. (These numbers are compatible with the study of Yoshida & Nakamura, 2008.) The slope is steeper at large sizes. The uncertainties are mainly due to a freedom in selection of the size range and the difference between $L_4$ and $L_5$ SFD's does not seem significant. The clusters have typically similar slope as background (within 0.1 uncertainty), thought sometimes the results are inconclusive due to small number of members. The Eurybates family with $-2.5 \pm 0.1$ slope is on the other hand significantly steeper than the mean slope of the whole Trojan population.[4] There are two more groups which exhibit a relatively steep slope, namely Laertes in $L_4$ ($\gamma = -3.1$) and 1988 $\mathrm{RG}_{10}$ in $L_5$ ($\gamma = -2.6$).

We should be aware, however, that even the background exhibits a trend with respect to inclinations (see Figure 3.6). Slope $\gamma$ typically decreases with inclination $\sin I$, which is especially prominent in case of the $L_4$ cloud. We have to admit if we compare the Eurybates family to its surroundings only ($\sin I = 0.1$ to 0.15), the difference in slopes is not so prominent. An interesting feature of the $L_5$ cloud is a dip in the interval $\sin I = 0.05$ to 0.1. This corresponds to the approximate location of the 1988 $\mathrm{RG}_{10}$ group.

The $\gamma(\sin I)$ dependence among Trojans is not unique. E.g. low-inclination bodies in the J3/2 resonance also have the SFD steeper than background ($\gamma = -2.5 \pm 0.1$ versus $-1.7 \pm 0.1$), without any clear family and a few big interlopers. May be, this feature reflects

[3] Of course, we have to select a 'suitable' value of the cut–off velocity for all clusters. Usually, we select that value for which $N(v_{\rm cutoff})$ is flat. Size-frequency distribution is not very sensitive to this selection anyway.

[4] Thought the number of the Eurybates members (105) is so small that it almost does not affect the mean slope of the whole $L_4$ population.

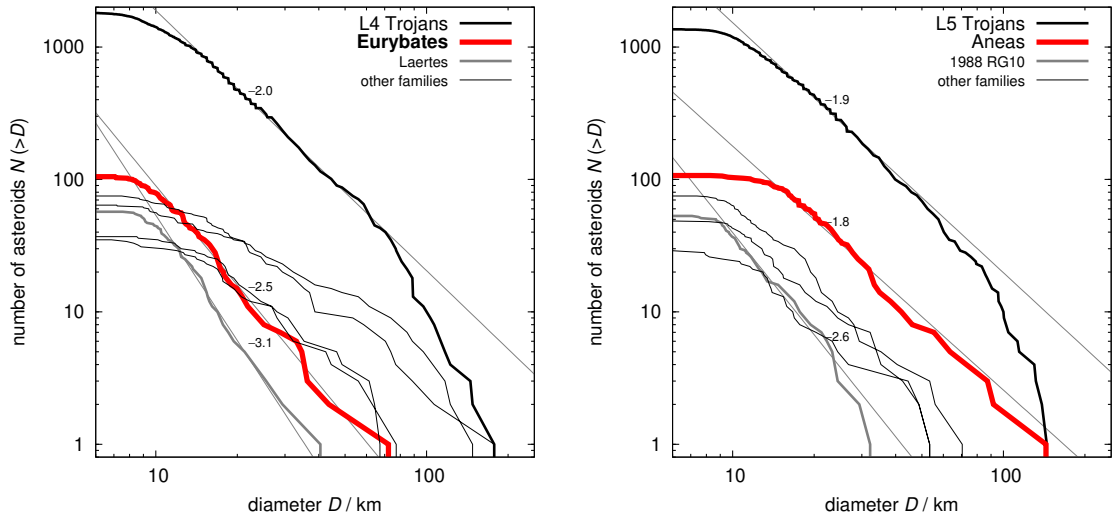


Figure 3.5: Left panel: size distributions of $L_4$ Trojans and the following clusters (there is a selected cut–off velocity in the parenthesis): Eurybates ($v_{\rm cutoff} = 50\,{\rm m/s}$), Laertes (94), Hektor (160), Teucer (175), Sinon (163), 1986 WD (120). Right panel: SFD's of $L_5$ Trojans and the following clusters: 1988 $RG_{10}$ (at $v_{\rm cutoff} = 130\,{\rm m/s}$), Aneas (150), Asios (155), Panthoos (130), Polydoros (130).

different *source reservoirs* of low- and high-inclination bodies among Trojans and J3/2?[5] It may be also in concert with a colour–inclination dependence reported by Szabó et al. (2007).

We also test albedo distributions dependent on size, since the measurements by Fernández et al. (2009) suggested small Trojans are significantly brighter and thus smaller. Large asteroids have $p_V = 0.044 \pm 0.008$ while small $p_V = 0.12 \pm 0.06$. This is a significant change of the SFD, which occurs around the size $D \simeq 30\,{\rm km}$. The SFD thus becomes shallower below this size, e.g. for Eurybates we would have $\gamma = -1.6$ and for L4 Trojans $\gamma = -1.5$, so the SFD's become comparable with respect to the slope. Thought, as we stated above, for a real collisional family we expect the albedo distribution to be rather homogeneous and independent of size.

### 3.2.4 Colour and spectral data

We used the Sloan Digital Sky Survey Moving Object catalogue version 4 (SDSS-MOC4) to check the families are spectrally homogeneous, as we expect. Due to a larger uncertainty in the $u$ colour in SDSS-MOC4, we used the color indices $a^*$ and $i-z$, where $a^* = 0.89(g-r) + 0.45(r-i) - 0.57$ (defined by Parker et al. 2008).

The result is shown in Figure 3.7. It is clearly visible that the distribution of the Eurybates family in the space of $(a^*, i-z)$ colours is different from the Trojan background. On contrary, the 1988 $RG_{10}$ group covers essentially the same area as the background. The Aneas is only slightly shifted towards larger $a^*$ and $i-z$ with respect to the background. There is a lack of data for the Ennomos group — three bodies are not sufficient to compare the colour distributions.

Alternatively, we may use principal component analysis of the SDSS colour indices. We use only data with uncertainties smaller than 0.2 mag, which resulted in 70 887 records. We calculated eigenvalues ($\lambda_{1,2,3,4} = 0.173,\ 0.0532,\ 0.0249,\ 0.0095$), corresponding eigenvectors

[5] Both Trojan and J3/2 regions are dynamically unstable during Jupiter–Saturn 1:2 mean motion resonance, so we expect the same bodies entering Trojan region may enter J3/2.

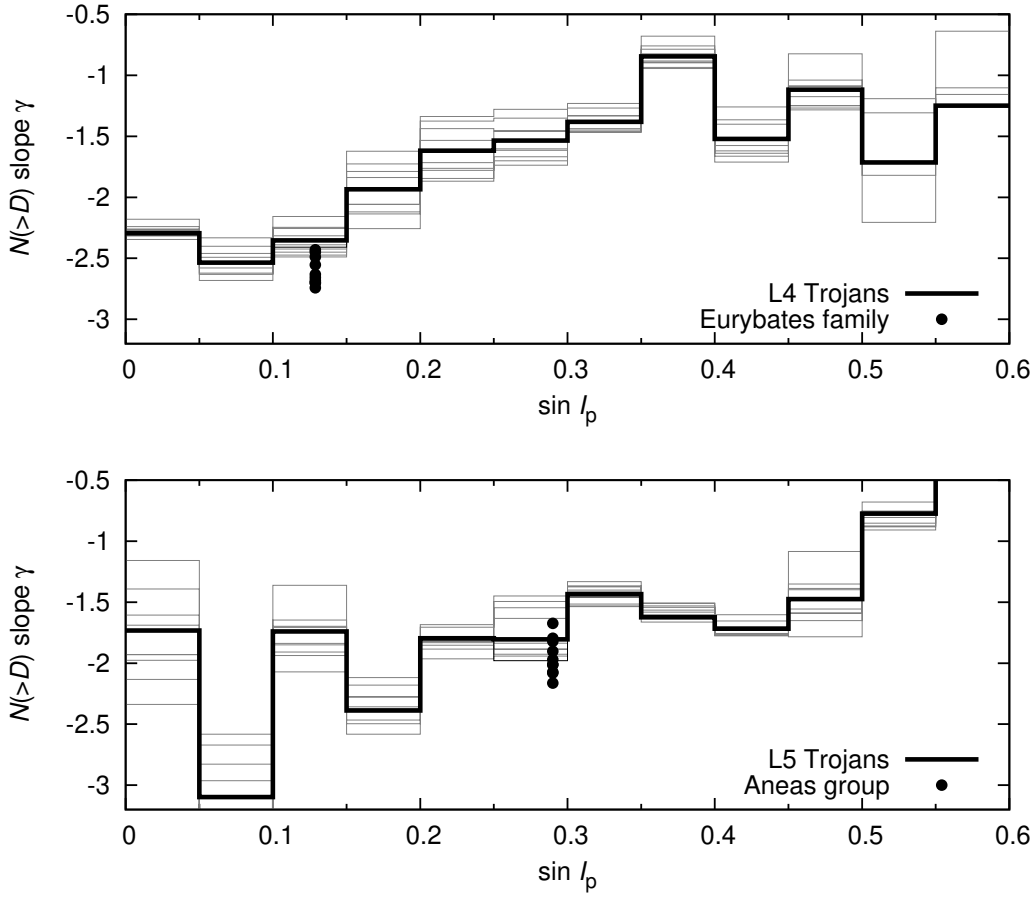


Figure 3.6: Slopes $\gamma$ of the size-frequency distributions $N(>D)$ for $L_4$ and $L_5$ Trojans and their dependence on the inclination $\sin I$. The range of diameters for which the SFD's were fitted is $D_{\min} = 12\,\mathrm{km}$, $D_{\max} = 30\,\mathrm{km}$. Thin lines were calculated for different ranges, which were varied as $D_{\min} \in (10, 15)\,\mathrm{km}$, $D_{\max} \in (20, 40)\,\mathrm{km}$. Their spread indicates the uncertainty of $\gamma$ in a given interval of $\sin I$. The populations are observationally complete down to $D \simeq 10\,\mathrm{km}$, because the characteristic change of slope due to incompleteness occurs at smaller sizes (see also Yoshida and Nakamura 2008).

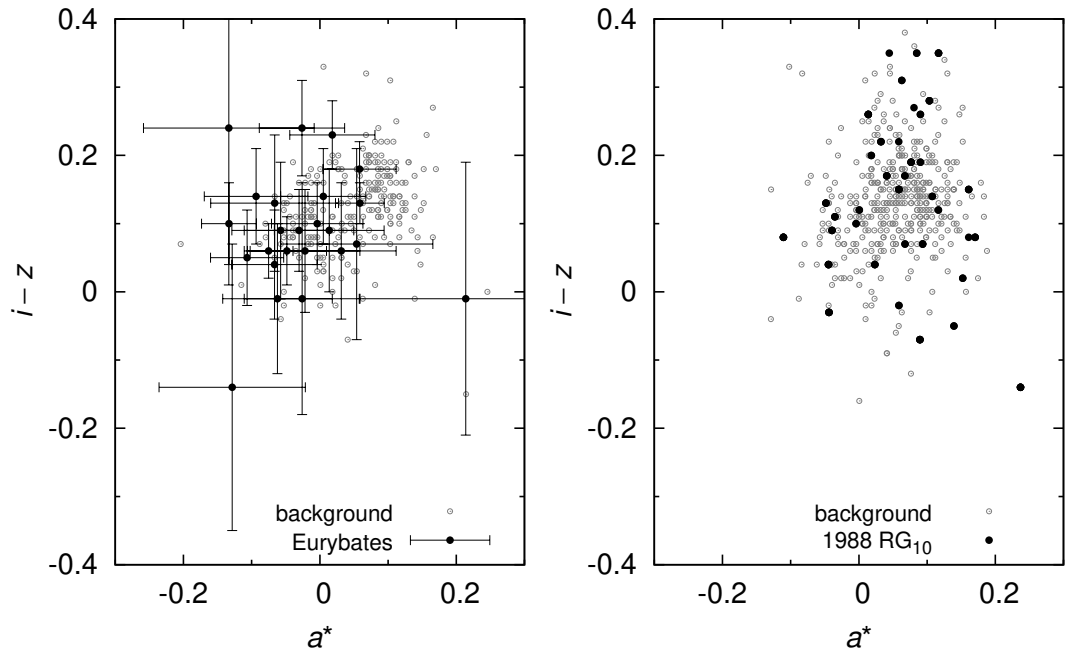


Figure 3.7: Left panel: The $(a^*, i-z)$ colours for the $L_4$ Trojans (gray dots) and the Eurybates family (black dots with error bars). The distributions differ significantly in this case. Right panel: A similar comparison for the $L_5$ Trojans and the 1988 $RG_{10}$ group, which seem to be indistinguishable.

and constructed the following three principal components (Trojanová 2010):

$$\begin{aligned} \mathrm{PC}_1 &= 0.235\,(u-g) + 0.416\,(g-r) + 0.598\,(g-i) \\ &\quad + 0.643\,(g-z)\,, \qquad (3.1) \\ \mathrm{PC}_2 &= 0.968\,(u-g) - 0.173\,(g-r) - 0.147\,(g-i) \\ &\quad - 0.106\,(g-z)\,, \qquad (3.2) \\ \mathrm{PC}_3 &= 0.078\,(u-g) + 0.601\,(g-r) + 0.330\,(g-i) \\ &\quad - 0.724\,(g-z)\,, \qquad (3.3) \end{aligned}$$

which have a clear physical interpretation: $\mathrm{PC}_1$ corresponds to an overall slope, $\mathrm{PC}_2$ is a variability in the $u$ band, and $\mathrm{PC}_3$ a depth of the $1\,\mu$m absorption band. The Eurybates family is different from Trojans in all three principal components (mean $\mathrm{PC}_1$ of the Eurybates members is smaller, $\mathrm{PC}_2$ and $\mathrm{PC}_3$ larger). The Aneas group has the same distribution of $\mathrm{PC}_2$ and $\mathrm{PC}_3$ as Trojans and the 1988 $\mathrm{RG}_{10}$ group is similar to Trojans even in all three components.

Hence, we confirm the Eurybates family seems distinct in color even in the fourth version of the SDSS-MOC. This fact is consistent with previous work of Roig et al. (2008), who used third version of the same catalogue and classified Eurybates family members as C-type asteroids.

Finally, note that De Luise et al. (2010) pointed out an absence of ice spectral features at 1.5 and 2.0 $\mu$m on several Eurybates members and Yang and Jewitt (2007) concluded the same for (4709) Ennomos. This puzzling fact may indicate that pure ice covers at most 10 % of the Ennomos surface.

### 3.2.5 Impact disruption model

We use a simple model of an isotropic disruption from Farinella et al. (1994). The distribution of velocities "at infinity" follows the function

$$\mathrm{d}N(v) = Cv(v^2 + v_{\mathrm{esc}}^2)^{-(\alpha+1)/2}\,, \tag{3.4}$$

with the exponent $\alpha$ being a free parameter, $C$ a normalisation constant and $v_{\mathrm{esc}}$ the escape velocity from the parent body, which is determined by its size $R_{\mathrm{PB}}$ and mean density $\rho_{\mathrm{PB}}$. The distribution is cut at a selected maximum allowed velocity $v_{\mathrm{max}}$ to prevent outliers. We typically use $v_{\mathrm{max}} = 300\,\mathrm{m/s}$. The orientations of velocity vectors in space are assigned randomly. We assume the velocity of fragments is independent on their size.[6]

There are several more free parameters, which determine the initial shape of the family in the space of proper elements: initial osculating eccentricity $e_{\mathrm{i}}$ of the parent body, initial inclination $i_{\mathrm{i}}$, as well as true anomaly $f_{\mathrm{imp}}$ and argument of perihelion $\omega_{\mathrm{imp}}$ at the time of impact disruption.

An example of a synthetic family just after disruption and its comparison to the observed Eurybates family is shown in Figure 3.8. Usually, there is a significant disagreement between this simple model of impact disruption and the observations. Synthetic families usually look like thin 'filaments' in the $(d, e, \sin I)$ space, which are curved due to the mapping from osculating elements to resonant ones. On the other hand, observed groups among Trojans are much more spread. However, this only indicates an importance of further long-term evolution by chaotic diffusion and possibly by planetary migration.[7]

In case of the Ennomos group members, they are distributed mostly on larger semi-major axes than (4709) Ennomos, thought isotropic impact disruptions produce fragments distributed evenly on larger and smaller $a$. May be, it is an indication of an anisotropic velocity field? Or a different parent body of this cluster?

### 3.2.6 Planetary migration

If asteroid families are very old, planetary migration might influence their current shape. In order to study of late stages of planetary migration, which is caused by interactions with a planetesimal disk, we construct the following model. We treat the migration analytically within a modified version of the numerical symplectic SWIFT-RMVS3 integrator (Levison & Duncan 1994), which accounts for gravitational perturbations of the Sun and four giant planets and includes also an energy-dissipation term, as described in Brož et al. (2011). The speed of migration is characterised by the exponential time scale $\tau_{\mathrm{mig}}$ and the required total change of semimajor axis $a_{\mathrm{i}} - a_{\mathrm{f}}$. We use an eccentricity damping formula too, which simulates the effects of dynamical friction and prevent an unrealistic increase of eccentricities (Morbidelli et al. 2010). The amount of damping is determined by the parameter $e_{\mathrm{damp}}$.

We try to adjust initial orbital parameters of planets and the parameters of migration in such a way to end up at currently observed orbits. The integration time step is $\Delta t = 36.525$ days and the time span is usually equal to $3\tau_{\mathrm{mig}}$, when planetary orbits almost stop to migrate.

### 3.2.7 Inefficient Yarkovsky/YORP effect

On long time scales, the Yarkovsky thermal force might cause significant perturbations of orbits. We use an implementation of the Yarkovsky thermal effect in the SWIFT N-body

[6] If we use a size-dependent relation for velocities similar to Vokrouhlický et al. (2006), our results do not change much, because the overall shape of the velocity distribution is quite similar to the size-independent case.

[7] Only very young clusters like the Karin family (Nesvorný et al. 2002) exhibit this kind of a 'filament' shape.

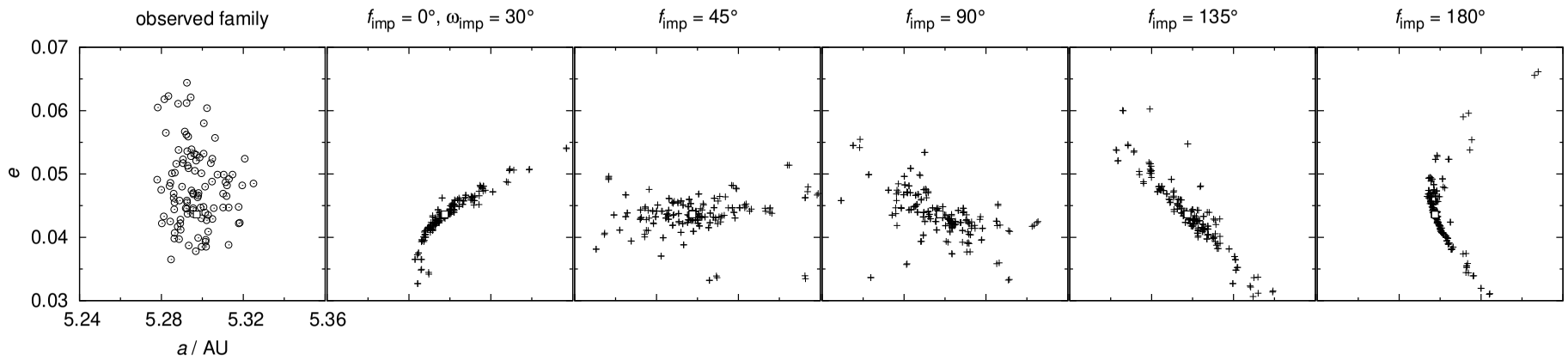


Figure 3.8: A comparison between the observed Eurybates family (open circles) and synthetic families (crosses) just after the impact disruption computed for several values of $f_{\mathrm{imp}} = 0°, 45°, 90°, 135°, 180°$ and $\omega_{\mathrm{imp}} = 30°$, $R_{\mathrm{PB}} = 47\,\mathrm{km}$, $\rho_{\mathrm{PB}} = 1300\,\mathrm{kg/m^3}$. Different geometry in $f$, $\omega$ produces a slightly different cluster, nevertheless, it is always tighter than the observed family. The position of the asteroid (3548) Eurybates is denoted by a square.

integrator (Brož 2006). It includes both the diurnal and seasonal variants.

The YORP effect (thermal torques affecting spin states; Vokrouhlický et al. 2006) was not taken into account in our simulations. The reason is that the respective time scale $\tau_{\mathrm{YORP}}$ is of the order 100 My to 1 Gyr So as a 'zero' approximation, we neglect the YORP effect on these "short" time scales and keep the orientations of the spin axes fixed.

For Trojan asteroids captured in a zero-order mean motion resonance, the Yarkovsky perturbation only affects the position of libration centre (Moldovan et al. 2010). Note that the perturbation acts 'instantly' — there is no systematic secular drift in eccentricity nor in other proper elements which is an important difference from first-order resonances, where a $e$-drift is expected (Brož & Vokrouhlický 2008, Appendix A). This is another reason we do not need a detailed YORP model here.

The thermal parameter we use are reasonable estimates for C/X-type bodies: $\rho_{\mathrm{surf}} = \rho_{\mathrm{bulk}} = 1300\,\mathrm{kg/m^3}$ for the surface and bulk densities, $K = 0.01\,\mathrm{W/m/K}$ for the surface thermal conductivity, $C = 680\,\mathrm{J/kg}$ for the heat capacity, $A = 0.02$ for the Bond albedo and $\epsilon_{\mathrm{IR}} = 0.95$ for the thermal emissivity.

## 3.3 Asteroid families and insignificant groups

In this section, we briefly discuss properties of selected clusters: Eurybates, Ennomos, Aneas and 1988 $\mathrm{RG}_{10}$. We focus on these four clusters, since they seem most prominent according to our previous analysis.

### 3.3.1 Eurybates family

The Eurybates family can be detected by the hierarchical clustering method for cut–off velocities $v_{\mathrm{cutoff}} = 38$ to $78\,\mathrm{m/s}$, when it merges with Menelaus (see Figure 3.3). Yet, we do not rely just on the HCM! Another selection criterion we use is a 'meaningful' shape of the family and its changes with respect to $v_{\mathrm{cutoff}}$. A very important characteristic of the Eurybates family at low values of $v_{\mathrm{cutoff}}$ is a tight confinement of inclinations ($\sin I$ within 0.01). It breaks down at $v_{\mathrm{cutoff}} \simeq 68\,\mathrm{m/s}$, so we consider this value as an upper limit. The Eurybates family is also confined in semimajor axis, being approximately twice smaller than other groups.

The diameter of the parent body is $D_{\mathrm{PB}} \doteq 97\,\mathrm{km}$ for albedo $p_V = 0.055$ if we sum the volumes of the known bodies. Of course, in reality it is slightly larger due to observational incompleteness. If we prolong the slope of the SFD $\gamma = -2.5$ down to zero we obtain $D_{\mathrm{PB}} \doteq 110\,\mathrm{km}$. The geometric method of Tanga et al. (1999) gives an upper limit $D_{\mathrm{PB}} \simeq 130\,\mathrm{km}$.

Spectral slopes of family members are rather homogeneous and correspond to C/P-types (Roig et al. 2008).

### 3.3.2 Ennomos group

The cluster around (4709) Ennomos can be recognised for a wide interval of cut–off velocities $v_{\mathrm{cutoff}} \in (69, 129)\,\mathrm{m/s}$ when it stays compact and confined in inclinations ($\sin I = 0.451$ to 0.466). Very probably, there are several interlopers, because we can count 4 to 10 asteroids in the surroundings, i.e., in the same volume of the $(d, e, \sin I)$ space (see Figure 3.9). Since small bodies dominate the Ennomos group we suspect large bodies might be actually interlopers.

A very intriguing feature is a high albedo of (4709) Ennomos $p_V \simeq 0.15$ measured by Fernández et al. (2003). Apart from other explanations, the authors speculated it may result from a recent impact which covered the surface with pristine ice. If true the relation between the fresh surface and the collisional family might be a unique opportunity to study cratering events.

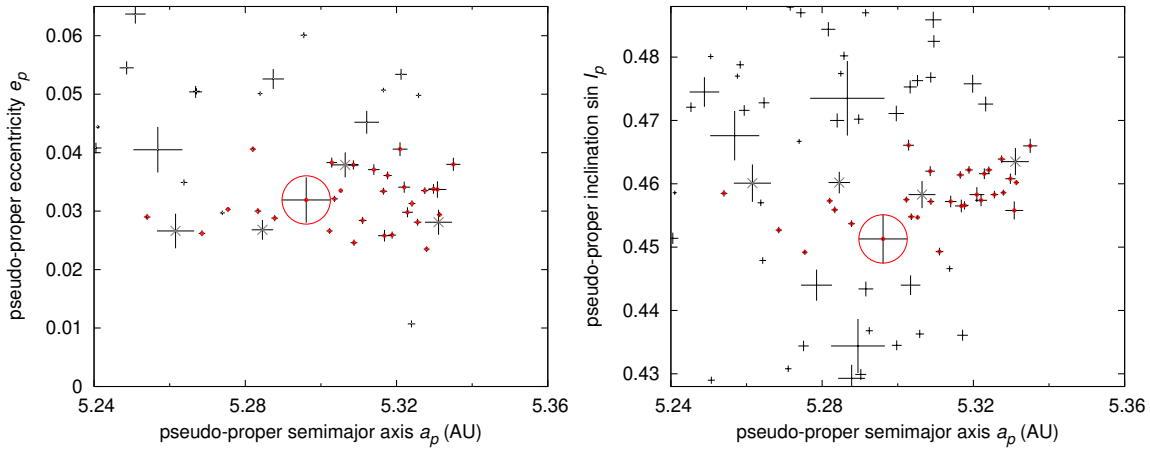


Figure 3.9: A detail of the $L_5$ Trojan population where the Ennomos group is visible. Left panel: resonant semimajor axis $a$ vs eccentricity $e$. Only asteroids occupying the same range of inclinations as the Ennomos group $\sin I \in (0.448, 0.468)$ are plotted to facilitate a comparison with the density of surroundings space (background). The sizes of plus signs are proportional to diameters of the asteroids. Probable family members are denoted by small red circles and probable interlopers by small grey crosses. Right panel: $a$ vs inclination $\sin I$, with range of eccentricities $e \in (0.02, 0.045)$.

We cannot exclude a possibility that (4709) Ennomos is actually an interloper and the family is not related to it at all. Nevertheless, our hypothesis is testable: family members should exhibit a similarity in spectra and albedos. The only information we have to date are SDSS colours for three members: 98362, 2005 $YG_{204}$ are probably C-types and 2005 $AR_{72}$ is a D-type. In case new data become available we can remove interlopers from our sample and improve our analysis.

The size distribution of the Ennomos group is barely constrained, since small bodies are at the observational limit. Moreover, removal of interlopers can change the SFD slope completely (from $\gamma = -1.4$ to $-3.2$ or so). The minimum parent body size is about $D_{\mathrm{PB}} \simeq 67$ km if all members have high albedo $p_V = 0.15$.

### 3.3.3 Group denoted Aneas

The Aneas group looks like a middle portion of the $L_5$ cloud with approximately background density. It spans whole range of semimajor axes, as background asteroids do.

The minimum size of a hypothetical parent body is $D_{\mathrm{PB}} = 160$ to 170 km (for albedo $p_V = 0.055$ to 0.041). This size is very large and an impact disruption of such body is less probable (see Section 3.4.4). The size-frequency distribution is shallow, with approximately the same slope as background.

According to Roig et al. (2008) the colours are rather homogeneous and correspond to D-types, with $\simeq 10\,\%$ of probable interlopers.

### 3.3.4 Group denoted 1988 $RG_{10}$

The group around asteroid (11487) 1988 $RG_{10}$ again looks like a lower portion of the $L_5$ cloud at low inclinations, with $\sin I \in (0.06, 0.1)$. The SFD is steeper ($\gamma = -2.6 \pm 0.1$) than surroundings in $L_5$ and the resulting parent body size $D \simeq 60$ km is relatively small. The colours seems heterogeneous (Roig et al. 2008) and we can confirm this statement based on the new SDSS-MOC version 4 data.

The remaining clusters (Hektor, Teucer, Sinon, 1986 WD, Laertes, Asios, Polydoros,

Panthoos, etc.) may be characterised as follows: (i) they have a density in $(d, e, \sin I)$ space comparable to that of background (surroundings); (ii) when identified by the HCM their semimajor axes span the whole range of Trojan region; (iii) the slopes of their SFD's are comparable to the background; (iv) they are often inhomogeneous with respect to colours (according to Roig et al. 2008). These reasons lead us to a conclusion that these clusters are not necessarily real collisional families.

## 3.4 Long-term evolution of Trojan families

### 3.4.1 Evolution due to chaotic diffusion

We try to model long-term evolution of the Eurybates family. At first, we generate a synthetic family (consisting of 42 bodies) by an impact disruption of the parent body with required size. Then we integrate the synthetic family and compare it at particular time to the observed Eurybates family. The time span of the integration is 4 Gyr.

The main driving mechanism is slow *chaotic diffusion* (the Yarkovsky effect is present but inefficient in the Trojan region). Initially, the spread of inclinations of the synthetic family is consistent with the observed one. On the other hand, the shape in $(a, e)$ elements is clearly inconsistent.

Since the inclinations evolve only barely we focus on the evolution of in the $(a, e)$ plane (see Figure 3.10). The point is the synthetic family, namely the 'filament' structure, has to disperse sufficiently. After 500 Myr it is still recognisable but after 1 Gyr of evolution it is not. So we may constrain the age of the Eurybates family from 1 to 4 Gyr.[8]

A similar analysis for the Ennomos group indicates that chaotic diffusion is faster in this region (given the large inclination) and the most probable age thus seems to be from 1 to 2 Gyr. Beyond 2 Gyr the inclinations of the synthetic family become too large compared to the observed Ennomos group, while the eccentricites are still compatible.

We try to model Aneas and 1988 $\mathrm{RG}_{10}$ groups too (see Figure 3.11). In these two cases, there is a strong disagreement between our model and observations. The observed groups are much larger and chaotic diffusion in respective regions is very slow. Even after 4 Gyr of orbital evolution, the synthetic family remains too small.

The only free parameter which may substantially change our results is the initial velocity distribution. Theoretically, the distribution might have been strongly anisotropic. However, we cannot choose initial velocities entirely freely, since their magnitude should be comparable to the escape velocity from the parent body, which is fixed by the size $D_{\mathrm{PB}}$ and only weakly dependent on a-priori unknown density $\rho_{\mathrm{PB}}$.

Another solution of this problem is possible if we assume families are very old and they experienced perturbations due to planetary migration.

### 3.4.2 Stability during planetary migration

The major perturbation acting on Trojans are *secondary resonances* between the libration period $P_{J1/1}$ of the asteroid in the J1/1 mean-motion resonance with Jupiter and the period $P_{1\mathrm{J}-2\mathrm{S}}$ of the critical argument of Jupiter–Saturn 1:2 resonance (Morbidelli et al. 2005)

$$P_{\mathrm{J1/1}} = nP_{1\mathrm{J}-2\mathrm{S}}\,, \tag{3.5}$$

[8] We verified these estimates by a 2-dimensional Kolmogorov–Smirnov test of the $(a, e)$ distributions: initially the KS distance is $D_{\mathrm{KS}} = 0.30$ and the probability $p_{\mathrm{KS}}(>D) = 0.02$, which means the distribution are incompatible. At $t = 1$ Gyr, the values are $D_{\mathrm{KS}} = 0.20$ and $p_{\mathrm{KS}}(>D) = 0.32$, which indicates a reasonable match.

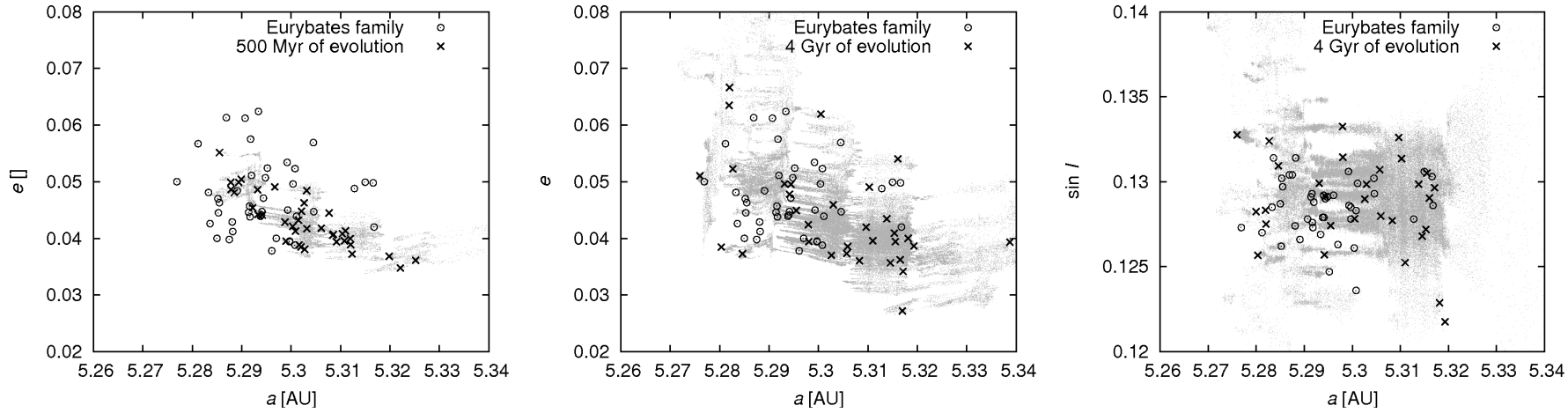


Figure 3.10: Orbital evolution of the synthetic family and its comparison with the observed Eurybates family. Left panel: the situation in the $(a, e)$ plane at 500 Myr. Middle panel: the situation after 4 Gyr. Chaotic diffusion disperses the synthetic family in course of time (see shaded tracks of particles). Right panel: the $(a, \sin I)$ plane at the same time. Inclinations evolve only barely.

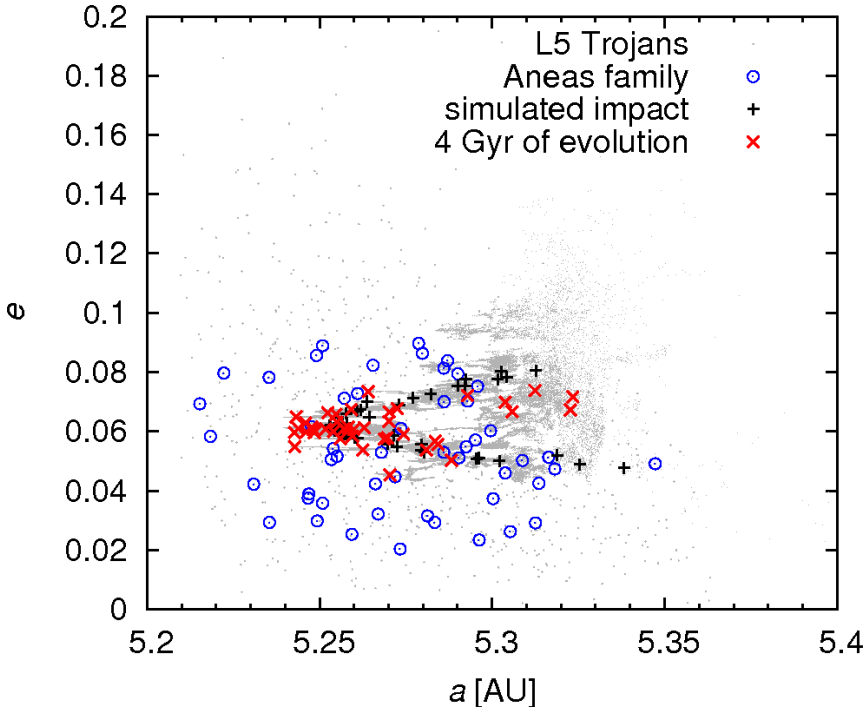


Figure 3.11: Evolution of the synthetic family over 4 Gyr versus the observed Aneas group. Chaotic diffusion is slow and it seems impossible to match the large spread of the observed group even after 4 Gyr.

where $n$ is a small integer number. Typical libration periods are $P_{\mathrm{J1/1}} \simeq 150\,\mathrm{yr}$ and $P_{\mathrm{1J-2S}}$ changes as planets migrate (it decreases because Jupiter and Saturn recede from their mutual 1:2 resonance).[9]

All synthetic families are strongly unstable when $P_{\mathrm{1J-2S}} \simeq 150\,\mathrm{yr}$ and even during later stages of migration with $P_{\mathrm{1J-2S}} \simeq 75\,\mathrm{yr}$ the eccentricities of family members are perturbed too much to match the observed families like Eurybates or Ennomos (see Figure 3.12). There are practically no plausible migration scenarios – regardless of time scale $\tau_{\mathrm{mig}}$ – which would produce a sufficiently compact group, unless Jupiter and Saturn are almost on their current orbits. We tested $\tau_{\mathrm{mig}} = 0.3, 3, 30\,\mathrm{Myr}$ and even for $\Delta a_{\mathrm{J}} \equiv a_{\mathrm{Jf}} - a_{\mathrm{Ji}}$ as small as $-0.08\,\mathrm{AU}$ and $\Delta a_{\mathrm{S}} = +0.25\,\mathrm{AU}$ the perturbation was too strong. The reason is that one has to avoid $n = 2$ secondary resonance to preserve a low spread of a synthetic family.

Let us conclude if any of Trojan families was created during planetary migration and if the migration was smooth (exponential) the family cannot be visible today. However, we cannot exclude a possibility that final stages of migration were entirely different, e.g., similar to the 'jumping-Jupiter' scenario (Morbidelli et al. 2010).

### 3.4.3 Families lost by the ejection of fragment outside the resonance

We studied a possibility that some families cannot be identified because the breakup occurred at the outskirts of the stable libration zone and some fragments were ejected outside the J1/1 resonance. We thus chose 30 largest asteroids near the edge of the $L_4$ libration zone and we simulated breakups of these asteroids which create families with 30 fragments each. We assumed the diameter of all parent bodies equal to $D_{\mathrm{PB}} = 100\,\mathrm{km}$ and their density $\rho_{\mathrm{PB}} = 1.3\,\mathrm{g\,cm^{-3}}$. The breakups always occurred at the same geometry $f_{\mathrm{imp}} = 0°$, $\omega_{\mathrm{imp}} = 30°$.

[9] Another source of instability might be a secondary resonance with $P_{\mathrm{2J-5S}}$ (the so called Great Inequality period) thought it is weaker than $P_{\mathrm{1J-2S}}$. We find no asteroids perturbed by secondary resonances connected with $P_{\mathrm{3J-7S}}$ or $P_{\mathrm{4J-9S}}$ which are present 'en route'. Neither Uranus nor Neptune play an important role.

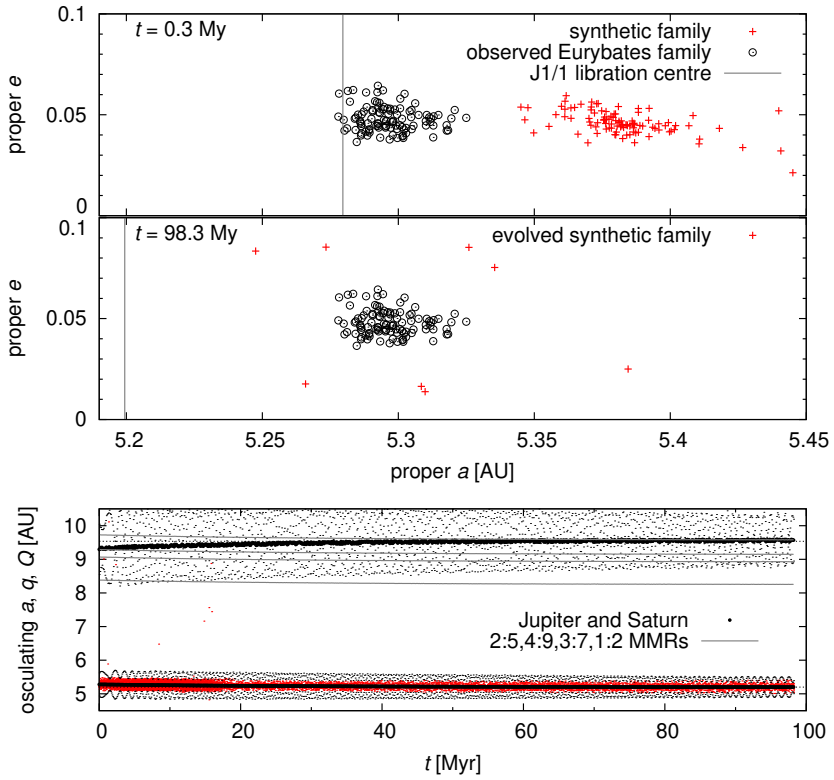


Figure 3.12: Evolution of a synthetic family during late phases of planetary migration ($\tau_{\mathrm{mig}} = 30\,\mathrm{Myr}$ in this case). Top panel: the state at 0 Myr, middle: 100 Myr, bottom: the respective orbital evolution of Jupiter and Saturn. The family is almost destroyed and it is definitely incompatible with the observed Eurybates family.

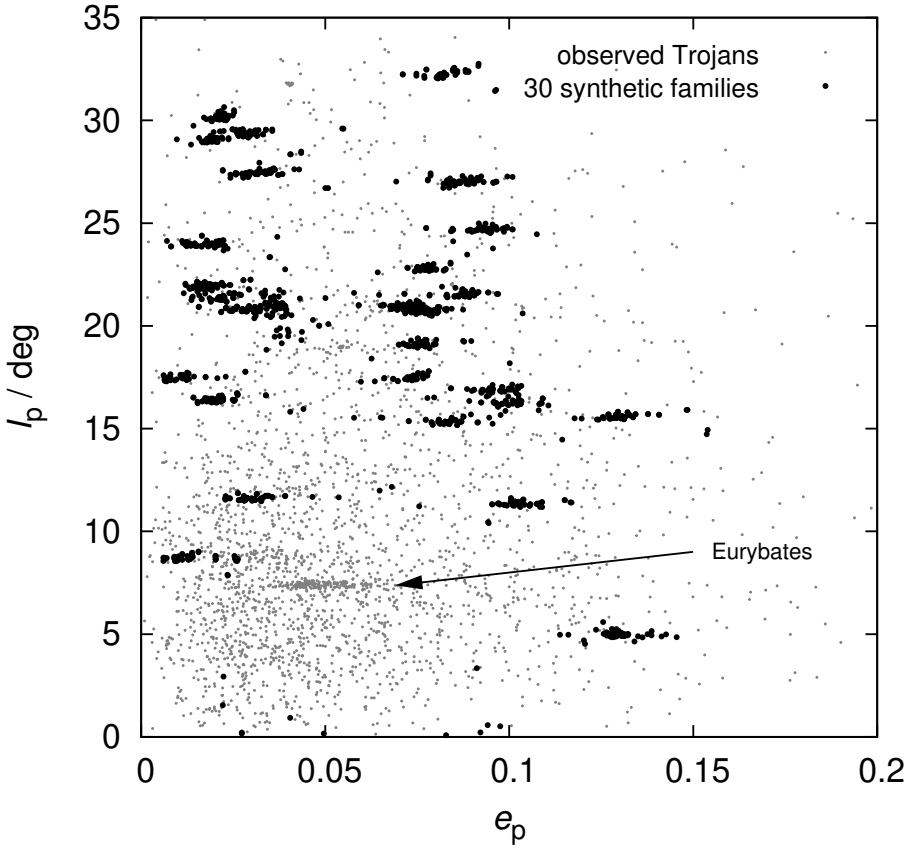


Figure 3.13: Proper eccentricities and inclinations of 30 *synthetic* families (black dots), which originated near the border of stable libration zone, compared to the observed L4 Trojans (gray dots).

After the breakup, we calculated proper elements of the family members and plotted their distribution (see Figure 3.13). We can see all 30 synthetic families can be easily identified. In most cases, more than 95 % of family members remained within the stable libration zone. We can thus conclude that the ejection of fragments outside the libration zone does not affect the number of observed families among Trojans.

### 3.4.4 Collisional rates

We can estimate collisional activity by means of a simple stationary model. Trojan–Trojan collisions play a major role here, because Trojans are detached from the Main Belt. In case of Eurybates, the target (parent body) diameter $D_{\mathrm{target}} = 110\,\mathrm{km}$, the mean impact velocity $V_{\mathrm{imp}} = 4.7\,\mathrm{km/s}$ (Dell'Oro et al. 1998), the strength $Q^\star_D = 10^5\,\mathrm{J/kg}$ (Benz & Asphaug 1999) and thus the necessary impactor size (Bottke et al. 2005)

$$d_{\mathrm{disrupt}} = \left(2Q^\star_D/V^2_{\mathrm{imp}}\right)^{1/3} D_{\mathrm{target}} \simeq 23\,\mathrm{km}\,. \tag{3.6}$$

Number of $\geq$23 km projectiles among $L_4$ Trojans is $n_{\mathrm{project}} = 371$ and we have $n_{\mathrm{target}} = 8$ available targets. An intrinsic collision probability for Trojan–Trojan collisions $P_{\mathrm{i}} = 7.8 \times 10^{-18}\,\mathrm{km^{-2}\,yr^{-1}}$ (Dell'Oro et al. 1998) and corresponding frequency of disruptions is

$$f_{\mathrm{disrupt}} = P_{\mathrm{i}} \frac{D^2_{\mathrm{target}}}{4} n_{\mathrm{project}} n_{\mathrm{target}} \simeq 7 \cdot 10^{-11}\,\mathrm{yr^{-1}}\,. \tag{3.7}$$

Over the age of the Solar System $T_{\mathrm{SS}} \simeq 4\,\mathrm{Gyr}$ (after the LHB), we have a very low number of such events $n_{\mathrm{events}} = T_{\mathrm{SS}} f_{\mathrm{disrupt}} \simeq 0.28$. This number seems to be in concert with only one

$D \geq 100\,\mathrm{km}$ family currently observed among Trojans.[10] In a less-likely case, the material of the Eurybates parent body was very weak and its strength may be at most one order of magnitude lower, $Q_D^\star \simeq 10^4\,\mathrm{J/kg}$ (see Leinhardt & Stewart 2009, Bottke et al. 2010). We then obtain $d_{\mathrm{disrupt}} \simeq 10\,\mathrm{km}$ and $n_{\mathrm{events}} \simeq 1.0$, so the conclusion about the low number of expected Trojan families remains essentially the same.

The parent body of Aneas group is 1.5 larger and consequently the resulting number of events is more than one order of magnitude lower. On the other hand, clusters with smaller parent bodies ($D_{\mathrm{PB}} \ll 100\,\mathrm{km}$) or significantly weaker ($Q_D^\star \ll 10^5\,\mathrm{J/kg}$) might be more frequent.

During the Late Heavy Bombardment epoch we may assume a substantial increase of collisional activity (Levison et al. 2009). Hypothetical old families were however probably 'erased' due to the late phases of planetary migration (see Section 3.4.2) unless the migration time scale for Jupiter and Saturn was significantly shorter than the time scale of the impactor flux from transneptunian region which is mainly controlled by the migration of Uranus and Neptune.

## 3.5 Conclusions

Increasing number of Trojan asteroids with available proper elements enables us to get new insights into this important population. Essentially, new faint/small asteroids filled the 'gaps' in the proper-element space between previously known clusters and today it seems most clusters are rather comparable to background. One should be aware that the number of families among Trojans may be low and one should not take the number of $\simeq 10$ families as a rule.

Only the C-type Eurybates family fulfils all criteria to be considered a collisional family. This is probably also true for the newly discovered Ennomos group. Moreover, there might be a potentially interesting relation between the high-albedo surface of (4709) Ennomos and the collisional family thought we do not have enough data yet to prove it independently (by colours, spectra or albedos).

Note there may exist clusters among Trojans which are not of collisional origin. They may be caused by: (i) differences in chaotic diffusion rates; (ii) $a/e/I$-dependent efficiency of original capture mechanism; or (iii) it may somehow reflect orbital distribution in source regions.

We cannot exclude a hypothetical existence of old families which were totally dispersed by dynamical processes, e.g., by perturbations due to planetary migration which is especially efficient in the Trojan region.

Finally, note there seem to be no D-type families anywhere in the Solar System — neither in the Trojan region, nor in the J3/2 (Brož et al. 2011) and Cybele regions (Vokrouhlický et al. 2010). May be, the D-type parent bodies are too weak and the target is completely pulverized during a collision? This might have important implications for collisional models of icy bodies.

## Acknowledgements

We thank David Vokrouhlický, David Nesvorný, Alessandro Morbidelli and William F. Bottke for valuable discussions on the subject. We also thank Lenka Trojanová for the pricipal component analysis of the SDSS-MOC4 data and Gonzalo Carlos de Elía for his review which helped to improve the final version of the paper. The work has been supported by

[10] A similar stationary estimate valid for the Main Asteroid Belt gives the number of events 12 while the number of observed families with $D_{\mathrm{PB}} \gtrsim 100\,\mathrm{km}$ is about 20 (Durda et al. 2007). These two numbers are comparable at least to order-of-magnitude.

the Grant Agency of the Czech Republic (grant 205/08/P196) and the Research Program MSM0021620860 of the Czech Ministry of Education. We acknowledge the usage of computers of the Observatory and Planetarium in Hradec Králové and Observatory and Planetarium of Prague.

# Chapter 4

# SPH simulations of high-speed collisions

This part is devoted to a study of mutual collisions of asteroids with cometary nuclei occurring at high relative velocities. We simulate impacts of icy, low-density ($\rho_{\rm bulk} = 1.14$ g.cm$^{-3}$) projectiles to basaltic monolithic targets at the velocity of 8 to 15 km/s. We focus on possible differences in the propagation of the shock wave, ejection of fragments and resulting differences in the size-frequency distribution (SFD) of synthetic asteroid families. We compare our results with simulations of mutual collision of basalt bodies, occuring at lower velocities (3 to 7 km/s), typical for the main asteroid belt. We also discuss a scaling of SFDs with respect to the 'nominal' target diameter $D = 100$ km, for which a number of simulations have been done so far (e.g., Durda et al. 2007; Benavidez et al. 2012, 2018; Jutzi 2015; Ševeček et al. 2017, 2019).

The purpose of this numerical experiment is to better understand impact processes shaping the *early* Solar System, namely the primordial asteroid belt during the Late Heavy Bombardment (LHB; as a continuation of Brož et al. 2013). For all hydrodynamical simulations we use a standard smoothed-particle hydrodynamics method (SPH), namely the lagrangian SPH5 code (Benz and Asphaug, 1994). Gravitational interactions between fragments (during the subsequent reaccumulation phase) are computed with the Pkdgrav tree-code (Richardson et al., 2000).

## 4.1 Introduction

In our work Brož et al. (2013), we asked a question whether some of the main-belt asteroid families had been formed by collisions with (originally trans-neptunian) comets during the period of the late heavy bombardment, as predicted by the Nice model (Gomes et al., 2005; Morbidelli et al., 2005), or its newer variants (Morbidelli et al., 2010; Nesvorný and Morbidelli, 2012).

We concluded that if asteroid families were created during the LHB, the final number of catastrophic disruptions with parent bodies larger than $D_{\rm PB} \simeq 100$ km should be $\sim 100$, i.e., almost one order of magnitude larger than the observed number (20). Also the synthetic production function, i.e., the number of families vs the respective $D_{\rm PB}$, is significantly steeper than observed.

There are three possible explanations for this discrepancy (apart from secondary disruptions of families members, which certainly contributes to the decrease of kilometre-sized bodies):

i) cometary flux could have been reduced by 80 % due to intrinsic activity and breakups of the cometary nuclei during their close approaches to the Sun;

ii) physical lifetime of the comets may be size-dependent, so that small comets are disintegrated substantially more than the large ones;

iii) collisions between solid monolithic targets (asteroids) and less cohesive projectiles (comets) occurring at high velocities ($v_{\rm imp} > 10\ {\rm km\,s^{-1}}$) can be generally different from collisions at lower velocities, which have been studied so far (Benz and Asphaug, 1999; Durda et al., 2007; Benavidez et al., 2012, 2018; Jutzi, 2015; Ševeček et al., 2017, 2019).

In this work, we focus on the latter possibility.

## 4.2 Methods

The method we chose for the simulations of collisions between a solid bodies is a meshless Lagrangian particle method – smooth particle hydrodynamics (SPH) (e.g. Benz (1990); Monaghan (1992); Benz and Asphaug (1994)).

Gas and solid bodies are modelled by the respective set of partial differential equations, which is summarized as follows (e.g., Brož 2021):

$$\frac{{\rm d}\rho}{{\rm d}t} = -\rho\nabla\cdot\mathbf{v}\,, \tag{4.1}$$

$$\frac{{\rm d}\mathbf{v}}{{\rm d}t} = -\frac{1}{\rho}\nabla P - \nabla\Phi + \frac{1}{\rho}\nabla\cdot\mathbf{S}\,, \tag{4.2}$$

$$\frac{{\rm d}U}{{\rm d}t} = -\frac{1}{\rho}P\nabla\cdot\mathbf{v} + \frac{1}{\rho}\frac{1}{2}(\nabla\mathbf{v} + (\nabla\mathbf{v})^{\rm T}) : \mathbf{S} \tag{4.3}$$

$$\nabla\cdot\nabla\Phi = 4\pi G\rho\,, \tag{4.4}$$

$$\frac{{\rm d}\mathbf{S}}{{\rm d}t} = \nabla\cdot\mu_1(\nabla\mathbf{v} + (\nabla\mathbf{v})^{\rm T}) + (\mu_2 - \frac{2}{3}\mu_1)\nabla\cdot\mathbf{v}\mathbf{I}\,, \tag{4.5}$$

$$\frac{{\rm d}D}{{\rm d}t} = \left(\frac{c_{\rm g}}{R_{\rm s}}\right)^3 + \left(\frac{m+3}{3}\alpha^{\frac{1}{3}}\epsilon^{\frac{m}{3}}\right)^3\,, \tag{4.6}$$

$$P \simeq A\left(\frac{\rho}{\rho_0} - 1\right) + B\left(\frac{\rho}{\rho_0} - 1\right)^2 + b\rho U\frac{1}{\frac{U}{U_0}\frac{\rho_0^2}{\rho^2} + 1} + a\rho U\,, \tag{4.7}$$

$$\mathbf{S} := (1-D)\min\left[\frac{Y^2}{\frac{3}{2}\mathbf{S}:\mathbf{S}}; 1\right]\mathbf{S}\,, \tag{4.8}$$

$$P := \mathcal{H}(P) + \mathcal{H}(-P)(1-D)P\,, \tag{4.9}$$

where $\rho$ denotes the bulk density, $\mathbf{v}$ velocity, $P$ pressure, $\Phi$ gravitational potential, $\mathbf{S}$ stress tensor, $U$ specific internal energy (per unit mass), $D$ scalar damage, $\mu_1$ shear modulus, $\mu_2$ bulk modulus, $Y$ von Mises limit, $c_{\rm g}$ crack propagation speed, $R_{\rm s}$ equivalent particle size, $\alpha \equiv 8\pi c_{\rm g}^3 k/[(m+1)(m+2)(m+3)]$, $k$, $m$ parameters of the Weibull distribution, $n(\epsilon) = k\epsilon^m$, $\epsilon$ flaw activation limit, $\mathcal{H}$ the Heaviside step function. The individual terms (right-hand sides) can be briefly described as follows: expansion, pressure gradient, gravity, stress, work, viscous heating, Poisson eq., shear stress, bulk stress, crack growth, activation, solid-state pressure, quadratic term, corrective term, ideal-gas term, fracture, plasticity, ditto for pressure. In the SPH5 code we used, the spatial discretisation of Eqs. (4.1)–(4.9) is performed in the standard SPH way (Monaghan, 1992; Benz and Asphaug, 1994), including the artificial viscosity to handle shocks. For the temporal discretisation, the predicor-corrector method is used (or

alternatively, we implemented the Bulirsch-Stoer). We assumed the Tillotson equation of state (Eq. (4.7); Tillotson 1962) and material properties, which were listed in Table 2.3.

We performed 125 simulations of impacts of various projectiles on targets with diameters $D_{\rm PB} = 100\,{\rm km}$. The projectile velocity $v_{\rm imp}$ was 8, 10, 12, 14 and 15 km.s$^{-1}$ and the impact angle $\varphi_{\rm imp}$ was $15°, 30°, 45°, 60°$ and $75°$.

The target was always basalt with the bulk density $\rho_{\rm targ} = 2.7$ g.cm$^{-3}$, while the projectiles consisted of silicated ice (30 % silicates) with the bulk density ($\rho_{\rm imp} = 1.14$ g.cm$^{-3}$).

The integration was controlled by the Courant number $C = 1.0$, a typical time step thus was $\Delta t \simeq 10^{-5}\,{\rm s}$, and the time span was $t_{\rm stop} = 100\,{\rm s}$. The Courant condition was the same in different materials, using always the maximum sound speed $c_{\rm s}$ among all SPH particles, as usually.

We used $N_{\rm SPH,st} = 10^5$ SPH particles for the single spherical target. Impactor was modelled by $N_{\rm SPH,i} = 10^3$ SPH particles.

We terminated SPH simulations after 50 s from the impact. This time interval is needed to establish a velocity field of fragments and to complete the fragmentation in our set of simulations. Then we handed the output of the SPH simulation as initial conditions to the N–body gravitational code Pkdgrav (Richardson et al., 2000), what is a parallel tree code used to simulate a gravitational reaccumulation of fragments. Unlike Durda et al. (2007), who calculated radii of fragments $R$ from the smoothing length $h$ as $R = h/3$, we calculated fragments radii from their masses $m$ and densities $\rho$ as $R = (m/(4\pi\rho))^{1/3}$.

We ran Pkdgrav with the time step $\Delta t = 5.0$ s and we terminated this simulation after $t_{\rm evol} = 3$ days of evolution. To ensure this is sufficiently long, we also ran several simulations with $t_{\rm evol} = 5$ days, but we had seen no significant differences between final results.

We used the nominal value for the tree opening angle, ${\rm d}\theta = 0.5\,{\rm rad}$, even though for the evolution of eventual moons it would be worth to use even smaller value, e.g. ${\rm d}\theta = 0.2\,{\rm rad}$.

To compare resulting SFDs properly, we varied the mass (and thus the size) of the projectile to obtain the same ratio of impactor specific energy $Q$ to the target strength $Q^*_{\rm D}$ within each simulation set.

## 4.3 Results

We processed the results of simulations and plotted spatial distribution at the end of fragmentation phase (e.g. Fig. 4.1 for the impact angle 45°), size-frequency distributions (Fig. 4.2), velocity histograms (Fig. 4.3), or energy vs. time (Fig. 4.4).

Impacts follow a regular pattern cratering → reaccumulative → catastrophic → super-catastrophic disruptions with increasing impact energy, as one can see by comparing Figures 4.1, 4.8 – 4.11. For low-energy impacts, there is cratering only, the bulk of the target remains with low ejection velocities (see Fig. 4.1) and its fragments are almost immediately reaccumulated; the target is fully damaged though. The impactor is vaporized, typically for low impact angles, or dispersed by the reverse shock, if its part misses the target.

The low-energy and high-impact-angle impacts are poorly resolved (Fig. 4.11, top left), and we should keep it in mind when interpreting the results.

**Size-frequency distributions.** At the end of reaccumulation phase, we used the original target density $\rho_0$ to compute diameters of fragments and derive the corresponding SFDs. Regarding the largest remnant (LR), the largest fragment (LF) as well as other fragments, they may be 'puffed-up' in our simulations. This procedure corresponds to a subsequent compaction of bodies (on long time scales).

Similarly as above, the SFDs follow a regular pattern. The LR becomes smallish for high-energy impacts until it 'disappears'; these are super-catastrophic disruptions. Consequently, the LF becomes bigger and bigger, until it turns to be smaller for the highest-energy impacts.

The largest largest fragment ('LLF') reaches $D \simeq 20\,\mathrm{km}$ in our simulations (see, e.g., Fig. 4.2, bottom right). A part of fragment distribution with sizes ranging somewhere (but not always) from $D \simeq 5\,\mathrm{km}$ up to $D \simeq 20\,\mathrm{km}$ can be described by a power law $\log N(>D) = c \log D + d$. Typically it is steep, with slope $c \ll -2.5$, i.e., steeper than a collisional equilibrium of Dohnanyi (1969), but for super-catastrophic impacts this steep slope soon becomes shallow around $D \simeq 10\,\mathrm{km}$. This is because these disruptions produce more fragments with diameter $D > 10\,\mathrm{km}$ and the the total mass must be conserved ($M_{\mathrm{tot}} = M_{\mathrm{PB}} + m_{\mathrm{imp}}$).

**Velocity distributions.** Regarding velocity distributions, we performed a transformation to the barycentre frame after the reaccumulation phase. To avoid a 'contamination' of our fragment sample by the fragments of impactor, we removed outliers, with the ejection velocity $v_{\mathrm{ej}} > 1000\,\mathrm{m\,s^{-1}}$.

For low-energy impacts, there is a peak at about the escape velocity, which is $v_{\mathrm{esc}} = 61\,\mathrm{m\,s^{-1}}$ for our targets. Practically all fragments are ejected within $2v_{\mathrm{esc}}$ (see Fig. 4.3; note the ordinate is logarithmic).

For high-energy impacts with a head-on geometry (the impact angle $\varphi_{\mathrm{imp}} \leq 45°$, a second peak appears at about $3v_{\mathrm{esc}}$, probably due to a direct momentum transfer from the projectile to the target. Eventually, the whole distribution shifts towards higher velocities (and the peaks merge). These observations are very similar to those in Ševeček et al. (2017).

**Energy conservation.** Let us note we experienced some problems with the energy conservation. In a majority of simulations the total energy (kinetic plus internal, target plus impactor) is conserved to within 1 % (or better). However, in a minority of simulations, in particular highest-energy and highest-impact-angle simulations, the energy is conserved to within 10 % (or even worse).

Regarding high impact angles, we tracked-down this issue to projectile particles which exhibit a strong shearing very late in the fragmentation phase, when the projectile is essentially 'cut' by the target. Practically, it does not affect the target at all, because this 'shearing instability' occurs elsewhere (approximately $\sim 300\,\mathrm{km}$ away from the impact site).

**Parametric relations.** In order to describe the overall statistical properties of collisions, it is useful to derive parametric relations, which describe the dependence of the largest remnant mass $M_{\mathrm{lr}}$, the largest fragment mass $M_{\mathrm{lf}}$, or the fragment size-distribution slope $q$ on a suitable measure of energy.

To this point, we use the scaling law (as Benz and Asphaug 1994):

$$Q(R) = Q_0 R^a + B\rho R^b\,, \tag{4.10}$$

and define the effective strength (as Ševeček et al. 2017)

$$Q_{\mathrm{eff}} = \frac{\frac{1}{2}mv^2}{M_{\mathrm{pb}}} \frac{A}{\pi r^2}\,, \tag{4.11}$$

where the interacting cross section $A$, at the closest distance $d = (r+R)\sin(\phi)$, is:

$$A = \begin{cases} \pi r^2 & \text{for } d \leq R - r\,, \\ r^2 \arccos\frac{d^2+r^2-R^2}{2dr} + R^2 \arccos\frac{d^2+R^2-r^2}{2dR} - & \\ \quad -\frac{1}{2}\sqrt{(R+r-d)(d+r-R)(d-r+R)(d+r+R)} & \text{for } d \in (R-r; R+r)\,, \\ 0 & \text{for } d \geq R + r\,. \end{cases} \tag{4.12}$$

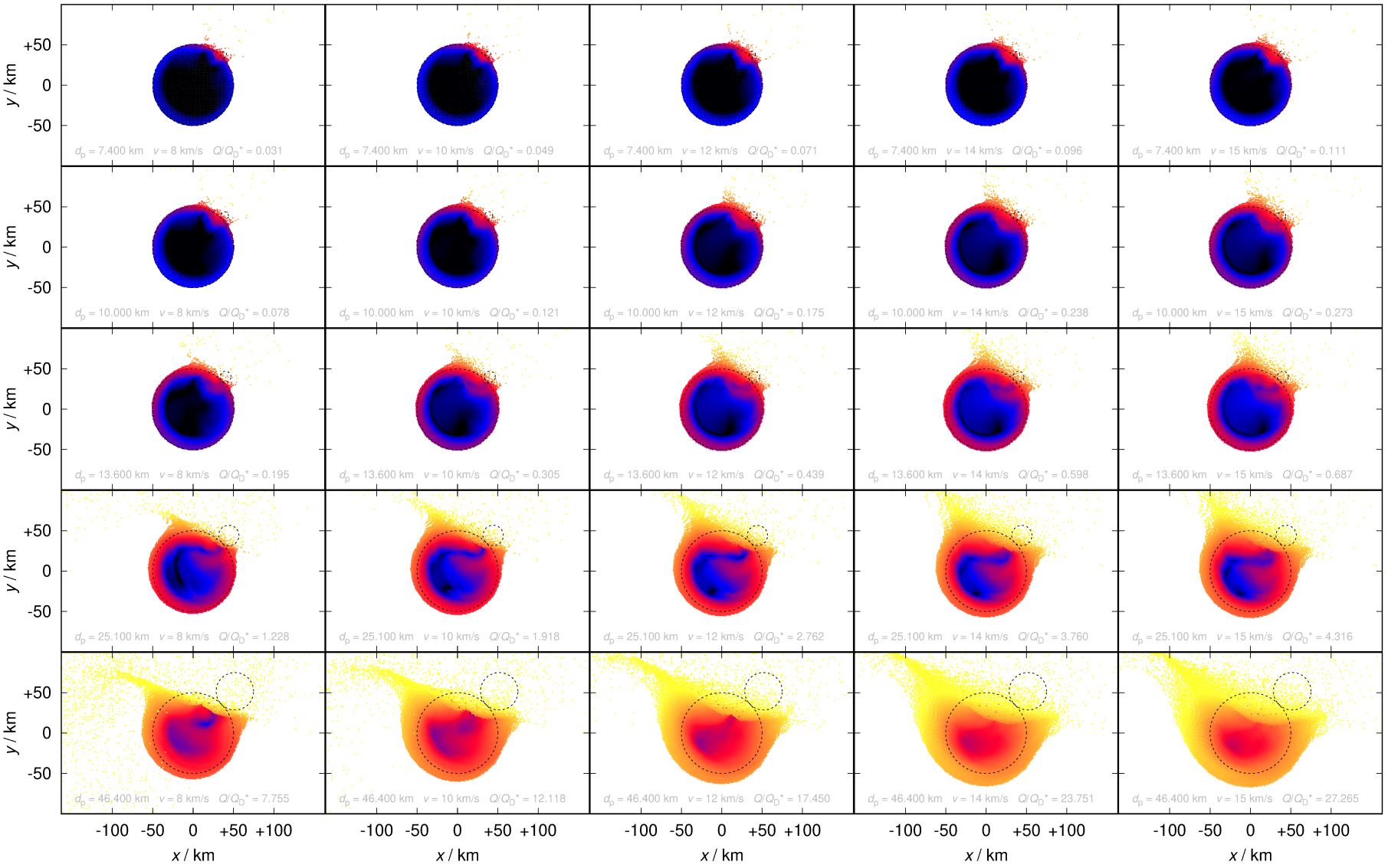


Figure 4.1: Spatial distribution of SPH particles at the end of fragmentation phase (i.e., time 50 s). The interior of the target is shown, with the $(x, y)$ cross-section and $z < 0$. The impact angle $\varphi_{\text{imp}} = 45°$ in this case. Colours correspond to the logarithm of velocity.

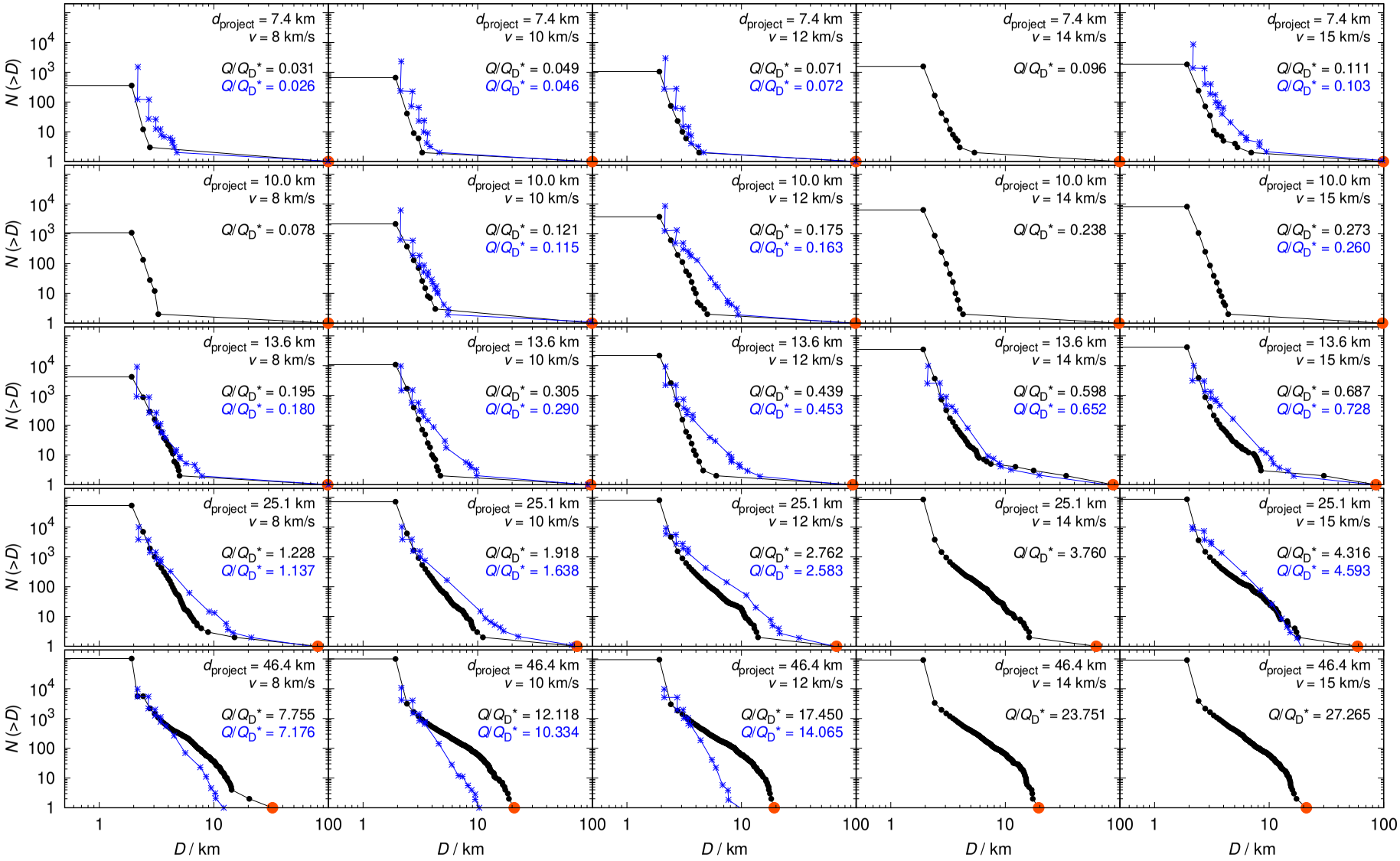


Figure 4.2: Size-frequency distributions $N(>D)$ for the impact angle 45° and various projectile sizes and impact velocities. A comparison with Durda et al. (2007) at a similar specific energy $Q/Q^{\star}_{\mathrm{D}}$ is plotted in blue.

→ 68 ←

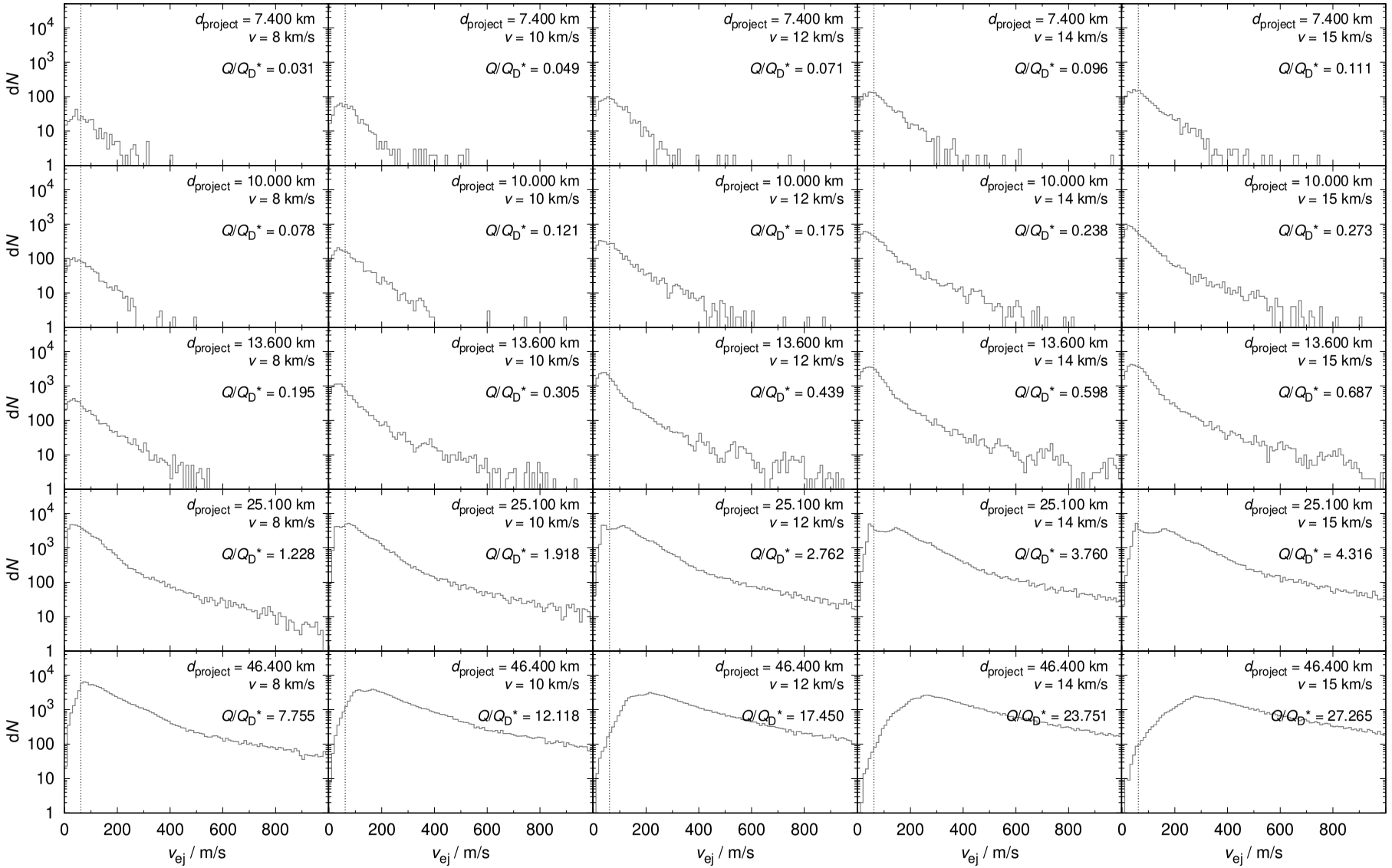


Figure 4.3: Histograms of ejection velocities $\mathrm{d}N(v, v + \mathrm{d}v)$ for the impact angle 45° and various projectile sizes and impact velocities. The velocities were transformed to the barycentric frame, with outliers ($v_{\text{ej}} > 1000\,\mathrm{m\,s^{-1}}$) removed. The escape velocity ($v_{\text{esc}} = 61\,\mathrm{m\,s^{-1}}$) is denoted by the vertical dotted line.

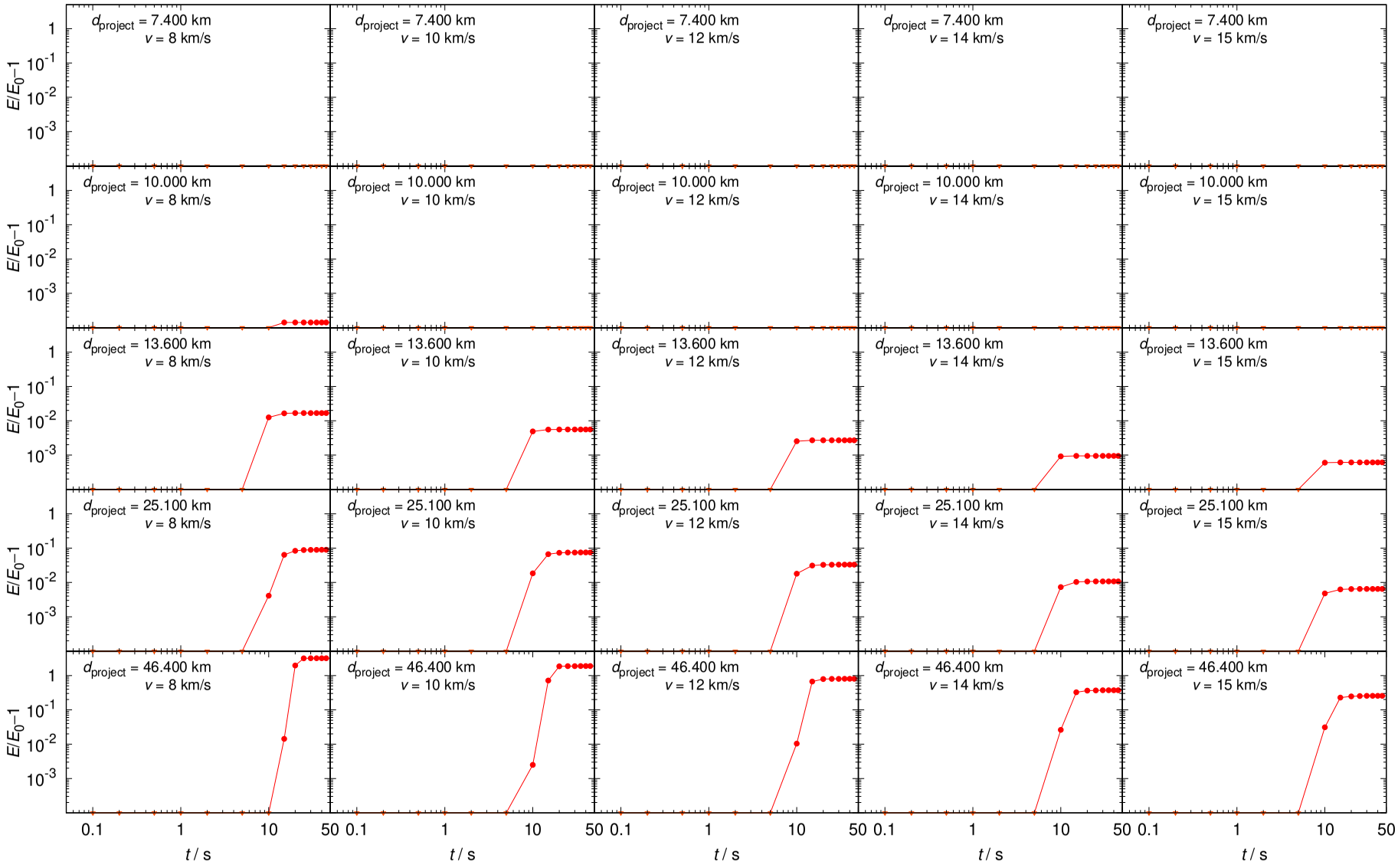


Figure 4.4: Relative total energy $|E/E(t=0)-1|$ vs. time $t$ for the impact angle 45° and various projectile sizes and impact velocities. If the relative energy difference less than $10^{-4}$, it is plotted at the ordinate (as triangle).

Using all our SPH simulations outcomes, we plotted Figs. 4.5, 4.6, 4.7 and derived the following relations for the LR:

$$\frac{M_{\rm lr}(Q_{\rm eff})}{M_{\rm tot}} = \begin{cases} 1 - 0.2\,Q_{\rm eff}/Q^\star_{\rm D} & \text{for } Q_{\rm eff}/Q^\star_{\rm D} < 0.2\,, \\ 0.96 - \frac{0.46}{0.8}(Q_{\rm eff}/Q^\star_{\rm D} - 0.2) & \text{for } Q_{\rm eff}/Q^\star_{\rm D} < 1\,, \\ 0.5 - 0.15\,(Q_{\rm eff}/Q^\star_{\rm D} - 1.0) & \text{for } Q_{\rm eff}/Q^\star_{\rm D} \geq 1\,; \end{cases} \tag{4.13}$$

for the LF:

$$\frac{M_{\rm lf}(Q_{\rm eff})}{M_{\rm tot}} = 0.003 \left(\frac{Q_{\rm eff}}{Q^\star_{\rm D}}\right)^{1.5} \exp\left[-\left(\frac{Q_{\rm eff}}{4.5 Q^\star_{\rm D}}\right)^{1.2}\right]; \tag{4.14}$$

and for the slope:

$$q(Q_{\rm eff}) = -8.0 + 7.0 \left(\frac{Q_{\rm eff}}{Q^\star_{\rm D}}\right)^{0.9} \exp\left[-\left(\frac{Q_{\rm eff}}{2.0 Q^\star_{\rm D}}\right)^{0.6}\right]. \tag{4.15}$$

These relations are approximations of our distributions, which are more complex, and exhibit numerous (possibly interesting) outliers. Uncertainties of the numerical parameters are of the order of the last digit.

Alternatively, we can fit SFDs with two slopes $q_1$, $q_2$ (similarly as in Ševeček et al. 2017):

$$K(x) = \frac{1}{2}(q_1 + q_2)x + \frac{1}{2}\frac{q_1 - q_2}{k} \ln(2\cosh kx)\,, \tag{4.16}$$

where $\log N(>D) = K(\log D - \log d) + c$, with $q_1, q_2, c, d$ treated as free parameters and the assumed values of $k = 10$, but the scatter of $q$ values is even larger and the fit still does not fully describe the outcomes of collisions. It may be even useful to think about a different implementation of fragmentation in the Boulder code, in order to account for the stochasticity of collisions (in terms of $M_{\rm lr}$, $M_{\rm lf}$, $q$).

## 4.4 Comparison with low-speed collisions

We can compare Eqs. (4.13) to (4.15) with the original parametric relations of Morbidelli et al. (2009), corresponding to low-speed collisions (see also the respective Figs. 4.5 to 4.7).

While $M_{\rm LR}$ seems to be very similar to previous results thanks to the appropriate scaling by $Q_{\rm eff}$, $M_{\rm LF}$ exhibits systematic differences, in particular, the peak is shifted to even higher energies. For cratering events and sub-catastrophic disruptions, with the ratio of impactor specific energy $Q$ to the target strength $Q^\star_{\rm D}$ smaller than $\sim 0.4$, the LF is substantially *smaller* by almost an order of magnitude in mass (or a factor of 2 in diameter).

This may have important consequences, because the observability of asteroid families is practically given by the presence of sufficiently massive LF; if it is too small, secondary collisions are unable to sustain the SFD for a long time and the family 'disappears'. This may at least partly explain the problem with the (excessive) number of LHB families, outlined in (Brož et al., 2013), but their arguments were based on catastrophic disruptions, not craterings.

In the super-catastrophic regime ($Q_{\rm eff}/Q^\star_{\rm D} \gtrsim 10$), our simulations show the LF (again, the LR doesn't exist anymore) is substantially bigger, which would make the observability problem even worse, but these collisions are rare. Nevertheless, our simulations also suggest that high-speed impacts produce actually more $D \gtrsim 10\,$km fragments, which may (temporarily) enhance the collisional cascade by secondary disruptions.

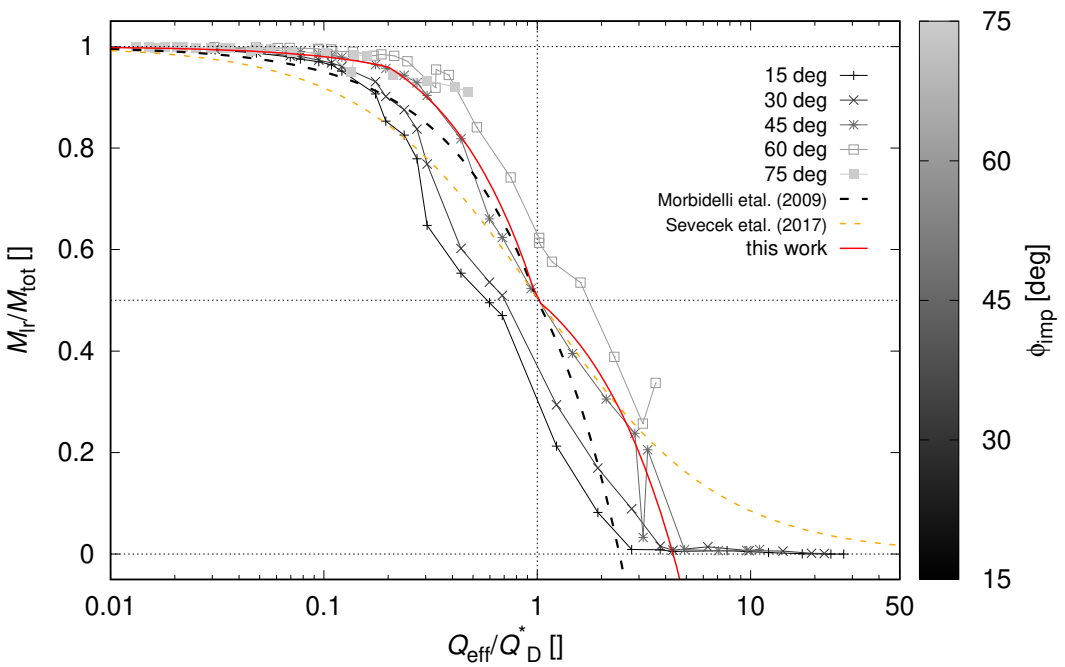


Figure 4.5: Mass of the largest remnant $M_{\rm lr}$ vs. the effective strength $Q_{\rm eff}$. Individual outcomes of our high-speed SPH simulations are plotted as points. The parametric relation Eq. (4.13) is also plotted (red line). In accord with the scaling law, $M_{\rm lr}/M_{\rm tot} \simeq 0.5$ for $Q = 1$. For comparison, we show the parametric relations for low-speed collisions (Morbidelli et al., 2009) and $D = 10\,$km bodies (Ševeček et al., 2017).

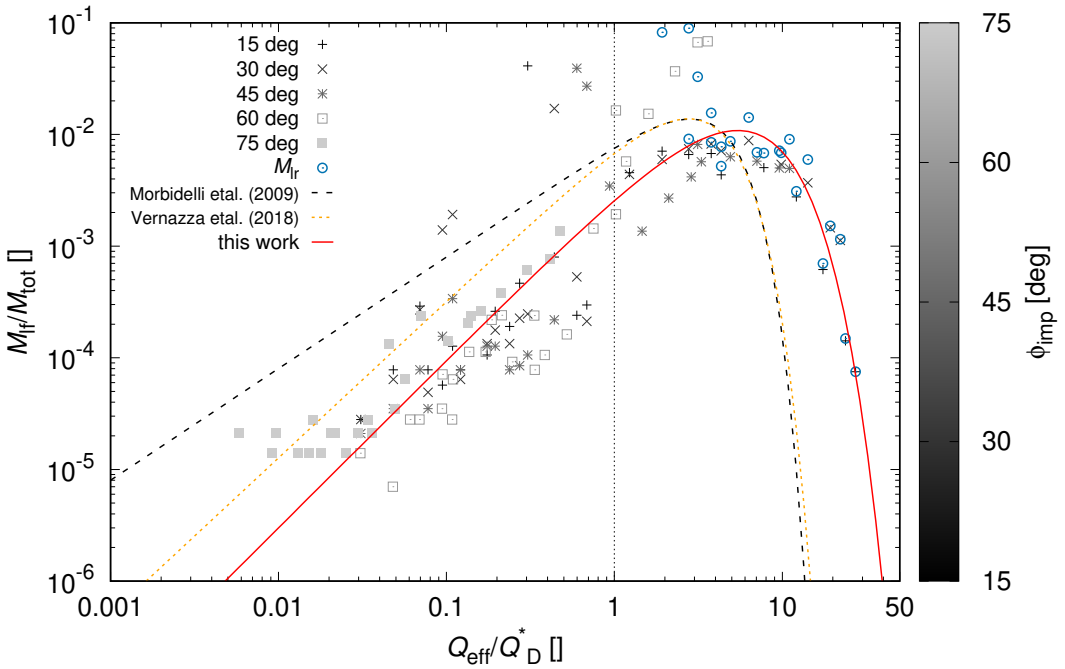


Figure 4.6: Mass of the largest fragment $M_{\rm lf}$ vs. the effective strength $Q_{\rm eff}$. Eq. (4.14) is plotted as red line. The largest remnant mass $M_{\rm lr}$ is also plotted, as it subsequently 'disappears' for high-energy impacts. For comparison, there are parametric relations of Morbidelli et al. (2009), Vernazza et al. (2018).

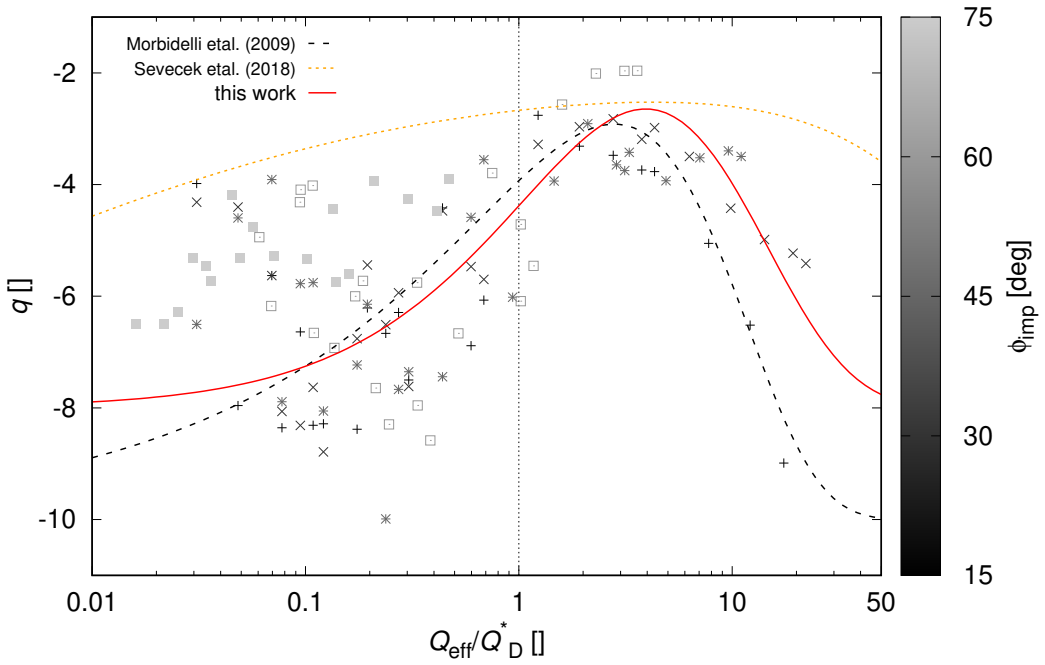


Figure 4.7: Power-law slope of the size-frequency distribution $q$ vs. the effective strength $Q_{\mathrm{eff}}$. Eq. (4.15) is plotted as red line. There is a large scatter for low-energy impacts though. Parametric relations of Morbidelli et al. (2009), Ševeček et al. (2017) are also shown.

## 4.5 Conclusions

Let us finally recall that relations for macroscopic rubble-pile bodies were derived in Cibulková et al. (2014) and for smaller $D = 10\,\mathrm{km}$ targets in Ševeček et al. (2017).

As a future work, we plan to use all these relations in complex collisional models of the late heavy bombardment, or the main belt composed of two (or more) rheologically different populations.

## 4.6 Supplementary figures

Figures for all simulations are attached: fragmentation phase (Figs. 4.8 to 4.11), size-frequency distributions (Figs. 4.12 to 4.16), velocity histograms (Figs. 4.17 to 4.20), energy vs. time (Figs. 4.21 to 4.24).

References are appended at the end of the thesis.

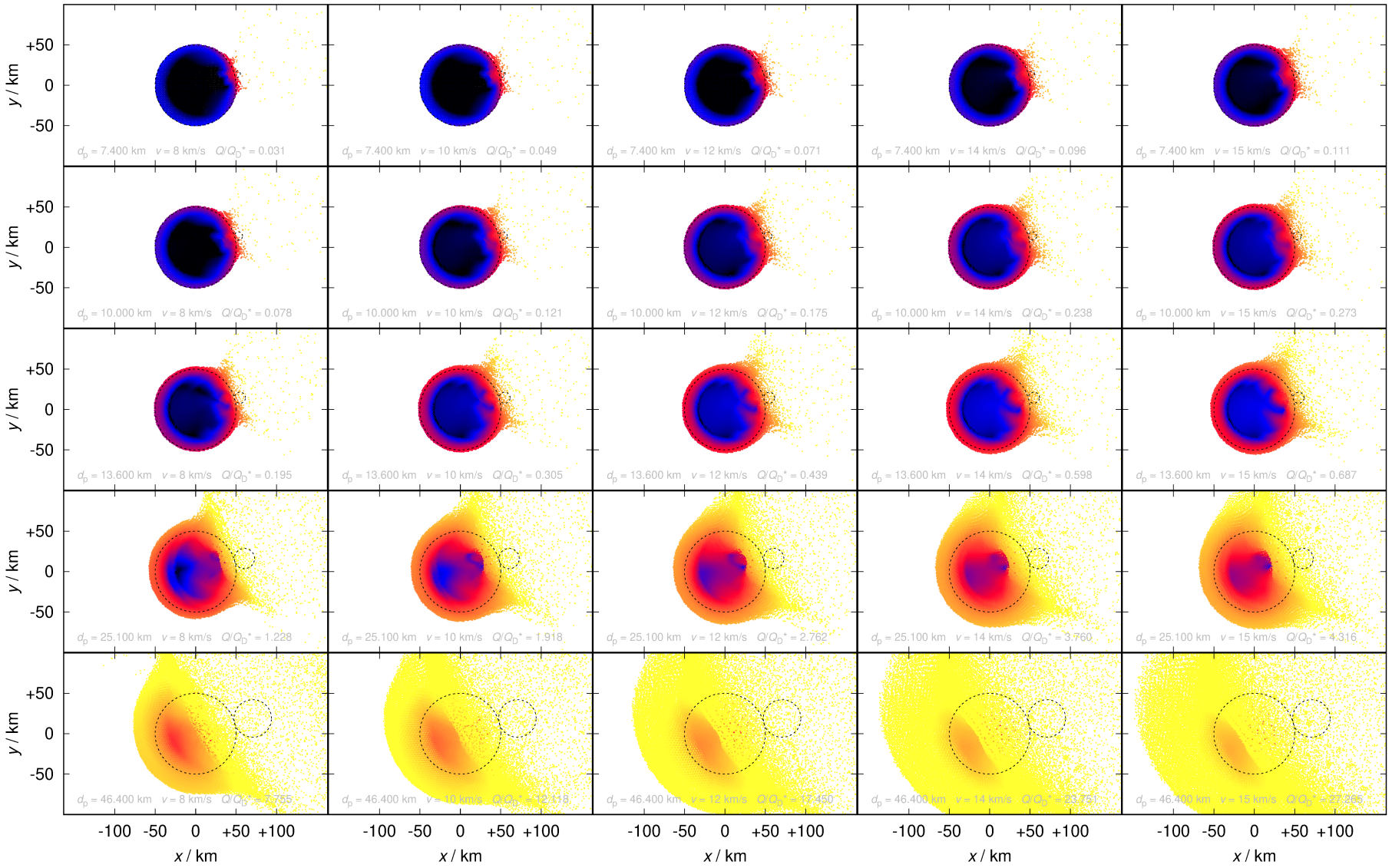


Figure 4.8: Same as Fig. 4.1 for the impact angle 15°.

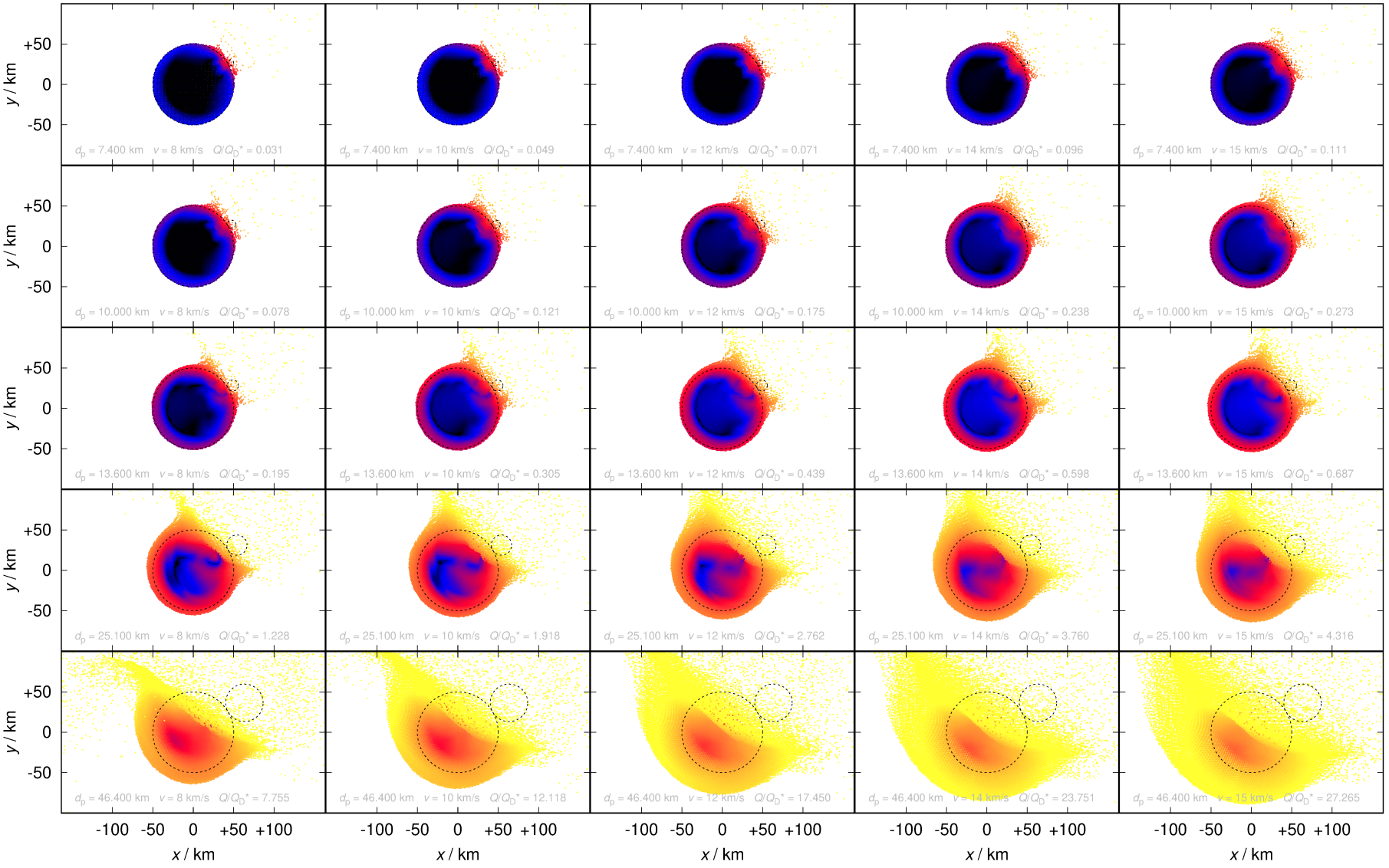


Figure 4.9: Same as Fig. 4.1 for the impact angle 30°.

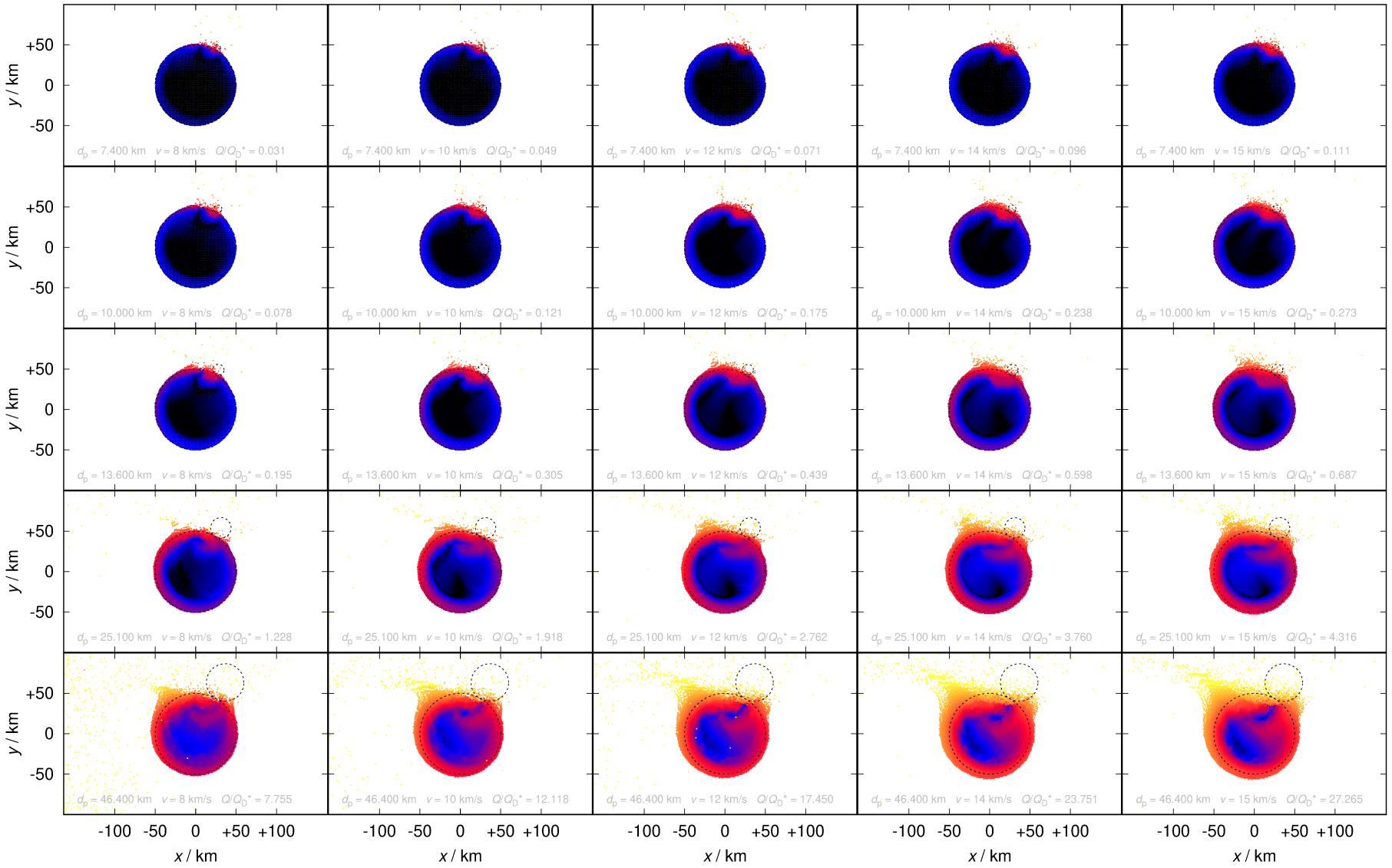


Figure 4.10: Same as Fig. 4.1 for the impact angle 60°.

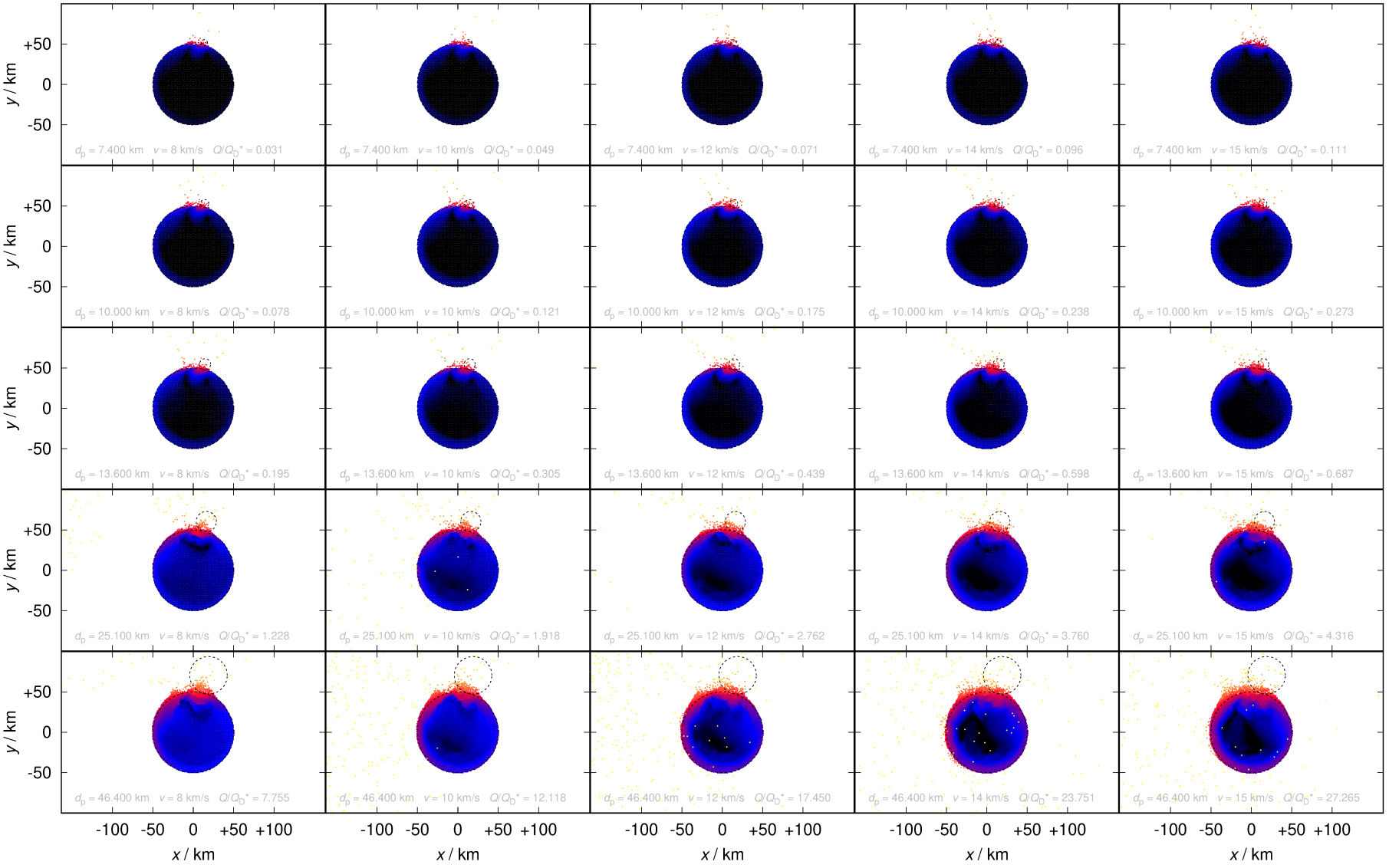


Figure 4.11: Same as Fig. 4.1 for the impact angle 75°.

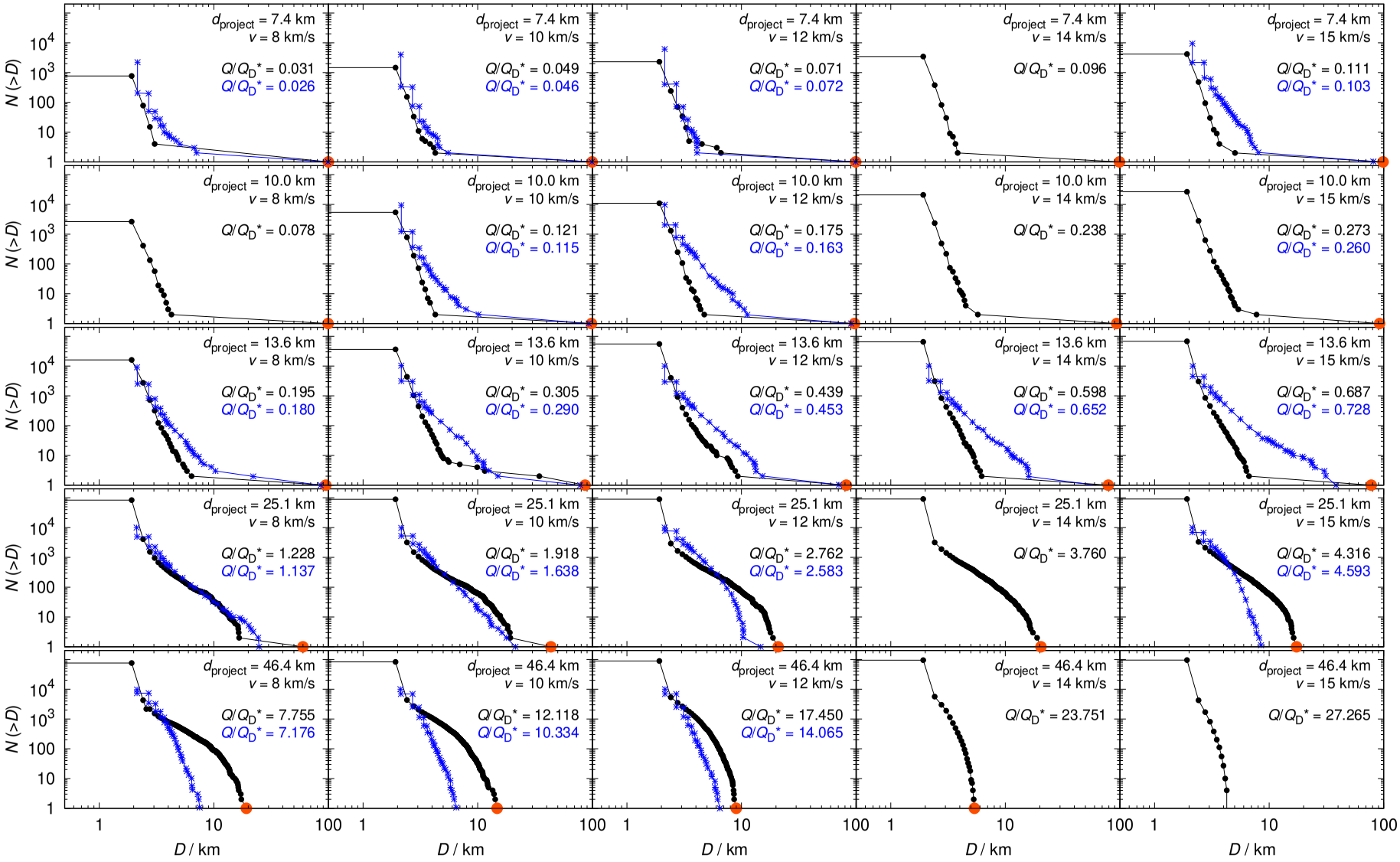


Figure 4.12: Same as Fig. 4.2 for the impact angle 15°.

→ 78 ←

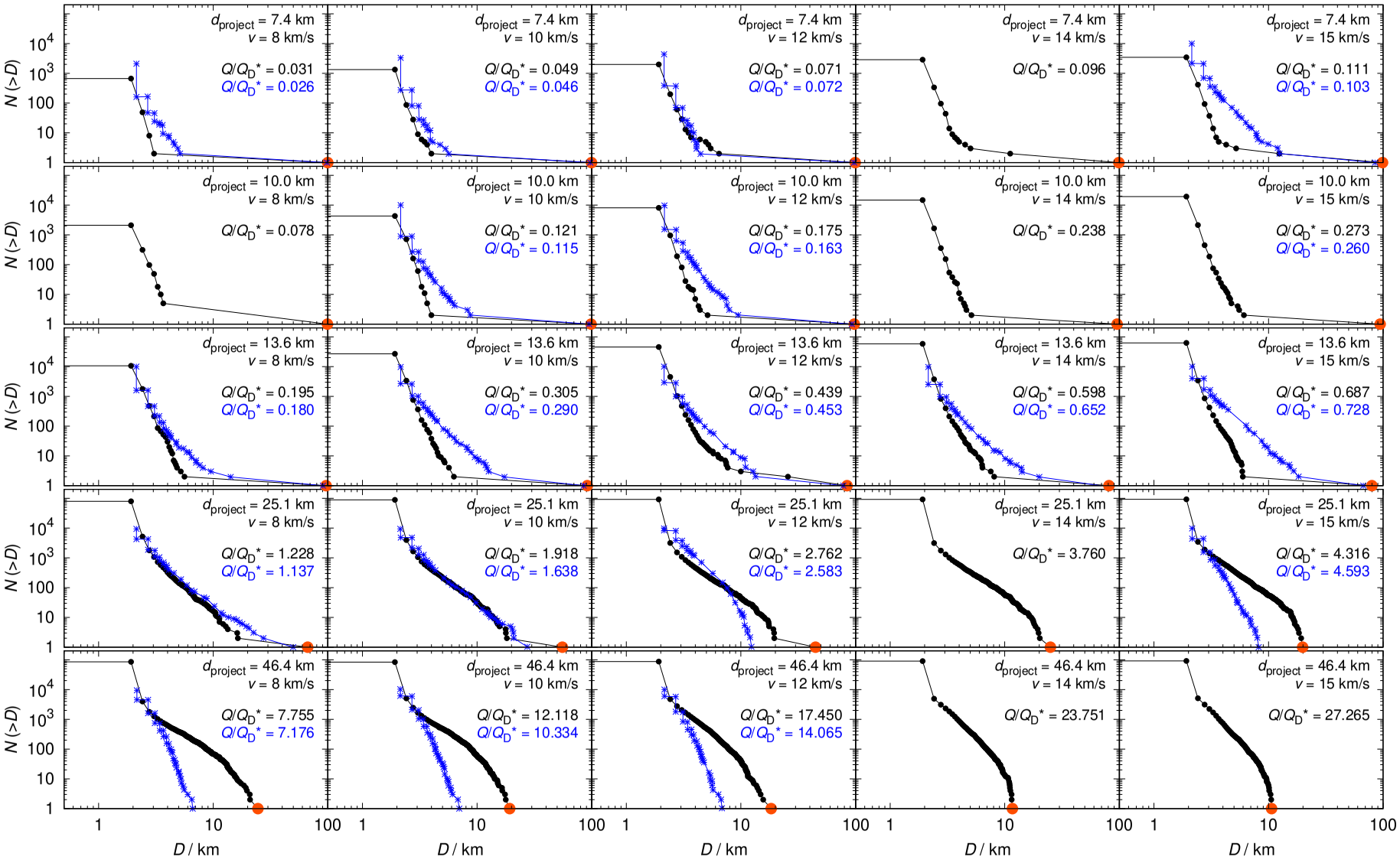


Figure 4.13: Same as Fig. 4.2 for the impact angle 30°.

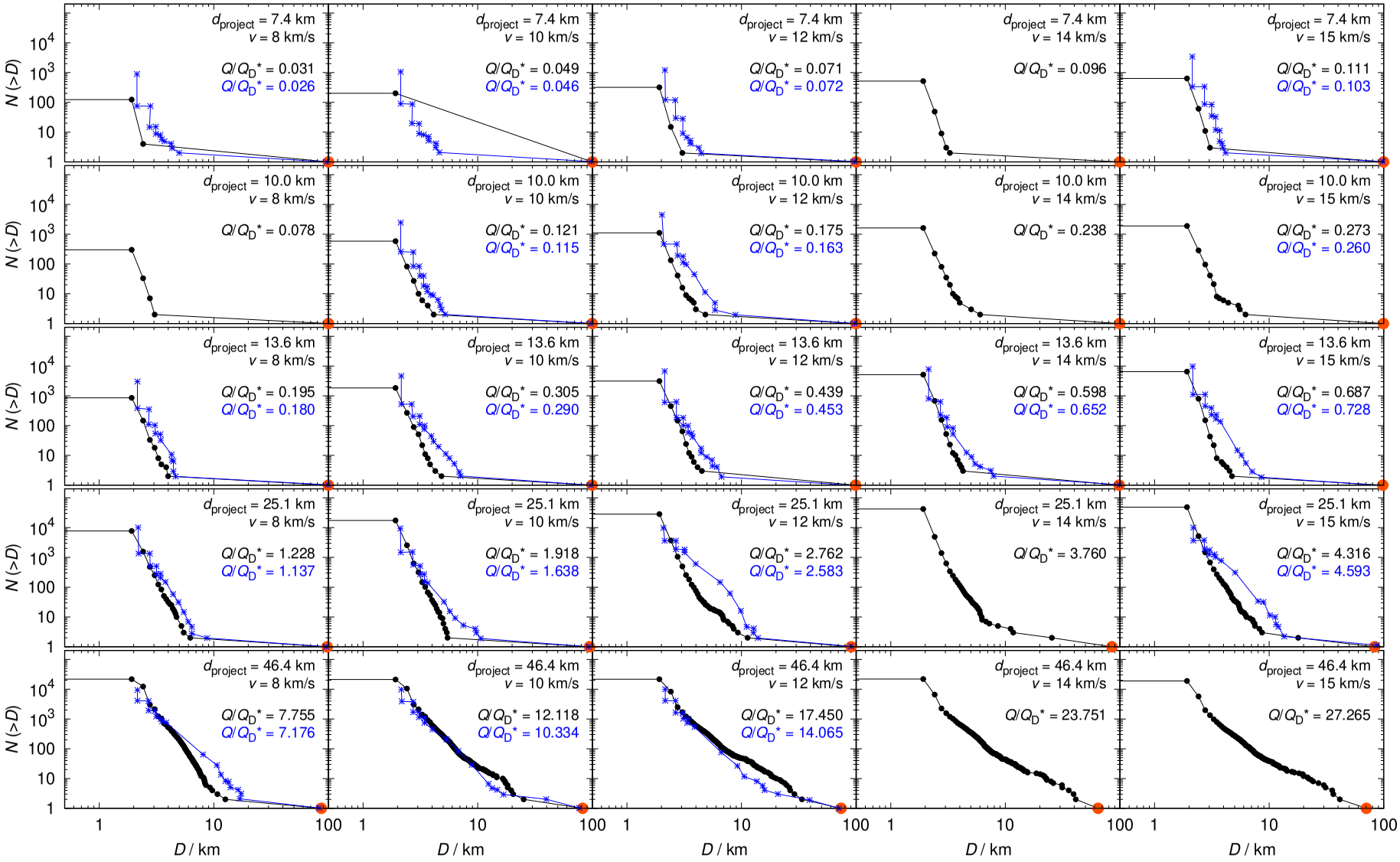


Figure 4.14: Same as Fig. 4.2 for the impact angle 60°.

→ 80 ←

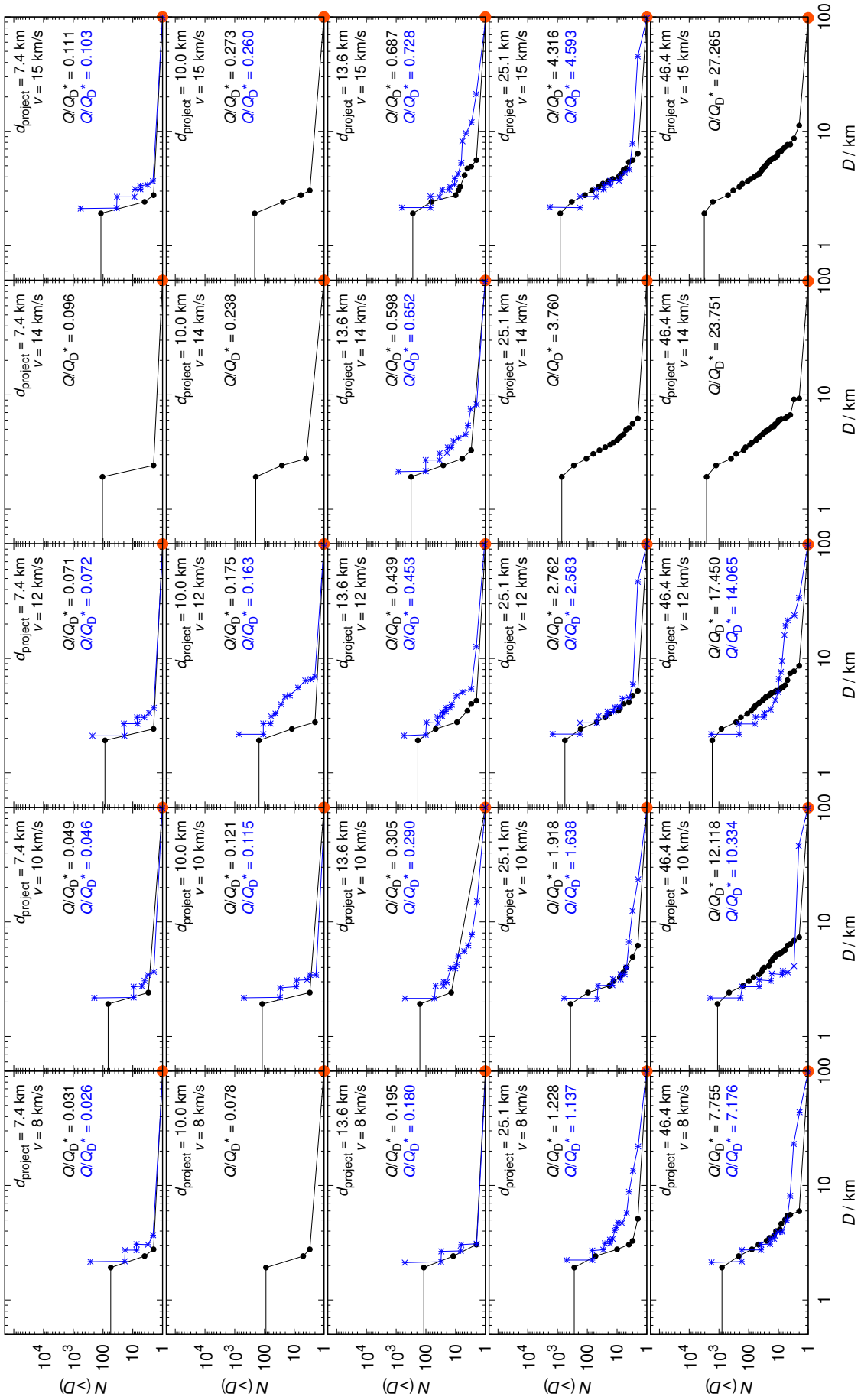


Figure 4.15: Same as Fig. 4.2 for the impact angle 75°.

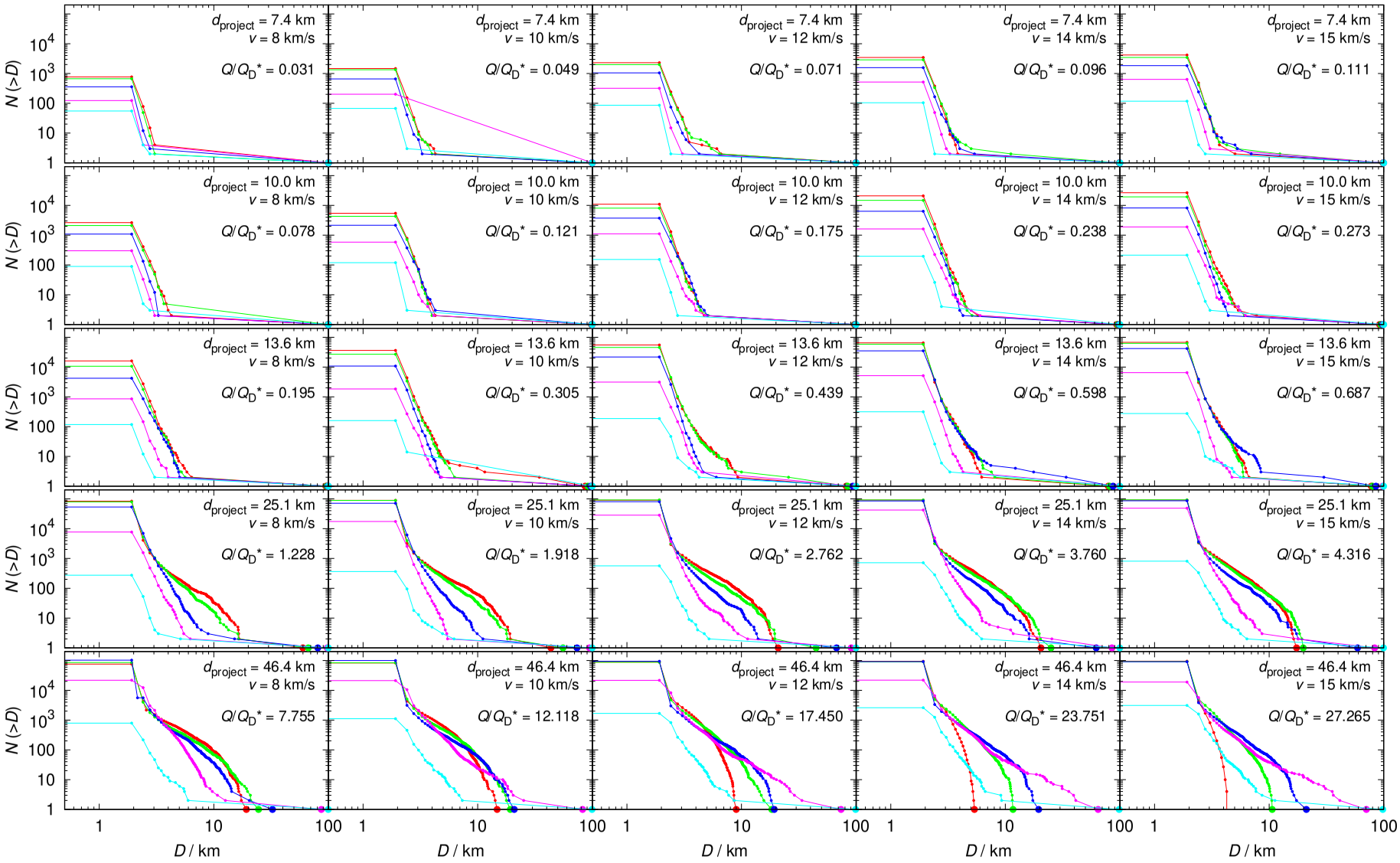


Figure 4.16: Same as Fig. 4.2 for all impact angles 15°, 30°, 45°, 60°, 75° (plotted in red, green, blue, magenta, cyan).

→ 82 ←

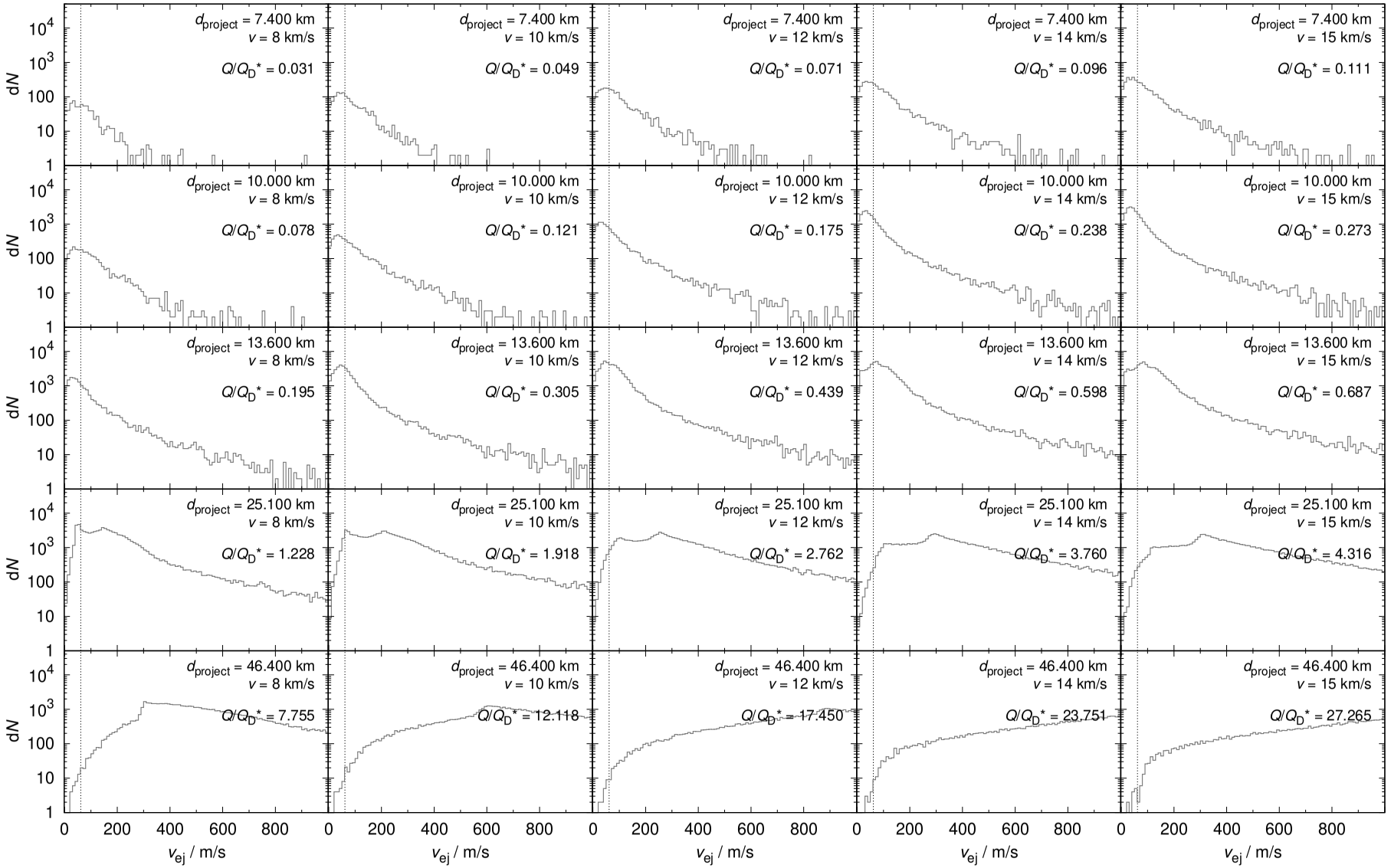


Figure 4.17: Same as Fig. 4.3 for the impact angle 15°.

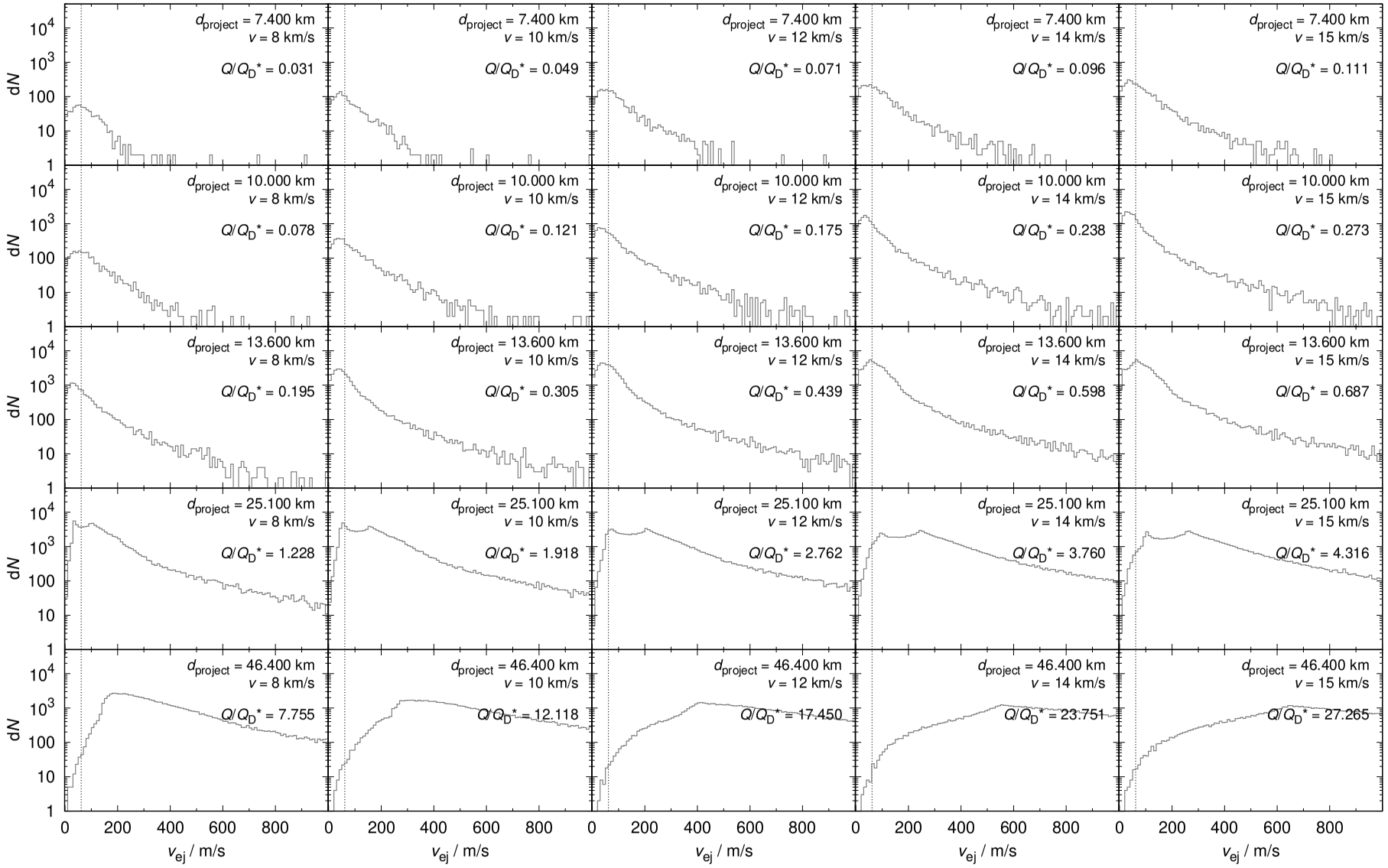


Figure 4.18: Same as Fig. 4.3 for the impact angle 30°.

→ 84 ←

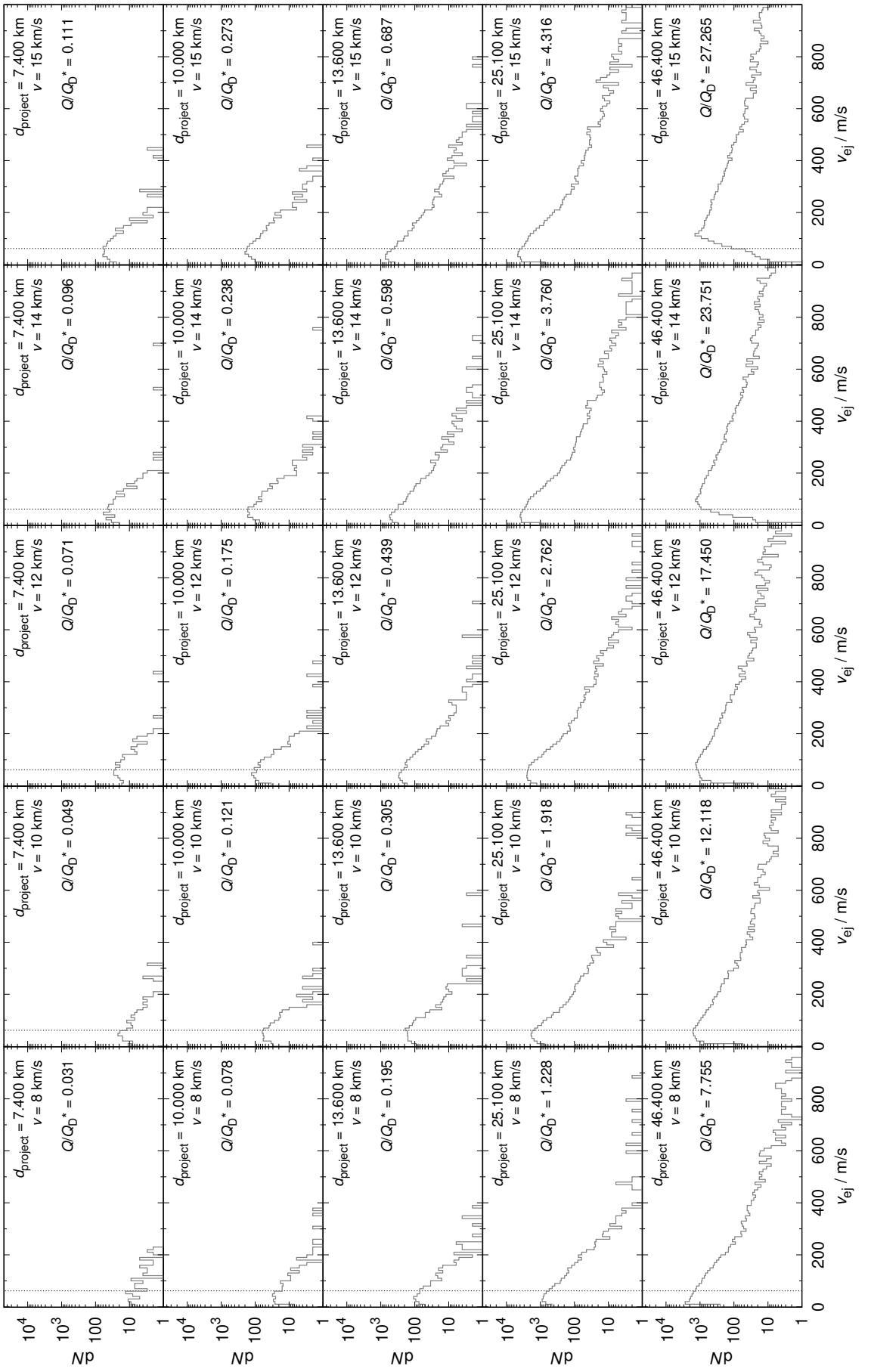


Figure 4.19: Same as Fig. 4.3 for the impact angle 60°.

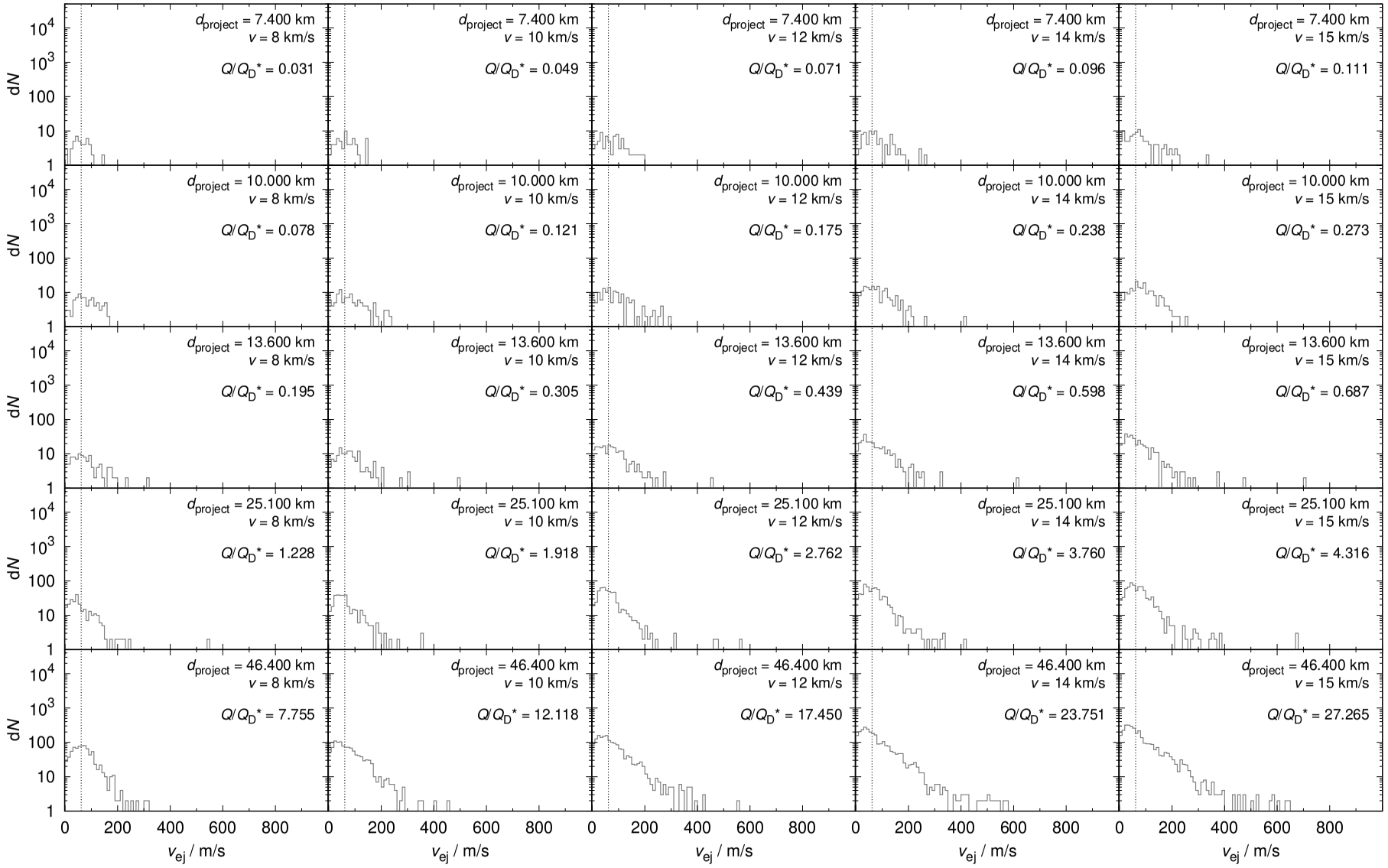


Figure 4.20: Same as Fig. 4.3 for the impact angle 75°.

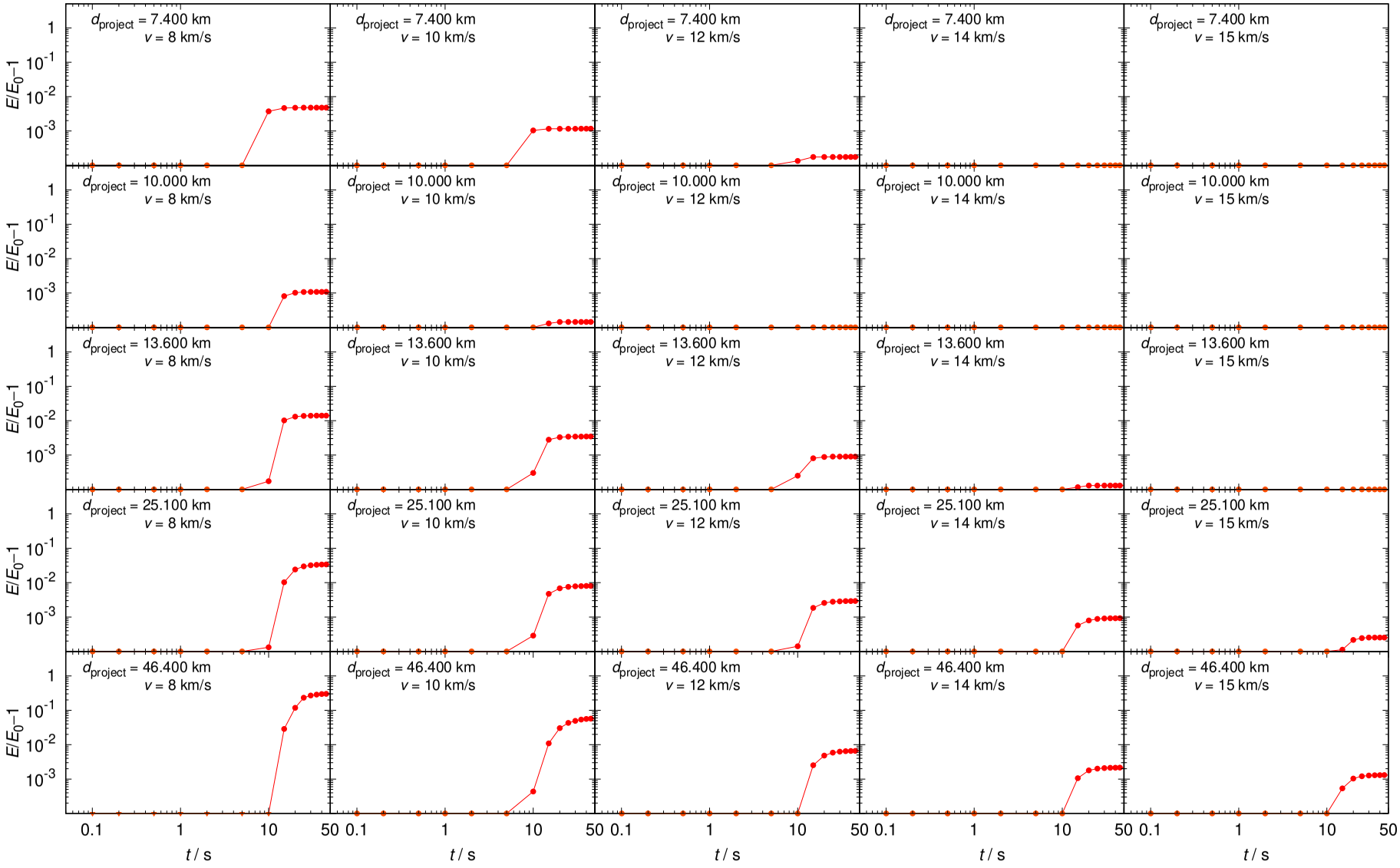


Figure 4.21: Same as Fig. 4.4 for the impact angle 15°.

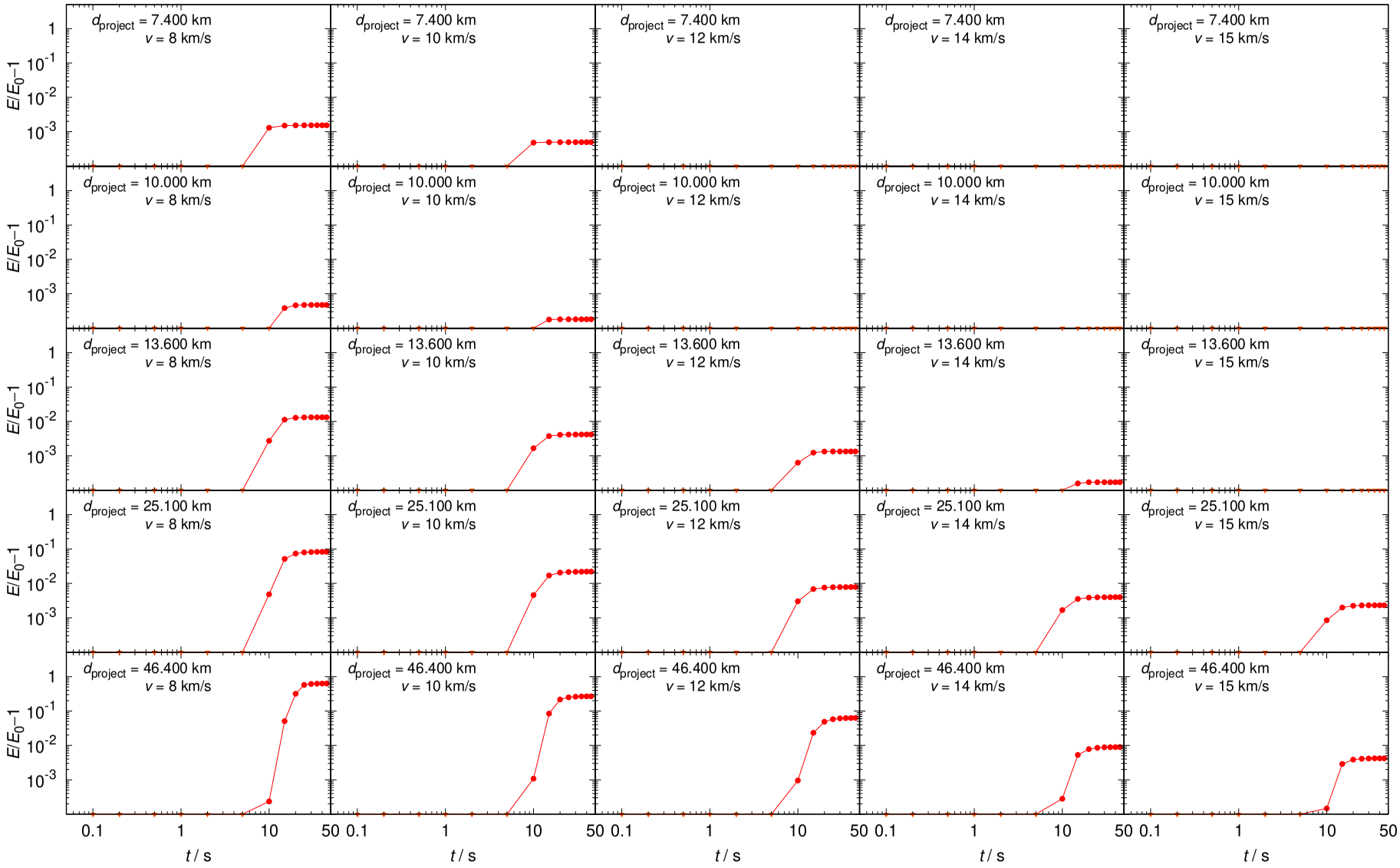


Figure 4.22: Same as Fig. 4.4 for the impact angle 30°.

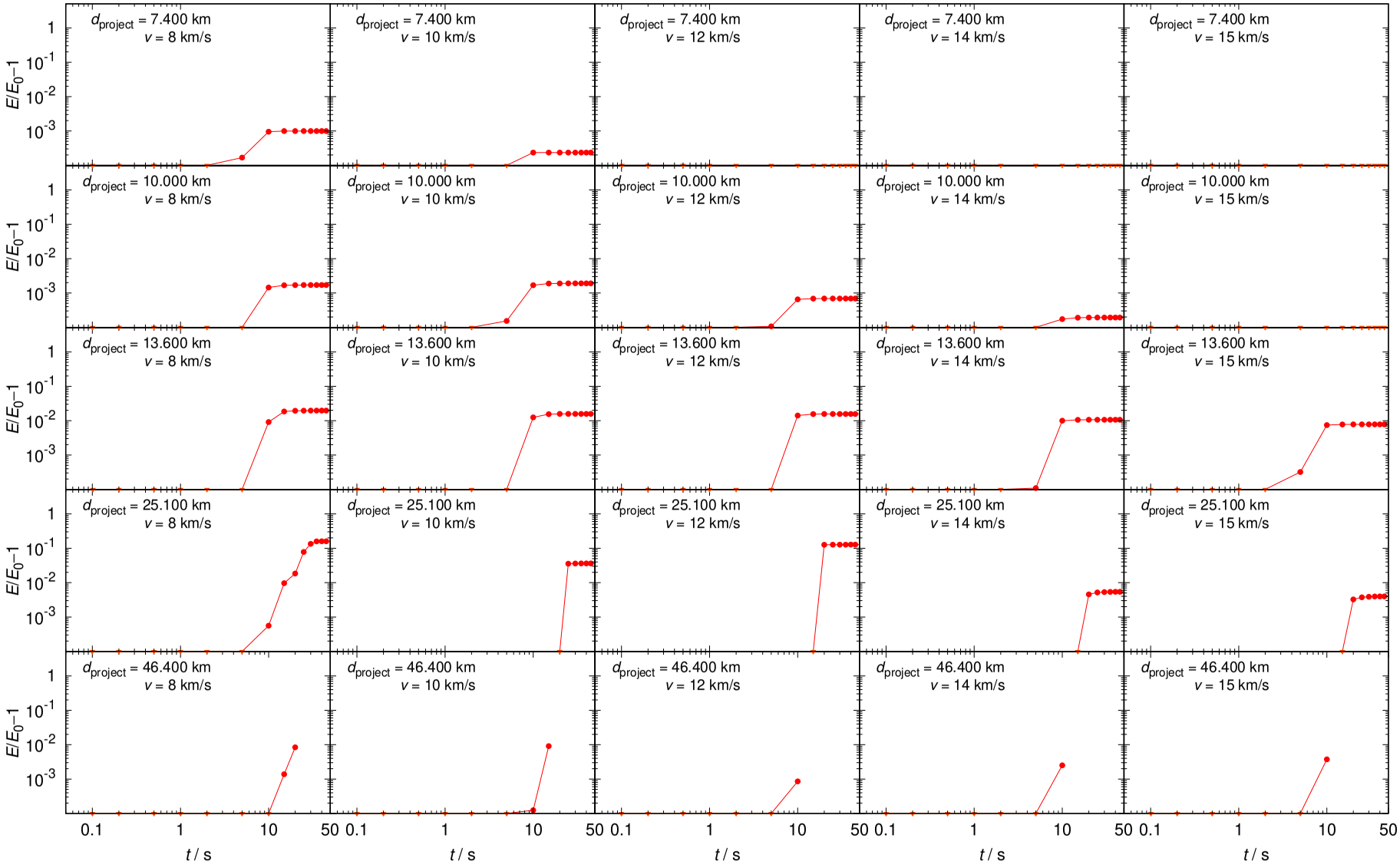


Figure 4.23: Same as Fig. 4.4 for the impact angle 60°.

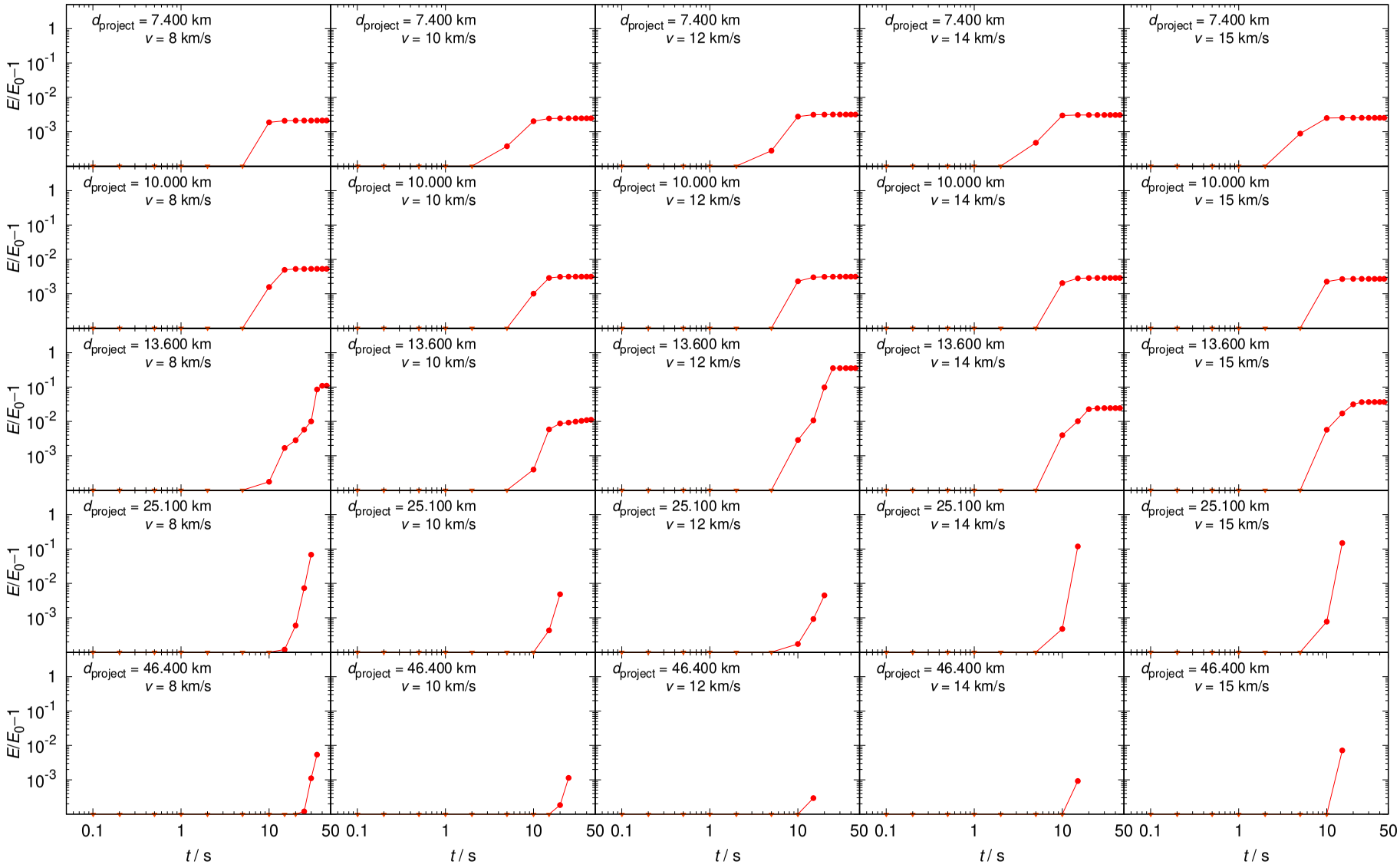


Figure 4.24: Same as Fig. 4.4 for the impact angle 75°.

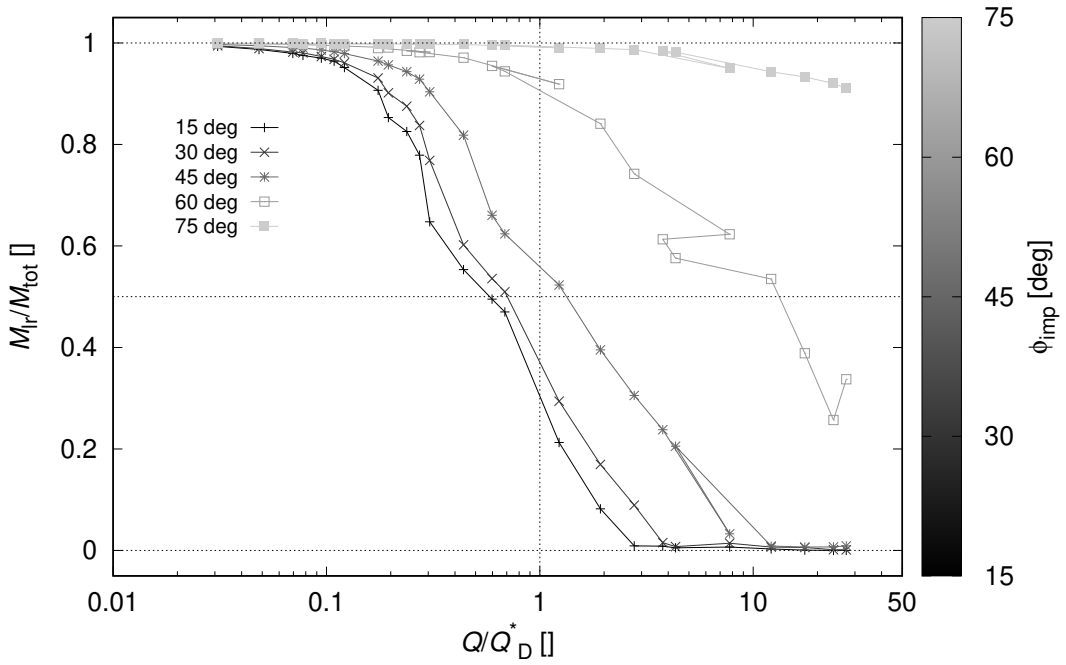


Figure 4.25: Same as Fig. 4.5, but with the nominal strength $Q$, instead of the effective stregth $Q_{\rm eff}$ (given by Eq. (4.11)). In this case, oblique impacts cannot follow the same dependence $M_{\rm lr}(Q)$.

## Acknowledgements

The work has been supported by the Grant Agency of the Charles University, GA UK No. 1109516, and by the Czech Science Foundation, GA CR No. P209/15/04816S.

# Chapter 5

# Conclusions

In this work, we used various models, whose combination allowed us to better understand Jupiter Trojans and to interpret the respective observations with a great amount detail.

For dynamical simulations, we used the orbital model based on the SWIFT symplectic integrator (Levison and Duncan, 1994), appropriately modified to include the Yarkovsky and YORP effects. Numerical simulations of the collisional evolution were based on the Boulder code (Morbidelli et al., 2009). Hydrodynamic simulations of impacts were performed with the SPH5 code (Benz and Asphaug, 1994) and the gravitational tree-code Pkdgrav (Richardson et al., 2000). For statistical analysis of orbital elements, we developed a new 'randombox' method, working independently on the common hierarchical clustering method (HCM).

We focused on populations (incl. families) rather than on individual bodies, because their distribution is non-random and statistically significant, although their central bodies (e.g., (3458) Eurybates or (624) Hektor) are of utmost interest!

Using the methods mentioned above and various independent data sources (e.g., MPCORB, SDSS-MOC, WISE/NEOWISE), we discovered several collisional families among Trojans (and we also rejected several families proposed earlier).

We successfully simulated the formation of the Hektor family by a cratering event and we managed to show that the moon of Hektor could have been formed at the same time.

We also described differences in the outcomes of low-speed and high-speed collisions, which were not studied so far, in the context of the late heavy bombardment (LHB). These findings contribute to the LHB modelling and to the theories describing the early evolution of the Solar System and its orbital instabilities.

**Future work.** An ongoing development of observational technology, e.g., the VLT/SPHERE instrument capable of adaptive-optics imaging of central bodies of asteroid families (as in Vernazza et al. 2018; Marsset et al. 2020), or *in-situ* observations with the Lucy spacecraft (Levison and Lucy Science Team, 2016; Souza-Feliciano et al., 2020) will allow us to study populations of small bodies in even more detail, providing us with a possibility to construct even more complex asteroid family models.

New description of overall statistical properties of various impacts, together with observed cratering records (and projectile → crater scaling laws), will allows us to constrain the 'integral' of collisional evolution and 'initial' conditions some 4–4.567 Gy ago.

New asteroid moons or possibly 'minimoons' (Granvik et al., 2012) will be soon discovered, e.g., with the VLT/Eris instrument, providing us with precise information about masses (volumes, densities, porosities, ...) of central bodies. This will remove one of the largest uncertainties in the modelling of impacts and subsequent orbital evolution due to non-gravitational effects.

We are also looking forward to further discoveries of very young families, composed of small bodies ($H > 20$ mag), as well as very old ("diffuse") families (Delbo' et al., 2017), possibly affected by early accretion (and fragmentation), as well as planetary migration.

# Appendix A

# Reprint of Rozehnal et al. (2016)

Monthly Notices
of the
ROYAL ASTRONOMICAL SOCIETY

MNRAS **462,** 2319–2332 (2016)
Advance Access publication 2016 July 19

doi:10.1093/mnras/stw1719

# Hektor – an exceptional D-type family among Jovian Trojans

J. Rozehnal,[1,2★] M. Brož,[1] D. Nesvorný,[3] D. D. Durda,[3] K. Walsh,[3]
D. C. Richardson[4] and E. Asphaug[5]

[1] *Institute of Astronomy, Charles University, Prague, V Holešovičkách 2, CZ-18000 Prague 8, Czech Republic*
[2] *Štefánik Observatory, Petřín 205, CZ-11800 Prague, Czech Republic*
[3] *Southwest Research Institute, 1050 Walnut St, Boulder, CO 80302, USA*
[4] *Department of Astronomy, University of Maryland, College Park, MD 20742-2421, USA*
[5] *School of Earth and Space Exploration, Arizona State University, Tempe, AZ 85287, USA*

Accepted 2016 July 14. Received 2016 July 11; in original form 2016 January 6

## ABSTRACT

In this work, we analyse Jovian Trojans in the space of suitable resonant elements and we identify clusters of possible collisional origin by two independent methods: the hierarchical clustering and a so-called randombox. Compared to our previous work, we study a twice larger sample. Apart from Eurybates, Ennomos and 1996 RJ families, we have found three more clusters – namely families around asteroids (20961) Arkesilaos, (624) Hektor in the $L_4$ libration zone and (247341) 2001 $UV_{209}$ in $L_5$. The families fulfill our stringent criteria, i.e. a high statistical significance, an albedo homogeneity and a steeper size–frequency distribution than that of background. In order to understand their nature, we simulate their long term collisional evolution with the Boulder code and dynamical evolution using a modified SWIFT integrator. Within the framework of our evolutionary model, we were able to constrain the age of the Hektor family to be either 1–4 Gyr or, less likely, 0.1–2.5 Gyr, depending on initial impact geometry. Since (624) Hektor itself seems to be a bilobed-shape body with a satellite, i.e. an exceptional object, we address its association with the D-type family and we demonstrate that the moon and family could be created during a single impact event. We simulated the cratering event using a smoothed particle hydrodynamics. This is also the first case of a family associated with a D-type parent body.

**Key words:** celestial mechanics.

## 1 INTRODUCTION

Jovian Trojans are actually large populations of minor bodies in the 1:1 mean motion resonance with Jupiter, librating around $L_4$ and $L_5$ Lagrangian points. In general, there are two classes of theories explaining their origin: (i) a theory in the framework of accretion model (e.g. Goldreich, Lithwick & Sari 2004; Lyra et al. 2009) and (ii) a capture of bodies located in libration zones during a migration of giant planets (Morbidelli et al. 2005; Morbidelli et al. 2010; Nesvorný, Vokrouhlický & Morbidelli 2013), which is preferred in our Solar system. Since the librating regions are very stable in the current configuration of planets and they are surrounded by strongly chaotic separatrices, bodies from other source regions (e.g. Main belt, Centaurs, Jupiter family comets) cannot otherwise enter the libration zones and Jupiter Trojans thus represent a rather primitive and isolated population.

Several recent analyses confirmed the presence of several families among Trojans (e.g. Nesvorný, Brož & Carruba 2015; Vinogradova 2015). The Trojan region as such is very favourable for dynamical studies of asteroid families, because there is no significant systematic Yarkovsky drift in semimajor axis due to the resonant dynamics. On the other hand, we have to be aware of boundaries of the libration zone, because ballistic transport can cause a partial depletion of family members. At the same time, as we have already shown in Brož & Rozehnal (2011), no family can survive either late phases of a slow migration of Jupiter, or Jupiter 'jump', that results from relevant scenarios of the Nice model (Morbidelli et al. 2010). We thus focus on post-migration phase in this paper.

We feel the need to evaluate again our previous conclusions on even larger data sets, that should also allow us to reveal as-of-yet unknown structures in the space of proper elements or unveil possible relations between orbital and physical properties (e.g. albedos, colours, diameters) of Jovian Trojans.

In Section 2, we use new observational data to compute appropriate resonant elements. In Section 3, we use albedos obtained by Grav et al. (2012) to derive size–frequency distributions (SFDs) and

★ E-mail: rozehnal@observatory.cz

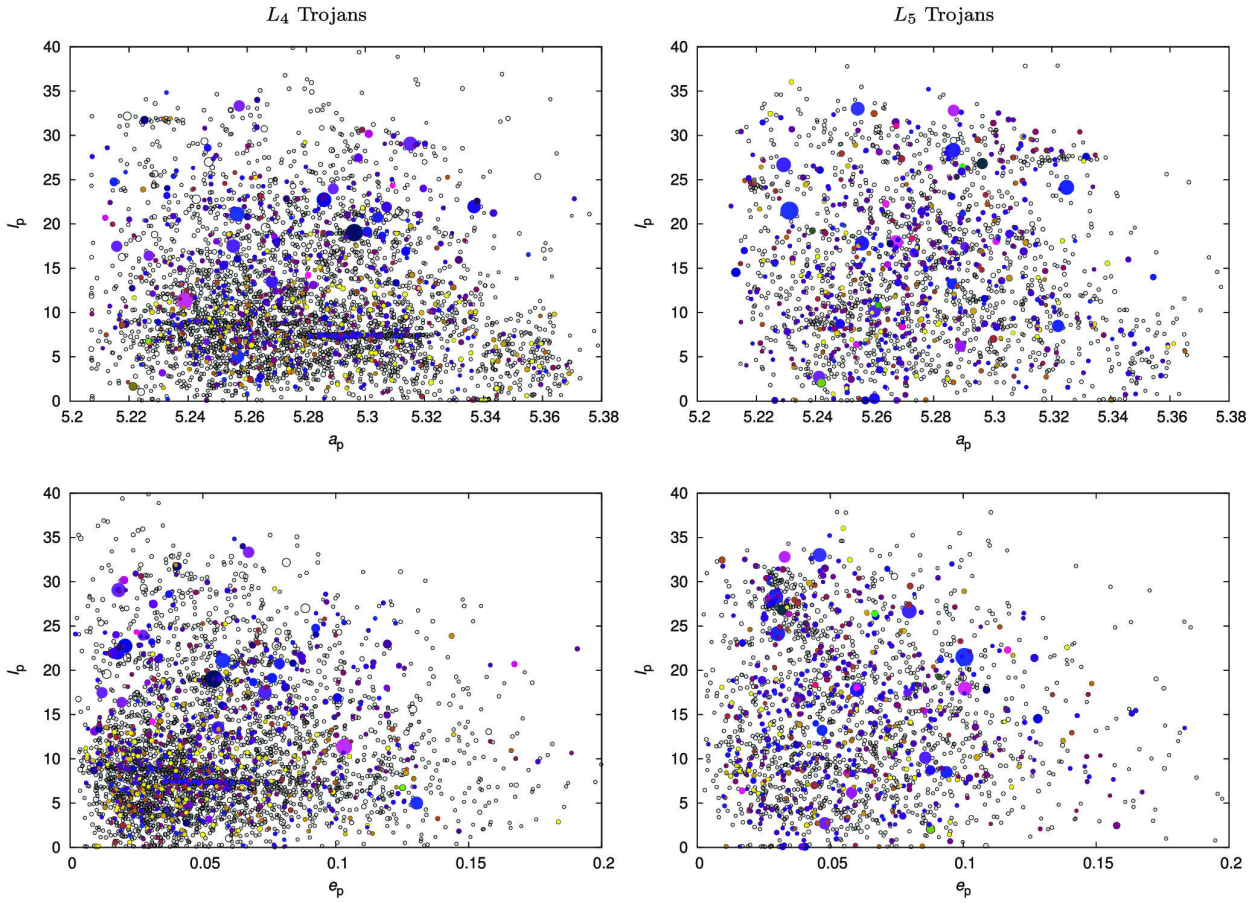


**Figure 1.** The resonant semimajor axis versus inclination ($a_p$, $I_p$) (top) and eccentricity versus inclination ($e_p$, $I_p$) (bottom) for $L_4$ (left) and $L_5$ Trojans (right). The circles indicate relative diameters of bodies, as determined by *WISE* (Grav et al. 2011), or when unavailable, computed from the absolute magnitude $H$ and geometric albedo $p_V$, which we assumed to be $p_V = 0.07$ for both the $L_4$ and $L_5$ Trojans (*WISE* median value is $p_V = 0.072$ for $L_4$ and $p_V = 0.069$ for $L_5$ Trojans). Colours correspond to the values of $p_V$, blue are dark ($p_V \simeq 0.05$) and yellow are bright ($p_V \simeq 0.25$). One can see clearly all asteroid families on this plot, especially in ($a_p$, $I_p$), because they tend to be confined in inclinations.

distribution of albedos, which seem to be slightly dependent on the proper inclination $I_p$. In Section 4, we identify families among Trojans with our new 'randombox' method. We discuss properties of statistically significant families in Section 5. Then we focus mainly on the Hektor family because of its unique D-type taxonomical classification, which is the first of its kind. We also discuss its long-term dynamical evolution. In Section 6, we simulate collisional evolution of Trojans and we estimate the number of observable families among Trojans. Finally, in Section 7, we simulate an origin of the Hektor family using smoothed particle hydrodynamics (SPH) and we compare results for single and bilobed targets. Section 8 is devoted to Conclusions.

## 2 NEW OBSERVATIONAL DATA

### 2.1 Resonant elements

We computed resonant elements, i.e. the averaged semimajor axis $\bar{a}$, libration amplitude $\Delta a_p$, eccentricity $e_p$ and inclination $I_p$ of 3907 Trojans in $L_4$ cloud and 1945 Trojans in $L_5$ cloud. As an input, we used osculating elements listed in AstOrb catalogue (Bowell et al. 2002), released in 2014 July. A detailed description of the resonant elements computation can be found in Brož & Rozehnal (2011). Positions of Trojans in the space of proper elements ($a_p$, $I_p$), where $a_p = \bar{a} + \Delta a_p$, and ($e_p$, $I_p$), calculated with a suitably modified version of the SWIFT integrator (Levison & Duncan 1994), are presented graphically in Fig. 1, together with their sizes and albedos.[1]

### 2.2 *WISE* and AKARI albedos and diameters

To construct SFDs of the whole $L_4$ and $L_5$ Trojan populations and later of individual families, we mostly used *WISE* albedos and diameters derived by Grav et al. (2012). We also compared the respective values to AKARI, as reported by Usui et al. (2011).[2]

We used albedo values of 1609 Trojans in both $L_4$ and $L_5$ clouds obtained by *WISE*; about one-third of these albedos were obtained during cryo-phase, the rest were measured in post-cryo-phase (see Grav et al. 2011).

[1] The table of resonant elements is listed online at http://sirrah.troja.mff.cuni.cz/~mira/mp/trojans/.

[2] While there are some differences between individual values even at $3\sigma$ level, they do not seem to be important for population studies like ours.

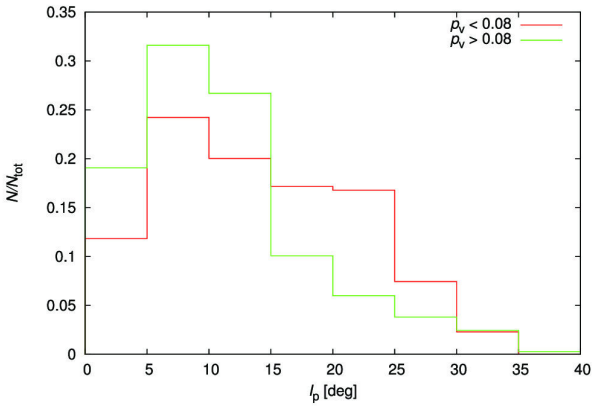


**Figure 2.** The differential histogram of the resonant inclination $I_p$ for $L_4$ Trojans with a lower albedo ($p_V < 0.08$, red) and a higher one ($p_V > 0.08$, green). Eurybates family was removed from the data set.

## 3 PHYSICAL CHARACTERIZATION OF TROJAN POPULATIONS

### 3.1 Albedo distribution and taxonomy

The values of visible albedos $p_V$ of Trojans derived by Grav et al. (2012) vary in the range from $p_V = 0.025$ to $\simeq 0.2$. Distributions of albedos are qualitatively the same for both $L_4$ and $L_5$ populations. The median albedo of *WISE* sample is $\widetilde{p}_v = 0.072 \pm 0.017$ for $L_4$ and $\widetilde{p}_v = 0.069 \pm 0.015$ for $L_5$. These values of visible albedos mostly correspond to C or D taxonomical classes in Tholen taxonomic classification scheme (Mainzer et al. 2011). However, there is a significant presence of small asteroids ($D < 15$ km) with apparently high albedo – almost 20 per cent of asteroids in $L_4$ and 13 per cent of asteroids in $L_5$ have albedo $p_V > 0.10$. As stated in Grav et al. (2012), this is probably not a physical phenomenon, it is rather due to the fact that for small diameters, the photon noise contribution becomes too significant.

When we compute the median albedo from AKARI data, we realize that its value is slightly lower ($\widetilde{p}_v = 0.054 \pm 0.005$) than that from *WISE*, but when we compute the median from *WISE* values for the same asteroids which are listed in AKARI catalogue, we obtain a similar value ($\widetilde{p}_v = 0.061 \pm 0.012$). What is more serious, AKARI and WISE *data* differ considerably for large asteroids with $D > 100$ km – the average difference between albedos is $|p_{V_{AKARI}} - p_{V_{WISE}}| = 0.02$. The same difference we see in derived diameters. These discrepancies may be caused, for example, by limitations of the thermal model (cf. spheres in NEATM models). Hereinafter, we prefer to use the *WISE* data when available, because they represent orders of magnitude larger sample than AKARI.

When we split Trojan asteroids according to their albedo into two rather artificial subpopulations with $p_V < 0.08$ and $p_V > 0.08$, respectively, and then we compute distributions of these subpopulations with respect to the resonant inclination $I_p$, we get two different pictures. As can be seen in Fig. 2, most bodies have resonant inclinations $I_p < 15°$, but there are 77 per cent of bodies with higher albedo with $I_p < 15°$, while only 55 per cent of the population with lower albedo is located in the same range of inclinations. This is a similar phenomenon as described by Vinogradova (2015), who reported different upper limits in inclinations for different taxonomical types obtained mostly from SDSS colour data.

### 3.2 Size–frequency distributions

The *WISE* data (Grav et al. 2011, 2012) provide very useful source of information on diameters we need to construct SFDs of Trojan populations in $L_4$ and $L_5$. However, the sample measured by *WISE* is not complete. In our previous work (Brož & Rozehnal 2011), we constructed the SFDs assuming a constant albedo which we set to be equal to the median albedo of Trojans that was measured back then. Since the number of measurements was very low (several tens), this was the only reasonable way. Now we choose another method to construct more reliable SFDs. As we calculated resonant elements for more than 5800 Trojans and we have more than one quarter of appropriate albedos, we constructed the SFDs by assigning albedos randomly from the observed *WISE* distribution to the remaining Trojans, whose albedo was not measured. To avoid a bias, we compared different SFDs constructed with different random generator seeds and we realized that the overall shape of SFDs does not change noticeably, the slope $\gamma$ varies in the range of $\pm 0.1$ at most. The SFDs we constructed this way are shown in Fig. 3.

The SFDs for the $L_4$ and $L_5$ clouds look slightly different, especially in the size range from 60 to 100 km. This part of the SFD is not influenced by the Eurybates family, the largest family among Trojans, because all its members have diameters $D < 50$ km. We used these SFDs to determine the ratio of the number of asteroids in $L_4$ and $L_5$ clouds. There are 2746 asteroids with diameter $D > 8$ km in $L_4$ and 1518 asteroids in $L_5$. When we remove all family members with diameters $D > 8$ km, we have 2436 asteroids in $L_4$ and 1399 in $L_5$. However, this sample may be still influenced by debris produced by catastrophic disruptions of small bodies ($D \geq 50$ km), which need not to be seen as families. Counting only asteroids with diameter $D > 20$ km, which corresponds to the absolute magnitude $H \simeq 12$, and removing family members, we get the ratio $N_{L_4}/N_{L_5} = 1.3 \pm 0.1$. As this is entirely consistent with value of Nesvorný et al. (2013), which was derived for Trojans with $H > 12$, and with Grav et al. (2012), whose estimate is $N_{L_4}/N_{L_5} = 1.4 \pm 0.2$, we can confirm a persisting asymmetry between the number of $L_4$ and $L_5$ Trojans in new data. Although for bodies with diameter $D > 100$ km, the $L_5$ cloud has more asteroids than $L_4$, the total number of these bodies is of the order of 10, so this is just an effect of small-number statistics and does not affect the $N_{L_4}/N_{L_5}$ ratio much.

## 4 FAMILIES DETECTION METHODS

A brief inspection of the resonant-element space ($a_p$, $e_p$, $I_p$) (see Fig. 1), reveals several locations with higher concentrations of bodies. These could be collisional families, created by a disruption of a parent body during a random collision, but they could also originate randomly by chaotic diffusion and due to effects of secular and high-order resonances. To be regarded as a family, the cluster must comply with, inter alia, the following criteria: (i) it must be concentrated in the space of proper elements; (ii) the cluster must have the SFD different from that of the whole $L_4$ and $L_5$ population; (iii) the last criterion is usually spectral, or at least, albedo homogeneity of family members, but so far, there are not enough sufficiently accurate data for Trojans, especially for bodies with diameters $D < 50$ km, which usually form a substantial part of Trojan families. Therefore, we cannot perform any detailed spectral analysis in this work.

We analysed the space of resonant elements both in terms of mutual distances among bodies and in terms of statistical probability that clusters are not random.

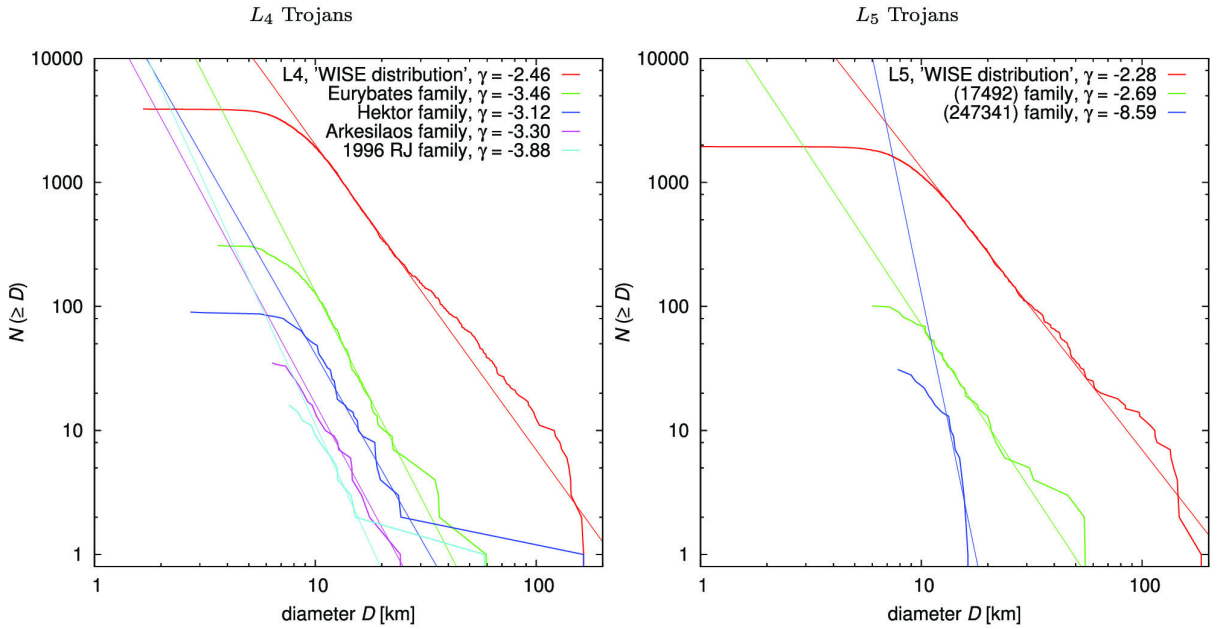


**Figure 3.** Size–frequency distributions for both $L_4$ and $L_5$ Trojans, constructed using the albedos measured by *WISE* satellite (Grav et al. 2012). Since *WISE* data cover just about 18 per cent of $L_4$ and 29 per cent of $L_5$ Trojans known today, we assigned albedos randomly from the *WISE* distribution to the remaining Trojans. We also present SFDs of individual asteroid families discussed in the main text. There are also our fits of each SFD in the range $D = 12$–30 km by the power law $N(>D) = CD^{\gamma}$. As we can see, both clouds seem to be near the collisional equilibrium ($\gamma \simeq -2.5$; Dohnanyi 1969), while most families have slope $\gamma$ significantly steeper. Of course, we can expect the slopes of the SFDs become shallower for smaller $D$ due to observational incompleteness.

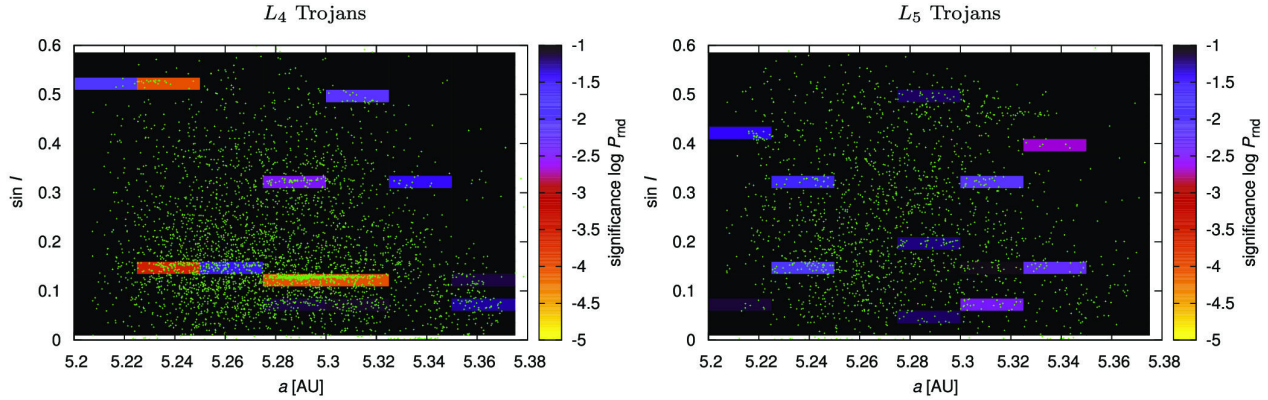


**Figure 4.** The statistical significance $p$ expressed as colour on the logarithmic scale for observed asteroids in the proper semimajor axis versus proper inclination plane ($a_p$, $\sin I_p$) (i.e. the same data as in Fig. 1). $L_4$ Trojans are on the left, $L_5$ Trojans on the right. We computed the values of $p$ for seven times in 18 boxes using our 'randombox' method. The range in proper eccentricity is 0.00–0.20. Statistically significant groups appear as orange boxes and they correspond to the families reported in Table 1.

### 4.1 Randombox method

Besides the commonly used hierarchical clustering method (HCM; Zappalà et al. 1994), we applied a 'randombox' method, based on numerical Monte Carlo (MC) simulations. This method allows us to compute the statistical significance of the clusters, i.e. the probability that the cluster is a random concentration of bodies in the space of proper elements ($a_p$, $e_p$, $\sin I_p$).

We divided the space of proper elements into equally sized 'boxes' with dimensions $\Delta a_p = 0.025$ au, $\Delta e_p = 0.2$ and $\Delta \sin I_p = 0.025$. Then we created $N = 100\,000$ random distributions of the same number of bodies which are observed together in the given box and two adjacent boxes (in the direction of the $y$-axis, cf. Fig. 4), and we counted number of positive trials $N^+$, for which the randomly generated number of bodies in the central box was larger than the observed one. From here, we can calculate the probability $P_{rnd}$, that the observed number of bodies in the box is random: $P_{rnd} = N^+/N$.

Alternatively, one can also use our analytical formula:

$$p_{rnd} = \frac{\sum_{k=n_2}^{n} C(n,k)V'(n_{box}-1, n-k)}{V'(n_{box}, n)}, \quad (1)$$

where $n$ denotes the total number of bodies, $n_{box}$ is the total number of boxes (three in our case), $n_2$ is the observed number of bodies in the middle box, $k$ is the number of observed bodies in the current

**Table 1.** Physical properties of Trojan families identified by both the 'randombox' and the HCM methods. We list family identification number (FIN; as in Nesvorný et al. 2015), the designation of the family, the designation of the asteroid with which the family is associated (i.e. usually the largest remnant of the parent body), the cut-off velocity $v_{\rm cutoff}$, for which family is still clearly detached from the background, and the number of members of the family $N_{\rm memb}$ corresponding to the respective $v_{\rm cutoff}$. Next, we list optical albedos $p_{\rm V}$ of associated bodies determined by Grav et al. (2012) from *WISE* observations, and their taxonomical classification.

| FIN | Family designation | Cloud | Asteroid designation | $v_{\rm cutoff}$ (m s$^{-1}$) | $N_{\rm memb}$ | $p_{\rm V}$(*WISE*) | Tax. type |
|---|---|---|---|---|---|---|---|
| 004 | Hektor | $L_4$ | (624) Hektor | 110 | 90 | $0.087 \pm 0.016$ | D |
| 005 | Eurybates | $L_4$ | (3548) Eurybates | 60 | 310 | $0.060 \pm 0.016$ | C/P |
| 006 | 1996 RJ | $L_4$ | (9799) 1996 RJ | 140 | 17 | $0.082 \pm 0.014$ | – |
| 008 | Arkesilaos | $L_4$ | (20961) Arkesilaos | 55 | 35 | n/a | – |
| 009 | Ennomos | $L_5$ | (17492) Hippasos | 100 | 104 | $0.064 \pm 0.012$ | – |
| 010 | 2001 $UV_{209}$ | $L_5$ | (247341) 2001 $UV_{209}$ | 120 | 30 | $0.088 \pm 0.023$ | – |

box, $C(n, k)$ are combinations without repetitions, i.e. the total number of trials to select $k$ bodies observed in the current box from the total number of $n$ bodies; $V'(n_{\rm box} - 1, n - k)$ are variations with repetitions, i.e. the total number of trials to distribute the remaining bodies into the remaining boxes; and $V'(n_{\rm box}, n)$ are also variations with repetitions, i.e. the total number of trials to distribute all $n$ bodies into all $n_{\rm box}$ boxes. We verified the results of the analytical formula (1) by the MC method.

We plot the results in Fig. 4 for both the $L_4$ and $L_5$ clouds. In comparison with Fig. 1, one can see that for all clusters we identified as families the probability $P_{\rm rnd}$ varies between $2 \cdot 10^{-3}$ and $5 \cdot 10^{-5}$, i.e. the probability that clusters are random fluctuations is indeed very low.

We also re-evaluated all families identified by the HCM using the 'randombox' method, which makes our decision whether the cluster is a real family much more quantitative.

### 4.2 Hierarchical clustering method

We also used the HCM independently to extract significant clusters. Families identified by both the 'randombox' and HCM methods are listed in Table 1. For each family, we constructed a dependence of the number of members of the cluster $N_{\rm memb}$ on the cut-off velocity $v_{\rm cutoff}$. Because the number of members of a real collisional family rises first slowly with rising $v_{\rm cutoff}$ (Brož & Rozehnal 2011) – in contrast with random clusters which are merging very quickly with the background – the constructed dependence allows us to guess a realistic number of family members $N_{\rm memb}$. For all families listed in Table 1, we were convinced that they fulfill this criterion. However, we cannot distinguish possible interlopers this way, and it is also possible that some fraction of family members with high $v_{\rm cutoff}$ (so called halo, as in Brož & Morbidelli 2013) remains unidentified in the surrounding background.

## 5 PROPERTIES OF STATISTICALLY SIGNIFICANT FAMILIES

### 5.1 Eurybates

As we have already demonstrated in Brož & Rozehnal (2011), the family associated with asteroid (3548) Eurybates is the largest collisional family, and it is the only family among Trojans with the parent body size $D_{\rm PB} > 100$ km, which originated by a catastrophic disruption (this means that the mass ratio of the largest remnant to the parent body $M_{\rm LR}/M_{\rm PB} < 0.5$).

Using new albedos derived by Grav et al. (2012), we recalculated the overall SFD slope of the family to be $\gamma = -3.4 \pm 0.1$. As the *WISE* sample provides albedos for only about one-fifth of the family members, we calculated two values of $\gamma$: the first one assuming that remaining asteroids have a constant albedo $p_{\rm V} = 0.06$, the second one by assigning albedos randomly from the *WISE* distribution, as described in Section 3.2. Both values are equal within their errorbars. The new slope $\gamma$ is significantly steeper than our previous calculation ($\gamma = -2.5 \pm 0.1$), derived with the assumption of a constant albedo of all members of the family. The lower value was most likely caused by a significant observational incompleteness in the size range from $D = 12$–$30$ km.

We also derived the new value of the parent body diameter, which is still above the limit of 100 km. An extrapolation of the SFD by a power law gives the value $D_{\rm PB} \simeq 140$ km. By fitting the synthetic SFDs from SPH simulations (Durda et al. 2007), we obtained the value $D_{\rm PB(SPH)} \simeq 155$ km.

### 5.2 Hektor – the first D-type family

Since asteroid (624) Hektor is a close binary with a satellite (Marchis et al. 2014), i.e. an exceptional object, we want to address its association with the family. The cluster around the largest Trojan asteroid appears in the space of proper elements as a relatively compact group, which is limited particularly in proper inclinations, $I_{\rm p} \in \langle 18\overset{\circ}{.}13; 19\overset{\circ}{.}77 \rangle$, and with resonant semimajor axes located in the interval $a_{\rm p} \in \langle 5.234; 5.336 \rangle$ au. The number of members of this group slowly increases with increasing cut-off velocity up to $v_{\rm cutoff} \simeq 110$ m s$^{-1}$, above which it quickly joins the background. With our randombox method, we estimated the probability that the family is just a random fluke to be as low as $P_{\rm rnd} \simeq 2 \cdot 10^{-3}$.

The nominal diameter of asteroid (624) Hektor derived from its albedo is 164 km (Grav et al. 2012), but the albedo measured by AKARI $p_{\rm V} = 0.034 \pm 0.001$ (Usui et al. 2011) totally differs from that measured by *WISE*, $p_{\rm V} = 0.087 \pm 0.016$. and these values do not match even within the error limits. This may be caused by applying a thermal model assuming spheres to the bilobed shape of the asteroid (Marchis et al. 2014). We hence do not determine Hektor's diameter from its albedo, but from fits of Marchis et al. (2014), which effective value $D = (250 \pm 26)$ km is suitable within its uncertainty for all possible geometries (convex, bilobe and binary). For other bodies in family, we use a nominal value $p_{\rm V} = 0.072$, which is the median of *WISE* measurements.

Asteroid (624) Hektor is often classified as D-type (e.g. Cruikshank et al. 2001; Emery, Cruikshank & Van Cleve 2006; Emery, Burr & Cruikshank 2011). We tried to evaluate taxonomical classification of other family members and we have found colours for two more expected family members in SDSS-MOC vers. 4 (Ivezić et al. 2002): asteroids (65000) 2002 AV63 and (163702) 2003 FR72. Even though the photometric noise in individual bands is not negligible ($\sigma_i = 0.02$ mag up to $\sigma_u = 0.12$ mag), both of them

are D-types, with principal components (also known as slopes) $PC_1 > 0.3$. This seems to support the D-type classification of the whole family.

We also tried to constrain the taxonomic classification of the family members by comparing their infrared (IR) albedos $p_{IR}$ and visual albedos $p_V$ as described in Mainzer et al. (2011), but there are no data for family members in the *W1* or *W2* band of the *WISE* sample, which are dominated by reflected radiation.

The fact that we observe a collisional family associated with a D-type asteroid is the main reason we use word 'exceptional' in connection with the Hektor family. As we claimed in Brož et al. (2013), in all regions containing a mixture of C-type and D-type asteroids (e.g. Trojans, Hildas, Cybeles), there have been only C-type families observed so far, which could indicate that disruptions of D-type asteroids leave no family behind, as suggested by Levison et al. (2009). Nevertheless, our classification of the Hektor family as D-type is not in direct contradiction with this conclusion, because Levison et al. (2009) were concerned with catastrophic disruptions, while we conclude below that the Hektor family originated from a cratering event, i.e. by an impactor with kinetic energy too small to disrupt the parent body.

#### 5.2.1 *Simulations of long-term dynamical evolution*

To get an upper limit of the age of the Hektor family, we simulated a long-term evolution of seven synthetic families created for different breakup geometries. Our model included four giant planets on current orbits, integrated by the symplectic integrator SWIFT (Levison & Duncan 1994), modified according to Laskar & Robutel (2001), with the timestep of $\Delta t = 91$ d and timespan 4 Gyr.

We also accounted for the Yarkovsky effect in our simulations. Although in a first-order theory, it is not effective in zero-order resonances (it could just shift libration centre, but there is no systematic drift in semimajor axis) and the observed evolution of proper elements is mainly due to chaotic diffusion, in higher order theories, the Yarkovsky effect can play some role. In our model, we assumed a random distribution of spins and rotation periods (typically several hours), the bulk and surface density $\rho_{bulk} = \rho_{surf} = 1.3\ \mathrm{g\,cm^{-3}}$, the thermal conductivity $K = 0.01\ \mathrm{W\,m^{-1}\,K^{-1}}$, the specific heat capacity $C = 680\ \mathrm{J\,kg^{-1}\,K^{-1}}$, the Bond albedo $A_B = 0.02$ and the IR emissivity $\epsilon = 0.95$.

We created each synthetic family by assigning random velocities to 234 bodies (i.e. three times more than the number of the observed family members), assuming an isotropic velocity field with a typical velocity of 70 $\mathrm{m\,s^{-1}}$, corresponding to the escape velocity from parent body (Farinella, Froeschlé & Gonczi 1994). Here we assumed the velocity of fragments to be size independent. Possible trends in the ejection velocity field cannot be easily revealed in the $(a, H)$ space in the case of the Hektor family, because of its origin by a cratering event – there is a large gap in the range between absolute magnitude of (624) Hektor ($H = 7.20$) and other bodies ($H > 11.9$), so we are not able to distinguish a simple Gaussian dispersion from the physical dependence (cf. Carruba & Nesvorný 2016). Either way, we are interested in the orbital distribution of mostly small bodies. Our assumption of size-independent ejection velocity is also in good agreement with results of SPH models (see subsection 7.3 and Fig. 13).

To create a synthetic family in the same position as occupied by the observed Hektor family, we integrated the orbit of asteroid (624) Hektor with osculating elements taken from AstOrb catalogue (Bowell et al. 2002), until we got appropriate values of the true anomaly $f$ and the argument of pericentre $\omega$. We tried values of $f$ ranging from 0° to 180° with the step of 30° and $\omega$ always satisfying the condition $f + \omega = 60°$, i.e. we fixed the angular distance from the node to ensure a comparably large perturbations in inclinations.

Initial positions of synthetic families members just after the disruption, compared to the observed Hektor family, are shown in Fig. 5. To make a quantitative comparison of the distribution in the space of proper elements, we used a two-dimensional Kolmogorov–Smirnov (KS) test to compute KS distance of the synthetic family to the observed one with the output timestep of 1 Myr. The results for different initial geometries are shown in Fig. 6.

Our two best fits corresponding to the lowest KS distance are displayed in Fig. 7. As we can see from the image of the whole Trojan L4 population, Hektor seems to be near the outskirts of the librating region (cf. Fig. 1). In Fig. 5, we can note that there are almost no observed asteroids in the shaded area with $a_p > 5.32$ au, but we can see some synthetic family members in the left-hand panel of Fig. 7 (initial geometry $f = 0°$, $\omega = 60°$).

On the other hand, when we look at right-hand panel of Fig. 7 (initial geometry $f = 150°$, $\omega = 270°$), we can see that there are many fewer bodies in the proximity of the border of the stable librating region. One can also see the initial 'fibre-like' structure is still visible on the left, but is almost dispersed on the right.

Hence, we conclude that the geometry at which the disruption occurred is rather $f = 150°$, $\omega = 270°$ and the corresponding age is between 1 and 4 Gyr. The second but less likely possibility is that the disruption could have occurred more recently (0.1–2.5 Gyr) at $f = 0°$, $\omega = 60°$.

#### 5.2.2 *Parent body size from SPH simulations*

We tried to estimate the parent body size of Hektor family and other families by the method described in Durda et al. (2007). To this point, we calculated a pseudo$-\chi^2$ for the whole set of synthetic SFDs as given by the SPH simulations results (see Fig. 8).

Parent body sizes $D_{PB(SPH)}$ and mass ratios of the largest fragment and parent body $M_{LF}/M_{PB}$ estimated by this method are listed in Table 2. The parent body size for Hektor family we derived from SPH simulations is $D_{PB(SPH)} = (260 \pm 10)$ km, the impactor diameter $D_{imp} = (24 \pm 2)$ km, the impactor velocity $v_{imp} = (4 \pm 1)\ \mathrm{km\,s^{-1}}$ and the impact angle $\varphi_{imp} = (60° \pm 15°)$. We will use these values as initial conditions for simulations of collisional evolution below.

### 5.3 1996 RJ – extremely compact family

In our previous work, we mentioned a small cluster associated with asteroid (9799) 1996 RJ, which consisted of just nine bodies. With the contemporary sample of resonant elements, we can confirm that this cluster is indeed visible. It is composed of 18 bodies situated near the edge of the librating zone on high inclinations, within the ranges $I_p \in \langle 31.^\circ 38;\ 32.^\circ 27\rangle$ and $a_p \in \langle 5.225; 5.238\rangle$ au. As it is detached from the background in the space of proper elements, it remains isolated even at high cut-off velocity $v_{cutoff} = 160\ \mathrm{m\,s^{-1}}$.

Unfortunately, we have albedos measured by *WISE* for just four members of this family. These albedos are not much dispersed. They range from $p_V = 0.079 \pm 0.019$ to $0.109 \pm 0.029$ and, compared to the median albedo of the whole $L_4$ population $\widetilde{p_V} = 0.072 \pm 0.017$, they seem to be a bit brighter, but this statement is a bit inconclusive.

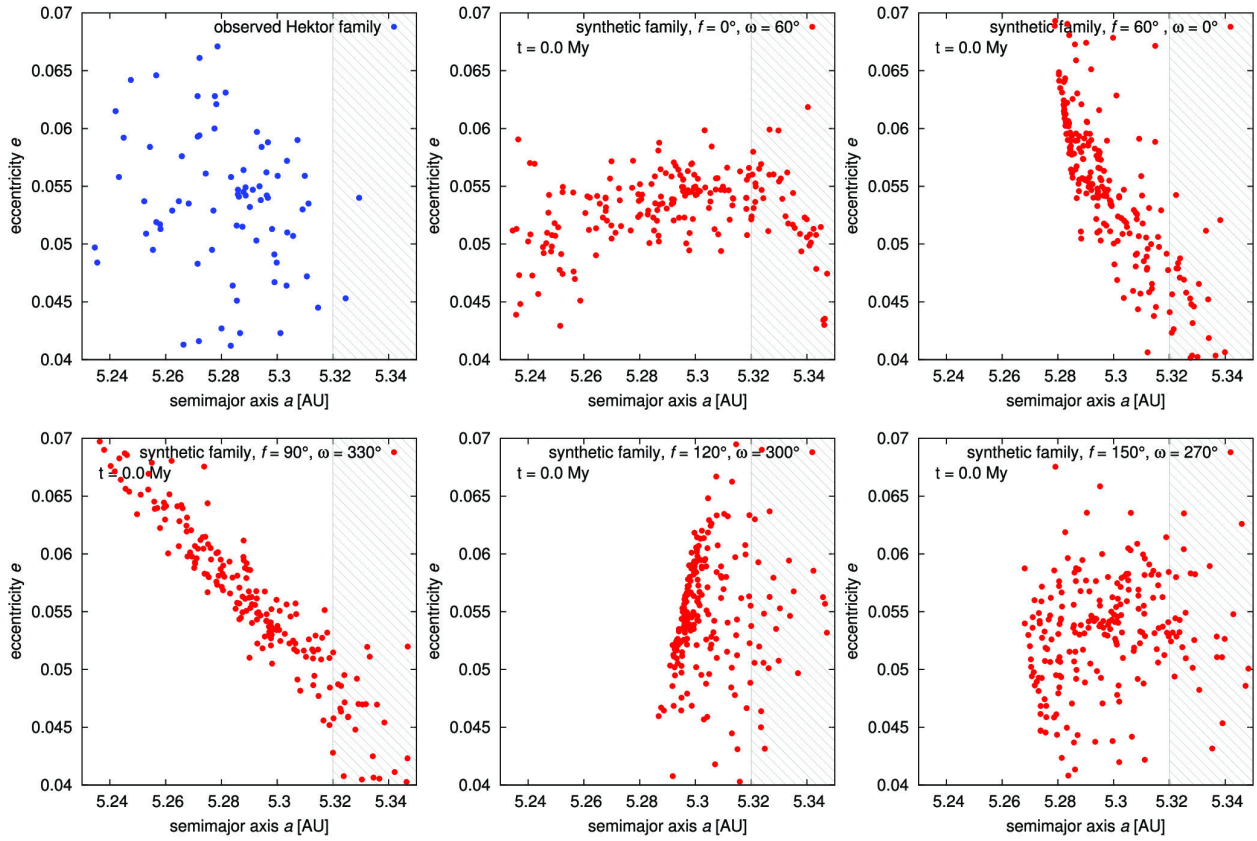


**Figure 5.** Initial conditions for simulations of long-term evolution of synthetic families (red), compared to the observed Hektor family (blue) in the space of proper elements ($a_p$, $e_p$). Each figure shows a different disruption geometry with different values of the true anomaly $f$ and the argument of pericentre $\omega$. Note the shaded area in the top-left figure – there are only two observed asteroids with proper semimajor axis $a_p > 5.32$ au. This is due to the proximity to the border of the stable librating region. As there are many more synthetic asteroids in this region in all cases of initial distributions, we need to simulate a dynamical evolution of the family.

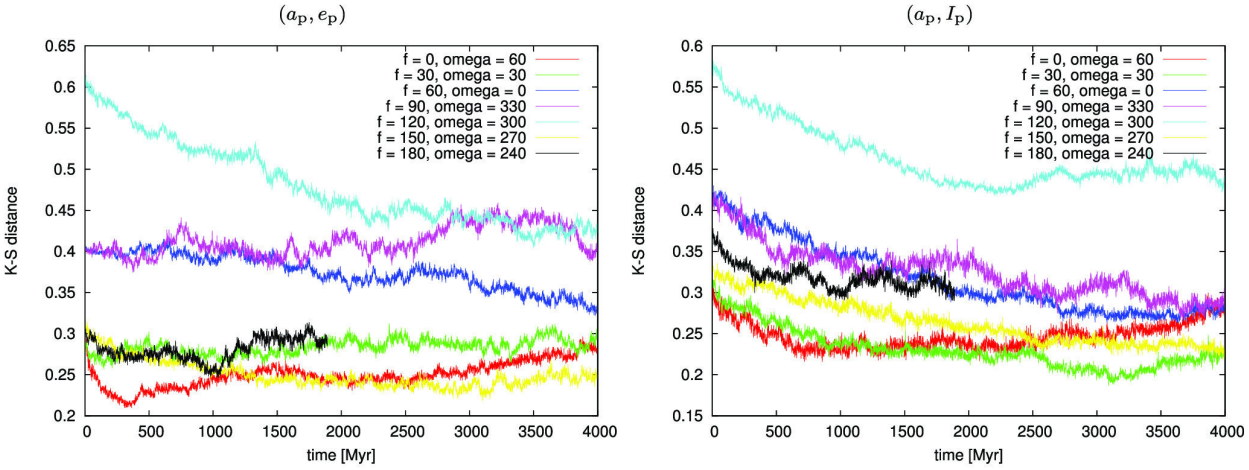


**Figure 6.** Kolmogorov–Smirnov distance $D_{KS}$ versus time for seven different synthetic families compared with the observed Hektor family. Two-dimensional KS test was computed for the distributions of synthetic and observed families in the space of proper elements ($a_p$, $e_p$) (left) and ($a_p$, $I_p$) (right). The synthetic families were created assuming different impact geometries, namely the true anomaly $f = 0°$, 30°, 60°, 90°, 120°, 150°, 180° and the argument of pericentre $\omega = 60°$, 30°, 0°, 330°, 300°, 270°, 240°, which were combined so that the sum $f + \omega = 60°$. The averaged distance $D_{KS}$ changes in the course of dynamical evolution and we can see two minima: for $f = 0°$ and $\omega = 60°$ (red curve), it is at about (350 ± 100) Myr; for $f = 150°$ and $\omega = 270°$ (yellow curve), there is a flat minimum at (2800 ± 1500) Myr. Since the red and yellow curves are overlapping in the range from 1800 to 2500 Myr, we adopt the values of possible ages as 100–2500 Myr for the $f = 0°$ and $\omega = 60°$ geometry (red curve) and 1000–4000 Myr for the $f = 150°$ and $\omega = 270°$ geometry (yellow curve).

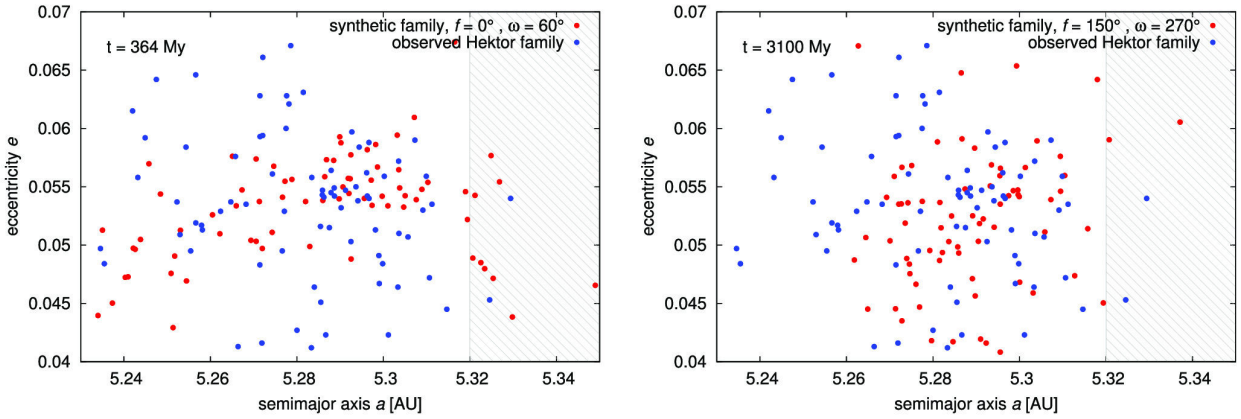


**Figure 7.** Two evolved synthetic families in the space of proper elements ($a_p$, $e_p$), which correspond to the minima of KS distance in Fig. 6. Left-hand picture shows the synthetic family (red) with $f = 0°$ and $\omega = 60°$ after 364 Myr of evolution in comparison with the observed Hektor family (blue). Right-hand picture corresponds to the synthetic family with $f = 150°$ and $\omega = 270°$ after 3100 Myr of evolution. These two pictures differ in fine details, which cannot be accounted for in the KS statistics: (i) the 'fibre-like' structure of the relatively young family is still visible in the left-hand picture; (ii) there are many fewer synthetic bodies in the shaded area of the right picture ($a_p > 5.32$ au) than on the left, which is closer to the observed reality.

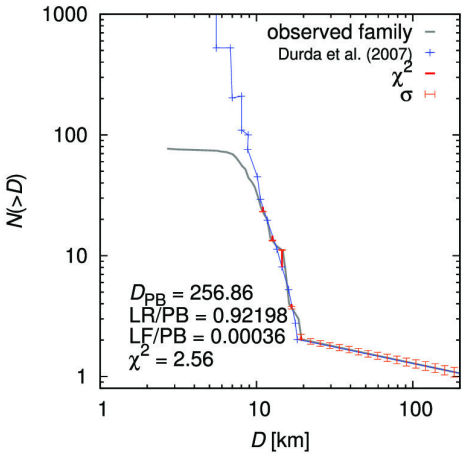


**Figure 8.** Our best-fitting size–frequency distribution of Hektor family by scaled SFDs from SPH simulations of Durda et al. (2007). In this particular case, $D_{PB(SPH)} = 257$ km, impactor diameter $D_{imp} = 48$ km, impactor velocity $v_{imp} = 4\,km\,s^{-1}$ and impact angle $\varphi_{imp} = 60°$. However, other fits with similar pseudo-$\chi^2$ suggest the uncertainties are as follows: $\Delta D_{PB(SPH)} = 10$ km, $\Delta D_{imp} = 2$ km, $\Delta v_{imp} = 1\,km\,s^{-1}$ and $\Delta\varphi_{imp} = 15°$. SFD shape seems to be more dependent on impact geometry than on impact velocity.

### 5.4 Arkesilaos

This family is located on low inclinations $I_p \in \langle 8.52°; 9.20°\rangle$, in the range of $a_p \in \langle 5.230; 5.304\rangle$ au. It is clearly visible in the space of proper elements, although this area of $L_4$ cloud is very dense.

Still, it is difficult to find the largest remnant of the parent body, because this region is populated mainly by small asteroids with absolute magnitudes $H > 12$. The only four asteroids with $H < 12$ are (2148) Epeios with $H = 10.7$, (19725) 1999 $WT_4$ with $H = 10.7$, (38600) 1999 $XR_{213}$ with $H = 11.7$ and (20961) Arkesilaos with $H = 11.8$. The only diameter derived from measured albedo is that of (2148) Epeios, which is $D = (39.02 \pm 0.65)$ km. Diameters of remaining bodies were calculated from their absolute magnitude assuming albedo $p_V = 0.072$, which is the median of $L_4$ Trojans. Although (20961) Arkesilaos has the diameter only $D = (24 \pm 5)$ km, it is the only asteroid with $H < 12$, for which the associated family has a reasonable number of members $N_{memb}$ even for small values of the cut-off velocity $v_{cutoff}$ (see Section 4.2). As this is also the only larger body located near the centre of the family in the space of proper elements, we treat (20961) Arkesilaos as the largest remnant of the parent body, whose diameter we estimate to be $D_{PB(SPH)} \simeq 87$ km. Given that the mass ratio of the largest remnant and the parent body, as derived from SPH simulations of Durda et al. (2007), is $M_{LR}/M_{PB} \simeq 0.02$ only, it seems this family inevitably originated from a catastrophic disruption.

### 5.5 Ennomos

In our previous work, we reported a discovery of a possible family associated with asteroid (4709) Ennomos. With new data, we can still confirm that there is a significant cluster near this body, but when we take into account our '$N_{memb}(v_{cutoff})$' criterion described above, it turns out that the family is rather associated with asteroid (17492) Hippasos. It is a relatively numerous group composed of almost 100 bodies, situated near the border of the stable librating zone $L_5$ at high inclinations, ranging from $I_p \in \langle 26.^\circ 86; 30.^\circ 97\rangle$, and $a_p \in \langle 5.225; 5.338\rangle$ au.

### 5.6 2001 $UV_{209}$

Using new data, we discovered a 'new' family around asteroid (247341) 2001 $UV_{209}$, which is the second and apparently the last observable family in our sample. Similar to the Ennomos family, it is located near the border of the $L_5$ zone on high inclinations $I_p \in \langle 24.^\circ 02; 26.^\circ 56\rangle$ and $a_p \in \langle 5.218; 5.320\rangle$ au. This family has an exceptionally steep slope of the SFD, with $\gamma = -8.6 \pm 0.9$, which may indicate a recent collisional origin or a disruption at the boundary of the libration zone, which may be indeed size-selective as explained in Chrenko et al. (2015).

**Table 2.** Derived properties of Trojan families. We list here the family designation, the diameter of the largest remnant $D_{LR}$, the minimal diameter of the parent body min $D_{PB}$, obtained as the sum of all observed family members, the diameter of the parent body $D_{PB(SPH)}$ and the mass ratio $M_{LR}/M_{PB}$ of the largest fragment and the parent body, both derived from our fits by scaled SPH simulations performed by Durda et al. (2007). We use this ratio to distinguish between the catastrophic disruption ($M_{LR}/M_{PB} < 0.5$) and the cratering ($M_{LR}/M_{PB} > 0.5$). Finally, there is the escape velocity $v_{esc}$ from the parent body and estimated age of the family derived in this and our previous work (Brož & Rozehnal 2011).

| Family designation | $D_{LR}$ (km) | min $D_{PB}$ | $D_{PB(SPH)}$ | $M_{LR}/M_{PB}$ | $v_{esc}$(m s$^{-1}$) | Age (Gyr) | Notes, references |
|---|---|---|---|---|---|---|---|
| Hektor | 250 ± 26 | 250 | 257 | 0.92 | 73 | 0.3–3 | 1, 3 |
| Eurybates | 59.4 ± 1.5 | 100 | 155 | 0.06 | 46 | 1.0–3.8 | 2 |
| 1996 RJ | 58.3 ± 0.9 | 61 | 88 | 0.29 | 26 | – | 2, 4 |
| Arkesilaos | 24 ± 5 | 37 | 87 | 0.02 | 16 | – | 2 |
| Ennomos | 55.2 ± 0.9 | 67–154 | 95–168 | 0.04–0.19 | 29–66 | 1–2 | 2, 5 |
| 2001 $UV_{209}$ | 16.3 ± 1.1 | 32 | 80 | 0.01 | 14 | – | 2 |

*Notes.* [1]$D_{LR}$ derived by Marchis et al. (2014),
[2]$D_{LR}$ derived by Grav et al. (2012),
[3]bilobe, satellite (Marchis et al. 2014),
[4]very compact, Brož & Rozehnal (2011),
[5]$D_{PB}$ strongly influenced by interlopers,
[6]The largest fragment of Ennomos family is (17492) Hippasos.

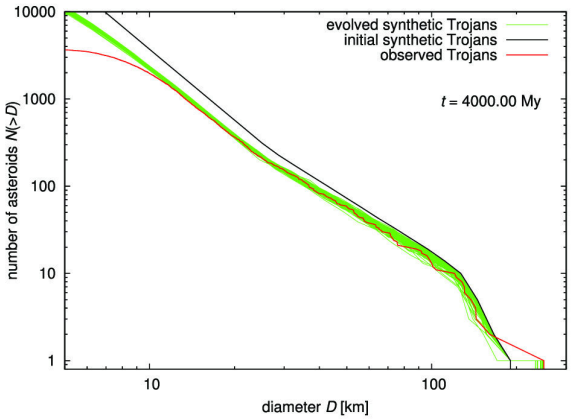


**Figure 9.** Simulations of the collisional evolution of $L_4$ Trojans with the Boulder code (Morbidelli et al. 2009). Shown here is the initial cumulative SFD of a synthetic population (black) and the SFD of the observed one (red). Green are the final SFDs of 100 synthetic populations with the same initial SFD but with different random seeds, after 4 Gyr of a collisional evolution. The evolution of bodies larger than $D > 50$ km is very slow, hence we can consider this part of the SFD as captured population.

## 6 COLLISIONAL MODELS OF THE TROJAN POPULATION

In order to estimate the number of collisional families among $L_4$ Trojans, we performed a set of 100 simulations of the collisional evolution of Trojans with the Boulder code (Morbidelli et al. 2009) with the same initial conditions, but with different values of the random seed.

### 6.1 Initial conditions

We set our initial conditions of the simulations such that 4 Gyr of collisional evolution leads to the observed cumulative SFD of $L_4$ Trojans (red curve in Fig. 9). We constructed the initial synthetic SFD as three power laws with the slopes $\gamma_a = -6.60$ in the size range from $D_1 = 117$ km to $D_{max} = 250$ km, $\gamma_b = -3.05$ from $D_2 = 25$ km to $D_1$ and $\gamma_c = -3.70$ from $D_{min} = 0.05$ km to $D_2$. The synthetic initial population was normalized to contain $N_{norm} = 11$ asteroids with diameters $D \geq D_1$.

To calculate the target strength $Q_D^*$, we used a parametric formula of Benz & Asphaug (1999):

$$Q_D^* = Q_0 R_{PB}^a + B\rho_{bulk} R_{PB}^b, \quad (2)$$

where $R_{PB}$ is the parent body radius in centimetres, $\rho_{bulk}$ its bulk density, which we set to be $\rho_{bulk} = 1.3$ g cm$^{-3}$ for synthetic Trojans (cf. Marchis et al. 2014). As of constants $a$, $b$, $B$ and $Q_0$, we used the values determined by Benz & Asphaug (1999) for ice at the impact velocity $v_{imp} = 3$ km s$^{-1}$, which are $a = -0.39$, $b = 1.26$, $B = 1.2$ erg cm$^3$ g$^{-2}$ and $Q_0 = 1.6 \cdot 10^7$ erg g$^{-1}$.

In our model, we take into account only Trojan versus Trojan collisions, as the Trojan region is practically detached from the main belt. Anyway, main-belt asteroids with eccentricities large enough to reach the Trojan region are usually scattered by Jupiter on a time-scale significantly shorter than the average time needed to collide with a relatively large Trojan asteroid. We thus assumed the values of collisional probability $P_i = 7.80 \cdot 10^{-18}$ km$^{-2}$ yr$^{-1}$ and the impact velocity $v_{imp} = 4.66$ km s$^{-1}$ (Dell'Oro et al. 1998). Unfortunately, Benz & Asphaug (1999) do not provide parameters for ice at the impact velocities $v_{imp} > 3$ km s$^{-1}$.

We also ran several simulations with appropriate values for basalt at impact velocity $v_{imp} = 5$ km s$^{-1}$ ($a = -0.36$, $b = 1.36$, $B = 0.5$ erg cm$^3$ g$^{-2}$ and $Q_0 = 9 \cdot 10^7$ erg g$^{-1}$).

Both models qualitatively exhibit the same evolution of SFD and they give approximately the same total numbers of disruptions and craterings occurred, but for basalt, the model gives three times fewer observable families originated by cratering than for ice. The results for the ice match the observation better, so we will further discuss the results for ice only.

### 6.2 Long-term collisional evolution

The results of our simulations of the collisional evolution are shown in Fig. 9. Our collisional model shows only little changes above $D > 50$ km over the last 3.85 Gyr (i.e. post-LHB phase only). Slopes of the initial synthetic population and the observed $L_4$ population differ by $\Delta\gamma < 0.1$ in the size range from 50 to 100 km, while a relative decrease of the number of asteroids after 3.85 Gyr of collisional evolution is only about 12 per cent in the same size

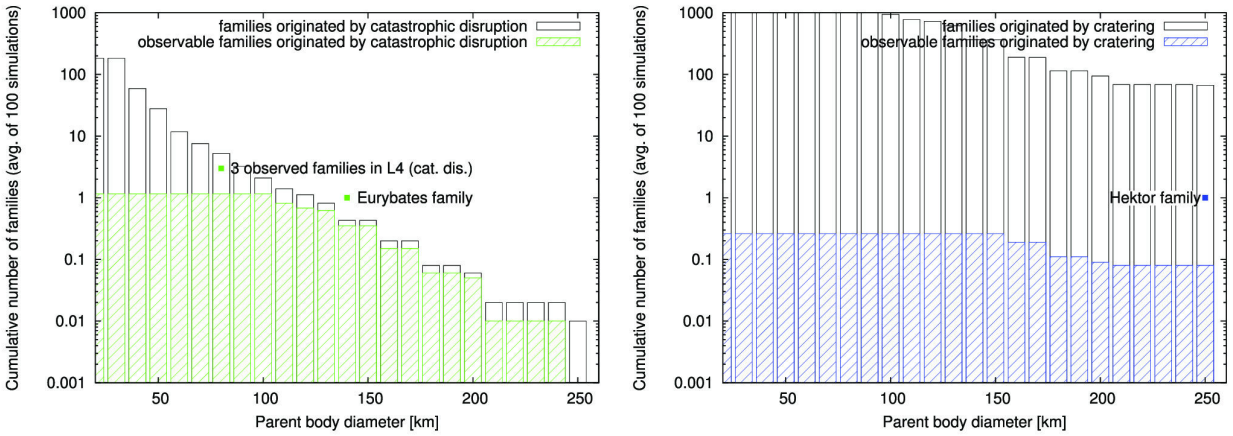


**Figure 10.** The dependence of the cumulative number (an average over 100 simulations) of catastrophic disruptions among Trojans (left-hand panel) and cratering events (right-hand panel) on the target diameter $D_{\rm PB}$ (black boxes), and a subset of those Trojan families, which should be detected in contemporary observational data, i.e. with the number of fragments $N(D > 10\,{\rm km}) > 10$ (green boxes for disruptions and blue boxes for craterings). In other words, colour boxes represent simulated detections of families based on the expected effectiveness of our detection methods. This is the reason, why the cumulative number of the observable families does not strictly increase with the decreasing parent body size, but is rather constant under the limit of about 95 km in the case of catastrophic disruptions and 145 km in the case of craterings. There are also observed families marked for a comparison. Three of the four observed families in $L_4$ cloud originated by catastrophic disruption, while only one (Hektor) originated by cratering event (cf. Table 1).

range. Hence, we can consider this part of the Trojan population as a representative sample of the source population, which is not much affected by collisional evolution. Therefore, these Trojans provide very useful information about the source population, from which they were captured (as modelled in Nesvorný et al. 2013).

### 6.3 An estimate of the number of observable families

From our set of simulations, we also obtained the number of collisions leading to collisional families among $L_4$ Trojans, namely catastrophic disruptions, where the mass ratio of the largest remnant and the parent body $M_{\rm LR}/M_{\rm PB} < 0.5$, and cratering events, where $M_{\rm LR}/M_{\rm PB} > 0.5$. As one can verify in Fig. 10, these numbers are dependent on the diameter of the parent body $D_{\rm PB}$.

However, not all of these collisions produce families which are in fact observable (detectable). There are generally two possible obstacles in the detection of a family in the space of proper elements: (i) somewhat more concentrated background population, due to which our detection methods (both 'randombox' and HCM, see Chapter 4) may fail, if the number of observed fragments is too low in comparison with the background, and (ii) an observational incompleteness, which means that in the case of Trojans, a substantial part of fragments with sizes $D < 10$ km is still unknown, what again reduces a chance of a family detection.

For these reasons, we constructed a criterion of observability that a synthetic family must fulfill in order to be detectable in the current conditions (i.e. we simulated a detection of synthetic families by the same methods we used to detect the real ones). The simplest criterion could be that a family must contain at least $N_{\rm min} = 10$ fragments with diameter $D \geq 10$ km.

Within 100 simulations, there were 93 catastrophic disruptions of bodies with diameters $D_{\rm PB} > 100$ km, but only 50 of them produced more than 10 fragments with $D \geq 10$ km, see Fig. 10. Hence, the probability that we would observe a collisional family originated by a catastrophic disruption of a parent body with $D_{\rm PB} > 100$ km is only 0.50, which matches the observations (namely Eurybates family with $D_{\rm PB(SPH)} \simeq 155$ km, see Table 2). This value is also roughly consistent with our previous estimate based on the stationary model (Brož & Rozehnal 2011), which gives the value 0.32 with new observational data.

As one can also see in Fig. 10, the number of cratering events is about one to two orders higher than the number of catastrophic disruptions, however, they do not produce enough fragments larger than $D \geq 10$ km. For the parent body size $D_{\rm PB} > 100$ km, there occurred almost 45 000 cratering events within 100 simulations which produced the largest fragment with $D_{\rm LF} \geq 1$ km, but only 10 of them fulfill our criterion of observability. Hence, the probability that we can observe a family originated by a cratering of a parent body with $D_{\rm PB} > 100$ km is only 0.10, at least with contemporary data. From a statistical point of view, this can actually correspond to the Hektor family.

As we have already demonstrated in Brož & Rozehnal (2011), the number of families is not significantly affected by chaotic diffusion or by a ballistic transport outside the libration zone.

## 7 SPH SIMULATIONS OF HEKTOR FAMILY

As we have already mentioned in Section 5.2, (624) Hektor is very interesting Trojan asteroid with possibly bilobed shape and a small moon. Diameters of (624) Hektor stated in Marchis et al. (2014) are as follows: equivalent diameter $D_{\rm eq} = (250 \pm 26)$ km for a convex model, the individual diameters of the lobes $D_{\rm A} = (220 \pm 22)$ km, $D_{\rm B} = (183 \pm 18)$ km for a bilobed version. Estimated parameters of the moon are: the diameter $D_{\rm m} = (12 \pm 3)$ km, the semimajor axis $a_{\rm m} = (623 \pm 10)$ km, the eccentricity $e_{\rm m} = (0.31 \pm 0.03)$ and the inclination (with respect to the primary equator) $I_{\rm m} = (50 \pm 1)^\circ$.

As we associate (624) Hektor with the collisional family, we would like to know, how the properties of the family are influenced by the shape of target body. We therefore performed a series of SPH simulations aiming to explain the origin of the Hektor family, for both cases of convex and bilobed shape of its parent body.

### 7.1 Methods and initial conditions

We simulated a collisional disruption using the SPH code SPH5 (Benz & Asphaug 1994). We performed two sets of simulations. In

**Table 3.** Material constants used in our SPH simulations for basalt and silicated ice (30 per cent of silicates). Listed here are: the zero-pressure density $\rho_0$, bulk modulus $A$, non-linear compressive term $B$, sublimation energy $E_0$, Tillotson parameters $a$, $b$, $\alpha$ and $\beta$, specific energy of incipient vaporization $E_{\rm iv}$, complete vaporization $E_{\rm cv}$, shear modulus $\mu$, plastic yielding $Y$, melt energy $E_{\rm melt}$ and Weibull fracture parameters $k$ and $m$. Values we used for silicated ice are identical to those of pure ice, except density $\rho_0$, bulk modulus $A$ and Weibull parameters $k$ and $m$. All values were adopted from Benz & Asphaug (1999).

| Quantity | Basalt | Silicated ice | Unit |
|---|---|---|---|
| $\rho_0$ | 2.7 | 1.1 | g cm$^{-3}$ |
| $A$ | $2.67 \cdot 10^{11}$ | $8.44 \cdot 10^{10}$ | erg cm$^{-3}$ |
| $B$ | $2.67 \cdot 10^{11}$ | $1.33 \cdot 10^{11}$ | erg cm$^{-3}$ |
| $E_0$ | $4.87 \cdot 10^{12}$ | $1.00 \cdot 10^{11}$ | erg g$^{-1}$ |
| $a$ | 0.5 | 0.3 | – |
| $b$ | 1.5 | 0.1 | – |
| $\alpha$ | 5.0 | 10.0 | – |
| $\beta$ | 5.0 | 5.0 | – |
| $E_{\rm iv}$ | $4.72 \cdot 10^{10}$ | $7.73 \cdot 10^{9}$ | erg g$^{-1}$ |
| $E_{\rm cv}$ | $1.82 \cdot 10^{11}$ | $3.04 \cdot 10^{10}$ | erg g$^{-1}$ |
| $\mu$ | $2.27 \cdot 10^{11}$ | $2.80 \cdot 10^{10}$ | erg cm$^{-3}$ |
| $Y$ | $3.5 \cdot 10^{10}$ | $1.0 \cdot 10^{10}$ | erg g$^{-1}$ |
| $E_{\rm melt}$ | $3.4 \cdot 10^{10}$ | $7.0 \cdot 10^{9}$ | erg g$^{-1}$ |
| $k$ | $4.0 \cdot 10^{29}$ | $5.6 \cdot 10^{38}$ | cm$^{-3}$ |
| $m$ | 9.0 | 9.4 | – |

the first one, we simulated an impact on a single spherical asteroid. In the second, on a bilobed asteroid represented by two spheres positioned next to each other. The two touching spheres have a narrow interface, so that the SPH quantities do not easily propagate between them. In this setup, we are likely to see differences between sinlge/bilobed cases as clearly as possible.

As for the main input parameters (target/impactor sizes, the impact velocity and the impact angle), we took the parameters of our best-fitting SFDs, obtained by Durda et al. (2007) scaling method, see Section 5.2.2 and Fig. 8.

To simulate a collision between the parent body and the impactor, we performed a limited set of simulations: (i) a single spherical basalt target with diameter $D_{\rm PB} = 260$ km versus a basalt impactor with diameter $D_{\rm imp} = 48$ km; (ii) the single basalt target $D_{\rm PB} = 260$ km versus an ice impactor (a mixture of ice and 30 per cent of silicates) with $D_{\rm imp} = 64$ km (impactor diameter was scaled to get the same kinetic energy); (iii) a bilobed basalt target approximated by two spheres with diameters $D_{\rm PB} = 200$ km each (the total mass is approximately the same) versus a basalt impactor with $D_{\rm imp} = 48$ km; (iv) a single spherical ice target $D_{\rm PB} = 260$ km versus an ice impactor $D_{\rm imp} = 38$ km (impactor diameter was scaled to get the same ratio of the specific kinetic energy $Q$ to the target strength $Q^*_{\rm D}$).

The integration was controlled by the Courant number $C = 1.0$, a typical timestep thus was $\Delta t \simeq 10^{-5}$ s, and the timespan was $t_{\rm stop} = 100$ s. The Courant condition was the same in different materials, using always the maximum sound speed $c_{\rm s}$ among all SPH particles, as usually.

We used $N_{\rm SPH,st} = 10^5$ SPH particles for the single spherical target and $N_{\rm SPH,\,bt} = 2 \cdot 10^5$ for the bilobed one. For impactor $N_{\rm SPH,\,i} = 10^3$ SPH particles. We assumed the Tillotson equation of state (Tillotson 1962) and material properties, which are listed in Table 3.

We terminated SPH simulations after 100 s from the impact. This time interval is needed to establish a velocity field of fragments and to complete the fragmentation. Then we handed the output of the SPH simulation as initial conditions to the $N$-body gravitational code Pkdgrav (Richardson et al. 2000), a parallel tree code used to simulate a gravitational re-accumulation of fragments. Unlike Durda et al. (2007), who calculated radii of fragments $R$ from the smoothing length $h$ as $R = h/3$, we calculated fragments radii from their masses $m$ and densities $\rho$ as $R = (m/(4\pi\rho))^{1/3}$.

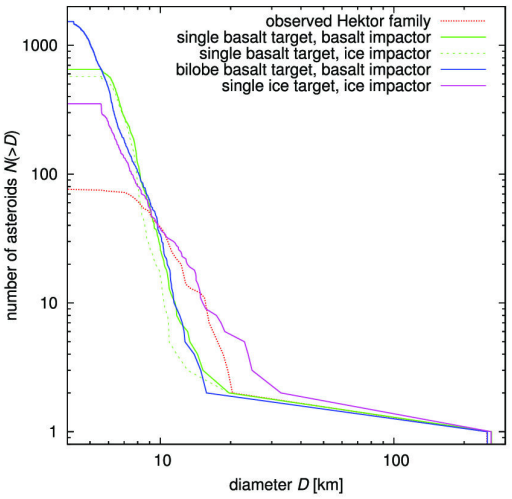


**Figure 11.** A comparison of size–frequency distributions of the observed Hektor family (red dotted) and SFDs of synthetic families created by different SPH simulations, always assuming the impactor velocity $v_{\rm imp} = 4$ km s$^{-1}$ and the impact angle $\varphi_{\rm imp} = 60°$. For a single spherical target (green lines), we assumed the diameter $D_{\rm PB} = 260$ km; for a bilobe target (blue line), we approximated the lobes as spheres with diameters $D_{\rm PB} = 200$ km each. The impactor size was assumed to be $D_{\rm imp} = 48$ km in the case of basalt, $D_{\rm imp} = 64$ km in the case of silicate ice impacting on basalt target (scaled to the same $E_{\rm imp}$) and $D_{\rm imp} = 38$ km in the case of silicate ice impacting on ice target (scaled to the same $Q/Q^*_{\rm D}$). Fragments of the impactor were purposely removed from this plot, as they do not remain in the libration zone for our particular impact orbital geometry.

We ran Pkdgrav with the timestep $\Delta t = 5.0$ s and we terminated this simulation after $t_{\rm evol} = 3$ d of evolution. To ensure this is sufficiently long, we also ran several simulations with $t_{\rm evol} = 5$ d, but we had seen no significant differences between final results.

We used the nominal value for the tree opening angle, $\mathrm{d}\theta = 0.5$ rad, even though for the evolution of eventual moons, it would be worth to use even smaller value, e.g. $\mathrm{d}\theta = 0.2$ rad.

### 7.2 Resulting SFDs

From the output of our simulations, we constructed SFDs of synthetic families, which we compare to the observed one, as demonstrated in Fig. 11. As one can see, there are only minor differences between SFDs of families created by the impacts on the single and bilobed target, except the number of fragments with diameter $D < 5$ km, but this is mostly due to different numbers of SPH particles. However, there are differences between ice and basalt targets. Basalt targets provide generally steeper SFDs with smaller largest remnants than the ice target.

To make the comparison of these synthetic initial SFDs to each other more realistic, we removed the fragments of the impactor from our synthetic families. This is because fragments of the impactor often do not remain in the libration zone. Note that this procedure does not substitute for a full simulation of further evolution; it serves just for a quick comparison of the SFDs.

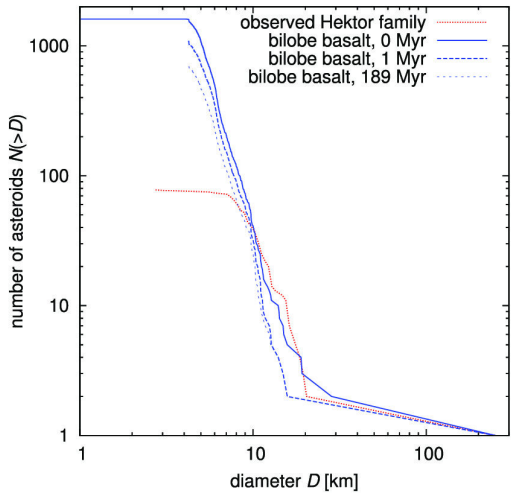


**Figure 12.** A simulation of evolution of the SFD of a synthetic Hektor family due to a ballistic transport and chaotic diffusion. One can see here a rapid change of SFD within the first 1 Myr after the breakup as the fragments of the impactor leaved the libration zone in our impact geometry. This ballistic transport resulted in a reduction of the number of particularly larger bodies in our case. Further evolution due to the chaotic diffusion seems to cause the reduction of mostly smaller bodies. Note that the initial SFD (0 Myr) contains some fragments of the impactor, so the blue solid curve looks different than the curve in Fig. 11, where the fragments of the impactor were removed.

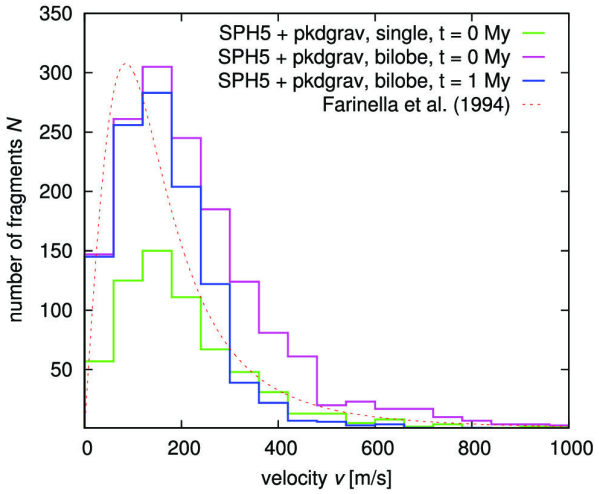


**Figure 13.** Velocity distributions of fragments originated in various SPH simulations (green, violet) in comparison with the model of Farinella et al. (1994) we used in our *N*-body simulations of isotropic disruption and dynamical evolution (see Section 5.2.1). Shown here is also the distribution of velocities after 1 Myr of evolution, i.e. of fragments that remained in libration zones.

To match the observed SFD of the Hektor family more accurately, we should perform a much larger set of simulations with different sizes of projectiles and also different compositions (mixtures of ice and basalt). However, material parameters of these mixtures are generally not known. Regarding the material constants of pure ice, we have them for the impact velocity $v_{\rm imp} = 3\,{\rm km\,s^{-1}}$ only (Benz & Asphaug 1999). There are also some differences between SFDs of single and bilobe targets, so we should perform these simulations for each target geometry. However, we postpone these detailed simulations for future work; in this work, we further analyse results of simulations with basalt targets and we focus on the evolution of the SFDs.

It should be emphasized that the SFDs presented here correspond to very young synthetic families, hence they are not affected by any dynamical and collisional evolution yet. To reveal possible trends of the evolution by a ballistic transport and chaotic diffusion, we prepared initial conditions for the SWIFT integrator, similarly as described in Section 5.2.1, let the simulation run and monitored the corresponding evolution of the SFD. The results can be seen in Fig. 12. The biggest difference between $t = 0$ and 1 Myr is caused by a ballistic transport outside the libration zone – fragments (especially of the impactor) missing from the SFD at $t = 1$ Myr were perturbed too much to remain in the libration zone, at least for a given impact geometry. We actually tested two impact geometries: in the direction tangential and perpendicular to the orbit.

This may be important for the method we used in Section 5.2.2 to derive a preliminary parent body size and other properties of the family. The SFDs obtained by Durda et al. (2007) were directly compared in their work to the main-belt families, however, there is a part of fragments among Trojans (in our case even the largest ones, see Fig. 12), which cannot be seen in the space of resonant elements, because they do not belong to Trojans any more. Fortunately, values of pseudo-$\chi^2$ we computed in Section 5.2.2 depend rather weakly on the distribution of a few largest bodies. Even so, we plan to analyse SFDs of synthetic families more carefully in future works.

### 7.3 Resulting velocity fields

In our *N*-body simulations, we used the model of isotropic disruption (Farinella et al. 1994). As we compared the synthetic family with the observed one (see Section 5.2.1), we simulated only the evolution of bodies with relatively low-ejection velocities ($v < 200\,{\rm m\,s^{-1}}$), because the observed family is confined by the cut-off velocity $v_{\rm cutoff} = 110\,{\rm m\,s^{-1}}$. Very small fragments with higher velocities may be still hidden in the background.

Here, we compare Farinella's model to the velocity fields of fragments from SPH simulations, see Fig. 13. We realized that Farinella's model is not offset substantially with respect to other velocity histograms, especially at lower velocities, $v < 200\,{\rm m\,s^{-1}}$. On the other side, there remained some fragments of the impactor with velocities $v > 2\,{\rm km\,s^{-1}}$ in our SPH simulations, which are not produced in the isotropic model. It does not affect a comparison of the synthetic and observed families in the space of proper elements, as these high-velocity fragments leaved the Trojan region in our case, but it does affect the SFD of the synthetic family. As a consequence, one should always analyse SFDs and velocity fields together.

We also simulated a further evolution of the velocity field. After just 1 Myr of evolution, there remained no bodies with $v > 1.5\,{\rm km\,s^{-1}}$ in our impact geometries, and as one can see in Fig. 13, there was a rapid decrease in the number of fragments with initial $v > 300\,{\rm m\,s^{-1}}$. The resulting histogram is again similar to that of the simple isotropic model.

### 7.4 Synthetic moons

In our simulation of the impact of basalt projectile on the bilobe-shape basalt target, we spotted two low-velocity fragments with original velocities 130 and $125\,{\rm m\,s^{-1}}$, which were consequently

**Table 4.** A comparison of the sizes and the orbital parameters (i.e. semi-major axis $a$, eccentricity $e$ and period $P$) of the observed moon of (624) Hektor as listed in Marchis et al. (2014), with the parameters of synthetic moons SPH I and SPH II captured in our SPH simulation of impact on the bilobed target.

| Desig. | Diam. (km) | $a$ (km) | $e$ | $P$ (d) |
|---|---|---|---|---|
| Observed | $12 \pm 3$ | $623.5 \pm 10$ | $0.31 \pm 0.03$ | $2.9651 \pm 0.0003$ |
| SPH I | 2.2 | 715 | 0.82 | 1.2 |
| SPH II | 2.7 | 370 | 0.64 | 0.4 |

captured as moons of the largest remnant. Their sizes and orbital parameters are listed in Table 4.

These satellites were captured on orbits with high eccentricities ($e = 0.82$ and 0.64, respectively), which are much higher than the eccentricity of the observed moon determined by Marchis et al. (2014) ($e = 0.31 \pm 0.03$). However, this could be partly caused by the fact, that we handed the output of (gravity-free) SPH simulations to the gravitational $N$-body code after first 100 s. Hence, fragments leaving the parent body could move freely without slowing down by gravity. More importantly, we do not account for any long-term dynamical evolution of the moons (e.g. by tides or binary YORP).

When compared to the observed satellite, the diameters of the synthetic moons are several times smaller. This is not too surprising, given that the results for satellite formation are at the small end of what can be estimated with our techniques (median smoothing length $h = 2.3$ km; satellite radius $r \simeq 1.2$ km). The size of captured fragments could also be dependent on impact conditions as different impact angles, impactor velocities and sizes (as is the case for scenarios of Moon formation) which we will analyse in detail in the future and study with more focused simulations.

## 8 CONCLUSIONS

In this paper, we updated the list of Trojans and their proper elements, what allowed us to update parameters of Trojan families and to discover a new one (namely 2001 $UV_{209}$ in $L_5$ population). We focused on the Hektor family, which seems the most interesting due to the bilobed shape of the largest remnant with a small moon and also its D-type taxonomical classification, which is unique among the collisional families observed so far.

At the current stage of knowledge, it seems to us there are no major inconsistencies among the observed number of Trojan families and their dynamical and collisional evolution, at least in the current environment.

As usual, we 'desperately' need new observational data, namely in the size range from 5 to 10 km, which would enable us to constrain the ages of asteroid families on the basis of collisional modelling and to decide between two proposed ages of Hektor family, 1–4 Gyr or 0.1–2.5 Gyr.

As expected, there are qualitative differences in impacts on single and bilobed targets. In our setup, the shockwave does not propagate easily into the secondary, so that only one half the mass is totally damaged as one can see in Fig. 14. On the other hand, the resulting SFDs are not that different, as we would expect.

Even so, there is a large parameter space, which is still not investigated (i.e. the impact geometry with respect to the secondary, secondary impacts, the position in the orbit). SPH simulations of impacts on bilobed or binary targets thus seem very worthy for future research.

Our work is also a strong motivation for research of disruptions of weak bodies (e.g. comets), better understanding the cometary disruption scaling law and also for experimental determination of material constants, which appear in the respective equation of state.

As a curiosity, we can also think of searching for the remaining projectile, which could be still present among Trojans on a trajectory substantially different from that of family. A substantial part of projectile momentum is preserved in our simulations, so we may turn the logic and we may assume the projectile most likely came from the Trojan region and then it should remain in this region too.

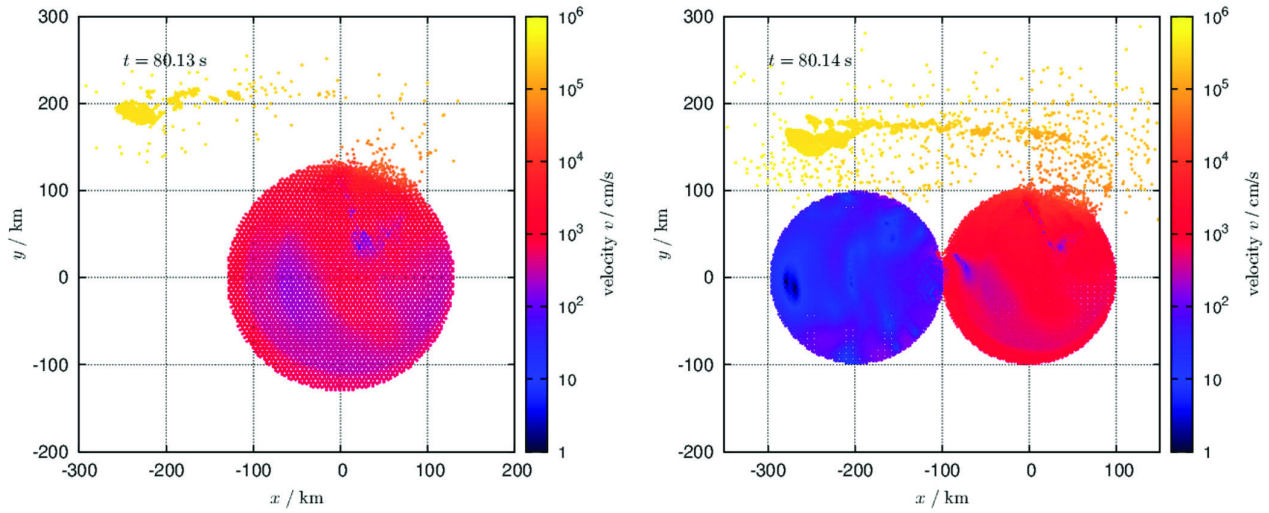


**Figure 14.** A comparison of SPH simulations of a disruption of a single body (basalt) with diameter $D_{target} = 250$ km, by an impactor with the diameter $D_{imp} = 48$ km (silicate ice) (left) and a disruption of a bilobe basalt target, with $D_{target} = 198$ km for each sphere, by an impactor with $D_{imp} = 46$ km (silicate ice) (right). Time elapsed is $t = 80.1$ s in both cases. There are notable physical differences between the two simulations, especially in the propagation of the shock wave, which is reflected from free surfaces, the number of secondary impacts, or the fragmentation (damage) of the target. Nevertheless, the amount of ejected material and the resulting size–frequency distributions do not differ that much (cf. Fig. 11).

## ACKNOWLEDGEMENTS

We thank Alessandro Morbidelli for his review which helped to improve the final version of the paper.

The work of MB was supported by the grant no. P209/13/01308S and that of JR by P209/15/04816S of the Czech Science Foundation (GA CR). We acknowledge the usage of computers of the Stefanik Observatory, Prague.

## REFERENCES

Benz W., Asphaug E., 1999, Icarus, 142, 5
Bowell E., Virtanen J., Muinonen K., Boattini A., 2002, in Bottke W. F., Jr, Cellino A., Paolicchi P., Binzel R. P., eds, Asteroids III. Univ. Arizona Press, Tucson, p. 27
Brož M., Morbidelli A., 2013, Icarus, 223, 844
Brož M., Rozehnal J., 2011, MNRAS, 414, 565
Brož M. et al., 2013, AAP, 551, A117
Carruba V., Nesvorný D., 2016, MNRAS, 457, 1332
Chrenko O., Brož M., Nesvorný D., Tsiganis K., Skoulidou D. K., 2015, MNRAS, 451, 2399
Cruikshank D. P., Dalle Ore C. M., Roush T. L., Geballe T. R., Owen T. C., de Bergh C., Cash M. D., Hartmann W. K., 2001, Icarus, 153, 348
Dell'Oro A., Marzari F., Paolicchi P., Dotto E., Vanzani V., 1998, A&A, 339, 272
Dohnanyi J. S., 1969, J. Geophys Res., 74, 2531
Durda D. D., Bottke W. F., Nesvorný D., Enke B. L., Merline W. J., Asphaug E., Richardson D. C., 2007, Icarus, 186, 498
Emery J. P., Cruikshank D. P., Van Cleve J., 2006, Icarus, 182, 496
Emery J. P., Burr D. M., Cruikshank D. P., 2011, AJ, 114, 25
Farinella P., Froeschlé C., Gonczi R., 1994, in Milani A., Di Martino M., Cellino A., eds., Asteroids, Comets, Meteors 1993. Kluwer Academic Publishers, Dordrecht, p. 205
Goldreich P., Lithwick Y., Sari R., 2004, ApJ, 614, 497
Grav T. et al., 2011, ApJ, 742, 40
Grav T., Mainzer A. K., Bauer J., Masiero J. R., Nugent C. R., 2012, ApJ, 759, 49
Ivezić Z., Jurić M., Lupton R. H., Tabachnik S., Quinn T., 2002, in Tyson J. A., Wolff S., eds, Proc. SPIE Conf. Ser. Vol. 4836, Survey and Other Telescope Technologies and Discoveries. Kluwer, Dordrecht, p. 98
Laskar J., Robutel P., 2001, Celest. Mech. Dyn. Astron., 80, 39
Levison H. F., Duncan M., 1994, Icarus, 108, 18
Levison H. F., Bottke W. F., Gounelle M., Morbidelli A., Nesvorný D., Tsiganis K., 2009, Nature, 460, 364
Lyra W., Johansen A., Klahr H., Piskunov N., 2009, A&A, 493, 1125
Mainzer A. et al., 2011, ApJ, 741, 90
Marchis F. et al., 2014, ApJ, 783, L37
Morbidelli A., Levison H. F., Tsiganis K., Gomes R., 2005, Nature, 435, 462
Morbidelli A., Bottke W. F., Nesvorný D., Levison H. F., 2009, Icarus, 204, 558
Morbidelli A., Brasser R., Gomes R., Levison H. F., Tsiganis K., 2010, AJ, 140, 1391
Nesvorný D., Vokrouhlický D., Morbidelli A., 2013, ApJ, 768, 45
Nesvorný D., Brož M., Carruba V., 2015, in Michel P., DeMeo F. E., Bottke W. F., eds, Asteroids IV. Arizona Univ. Press, Tucson, p. 297
Richardson D. C., Quinn T., Stadel J., Lake G., 2000, Icarus, 143, 45
Tillotson E, 1962, Nature, 195, 763
Usui F. et al., 2011, PASJ, 63, 1117
Vinogradova T. A., 2015, MNRAS, 454, 2436
Zappalà V., Cellino A., Farinella P., Milani A., 1994, AJ, 107, 772

This paper has been typeset from a TEX/LATEX file prepared by the author.

# Appendix B

# Reprint of Brož and Rozehnal (2011)

Monthly Notices
of the
ROYAL ASTRONOMICAL SOCIETY

Mon. Not. R. Astron. Soc. **414,** 565–574 (2011) doi:10.1111/j.1365-2966.2011.18420.x

# Eurybates – the only asteroid family among Trojans?

M. Brož[1]★ and J. Rozehnal[1,2]

[1]*Institute of Astronomy, Charles University, Prague, V Holešovičkách 2, 18000 Prague 8, Czech Republic*
[2]*Štefánik Observatory, Petřín 205, 11800 Prague, Czech Republic*

Accepted 2011 January 24. Received 2011 January 24; in original form 2010 November 11

**ABSTRACT**

We study the orbital and physical properties of Trojan asteroids of Jupiter. We try to discern all the families previously discussed in the literature, but we conclude that there is only one significant family among the Trojans, namely the cluster around the asteroid (3548) Eurybates. This is the only cluster that has all of the following characteristics: (i) it is clearly concentrated in the proper-element space; (ii) the size–frequency distribution is different from that of background asteroids; (iii) we have a reasonable collisional/dynamical model of the family. Henceforth, we can consider it as a real collisional family.

We also report the discovery of a possible family around the asteroid (4709) Ennomos, composed mostly of small asteroids. The asteroid (4709) Ennomos is known to have a very high albedo $p_V \simeq 0.15$, which may be related to the hypothetical cratering event that exposed ice. The relation between the collisional family and the exposed surface of the parent body offers a unique means to study the physics of cratering events. However, more data are needed to confirm the existence of this family and its relationship with Ennomos.

**Key words:** methods: numerical – celestial mechanics – minor planets, asteroids: general.

## 1 INTRODUCTION

Trojans of Jupiter, which reside in the neighbourhood of $L_4$ and $L_5$ Lagrangian points, serve as an important test of the planetary migration theory (Morbidelli et al. 2005). Their inclination distribution, namely the large spread of $I$, can be explained as a result of chaotic capture during a brief period when Jupiter and Saturn encountered a 1:2 mean-motion resonance. Moreover, the Late Heavy Bombardment provides the timing of this resonant encounter $\simeq 3.8$ Gyr ago (Gomes et al. 2005). It is thus important to understand the population of Trojans accurately.

There are several unresolved problems regarding Trojans, however; for example the number of families, which is a stringent constraint for collisional models. Roig, Ribeiro & Gil-Hutton (2008) studied as many as 10 suggested families, using relatively sparse SLOAN data and spectra. They noted that most families seem to be heterogeneous from the spectroscopic point of view, with one exception – the C-type Eurybates family. As we argue in this paper, the number of families (with parent-body size $D \gtrsim 100$ km) is indeed as low as one.

Another strange fact is the ratio of $L_4$ and $L_5$ Trojans. Szabó et al. (2007) used SLOAN colour data to reach fainter than orbital catalogues and estimated the ratio to $N(L_4)/N(L_5) = 1.6 \pm 0.1$. There is no clear explanation for this, since the chaotic capture as a gravitational interaction should be independent of the size or $L_4/L_5$ membership. Any hypothesis involving collisions would require a relatively recent disruption of a huge parent body, which is highly unlikely (O'Brien & Morbidelli 2008, D. O'Brien, private communication). This is again related to the actual observed number of Trojan families.

Brož & Vokrouhlický (2008) studied another resonant population, the so-called Hilda group in the 3/2 mean-motion resonance with Jupiter, and reported only two families: Hilda and Schubart, with approximately 200- and 100-km parent bodies. This number might be in accord with low collisional probabilities, assuming that the Hilda family is very old and experienced the Late Heavy Bombardment (Brož et al. 2011).

Levison et al. (2009) compared the observed distribution of D-type asteroids and the model of their delivery from transneptunian region. They found a good match assuming that the D-types (presumably of cometary origin) are easy-to-disrupt objects (with the strength more than five times lower than that of solid ice). Note that Trojan asteroids are a mixture of C- and D-type objects and we have to discriminate between them with respect to collisional behaviour.

All of the works mentioned above are a good motivation for us to focus on asteroid families in the Trojan population. The paper is organized as follows. First, we describe our data sources and methods in Section 2. A detailed study of orbital and physical properties of families (and other 'false' groupings) is presented in Section 3. Section 4 is devoted to the modelling of long-term dynamical evolution. Finally, there are concluding remarks in Section 5.

★E-mail: mira@sirrah.troja.mff.cuni.cz

## 2 METHODS

### 2.1 Resonant elements

We use the symplectic SWIFT integrator (Levison & Duncan 1994) for orbital calculations. Our modifications include a second-order scheme of Laskar & Robutel (2001) and online digital filters, which enable us to compute suitable resonant proper elements: libration amplitude $d$ of the $a - a'$ oscillations, where $a$ is the osculating semimajor axis of an asteroid and $a'$ is that of Jupiter, eccentricity $e$ and inclination $\sin I$. (In figures, we usually plot a mean value $\bar{a}$ of semimajor axis plus the libration amplitude $d$.) We employ their definition from Milani (1993). The source of initial osculating elements is the AstOrb catalogue, version JD = 245 5500.5 (2010 October 31).

There are actually two independent filters running in parallel: in the first one, we sample osculating elements every 1 yr, compute the mean elements using the filter sequence B, B with decimation factors 3, 3 (refer to Quinn, Tremaine & Duncan 1991) and store this data in a buffer spanning 1 kyr. We then estimate the libration frequency $f$ by a linear fit of $\phi(t) = \lambda - \lambda' - \chi$, where $\lambda$, $\lambda'$ are the mean longitudes of an asteroid and Jupiter and $\chi = \pm 60°$ for $L_4$ or $L_5$, respectively. The revolution of angle $\phi(t)$ must not be confined to the interval $[0, 360°)$, of course. The amplitude of $d$ is computed for the already known $f$ by a discrete Fourier transform. Finally, an offline running-average filter with a window of 1 Myr is used to smooth the data.[1]

In the second filter, we compute proper eccentricity $e$ and proper inclination $\sin I$ by sampling osculating elements (1-yr step), computing the mean elements using a filter sequence A, A, B and the decimation factors 10, 10, 3, and then we apply a frequency modified Fourier transform (Šidlichovský & Nesvorný 1996), which gives us the relevant proper amplitudes.

The values of the resonant elements agree very well with those listed in the AstDyS catalogue by Knežević & Milani (2003; see Fig. 1). There are only few outliers, probably due to a different time-span of integration. We computed the proper elements for 2647 $L_4$ and 1496 $L_5$ Trojan asteroids.[2] This sample is roughly twice larger than the one previously analysed. The ratio of populations valid for $H \lesssim 15$ mag asteroids is thus $N(L_4)/N(L_5) \simeq 1.8$.

The overall distribution of Trojans in the $(d, e, \sin I)$ space is shown in Fig. 2. Note that there is only one cluster visible immediately in the bottom-left panel – around (3548) Eurybates. The reason is its tight confinement in inclinations ($\sin I = 0.125$–$0.135$).

### 2.2 Hierarchical clustering

In order to detect clusters in the resonant element space we use a hierarchical clustering method (Zappalá et al. 1994) with a standard metric $d_1$, with $\delta a$ substituted by $d$. We run the HCM code many times with various starting bodies and different cut-off velocities $v_{\text{cut-off}}$ and determine the number of bodies $N$ in the given cluster. We find the $N(v_{\text{cut-off}})$ dependence to be a very useful diagnostic tool. We can see these dependences for $L_4$ and $L_5$ Trojans in Fig. 3.

[1] Equivalently, we may compute the amplitude $D$ of mean longitudes $\lambda - \lambda'$. Anyway, there is a linear relation between $d$ and $D$.

[2] The data are available in an electronic form on our web site http://sirrah.troja.mff.cuni.cz/~mira/mp/. We use also one-apparition orbits for the purposes of physical studies. Of course, orbital studies require more precise multi-apparition data.

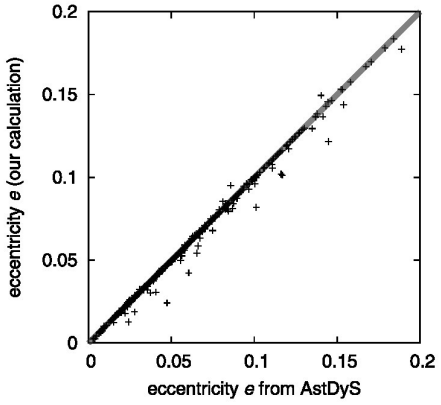


**Figure 1.** Comparison of the resonant eccentricity calculated by our code with that of Knežević & Milani (AstDyS catalogue). There is a line $x = y$ to aid a comparison.

It is easy to recognize if a cluster has a concentration towards the centre – even at a low $v_{\text{cut-off}}$ it must have more than one member ($N \gg 1$). It is also instructive to compare clusters with a random background (thin lines), which we generated artificially by a random-number generator in the same volume of the $(d, e, I)$ space. Insignificant (random) clusters usually exhibit an abrupt increase in $N$ at a high cut-off velocity.

As starting bodies we selected those listed in Roig et al. (2008). Only three clusters, namely the Eurybates, Aneas and 1988 $RG_{10}$, seem to be somewhat concentrated i.e. denser than the background. The Hektor cluster is also concentrated but it contains only a relatively small number of members (20–70) before it merges with the background. In other words, smaller asteroids do not seem to be concentrated around (624) Hektor. The remaining clusters are more or less comparable to the background.

Nevertheless, we report the detection of a previously unknown cluster around (4709) Ennomos in $L_5$. It is relatively compact, since the minimum cut-off velocity is only 70 m s$^{-1}$. The cluster contains mostly small bodies which were discovered only recently.

Finally, let us point out a very tight cluster around (9799) 1996 RJ, associated already at $v_{\text{cut-off}} = 20$ m s$^{-1}$. It is located at high inclinations and contains nine bodies, three of them having short arcs. The cluster seems to be peculiar in the osculating element space too since it exhibits a non-random distribution of nodes and perihelia (see Table 1). This is similar to very young families such as the Datura (Nesvorný, Vokrouhlický & Bottke 2006), and it makes the 1996 RJ cluster a particularly interesting case with respect to collisional dynamics. Because one has to use slightly different methods for studies of such young families, we postpone its detailed analysis to the next paper.

Let us compare Trojan clusters to the well-known asteroid families in the outer Main Belt (Fig. 4). Most families (e.g. Themis, Koronis, Eos) exhibit a steady increase of $N$ until they merge with another family or the entire outer Main Belt. Eurybates, Aneas and 1988 $RG_{10}$ are the only Trojan clusters which behave in a similar fashion. The Veritas family (dynamically young, Nesvorný et al. 2003) exhibits a different behaviour – for a large interval of $v_{\text{cut-off}}$ the number of members $N$ remains almost the same, which indicates a clear separation from the background population. With respect to the $N(v_{\text{cut-off}})$ dependence, the Ennomos cluster is similar to Veritas.

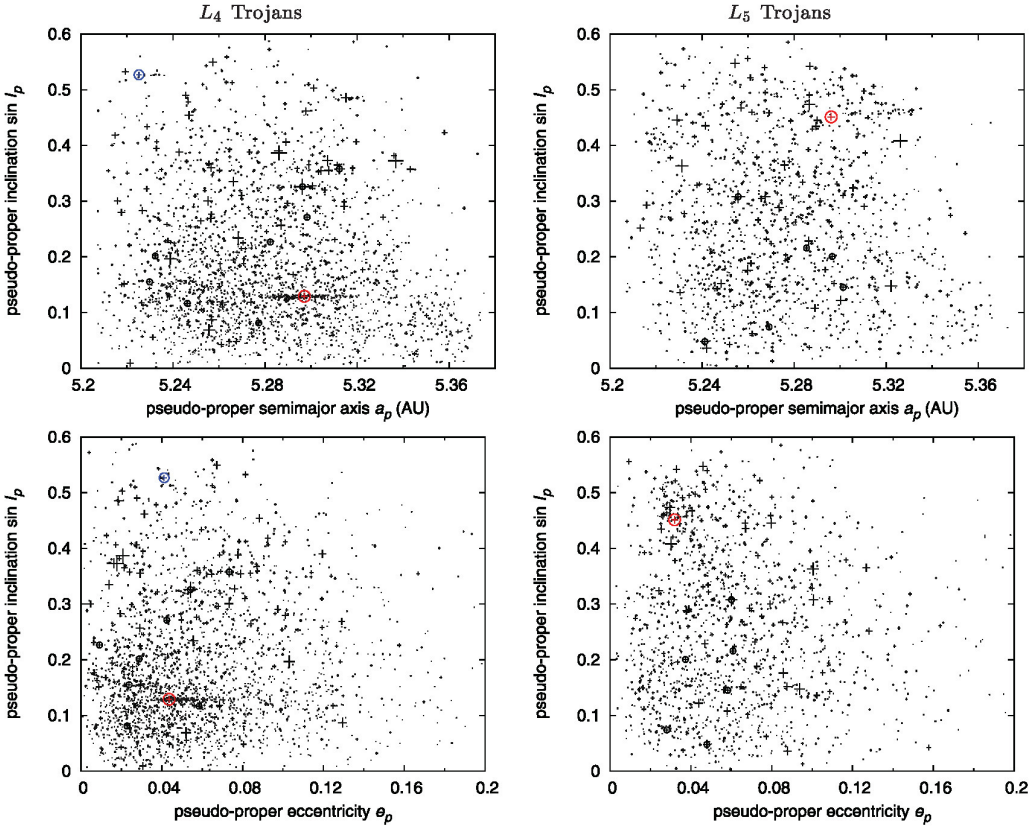


**Figure 2.** The resonant elements ($a \equiv \bar{a} + d$, sin $I$) and ($e$, sin $I$) for $L_4$ and $L_5$ Trojans. The crosses indicate relative sizes of bodies, taken either from the AstOrb catalogue or computed from absolute magnitude $H$ and geometric albedo $p_V$. In this plot, we assumed $p_V = 0.058$ for $L_4$ Trojans and 0.045 for those in $L_5$ (it corresponds to medians of known $p_V$s). The asteroids (3548) Eurybates in $L_4$ and (4709) Ennomos in $L_5$, around which significant clusters are visible, are shown in red. Moreover, the asteroid (9799) 1996 RJ in $L_4$, which is surrounded by a small cluster, is denoted by a blue circle. [This cluster is so tight that its members are located inside the circle on the ($e$, sin $I$) plot.]

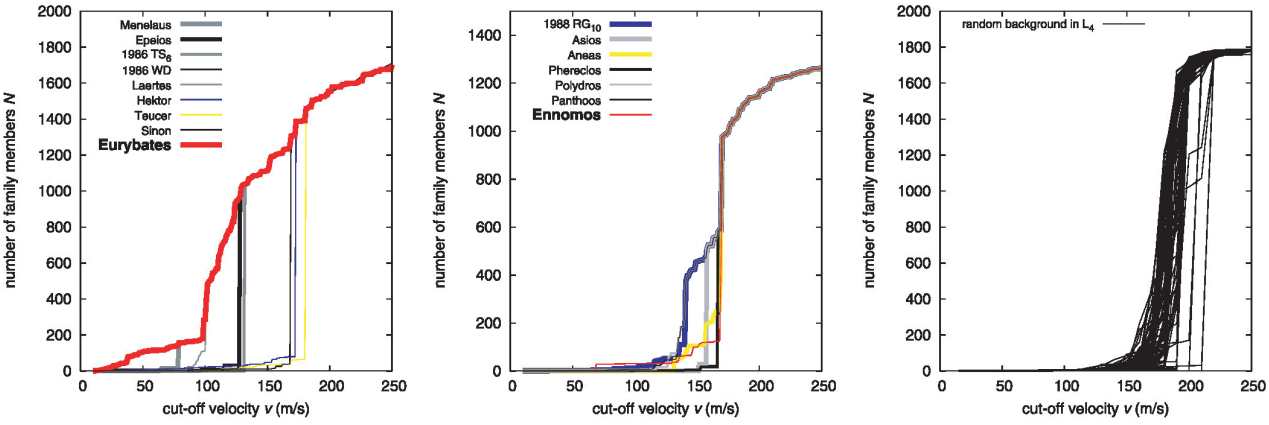


**Figure 3.** Left-hand panel: the dependence of the number of family members $N$ on the cut-off velocity $v_{\rm cut\text{-}off}$ computed by the hierarchical clustering method. Only clusters among $L_4$ Trojans are included in this plot. Middle panel: the same $N(v_{\rm cut\text{-}off})$ dependence for $L_5$ Trojans. Right-hand panel: artificial clusters selected from *random* distribution of asteroids generated in the same volume of the ($d$, $e$, sin $I$) space.

### 2.3 Size–frequency distribution

At first, let us assume a single value of albedo for all the family members. This is a reasonable assumption provided the family is of collisional origin. We can then calculate sizes from absolute magnitudes and construct size–frequency distributions (SFDs). Fig. 5 shows a comparison of SFDs for the clusters detected by the HCM[3] and for the whole population of $L_4$ and $L_5$ Trojans.

[3] Of course, we have to select a 'suitable' value of the cut-off velocity for all clusters. Usually, we select that value for which $N(v_{\rm cut-off})$ is flat. Size–frequency distribution is not very sensitive to this selection anyway.

**Table 1.** List of nine members of the (9799) 1996 RJ cluster and their proper ($a$, $e$, $\sin I$) and osculating ($\Omega_{\rm osc}$, $\varpi_{\rm osc}$) elements and absolute magnitude $H$. Note that the distribution of nodes and perihelia is not entirely uniform. Asteroids with short-arc orbits (<60 d) are denoted by the * symbol.

| Number | Designation | | $a$ | $e$ | $\sin I$ | $\Omega_{\rm osc}$ | $\varpi_{\rm osc}$ | $H$/mag |
|---|---|---|---|---|---|---|---|---|
| 9799 | 1996 RJ | | 5.2252 | 0.0412 | 0.5269 | 115.4 | 259.6 | 9.9 |
| 89938 | 2002 $FR_4$ | | 5.2324 | 0.0394 | 0.5274 | 70.0 | 23.1 | 12.5 |
| 226027 | 2002 $EK_{127}$ | | 5.2316 | 0.0399 | 0.5263 | 62.8 | 352.9 | 12.6 |
| 243316 | 2008 $RL_{32}$ | | 5.2340 | 0.0398 | 0.5268 | 27.3 | 358.2 | 12.8 |
| | 2005 $MG_{24}$ | | 5.2275 | 0.0404 | 0.5252 | 172.3 | 236.5 | 13.1 |
| | 2008 $OW_{22}$ | * | 5.2276 | 0.0401 | 0.5274 | 53.7 | 340.9 | 13.9 |
| | 2009 $RA_{17}$ | * | 5.2258 | 0.0409 | 0.5272 | 257.7 | 194.5 | 13.7 |
| | 2009 $RK_{63}$ | * | 5.2305 | 0.0407 | 0.5260 | 56.4 | 5.6 | 12.8 |
| | 2009 $SR_{30}$ | | 5.2362 | 0.0409 | 0.5258 | 103.6 | 22.0 | 13.3 |

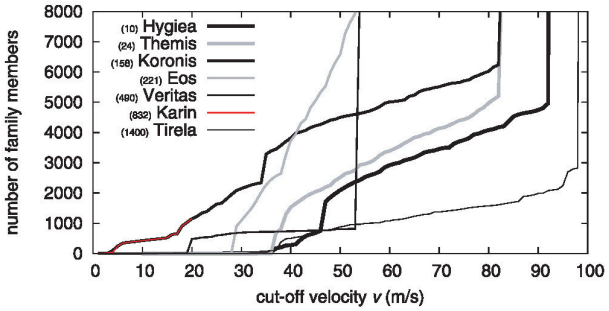


**Figure 4.** The $N(v_{\rm cut\text{-}off})$ dependence for seven outer main-belt families. If we would consider only a subset of asteroids brighter than $H = 15$ mag, which is an approximate observational limit for Trojans, the $N(v_{\rm cut\text{-}off})$ dependencies would be qualitatively the same, only slightly shifted to larger cut-off velocities.

A slope $\gamma$ of the cumulative distribution $N(>D) \propto D^{\gamma}$ is an indicative parameter. For $L_4$ and $L_5$ Trojans, it equals $-2.0 \pm 0.1$ and $-1.9 \pm 0.1$ in the intermediate size range of 15–60 km. (These numbers match the findings of the study of Yoshida & Nakamura 2008.) The slope is steeper at large sizes. The uncertainties are mainly due to a freedom in the selection of the size range, and the difference between $L_4$ and $L_5$ SFDs does not seem significant. The clusters have typically similar slope as background (within 0.1 uncertainty), though sometimes the results are inconclusive due to the small number of members. On the other hand, the slope $-2.5 \pm 0.1$ for the Eurybates family is significantly steeper than the mean slope of the whole Trojan population.[4] There are two more groups that exhibit a relatively steep slope, namely Laertes in $L_4$ ($\gamma = -3.1$) and 1988 $RG_{10}$ in $L_5$ ($\gamma = -2.6$).

We should be aware, however, that even the background exhibits a trend with respect to inclinations (see Fig. 6). Slope $\gamma$ typically decreases with inclination $\sin I$, which is especially prominent in case of the $L_4$ cloud. We have to admit that if we compare the Eurybates family to its surroundings only ($\sin I = 0.1$ to 0.15), the difference in slopes is not so prominent. An interesting feature of the $L_5$ cloud is a dip in the interval $\sin I = 0.05$ to 0.1. This corresponds to the approximate location of the 1988 $RG_{10}$ group.

The $\gamma(\sin I)$ dependence among the Trojans is not unique. For example, low-inclination bodies in the J3/2 resonance also have the SFD steeper than background ($\gamma = -2.5 \pm 0.1$ versus $-1.7 \pm 0.1$), without any clear family and a few big interlopers. Maybe, this feature reflects different *source reservoirs* of low- and high-inclination bodies among Trojans and J3/2?[5] It may also be in concert with the colour–inclination dependence reported by Szabó et al. (2007).

We also test albedo distributions dependent on size, since the measurements by Fernández, Jewitt & Ziffer (2009) suggested that small Trojans are significantly brighter and thus smaller. Large asteroids have $p_V = 0.044 \pm 0.008$ while small $p_V = 0.12 \pm 0.06$. This is a significant change of the SFD, which occurs around the size $D \simeq 30$ km. The SFD thus becomes shallower below this size e.g. for Eurybates we would have $\gamma = -1.6$ and for L4 Trojans $\gamma = -1.5$, so the SFDs become comparable with respect to the slope. Though, as we have stated above, for a real collisional family we expect the albedo distribution to be rather homogeneous and independent of size.

### 2.4 Colour and spectral data

We used the Sloan Digital Sky Survey Moving Object catalogue version 4 (SDSS-MOC4) to check that the families are spectrally homogeneous, similar to what we expect. Due to a larger uncertainty in the $u$ colour in SDSS-MOC4, we used the colour indices $a^*$ and $i - z$, where $a^* = 0.89(g - r) + 0.45(r - i) - 0.57$ (defined by Parker et al. 2008).

The result is shown in Fig. 7. It is clearly visible that the distribution of the Eurybates family in the space of ($a^*$, $i - z$) colours is different from the Trojan background. On the contrary, the 1988 $RG_{10}$ group covers essentially the same area as the background. The Aneas is only slightly shifted towards larger $a^*$ and $i - z$ with respect to the background. There is a lack of data for the Ennomos group – three bodies are not sufficient to compare the colour distributions.

Alternatively, we may use principal component analysis of the SDSS colour indices. We use only data with uncertainties smaller than 0.2 mag, which resulted in 70 887 records. We calculated eigenvalues ($\lambda_{1,2,3,4} = 0.173$, 0.0532, 0.0249, 0.0095), corresponding eigenvectors and constructed the following three principal components (Trojanová 2010):

$$\begin{aligned} {\rm PC}_1 &= 0.235\,(u-g) + 0.416\,(g-r) + 0.598\,(g-i) \\ &\quad + 0.643\,(g-z), \end{aligned} \tag{1}$$

[4] Though the number of the Eurybates members (105) is so small that it almost does not affect the mean slope of the whole $L_4$ population.

[5] Both the Trojan and J3/2 regions are dynamically unstable during Jupiter–Saturn 1:2 mean-motion resonance, so we expect that the same bodies entering Trojan region may also enter J3/2.

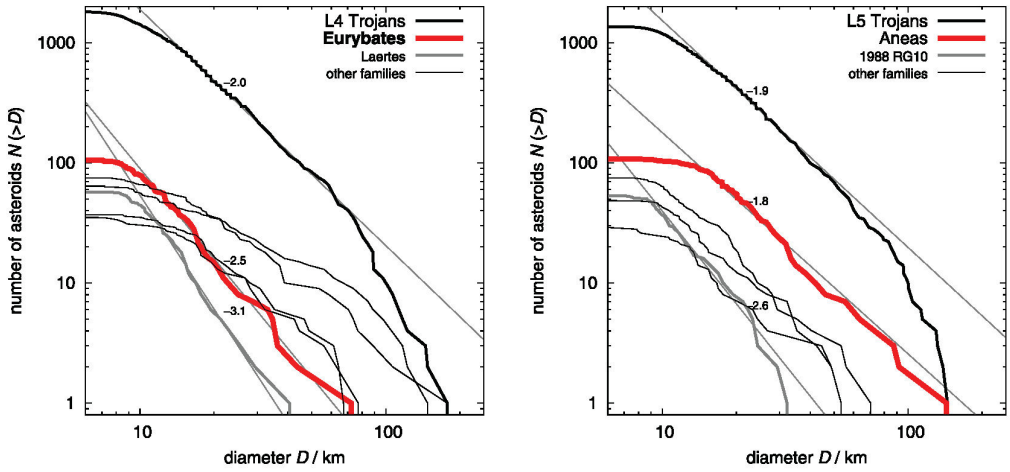


**Figure 5.** Left-hand panel: size–frequency distributions of $L_4$ Trojans and the following clusters (the selected cut-off velocities are given in the parentheses): Eurybates ($v_{\rm cut\text{-}off} = 50\,{\rm m\,s^{-1}}$), Laertes (94), Hektor (160), Teucer (175), Sinon (163), 1986 WD (120). Right-hand panel: SFDs of $L_5$ Trojans and the following clusters: 1988 $RG_{10}$ (at $v_{\rm cut\text{-}off} = 130\,{\rm m\,s^{-1}}$), Aneas (150), Asios (155), Panthoos (130), Polydoros (130).

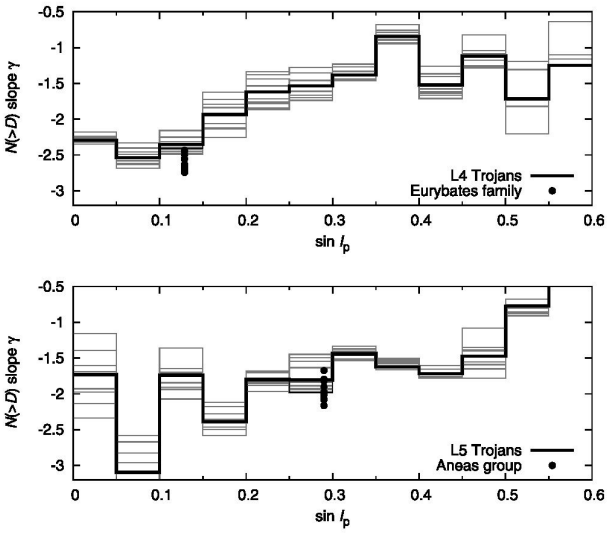


**Figure 6.** Slopes $\gamma$ of the size–frequency distributions $N(>D)$ for $L_4$ and $L_5$ Trojans and their dependence on the inclination $\sin I$. The range of diameters for which the SFDs were fitted is $D_{\rm min} = 12$ km, $D_{\rm max} = 30$ km. Thin lines were calculated for different ranges, which were varied as $D_{\rm min} \in (10, 15)$ km, $D_{\rm max} \in (20, 40)$ km. Their spread indicates the uncertainty of $\gamma$ in a given interval of $\sin I$. The populations are observationally complete down to $D \simeq 10$ km, because the characteristic change of slope due to the incompleteness occurs at smaller sizes (see also Yoshida & Nakamura 2008).

$$\mathrm{PC}_2 = 0.968\,(u-g) - 0.173\,(g-r) - 0.147\,(g-i) - 0.106\,(g-z), \quad (2)$$

$$\mathrm{PC}_3 = 0.078\,(u-g) + 0.601\,(g-r) + 0.330\,(g-i) - 0.724\,(g-z), \quad (3)$$

which have a clear physical interpretation: $\mathrm{PC}_1$ corresponds to an overall slope, $\mathrm{PC}_2$ is a variability in the $u$ band and $\mathrm{PC}_3$ a depth of the 1-μm absorption band. The Eurybates family is different

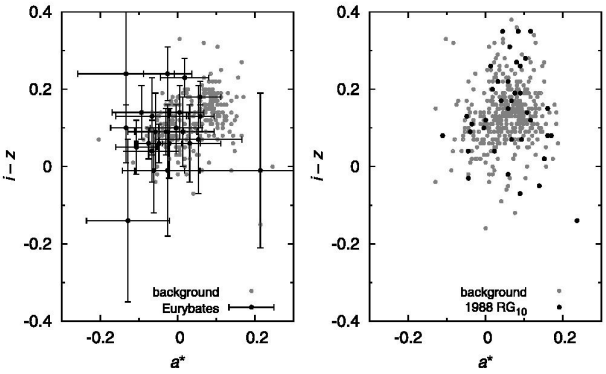


**Figure 7.** Left-hand panel: the $(a^*, i-z)$ colours for the $L_4$ Trojans (grey dots) and the Eurybates family (black dots with error bars). The distributions differ significantly in this case. Right-hand panel: a similar comparison for the $L_5$ Trojans and the 1988 $RG_{10}$ group, which seem to be indistinguishable.

from Trojans in all the three principal components (mean $\mathrm{PC}_1$ of the Eurybates members is smaller, $\mathrm{PC}_2$ and $\mathrm{PC}_3$ larger). The Aneas group has the same distribution of $\mathrm{PC}_2$ and $\mathrm{PC}_3$ as Trojans and the 1988 $RG_{10}$ group is similar to Trojans even in all three components.

Hence, we confirm that the Eurybates family seems distinct in colour even in the fourth version of the SDSS-MOC. This fact is consistent with the work of Roig et al. (2008), who used the third version of the same catalogue and classified Eurybates family members as C-type asteroids.

Finally, note that De Luise et al. (2010) pointed out an absence of ice spectral features at 1.5 and 2.0 μm on several Eurybates members and Yang & Jewitt (2007) concluded the same for (4709) Ennomos. This puzzling fact may indicate that pure ice covers at most 10 per cent of the Ennomos surface.

### 2.5 Impact disruption model

We use a simple model of an isotropic disruption from Farinella, Froeschlé & Gonczi (1994). The distribution of velocities 'at infinity' follows the function

$$\mathrm{d}N(v) = Cv(v^2 + v_{\rm esc}^2)^{-(\alpha+1)/2}, \quad (4)$$

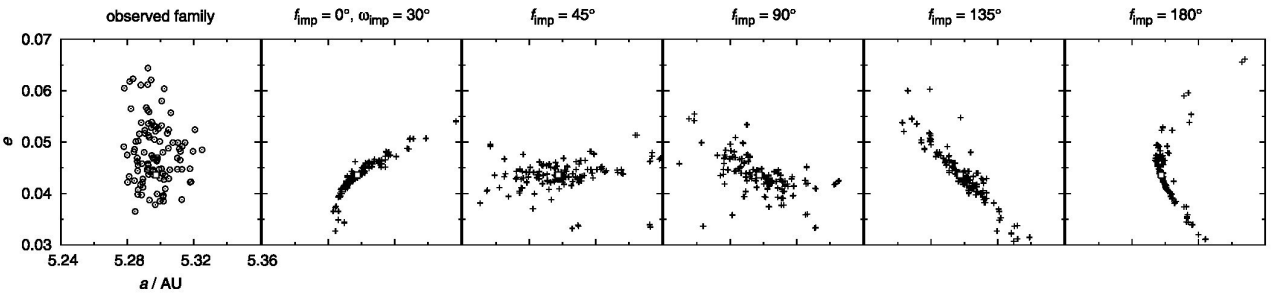


**Figure 8.** A comparison between the observed Eurybates family (open circles) and synthetic families (crosses) just after the impact disruption computed for several values of $f_{imp} = 0°, 45°, 90°, 135°, 180°$ and $\omega_{imp} = 30°$, $R_{PB} = 47$ km, $\rho_{PB} = 1300\,\mathrm{kg\,m^{-3}}$. Different geometry in $f$, $\omega$ produces a slightly different cluster; nevertheless, it is always tighter than the observed family. The position of the asteroid (3548) Eurybates is denoted by a square.

with the exponent $\alpha$ being a free parameter, $C$ a normalization constant and $v_{esc}$ the escape velocity from the parent body, which is determined by its size $R_{PB}$ and mean density $\rho_{PB}$. The distribution is cut at a selected maximum allowed velocity $v_{max}$ to prevent outliers. We typically use $v_{max} = 300\,\mathrm{m\,s^{-1}}$. The orientations of velocity vectors in space are assigned randomly. We assume that the velocity of fragments is independent on their size.[6]

There are several more free parameters, which determine the initial shape of the family in the space of proper elements: initial osculating eccentricity $e_i$ of the parent body, initial inclination $i_i$ as well as true anomaly $f_{imp}$ and argument of perihelion $\omega_{imp}$ at the time of impact disruption.

An example of a synthetic family just after disruption and its comparison to the observed Eurybates family is shown in Fig. 8. Usually, there is a significant disagreement between this simple model of impact disruption and the observations. Synthetic families usually look like thin 'filaments' in the $(d, e, \sin I)$ space, which are curved due to the mapping from osculating elements to resonant ones. On the other hand, the observed groups among Trojans are much more spread. However, this only indicates the importance of the further long-term evolution by chaotic diffusion and possibly by planetary migration.[7]

In case of the Ennomos group members, they are distributed mostly on larger semimajor axes compared to (4709) Ennomos, though isotropic impact disruptions produce fragments distributed evenly on larger and smaller $a$. Is it possibly the indication of an anisotropic velocity field? Or is it a different parent body of this cluster?

### 2.6 Planetary migration

If asteroid families are very old, planetary migration might influence their current shape. In order to study of late stages of planetary migration, which is caused by interactions with a planetesimal disc, we construct the following model. We treat the migration analytically within a modified version of the numerical symplectic SWIFT-RMVS3 integrator (Levison & Duncan 1994), which accounts for gravitational perturbations of the Sun and four giant planets and includes also an energy-dissipation term, as described in Brož et al. (2011). The speed of migration is characterized by the exponential time-scale $\tau_{mig}$ and the required total change of semimajor axis $a_i - a_f$. We use an eccentricity damping formula too, which simulates the effects of dynamical friction and prevents an unrealistic increase in eccentricities (Morbidelli et al. 2010). The amount of damping is determined by the parameter $e_{damp}$.

We try to adjust initial orbital parameters of planets and the parameters of migration in such a way as to end up at the currently observed orbits. The integration time-step is $\Delta t = 36.525$ d and the time-span is usually equal to $3\tau_{mig}$, when planetary orbits almost stop migrating.

### 2.7 Inefficient Yarkovsky/YORP effect

On long time-scales, the Yarkovsky thermal force might cause significant perturbations of orbits. We use an implementation of the Yarkovsky thermal effect in the SWIFT $N$-body integrator (Vokrouhlický et al. 2006). It includes both the diurnal and the seasonal variants.

The YORP effect (thermal torques affecting spin states; Vokrouhlický et al. 2006) was not taken into account in our simulations. The reason is that the respective time-scale $\tau_{YORP}$ is of the order of 100 Myr to 1 Gyr. So, as a 'zero' approximation, we neglect the YORP effect on these 'short' time-scales and keep the orientations of the spin axes fixed.

For Trojan asteroids captured in a zero-order mean-motion resonance, the Yarkovsky perturbation only affects the position of libration centre (Moldovan et al. 2010). Note that the perturbation acts 'instantly' – there is no systematic secular drift in eccentricity nor in other proper elements which is an important difference from first-order resonances, where an $e$-drift is expected (Brož & Vokrouhlický 2008, appendix A). This is another reason that we do not need a detailed YORP model here.

The thermal parameters we use are reasonable estimates for C/X-type bodies: $\rho_{surf} = \rho_{bulk} = 1300\,\mathrm{kg\,m^{-3}}$ for the surface and bulk densities, $K = 0.01\,\mathrm{W\,m^{-1}\,K^{-1}}$ for the surface thermal conductivity, $C = 680\,\mathrm{J\,kg^{-1}}$ for the heat capacity, $A = 0.02$ for the Bond albedo and $\epsilon_{IR} = 0.95$ for the thermal emissivity.

## 3 ASTEROID FAMILIES AND INSIGNIFICANT GROUPS

In this section, we briefly discuss the properties of selected clusters: Eurybates, Ennomos, Aneas and 1988 $RG_{10}$. We focus on these four clusters, since they seem most prominent according to our previous analysis.

[6] If we use a size-dependent relation for velocities similar to Vokrouhlický et al. (2006), our results do not change much, because the overall shape of the velocity distribution is quite similar to the size-independent case.

[7] Only very young clusters like the Karin family (Nesvorný et al. 2002) exhibit this kind of a 'filament' shape.

### 3.1 Eurybates family

The Eurybates family can be detected by the hierarchical clustering method for cut-off velocities $v_{\text{cut-off}} = 38$ to 78 m s$^{-1}$, when it merges with Menelaus (see Fig. 3). Yet, we do not rely just on the HCM! Another selection criterion we use is a 'meaningful' shape of the family and its changes with respect to $v_{\text{cut-off}}$. A very important characteristic of the Eurybates family at low values of $v_{\text{cut-off}}$ is a tight confinement of inclinations ($\sin I$ within 0.01). It breaks down at $v_{\text{cut-off}} \simeq 68$ m s$^{-1}$, so we consider this value as an upper limit. The Eurybates family is also confined in the semimajor axis, being approximately twice smaller than other groups.

The diameter of the parent body is $D_{\text{PB}} \doteq 97$ km for albedo $p_V = 0.055$ if we sum the volumes of the known bodies. Of course, in reality it is slightly larger due to observational incompleteness. If we prolong the slope of the SFD $\gamma = -2.5$ down to zero, we obtain $D_{\text{PB}} \doteq 110$ km. The geometric method of Tanga et al. (1999) gives the upper limit $D_{\text{PB}} \simeq 130$ km.

Spectral slopes of family members are rather homogeneous and correspond to C/P-types (Roig et al. 2008).

### 3.2 Ennomos group

The cluster around (4709) Ennomos can be recognized for a wide interval of cut-off velocities $v_{\text{cut-off}} \in (69, 129)$ m s$^{-1}$ when it stays compact and confined in inclinations ($\sin I = 0.451$ to 0.466). Very probably, there are several interlopers, because we can count four to 10 asteroids in the surroundings i.e. in the same volume of the ($d$, $e$, $\sin I$) space (see Fig. 9). Since small bodies dominate the Ennomos group, we suspect that large bodies might actually be interlopers.

A very intriguing feature is a high albedo of (4709) Ennomos $p_V \simeq 0.15$ measured by Fernández et al. (2003). Apart from other explanations, the authors speculated that it may result from a recent impact which covered the surface with pristine ice. If it is true, the relation between the fresh surface and the collisional family might be a unique opportunity to study cratering events.

We cannot exclude the possibility that (4709) Ennomos is actually an interloper and the family is not related to it at all. Nevertheless, our hypothesis is testable: family members should exhibit a similarity in spectra and albedos. The only information we have to date are SDSS colours for three members: 98362, 2005 YG$_{204}$ are probably C-types and 2005 AR$_{72}$ is a D-type. In case new data become available, we would be able to remove interlopers from our sample and improve our analysis.

The size distribution of the Ennomos group is barely constrained, since small bodies are at the observational limit. Moreover, removal of interlopers can change the SFD slope completely (from $\gamma = -1.4$ to $-3.2$ or so). The minimum parent body size is about $D_{\text{PB}} \simeq 67$ km if all members have a high albedo $p_V = 0.15$.

### 3.3 Group called Aneas

The Aneas group looks like the middle portion of the $L_5$ cloud with an approximate background density. It spans the whole range of semimajor axes, as background asteroids do.

The minimum size of a hypothetical parent body is $D_{\text{PB}} = 160$ to 170 km (for albedo $p_V = 0.055$–0.041). This size is very large and an impact disruption of such body is less probable (see Section 4.4). The size–frequency distribution is shallow, with approximately the same slope as that of the background.

According to Roig et al. (2008) the colours are rather homogeneous and correspond to D-types, with ≃10 per cent of probable interlopers.

### 3.4 Group called 1988 RG$_{10}$

The group around asteroid (11487) 1988 RG$_{10}$ again looks like a lower portion of the $L_5$ cloud at low inclinations, with $\sin I \in (0.06, 0.1)$. The SFD is steeper ($\gamma = -2.6 \pm 0.1$) than the surroundings in $L_5$ and the resulting parent body size $D \simeq 60$ km is relatively small. The colours seem heterogeneous (Roig et al. 2008) and we can confirm this statement based on the new SDSS-MOC version 4 data.

The remaining clusters (Hektor, Teucer, Sinon, 1986 WD, Laertes, Asios, Polydoros, Panthoos, etc.) may be characterized as follows: (i) they have a density in ($d$, $e$, $\sin I$) space comparable to that of background (surroundings); (ii) when identified by the HCM their semimajor axes span the whole range of Trojan region; (iii) the slopes of their SFDs are comparable to the background; (iv) they are often inhomogeneous with respect to colours (according to Roig et al. 2008). These reasons lead us to a conclusion that these clusters are not necessarily real collisional families.

## 4 LONG-TERM EVOLUTION OF TROJAN FAMILIES

### 4.1 Evolution due to chaotic diffusion

We try to model long-term evolution of the Eurybates family. At first, we generate a synthetic family (consisting of 42 bodies) by an

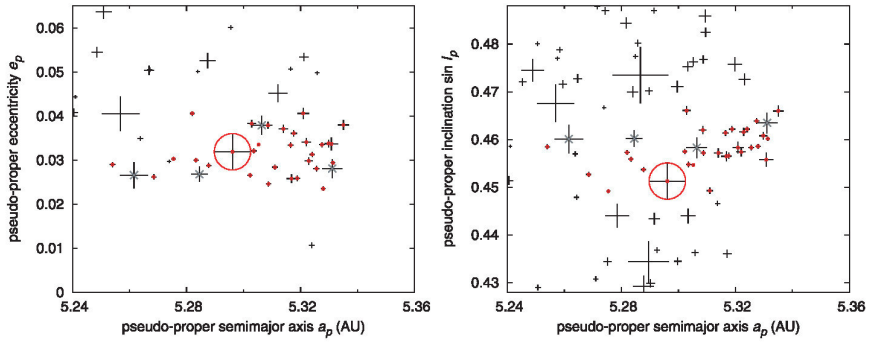


**Figure 9.** Details of the $L_5$ Trojan population where the Ennomos group is visible. Left-hand panel: the resonant semimajor axis $a$ versus eccentricity $e$. Only asteroids occupying the same range of inclinations as the Ennomos group $\sin I \in (0.448, 0.468)$ are plotted to facilitate a comparison with the density of surroundings space (background). The sizes of plus signs are proportional to diameters of the asteroids. The probable family members are denoted by small red circles and the possible interlopers by small grey crosses. Right-hand panel: $a$ versus inclination $\sin I$, with the range of eccentricities $e \in (0.02, 0.045)$.

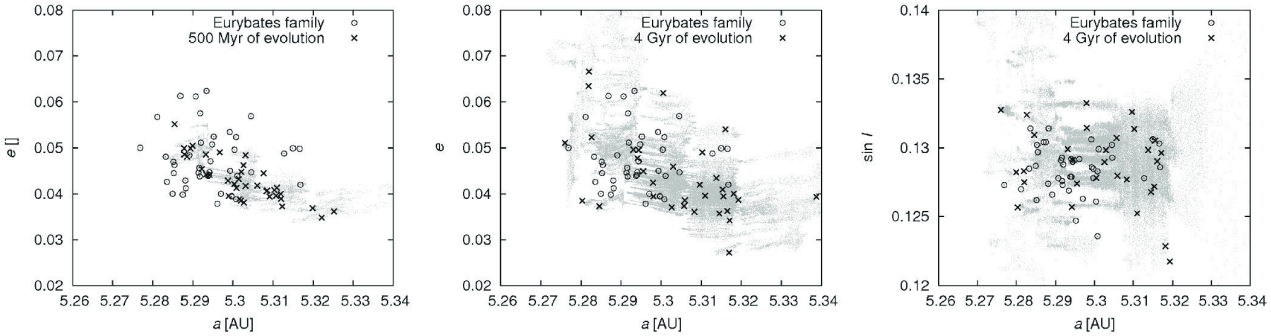


**Figure 10.** Orbital evolution of the synthetic family and its comparison with the observed Eurybates family. Left-hand panel: the situation in the ($a$, $e$) plane at 500 Myr. Middle panel: the situation after 4 Gyr. Chaotic diffusion disperses the synthetic family in course of time (see shaded tracks of particles). Right-hand panel: the ($a$, $\sin I$) plane at the same time. Inclinations evolve only barely.

impact disruption of the parent body with required size. Then we integrate the synthetic family and compare it at a particular time to the observed Eurybates family. The time-span of the integration is 4 Gyr.

The main driving mechanism is slow *chaotic diffusion* (the Yarkovsky effect is present but inefficient in the Trojan region). Initially, the spread of inclinations of the synthetic family is consistent with the observed one. On the other hand, the shape in ($a$, $e$) elements is clearly inconsistent.

Since the inclinations evolve only barely, we focus on the evolution in the ($a$, $e$) plane (see Fig. 10). The point is the synthetic family, namely the 'filament' structure, has to disperse sufficiently. After 500 Myr it is still recognizable but after 1 Gyr of evolution it is not. So we may constrain the age of the Eurybates family from 1 to 4 Gyr.[8]

A similar analysis for the Ennomos group indicates that the chaotic diffusion is faster in this region (given the large inclination) and the most probable age thus seems to be from 1 to 2 Gyr. Beyond 2 Gyr the inclinations of the synthetic family become too large compared to the observed Ennomos group, while the eccentricities are still compatible.

We try to model Aneas and 1988 $RG_{10}$ groups too (see Fig. 11). In these two cases, there is a strong disagreement between our model and observations. The observed groups are much larger and the chaotic diffusion in the respective regions is very slow. Even after 4 Gyr of orbital evolution, the synthetic family remains too small.

The only free parameter that may substantially change our results is the initial velocity distribution. Theoretically, the distribution might have been strongly anisotropic. However, we cannot choose initial velocities entirely freely, since their magnitude should be comparable to the escape velocity from the parent body, which is fixed by the size $D_{\rm PB}$ and is only weakly dependent on the a priori unknown density $\rho_{\rm PB}$.

Another solution of this problem is possible if we assume that families are very old and that they experienced perturbations due to planetary migration.

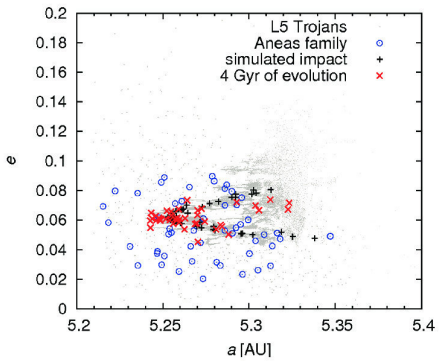


**Figure 11.** Evolution of the synthetic family over 4 Gyr versus the observed Aneas group. Chaotic diffusion is slow and it seems impossible to match the large spread of the observed group even after 4 Gyr.

### 4.2 Stability during planetary migration

The major perturbation acting on Trojans are *secondary resonances* between the libration period $P_{J1/1}$ of the asteroid in the J1/1 mean-motion resonance with Jupiter and the period $P_{\rm 1J-2S}$ of the critical argument of Jupiter–Saturn 1:2 resonance (Morbidelli et al. 2005):

$$P_{J1/1} = n P_{\rm 1J-2S}, \tag{5}$$

where $n$ is a small integer number. Typical libration periods are $P_{J1/1} \simeq 150$ yr, and $P_{\rm 1J-2S}$ changes as planets migrate (it decreases because Jupiter and Saturn recede from their mutual 1:2 resonance).[9]

All synthetic families are strongly unstable when $P_{\rm 1J-2S} \simeq 150$ yr and even during the later stages of migration with $P_{\rm 1J-2S} \simeq 75$ yr the eccentricities of family members are perturbed too much to match the observed families such as Eurybates or Ennomos (see Fig. 12). There are practically no plausible migration scenarios – regardless of time-scale $\tau_{\rm mig}$ – that would produce a sufficiently compact group, unless Jupiter and Saturn are almost on their current orbits. We tested $\tau_{\rm mig} = 0.3$, 3, 30 Myr and even for $\Delta a_{\rm J} \equiv a_{\rm Jf} - a_{\rm Ji}$ as small as $-0.08$ au and $\Delta a_{\rm S} = +0.25$ au the perturbation was

[8] We verified these estimates by a two-dimensional Kolmogorov–Smirnov test of the ($a$, $e$) distributions: initially the KS distance is $D_{\rm KS} = 0.30$ and the probability $p_{\rm KS}(>D) = 0.02$, which means the distribution are incompatible. At $t = 1$ Gyr, the values are $D_{\rm KS} = 0.20$ and $p_{\rm KS}(>D) = 0.32$, which indicate a reasonable match.

[9] Another source of instability might be a secondary resonance with $P_{\rm 2J-5S}$ (the so-called Great Inequality period) though it is weaker than $P_{\rm 1J-2S}$. We find no asteroids perturbed by secondary resonances connected with $P_{\rm 3J-7S}$ or $P_{\rm 4J-9S}$ which are present 'en route'. Neither Uranus nor Neptune plays an important role.

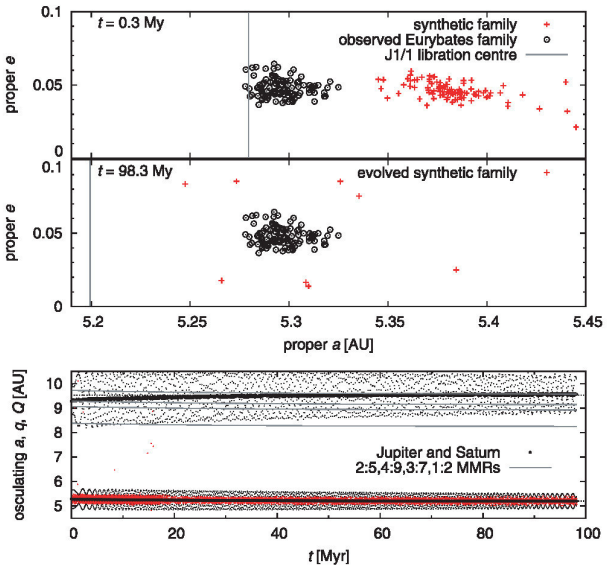


**Figure 12.** Evolution of a synthetic family during the late phases of planetary migration ($\tau_{\rm mig} = 30$ Myr in this case). Top panel: the state at 0 Myr, middle: 100 Myr; bottom panel: the respective orbital evolution of Jupiter and Saturn. The family is almost destroyed and it is definitely incompatible with the observed Eurybates family.

too strong. The reason is that one has to avoid $n = 2$ secondary resonance to preserve the low spread of a synthetic family.

Let us conclude that if any of Trojan families was created during planetary migration and if the migration was smooth (exponential), then the family cannot be visible today. However, we cannot exclude the possibility that the final stages of migration were entirely different e.g. similar to the 'jumping-Jupiter' scenario (Morbidelli et al. 2010).

### 4.3 Families lost by the ejection of fragment outside the resonance

We have studied the possibility that some families cannot be identified because the breakup occurred on the outskirts of the stable libration zone and some fragments were ejected outside the J1/1 resonance. We thus chose 30 largest asteroids near the edge of the $L_4$ libration zone and we simulated the breakups of these asteroids which create families with 30 fragments each. We assumed the diameter of all parent bodies to be $D_{\rm PB} = 100$ km and their density $\rho_{\rm PB} = 1.3\,{\rm g\,cm^{-3}}$. The breakups always occurred at the same geometry $f_{\rm imp} = 0°$, $\omega_{\rm imp} = 30°$. After the breakup, we calculated proper elements of the family members and plotted their distribution (see Fig. 13). We found that all the 30 synthetic families could be easily identified. In most cases, more than 95 per cent of the family members remained within the stable libration zone. We can thus conclude that the ejection of fragments outside the libration zone does not affect the number of observed families among the Trojans.

### 4.4 Collisional rates

We can estimate collisional activity by means of a simple stationary model. Trojan–Trojan collisions play a major role here, because Trojans are detached from the Main Belt. In case of Eurybates, the target (parent body) diameter $D_{\rm target} = 110$ km, the mean impact velocity $V_{\rm imp} = 4.7\,{\rm km\,s^{-1}}$ (Dell'Oro et al. 1998), the strength $Q_D^\star =$

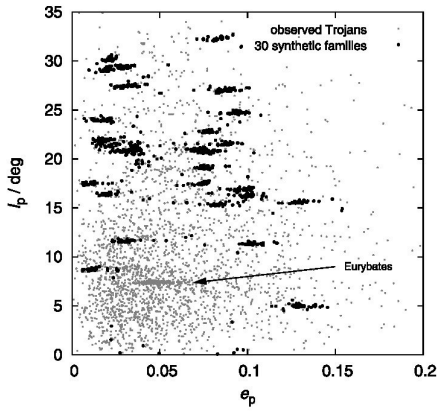


**Figure 13.** Proper eccentricities and inclinations of 30 *synthetic* families (black dots), which originated near the border of stable libration zone, compared to the observed L4 Trojans (grey dots).

$10^5\,{\rm J\,kg^{-1}}$ (Benz & Asphaug 1999) and thus the necessary impactor size (Bottke et al. 2005)

$$d_{\rm disrupt} = \left(2Q_D^\star/V_{\rm imp}^2\right)^{1/3} D_{\rm target} \simeq 23\,{\rm km}. \quad (6)$$

The number of $\geq$23 km projectiles among the $L_4$ Trojans is $n_{\rm project} = 371$ and we have $n_{\rm target} = 8$ available targets. The intrinsic collision probability for Trojan–Trojan collisions $P_{\rm i} = 7.8 \times 10^{-18}\,{\rm km^{-2}\,yr^{-1}}$ (Dell'Oro et al. 1998) and the corresponding frequency of disruptions is

$$f_{\rm disrupt} = P_{\rm i}\frac{D_{\rm target}^2}{4} n_{\rm project} n_{\rm target} \simeq 7 \times 10^{-11}\,{\rm yr^{-1}}. \quad (7)$$

Over the age of the Solar system $T_{\rm SS} \simeq 4$ Gyr (after the LHB), we have a very small number of such events $n_{\rm events} = T_{\rm SS} f_{\rm disrupt} \simeq 0.28$. This number seems to be in concert with only one $D \geq 100$ km family currently observed among the Trojans.[10] In a less likely case, the material of the Eurybates parent body was very weak and its strength may be at most 1 order of magnitude lower, $Q_D^\star \simeq 10^4\,{\rm J\,kg^{-1}}$ (see Leinhardt & Stewart 2009, Bottke et al. 2010). We then obtain $d_{\rm disrupt} \simeq 10$ km and $n_{\rm events} \simeq 1.0$, so the conclusion about the low number of expected Trojan families remains essentially the same.

The parent body of Aneas group is 1.5 larger and consequently the resulting number of events is more than 1 order of magnitude lower. On the other hand, clusters with smaller parent bodies ($D_{\rm PB} \ll 100$ km) or those that are significantly weaker ($Q_D^\star \ll 10^5\,{\rm J\,kg^{-1}}$) might be more frequent.

During the Late Heavy Bombardment epoch we may assume a substantial increase of collisional activity (Levison et al. 2009). Hypothetical old families were, however, probably 'erased' due to the late phases of planetary migration (see Section 4.2) unless the migration time-scale for Jupiter and Saturn was significantly shorter than the time-scale of the impactor flux from transneptunian region which is mainly controlled by the migration of Uranus and Neptune.

[10] A similar stationary estimate valid for the Main Asteroid Belt gives the number of events 12 while the number of observed families with $D_{\rm PB} \gtrsim 100$ km is about 20 (Durda et al. 2007). These two numbers are comparable at least to order-of-magnitude.

## 5 CONCLUSIONS

The increasing number of Trojan asteroids with available proper elements enables us to get new insights into this important population. Essentially, the new faint/small asteroids filled the 'gaps' in the proper-element space between previously known clusters, and today it seems most clusters are rather comparable to background. One should be aware of the fact that the number of families among the Trojans may be small and one should not take the number of $\simeq$10 families as a rule.

Only the C-type Eurybates family fulfils all the criteria to be considered a collisional family. This is probably also true for the newly discovered Ennomos group. Moreover, there might be a potentially interesting relation between the high-albedo surface of (4709) Ennomos and the collisional family though we do not have enough data yet to prove it independently (by colours, spectra or albedos).

Note that there may exist clusters among Trojans which are not of collisional origin. They may be caused by (i) differences in chaotic diffusion rates, (ii) *a-/e-/I*-dependent efficiency of original capture mechanism; or (iii) it may somehow reflect the orbital distribution in the source regions.

We cannot exclude the hypothetical existence of old families which were totally dispersed by dynamical processes e.g. by perturbations due to planetary migration which is especially efficient in the Trojan region.

Finally, note that there seem to be no D-type families anywhere in the Solar system – neither in the Trojan region, nor in the J3/2 (Brož et al. 2011) and Cybele regions (Vokrouhlický et al. 2010). Is it that the D-type parent bodies are too weak and the target is completely pulverized by a collision? This might have important implications for collisional models of icy bodies.

## ACKNOWLEDGMENTS

We thank David Vokrouhlický, David Nesvorný, Alessandro Morbidelli and William F. Bottke for valuable discussions on the subject. We also thank Lenka Trojanová for the principal component analysis of the SDSS-MOC4 data and Gonzalo Carlos de Elía for his review which helped to improve the final version of the paper. The work has been supported by the Grant Agency of the Czech Republic (grant 205/08/P196) and the Research Program MSM0021620860 of the Czech Ministry of Education. We acknowledge the usage of computers of the Observatory and Planetarium in Hradec Králové and Observatory and Planetarium of Prague.

## REFERENCES

Benz W., Asphaug E., 1999, Icarus, 142, 5
Bottke W. F., Durda D. D., Nesvorný D., Jedicke R., Morbidelli A., Vokrouhlický D., Levison H. F., 2005, Icarus, 175, 111
Bottke W. F., Nesvorný D., Vokrouhlický D., Morbidelli A., 2010, AJ, 139, 994
Brož M., Vokrouhlický D., 2008, MNRAS, 390, 715
Brož M., Vokrouhlický D., Morbidelli A., Bottke W. F., Nesvorný D., 2011, MNRAS, in press
De Luise F., Dotto E., Fornasier S., Barucci M. A., Pinilla Alonso N., Perna D., Marzari F., 2010, Icarus, 209, 586
Dell'Oro A., Marzari F., Paolicchi P., Dotto E., Vanzani V., 1998, A&A, 339, 272
Durda D. D., Bottke W. F., Nesvorný D., Enke B. L., Merline W. J., Aspaugh E., Richardson D. C., 2007, Icarus, 186, 498
Farinella P., Froeschlé C., Gonczi R., 1994, in Milani A., Di Martino M., Cellino A., eds, Asteroids, Comets, Meteors 1993. Kluwer, Dordrecht, p. 205
Fernández Y. R., Sheppard S. S., Jewitt D. C., 2003, AJ, 126, 1536
Fernández Y. R., Jewitt D. C., Ziffer J. E., 2009, AJ, 138, 240
Gomes R., Levison H. F., Tsiganis K., Morbidelli A., 2005, Nat, 435, 466
Knežević Z., Milani A., 2003, A&A, 403, 1165
Laskar J., Robutel P., 2001, Celest. Mech. Dynamical Astron., 80, 39
Leinhardt Z. M., Stewart S. T., 2009, Icarus, 199, 542
Levison H. F., Duncan M., 1994, Icarus, 108, 18
Levison H. F., Bottke W. F., Gounelle M., Morbidelli A., Nesvorný D., Tsiganis K., 2009, Nat, 460, 364
Milani A., 1993, Celest. Mech. Dynamical Astron, 57, 59
Moldovan R., Matthews J. M., Gladman B., Bottke W. F., Vokrouhlický D., 2010, ApJ, 716, 315
Morbidelli A., Levison H. F., Tsiganis K., Gomes R., 2005, Nat, 435, 462
Morbidelli A., Brasser R., Gomes R., Levison H. F., Tsiganis K., 2010, AJ, 140, 1391
Nesvorný D., Bottke W. F., Dones L., Levison H. F., 2002, Nat, 417, 720
Nesvorný D., Bottke W. F., Levison H. F., Dones L., 2003, ApJ, 591, 486
Nesvorný D., Vokrouhlický D., Bottke W. F., 2006, Sci, 312, 1490
O'Brien D., Morbidelli A., 2008, LPI Contr., 1405, 8367
Parker A., Ivezić Ž, Jurić M., Lupton R., Sekora M. D., Kowalski A., 2008, Icarus, 198, 138
Quinn T. R., Tremaine S., Duncan M., 1991, AJ, 101, 2287
Roig F., Ribeiro A. O., Gil-Hutton R., 2008, A&A, 483, 911
Šidlichovský M., Nesvorný D., 1997, Celest. Mech. Dynamical Astron., 65, 137
Szabó Gy. M., Ivezić Ž, Jurić M., Lupton R., 2007, MNRAS, 377, 1393
Tanga P., Cellino A., Michel P., Zappalà V., Paolicchi P., Dell'Oro A., 1999, Icarus, 141, 65
Trojanová L., 2010, B.Sc. thesis, Univ. Hradec Králové
Vokrouhlický D., Brož M., Bottke W. F., Nesvorný D., Morbidelli A., 2006, Icarus, 182, 118
Vokrouhlický D., Nesvorný D., Bottke W. F., Morbidelli A., 2010, AJ, 139, 2148
Yang B., Jewitt D., 2007, AJ, 134, 223
Yoshida F., Nakamura T., 2008, PASJ, 60, 297
Zappalá V., Cellino A., Farinella P., Milani A., 1994, AJ, 107, 772

This paper has been typeset from a TEX/LATEX file prepared by the author.

# Appendix C

# Reprint of Brož et al. (2013)

A&A 551, A117 (2013)
DOI: 10.1051/0004-6361/201219296


Astronomy & Astrophysics

# Constraining the cometary flux through the asteroid belt during the late heavy bombardment*

M. Brož[1], A. Morbidelli[2], W. F. Bottke[3], J. Rozehnal[1], D. Vokrouhlický[1], and D. Nesvorný[3]

[1] Institute of Astronomy, Charles University, Prague, V Holešovičkách 2, 18000 Prague 8, Czech Republic
e-mail: mira@sirrah.troja.mff.cuni.cz, rozehnal@observatory.cz, davok@cesnet.cz
[2] Observatoire de la Côte d'Azur, BP 4229, 06304 Nice Cedex 4, France
e-mail: morby@oca.eu
[3] Department of Space Studies, Southwest Research Institute, 1050 Walnut St., Suite 300, Boulder, CO 80302, USA
e-mail: [bottke;davidn]@boulder.swri.edu

Received 28 March 2012 / Accepted 28 November 2012

**ABSTRACT**

In the Nice model, the late heavy bombardment (LHB) is related to an orbital instability of giant planets which causes a fast dynamical dispersion of a trans-Neptunian cometary disk. We study effects produced by these hypothetical cometary projectiles on main belt asteroids. In particular, we want to check whether the observed collisional families provide a lower or an upper limit for the cometary flux during the LHB. We present an updated list of observed asteroid families as identified in the space of synthetic proper elements by the hierarchical clustering method, colour data, albedo data and dynamical considerations and we estimate their physical parameters. We selected 12 families which may be related to the LHB according to their dynamical ages. We then used collisional models and $N$-body orbital simulations to gain insight into the long-term dynamical evolution of synthetic LHB families over 4 Gyr. We account for the mutual collisions between comets, main belt asteroids, and family members, the physical disruptions of comets, the Yarkovsky/YORP drift in semimajor axis, chaotic diffusion in eccentricity/inclination, or possible perturbations by the giant-planet migration. Assuming a "standard" size-frequency distribution of primordial comets, we predict the number of families with parent-body sizes $D_{\rm PB} \geq 200$ km – created during the LHB and subsequent $\simeq$4 Gyr of collisional evolution – which seems consistent with observations. However, more than 100 asteroid families with $D_{\rm PB} \geq 100$ km should be created at the same time which are not observed. This discrepancy can be nevertheless explained by the following processes: i) asteroid families are efficiently destroyed by comminution (via collisional cascade), ii) disruptions of comets below some critical perihelion distance ($q \lesssim 1.5$ AU) are common. Given the freedom in the cometary-disruption law, we cannot provide stringent limits on the cometary flux, but we can conclude that the observed distribution of asteroid families does not contradict with a cometary LHB.

**Key words.** celestial mechanics – minor planets, asteroids: general – comets: general – methods: numerical

## 1. Introduction

The late heavy bombardment (LHB) is an important period in the history of the solar system. It is often defined as the process that made the huge but relatively young impact basins (a 300 km or larger diameter crater) on the Moon like Imbrium and Orientale. The sources and extent of the LHB, however, has been undergoing recent revisions. In the past, there were two end-member schools of thought describing the LHB. The first school argued that nearly all lunar basins, including the young ones, were made by impacting planetesimals left over from terrestrial planet formation (Neukum et al. 2001; Hartmann et al. 2000, 2007; see Chapman et al. 2007, for a review). The second school argued that most lunar basins were made during a spike of impacts that took place near 3.9 Ga (e.g., Tera et al. 1974; Ryder et al. 2000).

Recent studies, however, suggest that a compromise scenario may be the best solution: the oldest basins were mainly made by leftover planetesimals, while the last 12–15 or so lunar basins were created by asteroids driven out of the primordial main belt by the effects of late giant-planet migration (Tsiganis et al. 2005; Gomes et al. 2005; Minton & Malhotra 2009; Morbidelli et al. 2010; Marchi et al. 2012; Bottke et al. 2012). This would mean the LHB is limited in extent and does not encompass all lunar basins. If this view is correct, we can use studies of lunar and asteroid samples heated by impact events, together with dynamical modelling work, to suggest that the basin-forming portion of the LHB lasted from approximately 4.1–4.2 to 3.7–3.8 billion years ago on the Moon (Bogard 1995, 2011; Swindle et al. 2009; Bottke et al. 2012; Norman & Nemchin 2012).

The so-called "Nice model" provides a coherent explanation of the origin of the LHB as an impact spike or rather a "saw-tooth" (Morbidelli et al. 2012). According to this model, the bombardment was triggered by a late dynamical orbital instability of the giant planets, in turn driven by the gravitational interactions between said planets and a massive trans-Neptunian disk of planetesimals (see Morbidelli 2010, for a review). In this scenario, three projectile populations contributed to the LHB: the comets from the original trans-Neptunian disk (Gomes et al. 2005), the asteroids from the main belt (Morbidelli et al. 2010) and those from a putative extension of the main belt towards Mars, inwards of its current inner edge (Bottke et al. 2012). The last could have been enough of a source for the LHB, as recorded in the lunar crater record (Bottke et al. 2012), while the asteroids from the current main belt boundaries would have only been a minor contributor (Morbidelli et al. 2010).

The Nice model, however, predicts a very intense cometary bombardment of which there seems to be no obvious traces on

* Table 1 is available in electronic form at http://www.aanda.org

the Moon. In fact, given the expected total mass in the original trans-Neptunian disk (Gomes et al. 2005) and the size distribution of objects in this disk (Morbidelli et al. 2009), the Nice model predicts that about $5 \times 10^4$ km-size comets should have hit the Moon during the LHB. This would have formed 20 km craters with a surface density of $1.7 \times 10^{-3}$ craters per km$^2$. But the highest crater densities of 20 km craters on the lunar highlands is less than $2 \times 10^{-4}$ (Strom et al. 2005). This discrepancy might be explained by a gross overestimate of the number of small bodies in the original trans-Neptunian disk in Morbidelli et al. (2009). However, all impact clast analyses of samples associated to major LHB basins (Kring & Cohen 2002; Tagle 2005) show that also the major projectiles were not carbonaceous chondrites or similar primitive, comet-like objects.

The lack of evidence of a cometary bombardment of the Moon can be considered as a fatal flaw in the Nice model. Curiously, however, in the outer solar system we see evidence of the cometary flux predicted by the Nice model. Such a flux is consistent with the number of impact basins on Iapetus (Charnoz et al. 2009), with the number and the size distribution of the irregular satellites of the giant planets (Nesvorný et al. 2007; Bottke et al. 2010) and of the Trojans of Jupiter (Morbidelli et al. 2005), as well as with the capture of D-type asteroids in the outer asteroid belt (Levison et al. 2009). Moreover, the Nice model cometary flux is required to explain the origin of the collisional break-up of the asteroid (153) Hilda in the 3/2 resonance with Jupiter (located at ≃4 AU, i.e. beyond the nominal outer border of the asteroid belt at ≃3.2 AU; Brož et al. 2011).

Missing signs of an intense cometary bombardment on the Moon and the evidence for a large cometary flux in the outer solar system suggest that the Nice model may be correct in its basic features, but most comets disintegrated as they penetrated deep into the inner solar system.

To support or reject this possibility, this paper focusses on the main asteroid belt, looking for constraints on the flux of comets through this region at the time of the LHB. In particular we focus on old asteroid families, produced by the collisional break-up of large asteroids, which may date back at the LHB time. We provide a census of these families in Sect. 2.

In Sect. 3, we construct a collisional model of the main belt population. We show that, on average, this population alone could not have produced the observed number of families with $D_{\rm PB}$ = 200–400 km. Instead, the required number of families with large parent bodies is systematically produced if the asteroid belt was crossed by a large number of comets during the LHB, as expected in the Nice model (see Sect. 4). However, for any reasonable size distribution of the cometary population, the same cometary flux that would produce the correct number of families with $D_{\rm PB}$ = 200–400 km would produce too many families with $D_{\rm PB} \simeq 100$ km relative to what is observed. Therefore, in the subsequent sections we look for mechanisms that might prevent detection of most of these families.

More specifically, in Sect. 5 we discuss the possibility that families with $D_{\rm PB} \simeq 100$ km are so numerous that they cannot be identified because they overlap with each other. In Sect. 6 we investigate their possible dispersal below detectability due to the Yarkovsky effect and chaotic diffusion. In Sect. 7 we discuss the role of the physical lifetime of comets. In Sect. 8 we analyse the dispersal of families due to the changes in the orbits of the giant planets expected in the Nice model. In Sect. 9 we consider the subsequent collisional comminution of the families. Of all investigated processes, the last one seems to be the most promising for reducing the number of visible families with $D_{\rm PB} \simeq 100$ km while not affecting the detectability of old families with $D_{\rm PB}$ = 200–400 km.

Finally, in Sect. 10 we analyse a curious portion of the main belt, located in a narrow semi-major axis zone bounded by the 5:2 and 7:3 resonances with Jupiter. This zone is severely deficient in small asteroids compared to the other zones of the main belt. For the reasons explained in the section, we think that this zone best preserves the initial asteroid belt population, and therefore we call it the "pristine zone". We checked the number of families in the pristine zone, their sizes, and ages and we found that they are consistent with the number expected in our model invoking a cometary bombardment at the LHB time and a subsequent collisional comminution and dispersion of the family members. The conclusions follow in Sect. 11.

## 2. A list of known families

Although several lists of families exist in the literature (Zappalá et al. 1995; Nesvorný et al. 2005; Parker et al. 2008; Nesvorný 2010), we are going to identify the families once again. The reason is that we seek an upper limit for the number of old families that may be significantly dispersed and depleted, while the previous works often focussed on well-defined families. Moreover, we need to calculate several physical parameters of the families (such as the parent-body size, slopes of the size-frequency distribution (SFD), a dynamical age estimate if not available in the literature) which are crucial for further modelling. Last but not least, we use more precise synthetic proper elements from the AstDyS database (Knežević & Milani 2003, version Aug. 2010) instead of semi-analytic ones.

We employed a hierarchical clustering method (HCM, Zappalá et al. 1995) for the initial identification of families in the proper element space ($a_{\rm p}$, $e_{\rm p}$, $\sin I_{\rm p}$), but then we had to perform a lot of manual operations, because i) we had to select a reasonable cut-off velocity $v_{\rm cutoff}$, usually such that the number of members $N(v_{\rm cutoff})$ increases relatively slowly with increasing $v_{\rm cutoff}$. ii) The resulting family should also have a "reasonable" shape in the space of proper elements, which should somehow correspond to the local dynamical features[1]. iii) We checked taxonomic types (colour indices from the Sloan DSS MOC catalogue version 4, Parker et al. 2008), which should be consistent among family members. We can recognise interlopers or overlapping families this way. iv) Finally, the SFD should exhibit one or two well-defined slopes, otherwise the cluster is considered uncertain.

Our results are summarised in online Table 1 and the positions of families within the main belt are plotted in Fig. 1. Our list is "optimistic", so that even not very prominent families are included here[2].

There are, however, several potential problems we are aware of:

1. There may be inconsistencies among different lists of families. For example, sometimes a clump may be regarded as a single family or as two separate families. This may be the case of: Padua and Lydia, Rafita and Cameron.
2. To identify families we used synthetic proper elements, which are more precise than the semi-analytic ones.

[1] For example, the Eos family has a complicated but still reasonable shape, since it is determined by several intersecting high-order mean-motion or secular resonances, see Vokrouhlický et al. (2006).

[2] On the other hand, we do not include all of the small and less-certain clumps in a high-inclination region as listed by Novaković et al. (2011). We do not focus on small or high-$I$ families in this paper.

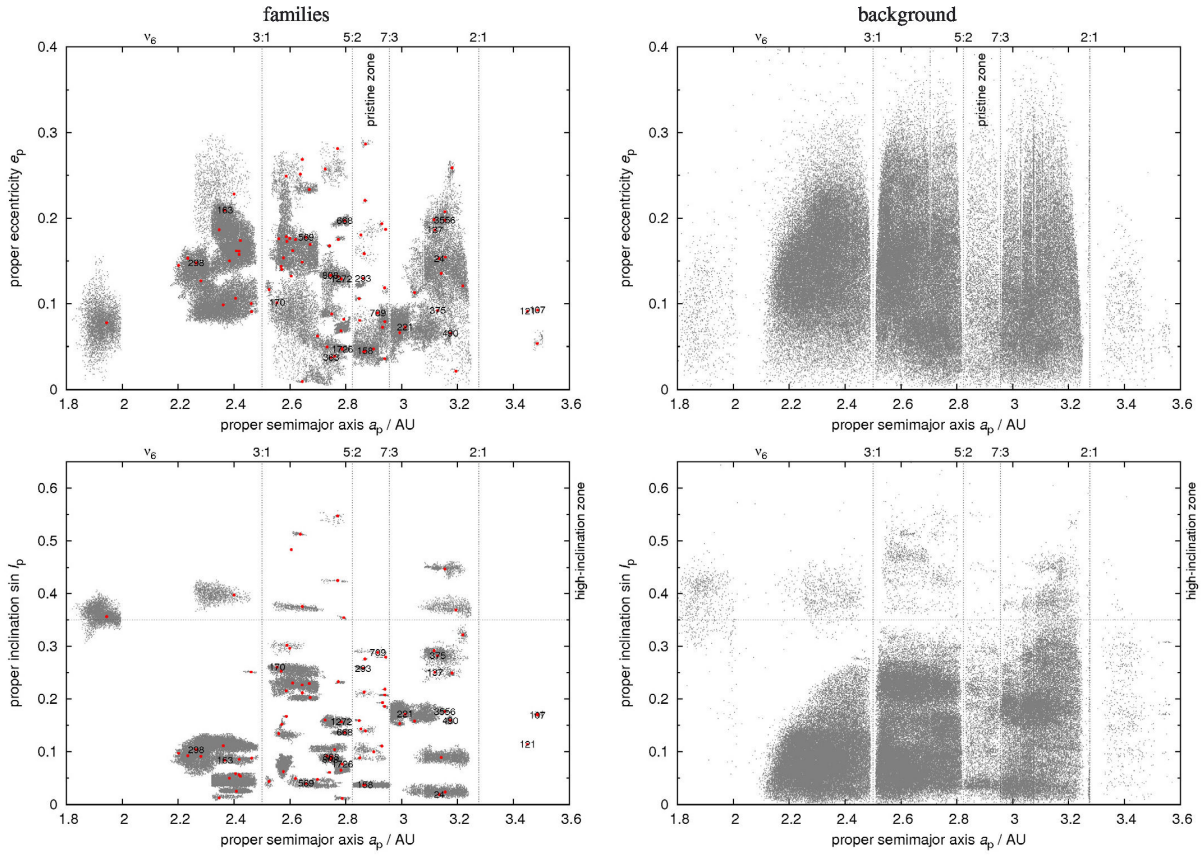


**Fig. 1.** Asteroids from the synthetic AstDyS catalogue plotted in the proper semimajor axis $a_p$ vs. proper eccentricity $e_p$ (*top panels*) and $a_p$ vs. proper inclination sin $I_p$ planes (*bottom panels*). We show the identified asteroid families (*left panels*) with the positions of the largest members indicated by red symbols, and also remaining background objects (*right panels*). The labels correspond to designations of the asteroid families that we focus on in this paper. There are still some structures consisting of small objects in the background population, visible only in the inclinations (*bottom right panel*). These "halos" may arise for two reasons: i) a family has no sharp boundary and its transition to the background is smooth, or ii) there are bodies escaping from the families due to long-term dynamical evolution. Nevertheless, we checked that these halo objects do not significantly affect our estimates of parent-body sizes.

Sometimes the families look more regular (e.g., Teutonia) or more tightly clustered (Beagle) when we use the synthetic elements. This very choice may, however, affect results substantially! A clear example is the Teutonia family, which also contains the big asteroid (5) Astraea if the synthetic proper elements are used, but not if the semi-analytic proper elements are used. This is due to the large differences between the semi-analytic and synthetic proper elements of (5) Astraea. Consequently, the physical properties of the two families differ considerably. We believe that the family defined from the synthetic elements is more reliable.

3. Durda et al. (2007) often claim a larger size for the parent body (e.g., Themis, Meliboea, Maria, Eos, Gefion), because they try to match the SFD of larger bodies and the results of SPH experiments. This way they also account for small bodies that existed at the time of the disruption, but which do not exist today since they were lost due to collisional grinding and the Yarkovsky effect. We prefer to use $D_{\rm Durda}$ instead of the value $D_{\rm PB}$ estimated from the currently observed SFD. The geometric method of Tanga et al. (1999), which uses the sum of the diameters of the first and third largest family members as a first guess of the parent-body size, is essentially similar to our approach[3].

### 2.1. A definition of the production function

To compare observed families to simulations, we define a "production function" as the cumulative number $N(>D)$ of families with parent-body size $D_{\rm PB}$ larger than a given $D$. The observed production function is shown in Fig. 2, and it is worth noting that it is very shallow. The number of families with $D_{\rm PB} \simeq 100$ km is comparable to the number of families in the $D_{\rm PB} = 200$–$400$ km range.

It is important to note that the observed production function is likely to be affected by biases (the family sample may not be complete, especially below $D_{\rm PB} \lesssim 100$ km) and also by long-term collisional/dynamical evolution which may

[3] A complete list of all families' members is available at our web site http://sirrah.troja.mff.cuni.cz/~mira/mp/fams/, including supporting figures.

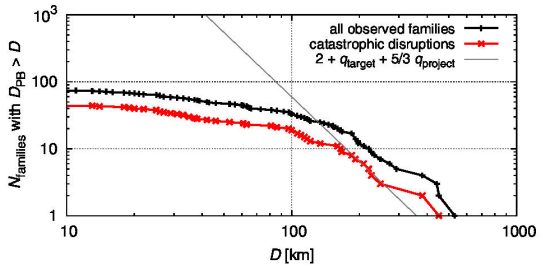


**Fig. 2.** A production function (i.e. the cumulative number $N(>D)$ of families with parent-body size $D_{\rm PB}$ larger than $D$) for all observed families (black) and families corresponding to catastrophic disruptions (red), i.e. with largest remnant/parent body mass ratio lower than 0.5. We also plot a theoretical slope according to Eq. (1), assuming $q_{\rm target} = -3.2$ and $q_{\rm project} = -1.2$, which correspond to the slopes of the main belt population in the range $D = 100$–$200$ km and $D = 15$–$60$ km, respectively.

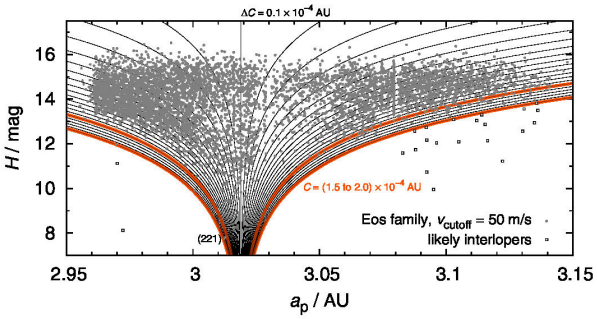


**Fig. 3.** An example of the Eos asteroid family, shown on the proper semimajor axis $a_{\rm p}$ vs. absolute magnitude $H$ plot. We also plot curves defined by Eq. (2) and parameters $a_{\rm c} = 3.019$ AU, $C = 1.5$ to $2.0 \times 10^{-4}$ AU, which is related to the upper limit of the dynamical age of the family.

prevent a detection of old comminutioned/dispersed families today (Marzari et al. 1999).

From the theoretical point of view, the slope $q$ of the production function $N(>D) \propto D^q$ should correspond to the cumulative slopes of the SFDs of the target and projectile populations. It is easy to show[4] that the relation is

$$q = 2 + q_{\rm target} + \frac{5}{3} q_{\rm project}. \quad (1)$$

Of course, real populations may have complicated SFDs, with different slopes in different ranges. Nevertheless, any populations that have a steep SFD (e.g. $q_{\rm target} = q_{\rm project} = -2.5$) would inevitably produce a steep production function ($q \doteq -4.7$).

In the following analysis, we drop cratering events and discuss catastrophic disruptions only, i.e. families which have largest remnant/parent body mass ratio less than 0.5. The reason is that the same criterion LR/PB $< 0.5$ is used in collisional models. Moreover, cratering events were not yet systematically explored by SPH simulations due to insufficient resolution (Durda et al. 2007).

### 2.2. Methods for family age determination

If there is no previous estimate of the age of a family, we used one of the following three dynamical methods to determine it: i) a simple $(a_{\rm p}, H)$ analysis as in Nesvorný et al. (2005); ii) a $C$-parameter distribution fitting as introduced by Vokrouhlický et al. (2006); iii) a full $N$-body simulation described e.g. in Brož et al. (2011).

In the first approach, we assume zero initial velocities, and the current extent of the family is explained by the size-dependent Yarkovsky semimajor axis drift. This way we can obtain only an upper limit for the dynamical age, of course. We show an example for the Eos family in Fig. 3. The extent of the family in the proper semimajor axis vs the absolute magnitude $(a_{\rm p}, H)$ plane can be described by the parametric relation

$$0.2H = \log_{10} \frac{|a_{\rm p} - a_{\rm c}|}{C}, \quad (2)$$

where $a_{\rm c}$ denotes the centre of the family, and $C$ is the parameter. Such relation can be naturally expected when the semimajor-axis drift rate is inversely proportional to the size, $\mathrm{d}a/\mathrm{d}t \propto 1/D$, and the size is related to the absolute magnitude via the Pogson equation $H = -2.5 \log_{10}(p_V D^2/D_0^2)$, where $D_0$ denotes the reference diameter and $p_V$ the geometric albedo (see Vokrouhlický et al. 2006 for a detailed discussion). The limiting value, for which all Eos family members (except interlopers) are above the corresponding curve, is $C = 1.5$ to $2.0 \times 10^{-4}$ AU. Assuming reasonable thermal parameters (summarised in Table 2), we calculate the expected Yarkovsky drift rates $\mathrm{d}a/\mathrm{d}t$ (using the theory from Brož 2006) and consequently can determine the age to be $t < 1.5$ to $2.0$ Gyr.

**Table 2.** Nominal thermal parameters for S and C/X taxonomic types of asteroids.

| Type | $\rho_{\rm bulk}$ (kg/m$^3$) | $\rho_{\rm surf}$ (kg/m$^3$) | $K$ (W/m/K) | $C_{\rm th}$ (J/kg/K) | $A_{\rm Bond}$ | $\epsilon$ |
|---|---|---|---|---|---|---|
| S | 2500 | 1500 | 0.001 | 680 | 0.1 | 0.9 |
| C/X | 1300 | 1300 | 0.01 | 680 | 0.02 | 0.9 |

**Notes.** $\rho_{\rm bulk}$ denotes the bulk density, $\rho_{\rm surf}$ the surface density, $K$ the thermal conductivity, $C_{\rm th}$ the specific thermal capacity, $A_{\rm Bond}$ the Bond albedo and $\epsilon$ the infrared emissivity.

The second method uses a histogram $N(C, C + \Delta C)$ of the number of asteroids with respect to the $C$ parameter defined above, which is fitted by a dynamical model of the initial velocity field and the Yarkovsky/YORP evolution. This enables us to determine the lower limit for the age too (so the resulting age estimate is $t = 1.3^{+0.15}_{-0.2}$ Gyr for the Eos family).

In the third case, we start an $N$-body simulation using a modified SWIFT integrator (Levison & Duncan 1994), with the Yarkovsky/YORP acceleration included, and evolve a synthetic family up to 4 Gyr. We try to match the shape of the observed family in all three proper orbital elements ($a_{\rm p}$, $e_{\rm p}$, $\sin I_{\rm p}$). In principle, this method may provide a somewhat independent estimate of the age. For example, there is a "halo" of asteroids in the surroundings of the nominal Eos family, which are of the same taxonomic type K, and we may fit the ratio $N_{\rm halo}/N_{\rm core}$ of the number of objects in the "halo" and in the family "core" (Brož et al., in prep.).

The major source of uncertainty in all methods are unknown bulk densities of asteroids (although we use the most likely values for the S or C/X taxonomic classes, Carry 2012). The age scales approximately as $t \propto \rho_{\rm bulk}$. Nevertheless, we are still able to distinguish families that are young from those that

[4] Assuming that the strength is approximately $Q_D^\star \propto D^2$ in the gravity regime, the necessary projectile size $d \propto (Q_D^\star)^{1/3} D$ (Bottke et al. 2005), and the number of disruptions $n \propto D^2 D^{q_{\rm target}} d^{q_{\rm project}}$.

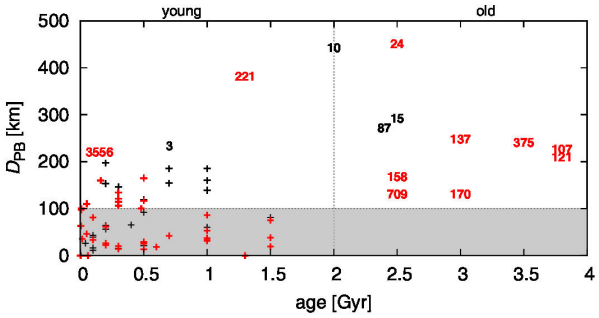


**Fig. 4.** The relation between dynamical ages of families and the sizes of their parent bodies. Red labels correspond to catastrophic disruptions, while cratering events are labelled in black. Some of the families are denoted by the designation of the largest member. The uncertainties of both parameters are listed in Table 1 (we do not include overlapping error bars here for clarity).

are old, because the allowed ranges of densities for S-types (2 to 3 g/cm$^3$) and C/X-types (1 to 2 g/cm$^3$) are limited (Carry 2012) and so are the allowed ages of families.

### 2.3. Which families can be of LHB origin?

The ages of the observed families and their parent-body sizes are shown in Fig. 4. Because the ages are generally very uncertain, we consider that any family whose nominal age is older than 2 Gyr is potentially a family formed ~4 Gyr ago, i.e. at the LHB time. If we compare the number of "young" (<2 Gyr) and old families (>2 Gyr) with $D_{PB}$ = 200–400 km, we cannot see a significant over-abundance of old family formation events. On the other hand, we almost do not find any small old families.

Only 12 families from the whole list may be possibly dated back to the LHB, because their dynamical ages approach ~3.8 Gyr (including the relatively large uncertainties; see Table 3, which is an excerpt from Table 1).

If we drop cratering events and the families of Camilla and Hermione, which do not exist any more today (their existence was inferred from the satellite systems, Vokrouhlický et al. 2010), we end up with only five families created by catastrophic disruptions that may potentially date from the LHB time (i.e. their nominal age is more than 2 Gy). As we shall see in Sect. 4, this is an unexpectedly low number.

Moreover, it is really intriguing that most "possibly-LHB" families are larger than $D_{PB} \simeq 200$ km. It seems that old families with $D_{PB} \simeq 100$ km are missing in the observed sample. This is an important aspect that we have to explain, because it contradicts our expectation of a steep production function.

## 3. Collisions in the main belt alone

Before we proceed to scenarios involving the LHB, we try to explain the observed families with ages spanning 0–4 Gyr as a result of collisions only among main belt bodies. To this purpose, we used the collisional code called Boulder (Morbidelli et al. 2009) with the following setup: the intrinsic probabilities $P_i = 3.1 \times 10^{-18}$ km$^{-2}$ yr$^{-1}$, and the mutual velocities $V_{imp} = 5.28$ km s$^{-1}$ for the MB vs. MB collisions (both were taken from the work of Dahlgren 1998). The assumption of a single $V_{imp}$ value is a simplification, but about 90% collisions have mutual velocities between 2 and 8 km s$^{-1}$ (Dahlgren 1998), which assures a similar collisional regime.

**Table 3.** Old families with ages possibly approaching the LHB.

| Designation | | $D_{PB}$ (km) | $D_{Durda}$ (km) | Note |
|---|---|---|---|---|
| 24 | Themis | 209c | 380–430! | |
| 10 | Hygiea | 410 | 442 | cratering |
| 15 | Eunomia | 259 | 292 | cratering |
| 702 | Alauda | 218c | 290–330! | high-$I$ |
| 87 | Sylvia | 261 | 272 | cratering |
| 137 | Meliboea | 174c | 240–290! | |
| 375 | Ursula | 198 | 240–280 | cratering |
| 107 | Camilla | >226 | – | non-existent |
| 121 | Hermione | >209 | – | non-existent |
| 158 | Koronis | 122c | 170–180 | |
| 709 | Fringilla | 99c | 130–140 | cratering |
| 170 | Maria | 100c | 120–130 | |

**Notes.** They are sorted according to the parent body size, where $D_{Durda}$ determined by the Durda et al. (2007) method is preferred to the estimate $D_{PB}$ inferred from the observed SFD. An additional "c" letter indicates that we extrapolated the SFD down to $D = 0$ km to account for small (unobserved) asteroids, an exclamation mark denotes a significant mismatch between $D_{PB}$ and $D_{Durda}$.

The scaling law is described by the polynomial relation ($r$ denotes radius in cm)

$$Q_D^\star(r) = \frac{1}{q_{fact}} \left( Q_0 r^a + B\rho r^b \right) \quad (3)$$

with the parameters corresponding to basaltic material at 5 km s$^{-1}$ (Benz & Asphaug 1999, Table 4):

**Table 4.** Parameters of the scaling law (Eq. (3)) corresponding to basaltic material at 5 km s$^{-1}$, according to Benz & Asphaug (1999).

| $\rho$ (g/cm$^3$) | $Q_0$ (erg/g) | $a$ | $B$ (erg/g) | $b$ | $q_{fact}$ |
|---|---|---|---|---|---|
| 3.0 | $7 \times 10^7$ | −0.45 | 2.1 | 1.19 | 1.0 |

Even though not all asteroids are basaltic, we use the scaling law above as a mean one for the main belt population. Below, we discuss also the case of significantly lower strengths (i.e. higher $q_{fact}$ values).

We selected the time span of the simulation 4 Gyr (not 4.5 Gyr) since we are interested in this last evolutionary phase of the main belt, when its population and collisional activity is nearly same as today (Bottke et al. 2005). The outcome of a single simulation also depends on the "seed" value of the random-number generator that is used in the Boulder code to decide whether a collision with a fractional probability actually occurs or not in a given time step. We thus have to run multiple simulations (usually 100) to obtain information on this stochasticity of the collisional evolution process.

The initial SFD of the main belt population conditions was approximated by a three-segment power law (see also thin grey line in Fig. 5, 1st row) with differential slopes $q_a = -4.3$ (for $D > D_1$), $q_b = -2.2$, $q_c = -3.5$ (for $D < D_2$) where the size ranges were delimited by $D_1 = 80$ km and $D_2 = 16$ km. We also added a few big bodies to reflect the observed shape of the SFD at large sizes ($D > 400$ km). The normalisation was $N_{norm}(D > D_1) = 350$ bodies in this case.

We used the observed SFD of the main belt as the first constraint for our collisional model. We verified that the outcome

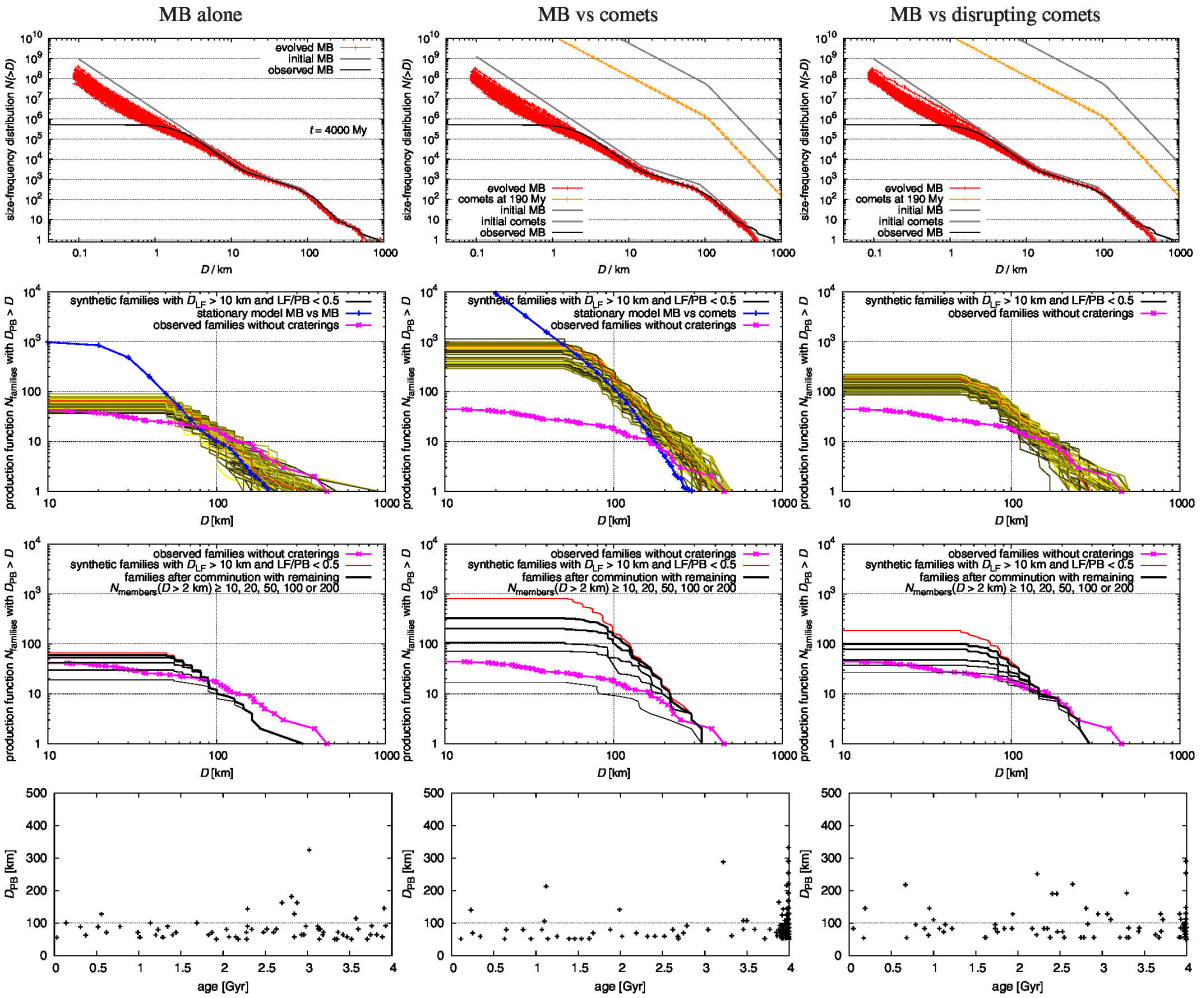


**Fig. 5.** Results of three different collisional models: main belt alone which is discussed in Sect. 3 (*left column*), main belt and comets from Sect. 4 (*middle column*), main belt and disrupting comets from Sect. 7 (*right column*). *1st row*: the initial and evolved SFDs of the main belt populations for 100 Boulder simulations; *2nd row*: the resulting family production functions (in order to distinguish 100 lines we plot them using different colours ranging from black to yellow) and their comparison to the observations; *3rd row*: the production function affected by comminution for a selected simulation; and *4th row*: the distribution of synthetic families with $D_{\rm PB} \geq 50$ km in the (age, $D_{\rm PB}$) plot for a selected simulation, without comminution. The positions of synthetic families in the *4th-row* figures may differ significantly for a different Boulder simulation due to stochasticity and low-number statistics. Moreover, in the middle and right columns, many families were created during the LHB, so there are many overlapping crosses close to 4 Gyr.

our model after 4 Gyr is not sensitive to the value of $q_c$. Namely, a change of $q_c$ by as much as $\pm 1$ does not affect the final SFD in any significant way. On the other hand, the values of the remaining parameters ($q_a$, $q_b$, $D_1$, $D_2$, $N_{\rm norm}$) are enforced by the observed SFD. To obtain a reasonable fit, they cannot differ much (by more than 5–10%) from the values presented above.

We do not use only a single number to describe the number of observed families (e.g. $N = 20$ for $D_{\rm PB} \geq 100$ km), but we discuss a complete production function instead. The results in terms of the production function are shown in Fig. 5 (left column, 2nd row). On average, the synthetic production function is steeper and below the observed one, even though there is approximately a 5% chance that a single realization of the computer model will resemble the observations quite well. This also holds for the distribution of $D_{\rm PB} = 200$–$400$ km families in the course of time (age).

In this case, the synthetic production function of $D_{\rm PB} \gtrsim 100$ km families is not significantly affected by comminution. According to Bottke et al. (2005), most of $D > 10$ km fragments survive intact and a $D_{\rm PB} \gtrsim 100$ km family should be recognisable today. This is also confirmed by calculations with Boulder (see Fig. 5, left column, 3rd row).

To improve the match between the synthetic and the observed production function, we can do the following: i) modify the scaling law, or ii) account for a dynamical decay of the MB population. Using a substantially lower strength ($q_{\rm fact} = 5$ in Eq. (3), which is not likely, though) one can obtain a synthetic production function which is on average consistent with the observations in the $D_{\rm PB} = 200$–$400$ km range.

Regarding the dynamical decay, Minton & Malhotra (2010) suggest that initially the MB was three times more populous than today while the decay timescale was very short: after 100 Myr

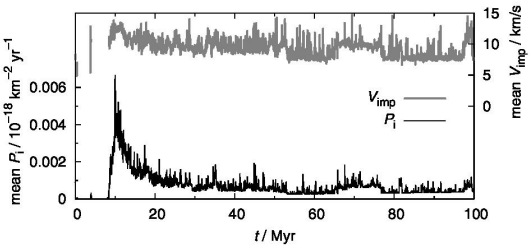


**Fig. 6.** Temporal evolution of the intrinsic collisional probability $P_i$ (*bottom*) and mean collisional velocity $V_{imp}$ (*top*) computed for collisions between cometary-disk bodies and the main belt asteroids. The time $t = 0$ is arbitrary here; the sudden increase in $P_i$ values corresponds to the beginning of the LHB.

of evolution the number of bodies is almost at the current level. In this brief period of time, about 50% more families will be created, but all of them will be old, of course. For the remaining ~3.9 Gyr, the above model (without any dynamical decay) is valid.

To conclude, it is possible – though not very likely – that the observed families were produced by the collisional activity in the main belt alone. A dynamical decay of the MB population would create more families that are old, but technically speaking, this cannot be distinguished from the LHB scenario, which is discussed next.

## 4. Collisions between a "classical" cometary disk and the main belt

In this section, we construct a collisional model and estimate an expected number of families created during the LHB due to collisions between cometary-disk bodies and main belt asteroids. We start with a simple stationary model and we confirm the results using a more sophisticated Boulder code (Morbidelli et al. 2009).

Using the data from Vokrouhlický et al. (2008) for a "classical" cometary disk, we can estimate the intrinsic collisional probability and the collisional velocity between comets and asteroids. A typical time-dependent evolution of $P_i$ and $V_{imp}$ is shown in Fig. 6. The probabilities increase at first, as the trans-Neptunian cometary disk starts to decay, reaching up to $6 \times 10^{-21}$ km$^{-2}$ yr$^{-1}$, and after 100 Myr they decrease to zero. These results do not differ significantly from run to run.

### 4.1. Simple stationary model

In a stationary collisional model, we choose an SFD for the cometary disk, we assume a current population of the main belt; estimate the projectile size needed to disrupt a given target according to (Bottke et al. 2005)

$$d_{\rm disrupt} = \left(2Q_D^\star / V_{\rm imp}^2\right)^{1/3} D_{\rm target}, \quad (4)$$

where $Q_D^\star$ denotes the specific energy for disruption and dispersion of the target (Benz & Asphaug 1999); and finally calculate the number of events during the LHB as

$$n_{\rm events} = \frac{D_{\rm target}^2}{4}\, n_{\rm target} \int P_i(t)\, n_{\rm project}(t)\, {\rm d}t, \quad (5)$$

where $n_{\rm target}$ and $n_{\rm project}$ are the number of targets (i.e. main belt asteroids) and the number of projectiles (comets), respectively.

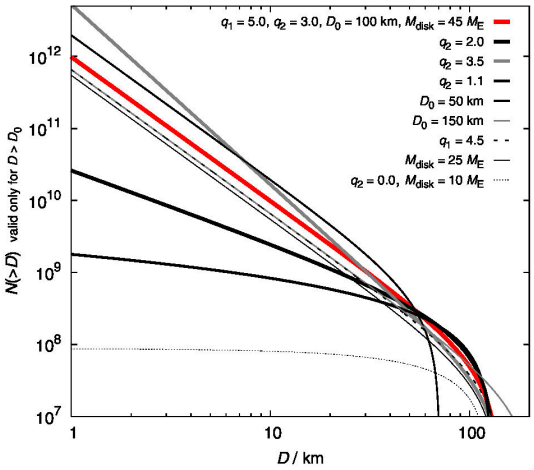


**Fig. 7.** Cumulative SFDs of the cometary disk tested in this work. All the parameters of our nominal choice are given in the top label; the other labels just report the parameters that changed relative to our nominal choice.

The actual number of bodies (27 000) in the dynamical simulation of Vokrouhlický et al. (2008) changes in the course of time, and it was scaled such that it was initially equal to the number of projectiles $N(>d_{\rm disrupt})$ inferred from the SFD of the disk. This is clearly a lower limit for the number of families created, since the main belt was definitely more populous in the past.

The average impact velocity is $V_{\rm imp} \simeq 10\,{\rm km\,s^{-1}}$, so we need the projectile sizes to disrupt given target sizes listed in Table 5.

**Table 5.** Projectile sizes $d_{\rm disrupt}$ needed to disrupt targets with sizes $D_{\rm target}$, as computed from Eq. (4).

| $D_{\rm target}$ (km) | $N_{\rm targets}$ in the MB | $Q_D^\star$ (J/kg) | $d_{\rm disrupt}$ for $\frac{\rho_{\rm target}}{\rho_{\rm project}} = 3$ to 6 (km) |
|---|---|---|---|
| 100 | ~192 | $1 \times 10^5$ | 12.6 to 23 |
| 200 | ~23 | $4 \times 10^5$ | 40.0 to 73 |

**Notes.** $N_{\rm targets}$ denotes the number of targets in the main belt, $Q_D^\star$ the specific energy needed for disruption, and $\rho_{\rm target}/\rho_{\rm project}$ the ratio of the respective bulk densities.

We tried to use various SFDs for the cometary disk (i.e., with various differential slopes $q_1$ for $D > D_0$ and $q_2$ for $D < D_0$, the elbow diameter $D_0$ and total mass $M_{\rm disk}$), including rather extreme cases (see Fig. 7). The resulting numbers of LHB families are summarised in Table 6. Usually, we obtain several families with $D_{\rm PB} \simeq 200$ km and about 100 families with $D_{\rm PB} \simeq 100$ km. This result is robust with respect to the slope $q_2$, because even very shallow SFDs should produce a lot of these families[5]. The only way to decrease the number of families significantly is to assume the elbow at a larger diameter $D_0 \simeq 150$ km.

[5] The extreme case with $q_2 = 0$ is not likely at all, e.g. because of the continuous SFD of basins on Iapetus and Rhea, which only exhibits a mild depletion of $D \simeq 100$ km size craters; see Kirchoff & Schenk (2010). On the other hand, Sheppard & Trujillo (2010) report an extremely shallow cumulative SFD of Neptune Trojans that is akin to low $q_2$.

**Table 6.** Results of a stationary collisional model between the cometary disk and the main belt.

| $q_1$ | $q_2$ | $D_0$ (km) | $M_{\rm disk}$ ($M_\oplus$) | $n_{\rm events}$ for $D_{\rm PB} \geq 100$ km | $D_{\rm PB} \geq 200$ km | Vesta craterings | Notes |
|---|---|---|---|---|---|---|---|
| 5.0 | 3.0 | 100 | 45 | 115–55 | 4.9–2.1 | 2.0 | nominal case |
| 5.0 | 2.0 | 100 | 45 | 35–23 | 4.0–2.2 | 1.1 | shallow SFD |
| 5.0 | 3.5 | 100 | 45 | 174–70 | 4.3–1.6 | 1.8 | steep SFD |
| 5.0 | 1.1 | 100 | 45 | 14–12 | 3.1–2.1 | 1.1 | extremely shallow SFD |
| 4.5 | 3.0 | 100 | 45 | 77–37 | 3.3–1.5 | 1.3 | lower $q_1$ |
| 5.0 | 3.0 | 50 | 45 | 225–104 | 7.2–1.7 | 3.2 | smaller turn-off |
| 5.0 | 3.0 | 100 | 25 | 64–40 | 2.7–1.5 | 1.1 | lower $M_{\rm disk}$ |
| 5.0 | 3.0 | 100 | 17 | 34 | 1.2 | 1.9 | $\rho_{\rm comets} = 500\,{\rm kg/m^3}$ |
| 5.0 | 3.0 | 150 | 45 | 77–23 | 3.4–0.95 | 0.74 | larger turn-off |
| 5.0 | 0.0 | 100 | 10 | 1.5–1.4 | 0.5–0.4 | 0.16 | worst case (zero $q_2$ and low $M_{\rm disk}$) |

**Notes.** The parameters characterise the SFD of the disk: $q_1$, $q_2$ are differential slopes for the diameters larger/smaller than the elbow diameter $D_0$, $M_{\rm disk}$ denotes the total mass of the disk, and $n_{\rm events}$ is the resulting number of families created during the LHB for a given parent body size $D_{\rm PB}$. The ranges of $n_{\rm events}$ are due to variable density ratios $\rho_{\rm target}/\rho_{\rm project} = 1$ to 3/1.

**Table 7.** Parameters of the scaling law (Eq. (3)) corresponding to basaltic material at 5 km s$^{-1}$ (first row), and to water ice (second row), according to Benz & Asphaug (1999).

| | $\rho$ (g/cm$^3$) | $Q_0$ (erg/g) | $a$ | $B$ (erg/g) | $b$ | $q_{\rm fact}$ |
|---|---|---|---|---|---|---|
| Asteroids | 3.0 | $7 \times 10^7$ | −0.45 | 2.1 | 1.19 | 1.0 |
| Comets | 1.0 | $1.6 \times 10^7$ | −0.39 | 1.2 | 1.26 | 3.0 |

It is thus no problem to explain the existence of approximately five large families with $D_{\rm PB} = 200$–$400$ km, which are indeed observed, since they can be readily produced during the LHB. On the other hand, the high number of $D_{\rm PB} \simeq 100$ km families clearly contradicts the observations, since we observe almost no LHB families of this size.

### 4.2. Constraints from (4) Vesta

The asteroid (4) Vesta presents a significant constraint for collisional models, being a differentiated body with a preserved basaltic crust (Keil 2002) and a 500 km large basin on its surface (a feature indicated by the photometric analysis of Cellino et al. 1987), which is significantly younger than 4 Gyr (Marchi et al. 2012). It is highly unlikely that Vesta experienced a catastrophic disruption in the past, and even large cratering events were limited. We thus have to check the number of collisions between one $D = 530$ km target and $D \simeq 35$ km projectiles, which are capable of producing the basin and the Vesta family (Thomas et al. 1997). According to Table 6, the predicted number of such events does not exceed ~2, so given the stochasticity of the results there is a significant chance that Vesta indeed experienced zero such impacts during the LHB.

### 4.3. Simulations with the Boulder code

To confirm results of the simple stationary model, we also performed simulations with the Boulder code. We modified the code to include a time-dependent collisional probability $P_{\rm i}(t)$ and impact velocity $V_{\rm imp}(t)$ of the cometary-disk population.

We started a simulation with a setup for the cometary disk resembling the nominal case from Table 6. The scaling law is described by Eq. (3) with the parameters given in Table 7, suitable for asteroids (basalt) and comets (water ice).

The intrinsic probabilities $P_{\rm i} = 3.1 \times 10^{-18}\,{\rm km^{-2}\,yr^{-1}}$ and velocities $V_{\rm imp} = 5.28\,{\rm km\,s^{-1}}$ for the MB vs MB collisions were again taken from the work of Dahlgren (1998). We do not account for comet-comet collisions since their evolution is dominated by the dynamical decay. The initial SFD of the main belt was similar to the one in Sect. 3, $q_a = -4.2$, $q_b = -2.2$, $q_c = -3.5$, $D_1 = 80$ km, $D_2 = 14$ km, and only the normalisation was increased up to $N_{\rm norm}(D > D_1) = 560$ in this case.

The resulting SFDs of 100 independent simulations with different random seeds are shown in Fig. 5 (middle column). The number of LHB families (approximately 10 with $D_{\rm PB} \simeq 200$ km and 200 with $D_{\rm PB} \simeq 100$ km) is even larger compared to the stationary model, as expected, because we had to start with a larger main belt to get a good fit of the currently observed MB after 4 Gyr of collisional evolution.

To conclude, the stationary model and the Boulder code give results that are compatible with each other, but that clearly contradict the observed production function of families. In particular, they predict far too many families with $D = 100$ km parent bodies. At first sight, this may be interpreted as proof that there was no cometary LHB on the asteroids. Before jumping to this conclusion, however, one has to investigate whether there are biases against identifying of $D_{\rm PB} = 100$ km families. In Sects. 5–9 we discuss several mechanisms that all contribute, at some level, to reducing the number of observable $D_{\rm PB} = 100$ km families over time. They are addressed in order of relevance, from the least to the most effective.

## 5. Families overlap

Because the number of expected $D_{\rm PB} \geq 100$ km LHB families is very high (of the order of 100) we now want to verify if these families can overlap in such a way that they cannot be distinguished from each other and from the background. We thus took 192 main belt bodies with $D \geq 100$ km and selected randomly 100 of them that will break apart. For each one we created an artificial family with $10^2$ members, assume a size-dependent ejection velocity $V \propto 1/D$ (with $V = 50$ m/s for $D = 5$ km) and the size distribution resembling that of the Koronis family. The choice of the true anomaly and the argument of perihelion at the instant of the break-up event was random. We then calculated proper elements ($a_{\rm p}, e_{\rm p}, \sin I_{\rm p}$) for all bodies. This type of analysis is in some respects similar to the work of Bendjoya et al. (1993).

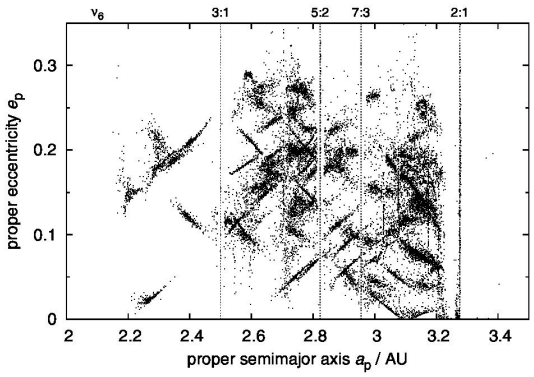


**Fig. 8.** Proper semimajor axis $a_p$ vs. proper eccentricity $e_p$ for 100 synthetic families created in the main belt. It is the initial state, shortly after disruption events. We assume the SFD of bodies in each synthetic family similar to that of the Koronis family (down to $D \simeq 2$ km). Break-ups with the true anomaly $f \simeq 0$ to 30° and 150° to 180° are more easily visible on this plot, even though the choice of both $f$ and the argument of perihelion $\varpi$ was random for all families.

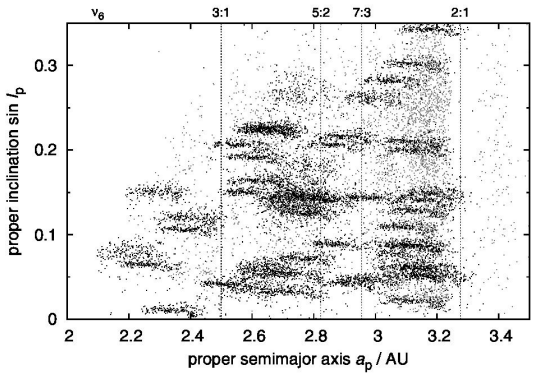


**Fig. 9.** Proper semimajor axis $a_p$ vs. proper inclination $\sin I_p$ for 100 synthetic asteroid families (black dots), evolved over 4 Gyr using a Monte-Carlo model. The assumed SFDs correspond to the Koronis family, but we show only $D > 10$ km bodies here. We also include $D > 10$ km background asteroids (grey dots) for comparison.

According to the resulting Fig. 8 the answer to the question is simple: the families do not overlap sufficiently, and they cannot be hidden that way. Moreover, if we take only bigger bodies ($D > 10$ km), these would be clustered even more tightly. The same is true for proper inclinations, which are usually more clustered than eccentricities, so families could be more easily recognised.

## 6. Dispersion of families by the Yarkovsky drift

In this section, we model long-term evolution of synthetic families driven by the Yarkovsky effect and chaotic diffusion. For one synthetic family located in the outer belt, we have performed a full $N$-body integration with the SWIFT package (Levison & Duncan 1994), which includes also an implementation of the Yarkovsky/YORP effect (Brož 2006) and second-order integrator by Laskar & Robutel (2001). We included 4 giant planets in this simulation. To speed-up the integration, we used ten times smaller sizes of the test particles and thus a ten times shorter time span (400 Myr instead of 4 Gyr). The selected time step is $\Delta t = 91$ d. We computed proper elements, namely their differences $\Delta a_p, \Delta e_p, \Delta \sin I_p$ between the initial and final positions.

Then we used a simple Monte-Carlo approach for the whole set of 100 synthetic families – we assigned a suitable drift $\Delta a_p(D)$ in semimajor axis, and also drifts in eccentricity $\Delta e_p$ and inclination $\Delta \sin I_p$ to each member of 100 families, respecting asteroid sizes, of course. This way we account for the Yarkovsky semimajor axis drift and also for interactions with mean-motion and secular resonances. This Monte-Carlo method tends to smear all structures, so we can regard our results as the upper limits for dispersion of families.

While the eccentricities of small asteroids (down to $D \simeq 2$ km) seem to be dispersed enough to hide the families, there are still some persistent structures in inclinations, which would be observable today. Moreover, large asteroids ($D \geq 10$ km) seem to be clustered even after 4 Gyr, so that more than 50% of families can be easily recognised against the background (see Fig. 9). We thus can conclude that it is not possible to disperse the families by the Yarkovsky effect alone.

## 7. Reduced physical lifetime of comets in the MB crossing zone

To illustrate the effects that the physical disruption of comets (due to volatile pressure build-up, amorphous/crystalline phase transitions, spin-up by jets, etc.) can have on the collisional evolution of the asteroid belt, we adopted here a simplistic assumption. We considered that no comet disrupt beyond 1.5 AU, whereas all comets disrupt the first time that they penetrate inside 1.5 AU. Both conditions are clearly not true in reality: some comets are observed to blow up beyond 1.5 AU, and others are seen to survive on an Earth-crossing orbit. Thus we adopted our disruption law just as an example of a drastic reduction of the number of comets with small perihelion distance, as required to explain the absence of evidence for a cometary bombardment on the Moon.

We then removed all those objects from output of comet evolution during the LHB that had a passage within 1.5 AU from the Sun, from the time of their first passage below this threshold. We then recomputed the mean intrinsic collision probability of a comet with the asteroid belt. The result is a factor ~3 smaller than when no physical disruption of comets is taken into account as in Fig. 6. The mean impact velocity with asteroids also decreases, from 12 km s$^{-1}$ to 8 km s$^{-1}$.

The resulting number of asteroid disruption events is thus decreased by a factor ~4.5, which can be also seen in the production function shown in Fig. 5 (right column). The production of families with $D_{PB} = 200$–$400$ km is consistent with observations, while the number of $D_{PB} \simeq 100$ km families is reduced to 30–70, but is still too high, by a factor 2–3. More importantly, the slope of the production function remains steeper than that of the observed function. Thus, our conclusion is that physical disruptions of comets alone cannot explain the observation, but may be an important factor to keep in mind for reconciling the model with the data.

## 8. Perturbation of families by migrating planets (a jumping-Jupiter scenario)

In principle, families created during the LHB may be perturbed by still-migrating planets. It is an open question what the exact orbital evolution of planets was at that time. Nevertheless, a

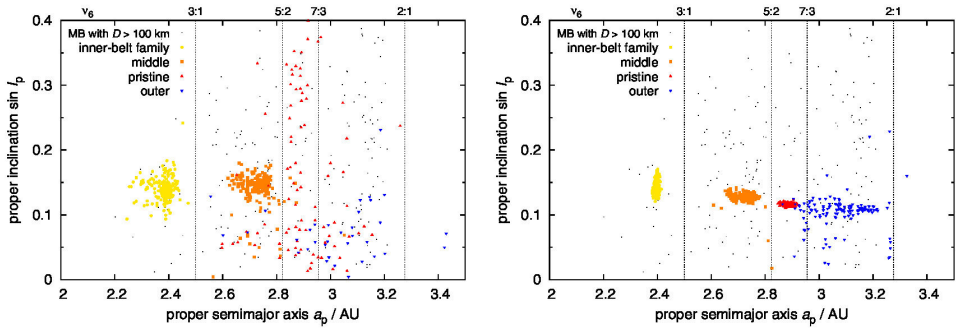


**Fig. 10.** Proper semimajor axis vs. proper inclination for four synthetic families (distinguished by symbols) as perturbed by giant-planet migration. *Left panel*: the case when families were evolved over the "jump" due to the encounter between Jupiter and Neptune. *Right panel*: the families created just after the jump and perturbed only by later phases of migration.

plausible scenario called a "jumping Jupiter" was presented by Morbidelli et al. (2010). It explains major features of the main belt (namely the paucity of high-inclination asteroids above the $\nu_6$ secular resonance), and is consistent with amplitudes of the secular frequencies of both giant and terrestrial planets and also with other features of the solar system. In this work, we thus investigated this particular migration scenario.

We used the data from Morbidelli et al. (2010) for the orbital evolution of giant planets. We then employed a modified SWIFT integrator, which read orbital elements for planets from an input file and calculated only the evolution of test particles. Four synthetic families located in the inner/middle/outer belt were integrated. We started the evolution of planets at various times, ranging from $t_0$ to $(t_0 + 4\,\mathrm{Myr})$ and stopped the integration at $(t_0 + 4\,\mathrm{My})$, in order to test the perturbation on families created in different phases of migration. Finally, we calculated proper elements of asteroids when the planets do not migrate anymore. (We also had to move planets smoothly to their exact current orbital positions.)

The results are shown in Fig. 10. While the proper eccentricities seem to be sufficiently perturbed and families are dispersed even when created at late phases of migration, the proper inclinations are not very dispersed, except for families in the outer asteroid belt that formed at the very beginning of the giant planet instability (which may be unlikely, as there must be a delay between the onset of planet instability and the beginning of the cometary flux through the asteroid belt). In most cases, the LHB families could still be identified as clumps in semi-major axis vs inclination space. We do not see any of such $(a_p, \sin I_p)$-clumps, dispersed in eccentricity, in the asteroid belt[6].

The conclusion is clear: it is not possible to destroy low-$e$ and low-$I$ families by perturbations arising from giant-planet migration, at least in the case of the "jumping-Jupiter" scenario[7].

## 9. Collisional comminution of asteroid families

We have already mentioned that the comminution is not sufficient to destroy a $D_{\mathrm{PB}} = 100\,\mathrm{km}$ family in the current environment of the main belt (Bottke et al. 2005).

However, the situation in case of the LHB scenario is different. Both the large population of comets and the several-times larger main belt, which has to withstand the cometary bombardment, contribute to the enhanced comminution of the LHB families. To estimate the amount of comminution, we performed the following calculations: i) for a selected collisional simulation, whose production function is close to the average one, we recorded the SFDs of all synthetic families created in the course of time; ii) for each synthetic family, we restarted the simulation from the time $t_0$ when the family was crated until 4 Gyr and saved the final SFD, i.e. after the comminution. The results are shown in Fig. 11.

It is now important to discuss criteria, which enable us to decide if the comminutioned synthetic family would indeed be observable or not. We use the following set of conditions: $D_{\mathrm{PB}} \geq 50\,\mathrm{km}$, $D_{\mathrm{LF}} \geq 10\,\mathrm{km}$ (largest fragment is the first or the second largest body, where the SFD becomes steep), LR/PB $< 0.5$ (i.e. a catastrophic disruption). Furthermore, we define $N_{\mathrm{members}}$ as the number of the remaining family members larger than observational limit $D_{\mathrm{limit}} \simeq 2\,\mathrm{km}$ and use a condition $N_{\mathrm{members}} \geq 10$. The latter number depends on the position of the family within the main belt, though. In the favourable "almost-empty" zone (between $a_p = 2.825$ and 2.955 AU), $N_{\mathrm{members}} \geq 10$ may be valid, but in a populated part of the MB one would need $N_{\mathrm{members}} \gtrsim 100$ to detect the family. The size distributions of synthetic families selected this way resemble the observed SFDs of the main belt families.

According to Fig. 5 (3rd row), where we can see the production functions after comminution for increasing values of $N_{\mathrm{members}}$, families with $D_{\mathrm{PB}} = 200$–$400\,\mathrm{km}$ remain more prominent than $D_{\mathrm{PB}} \simeq 100\,\mathrm{km}$ families simply because they contain much more members with $D > 10\,\mathrm{km}$ that survive intact. Our conclusion is thus that comminution may explain the paucity of the observed $D_{\mathrm{PB}} \simeq 100\,\mathrm{km}$ families.

## 10. "Pristine zone" between the 5:2 and 7:3 resonances

We now focus on the zone between the 5:2 and 7:3 mean-motion resonances, with $a_p = 2.825$ to 2.955 AU, which is not as populated as the surrounding regions of the main belt (see Fig. 1). This is a unique situation, because both bounding resonances are strong enough to prevent any asteroids from outside to enter this zone owing the Yarkovsky semimajor axis drift. Any family formation event in the surroundings has only a minor influence on this narrow region. It thus can be called "pristine zone" because it may resemble the belt prior to creation of big asteroid families.

[6] High-inclination families would be dispersed much more owing to the Kozai mechanism, because eccentricities that are sufficiently perturbed exhibit oscillations coupled with inclinations.

[7] The currently non-existent families around (107) Camilla and (121) Hermione – inferred from the existence of their satellites – cannot be destroyed in the jumping-Jupiter scenario, unless the families were actually pre-LHB and had experienced the jump.

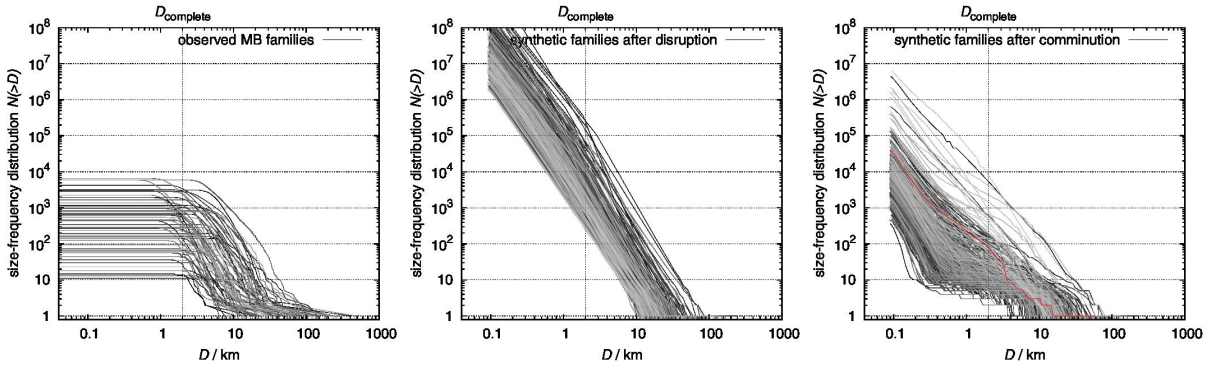


**Fig. 11.** *Left panel*: SFDs of the observed asteroid families. *Middle panel*: SFDs of 378 distinct synthetic families created during one of the collisional simulations of the MB and comets. Initially, all synthetic SFDs are very steep, in agreement with SPH simulations (Durda et al. 2007). We plot only the SFDs that fulfil the following criteria: $D_{\rm PB} \geq 50$ km, $D_{\rm LF} \geq 10$ km, LR/PB $< 0.5$ (i.e. catastrophic disruptions). *Right panel*: the evolved SFDs after comminution. Only a minority of families are observable now, since the number of remaining members larger than the observational limit $D_{\rm limit} \simeq 2$ km is often much smaller than 100. The SFD that we use for the simulation in Sect. 10 is denoted by red.

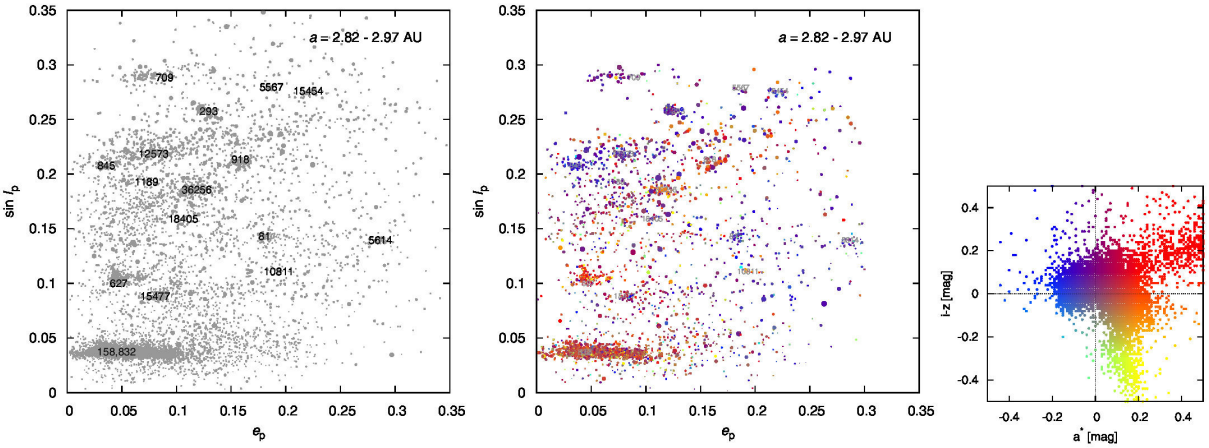


**Fig. 12.** "Pristine zone" of the main belt ($a_{\rm p} = 2.825$ to 2.955 AU) displayed on the proper eccentricity $e_{\rm p}$ vs. proper inclination $\sin I_{\rm p}$ plot. *Left panel*: the sizes of symbols correspond to the sizes of asteroids, the families are denoted by designations. *Right panel*: a subset of bodies for which SDSS data are available; the colours of symbols correspond to the SDSS colour indices $a^*$ and $i - z$ (Parker et al. 2008).

We identified nine previously unknown small families that are visible on the $(e_{\rm p}, \sin I_{\rm p})$ plot (see Fig. 12). They are confirmed by the SDSS colours and WISE albedos, too. Nevertheless, there is only one big and old family in this zone ($D_{\rm PB} \geq 100$ km), i.e. Koronis.

That at most one LHB family (Koronis) is observed in the "pristine zone" can give us a simple probabilistic estimate for the maximum number of disruptions during the LHB. We take the 192 existing main belt bodies which have $D \geq 100$ km and select randomly 100 of them that will break apart. We repeat this selection 1000 times and always count the number of families in the pristine zone. The resulting histogram is shown in Fig. 13. As we can see, there is very low (<0.001) probability that the number of families in the pristine zone is zero or one. On average we get eight families there, i.e. about half of the 16 asteroids with $D \geq 100$ km present in this zone. It seems that either the number of disruptions should be substantially lower than 100 or we expect to find at least some "remnants" of the LHB families here.

It is interesting that the SFD of an old comminutioned family is very flat in the range $D = 1$ to 10 km (see Fig. 11) – similar to those of some of the "less certain" observed families! We may speculate that the families like (918) Itha, (5567) Durisen,

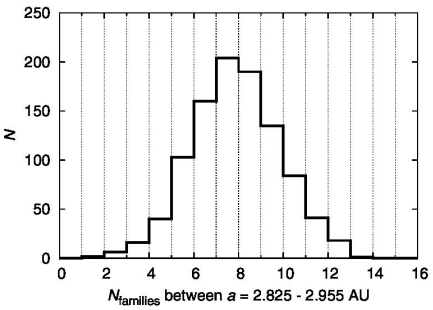


**Fig. 13.** Histogram for the expected number of LHB families located in the "pristine zone" of the main belt.

(12573) 1999 $NJ_{53}$, or (15454) 1998 $YB_3$ (all from the pristine zone) are actually remnants of larger and older families, even though they are denoted as young. It may be that the age estimate based on the $(a_{\rm p}, H)$ analysis is incorrect since small bodies were destroyed by comminution and spread by the Yarkovsky effect too far away from the largest remnant, so they can no longer be identified with the family.

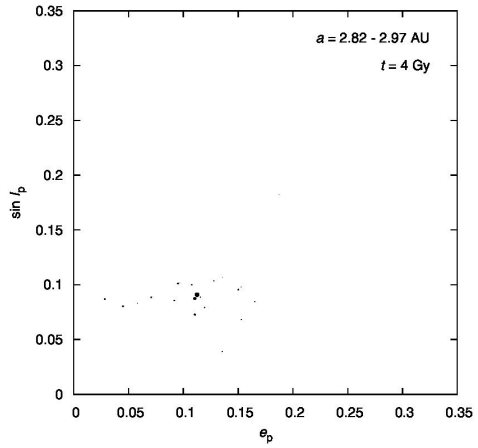


**Fig. 14.** Proper eccentricity vs. proper inclination of one synthetic old/comminutioned family evolved dynamically over 4 Gyr. Only a few family members ($N \simeq 10^1$) remained from the original number of $N(D \geq 2\,\mathrm{km}) \simeq 10^2$. The scales are the same as in Fig. 12, so we can compare it easily to the "pristine zone".

Finally, we have to ask an important question: what does an old/comminutioned family with $D_{\mathrm{PB}} \simeq 100$ km look like in proper-element space? To this aim, we created a synthetic family in the "pristine zone", and assumed the family has $N_{\mathrm{members}} \simeq 100$ larger than $D_{\mathrm{limit}} \simeq 2$ km and that the SFD is already flat in the $D = 1$ to 10 km range. We evolved the asteroids up to 4 Gyr due to the Yarkovsky effect and gravitational perturbations, using the $N$-body integrator as in Sect. 6. Most of the $D \simeq 2$ km bodies were lost in the course of the dynamical evolution, of course. The resulting family is shown in Fig. 14. We can also imagine that this family is placed in the pristine zone among other observed families, to get a feeling of whether it is easily observed or not (refer to Fig. 12).

It is clear that such family is hardly observable even in the almost empty zone of the main belt! Our conclusion is that the comminution (as given by the Boulder code) can explain the paucity of $D_{\mathrm{PB}} \simeq 100$ km LHB families, since we can hardly distinguish old families from the background.

## 11. Conclusions

In this paper we investigated the cometary bombardment of the asteroid belt at the time of the LHB, in the framework of the Nice model. There is much evidence of a high cometary flux through the giant planet region, but no strong evidence of a cometary bombardment on the Moon. This suggests that many comets broke up on their way to the inner solar system. By investigating the collisional evolution of the asteroid belt and comparing the results to the collection of actual collisional families, our aim was to constrain whether the asteroid belt experienced an intense cometary bombardment at the time of the LHB and, if possible, constrain the intensity of this bombardment.

Observations suggest that the number of collisional families is a very shallow function of parent-body size (that we call in this paper the "production function"). We show that the collisional activity of the asteroid belt as a closed system, i.e. without any external cometary bombardment, in general does not produce such a shallow production function. Moreover, the number of families with parent bodies larger than 200 km in diameter is in general too small compared to the observations. However, there is a lot of stochasticity in the collisional evolution of the asteroid belt, and about 5% of our simulations actually fit the observational constraints (shallowness of the production function and number of large families) quite well. Thus, in principle, there is no need for a bombardment due to external agents (i.e. the comets) to explain the asteroid family collection, provided that the real collisional evolution of the main belt was a "lucky" one and not the "average" one.

If one accounts for the bombardment provided by the comets crossing the main belt at the LHB time, predicted by the Nice model, one can easily justify the number of observed families with parent bodies larger than 200 km. However, the resulting production function is steep, and the number of families produced by parent bodies of 100 km is almost an order of magnitude too large.

We have investigated several processes that may decimate the number of families identifiable today with 100 km parent bodies, without considerably affecting the survival of families formed from larger parent bodies. Of all these processes, the collisional comminution of the families and their dispersal by the Yarkovsky effect are the most effective ones. Provided that the physical disruption of comets due to activity reduced the effective cometary flux through the belt by a factor of ≈5, the resulting distribution of families (and consequently the Nice model) is consistent with observations.

To better quantify the effects of various cometary-disruption laws, we computed the numbers of asteroid families for different critical perihelion distances $q_{\mathrm{crit}}$ and for different disruption probabilities $p_{\mathrm{crit}}$ of comets during a given time step ($\Delta t = 500$ yr in our case). The results are summarised in Fig. 15. Provided that comets are disrupted frequently enough, namely the critical perihelion distance has to be at least $q_{\mathrm{crit}} \gtrsim 1$ AU, while the probability of disruption is $p_{\mathrm{crit}} = 1$, the number of $D_{\mathrm{PB}} \geq 100$ km families drops by the aforementioned factor of ≈5. Alternatively, $q_{\mathrm{crit}}$ may be larger, but then comets have to survive multiple perihelion passages (i.e. $p_{\mathrm{crit}}$ have to be lower than 1). It would be very useful to test these conditions by independent models of the evolution and physical disruptions of comets. Such additional constraints on cometary-disruption laws would then enable study of the original SFD of the cometary disk in more detail.

We can also think of two "alternative" explanations: i) physical lifetime of comets was strongly size-dependent so that smaller bodies break up easily compared to bigger ones; ii) high-velocity collisions between hard targets (asteroids) and very weak projectiles (comets) may result in different outcomes than in low-velocity regimes explored so far. Our work thus may also serve as a motivation for further SPH simulations.

We finally emphasize that any collisional/dynamical models of the main asteroid belt would benefit from the following advances:

i) determination of reliable masses of asteroids of various classes. This may be at least partly achieved by the *Gaia* mission in the near future. Using up-to-date sizes and shape models (volumes) of asteroids one can then derive their densities, which are directly related to ages of asteroid families.
ii) Development of methods for identifying asteroid families and possibly targeted observations of larger asteroids addressing their membership, which is sometimes critical for constructing SFDs and for estimating parent-body sizes.
iii) An extension of the SHP simulations for both smaller and larger targets, to assure that the scaling we use now is valid. Studies and laboratory measurements of equations of states for different materials (e.g. cometary-like, porous) are closely related to this issue.

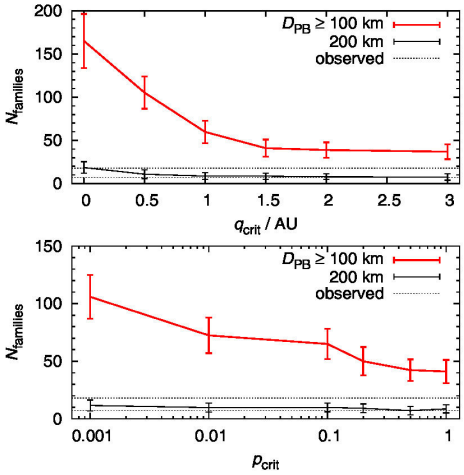


**Fig. 15.** Numbers of collisional families for different critical perihelion distances $q_{crit}$ at which comets break up and disruption probabilities $p_{crit}$ during one time step ($\Delta t$ = 500 yr). In the *top panel*, we vary $q_{crit}$ while keeping $p_{crit}$ = 1 constant. In the *bottom panel*, $q_{crit}$ = 1.5 AU is constant and we vary $p_{crit}$. We always show the number of catastrophic disruptions with parent-body sizes $D_{PB} \geq 100$ km (red line) and 200 km (black line). The error bars indicate typical (1-$\sigma$) spreads of Boulder simulations with different random seeds. The observed numbers of corresponding families are indicated by thin dotted lines.

The topics outlined above seem to be the most urgent developments to be pursued in the future.

*Acknowledgements.* The work of M.B. and D.V. has been supported by the Grant Agency of the Czech Republic (grants no. 205/08/0064, and 13-01308S) and the Research Programme MSM0021620860 of the Czech Ministry of Education. The work of W.B. and D.N. was supported by NASA's Lunar Science Institute (Center for Lunar Origin and Evolution, grant number NNA09DB32A). We also acknowledge the usage of computers of the Observatory and Planetarium in Hradec Králové. We thank Alberto Cellino for a careful review which helped to improve final version of the paper.

## References

Bendjoya, P., Cellino, A., Froeschlé, C., & Zappalà, V. 1993, A&A, 272, 651
Benz, W., & Asphaug, E. 1999, Icarus, 142, 5
Bogard, D. D. 1995, Meteoritics, 30, 244
Bogard, D. D. 2011, Chemie der Erde – Geochemistry, 71, 207
Bottke, W. F., Vokrouhlický, D., Brož, M., Nesvorný, D., & Morbidelli, A. 2001, Science, 294, 1693
Bottke, W. F., Durda, D. D., Nesvorný, D., et al. 2005, Icarus, 175, 111
Bottke, W. F., Nesvorný, D., Vokrouhlický, D., & Morbidelli, A. 2010, AJ, 139, 994
Bottke, W. F., Vokrouhlický, D., Minton, D., et al. 2012, Nature, 485, 78
Brož, M. 2006, Ph.D. Thesis, Charles University
Brož, M., Vokrouhlický, D., Morbidelli, A., Nesvorný, D., & Bottke, W. F. 2011, MNRAS, 414, 2716
Carruba, V. 2009, MNRAS, 398, 1512
Carruba, V. 2010, MNRAS, 408, 580
Carry, B. 2012, Planet. Space Sci., 73, 98
Cellino, A., Zappalà, V., di Martino, M., Farinella, P., & Paolicchi, P. 1987, Icarus, 70, 546
Chapman, C. R., Cohen, B. A., & Grinspoon, D. H. 2007, Icarus, 189, 233
Charnoz, S., Morbidelli, A., Dones, L., & Salmon, J. 2009, Icarus, 199, 413
Cohen, B. A., Swindle, T. D., & Kring, D. A. 2000, Science, 290, 1754
Dahlgren, M. 1998, A&A, 336, 1056
Durda, D. D., Bottke, W. F., Nesvorný, D., et al. 2007, Icarus, 186, 498
Foglia, S., & Masi, G., 2004, Minor Planet Bull., 31, 100
Gil-Hutton, R. 2006, Icarus, 183, 83
Gomes, R., Levison, H. F., Tsiganis, K., & Morbidelli, A. 2005, Nature, 435, 466
Hartmann, W. K., Ryder, G., Dones, L., & Grinspoon, D. 2000, in Origin of the Earth and Moon, eds. R. M. Canup, & K. Righter (Tucson: University of Arizona Press), 493
Hartmann, W. K., Quantin, C., & Mangold, N. 2007, Icarus, 186, 11
Keil, K. 2002, in Asteroids III, eds. W. F. Bottke Jr., A. Cellino, P. Paolicchi, & R. P. Binzel (Tucson: University of Arizona Press), 573
Kirchoff, M. R., & Schenk, P. 2010, Icarus, 206, 485
Knežević, Z., & Milani, A. 2003, A&A, 403, 1165
Koeberl, C. 2004, Geochim. Cosmochim. Acta, 68, 931
Kring, D. A., & Cohen, B. A. 2002, J. Geophys. Res., 107, 41
Laskar, J., & Robutel, P. 2001, Celest. Mech. Dyn. Astron., 80, 39
Levison, H. F., & Duncan, M. 1994, Icarus, 108, 18
Levison, H. F., Bottke, W. F., Gounelle, M., et al. 2009, Nature, 460, 364
Margot, J.-L., & Rojo, P. 2007, BAAS, 39, 1608
Marzari, F., Farinella, P., & Davis, D. R. 1999, Icarus, 142, 63
Masiero, J. P., Mainzer A. K., Grav, T., et al. 2011, ApJ, 741, 68
Michel, P., Tanga, P., Benz, W., & Richardson, D. C. 2002, Icarus, 160, 10
Michel, P., Jutzi, M., Richardson, D. C., & Benz, W. 2011, Icarus, 211, 535
Minton, D. A., & Malhotra, R. 2009, Nature, 457, 1109
Minton, D. A., & Malhotra, R. 2010, Icarus, 207, 744
Morbidelli, A. 2010, Comptes Rendus Phys., 11, 651
Morbidelli, A., Tsiganis, K., Crida, A., Levison, H. F., & Gomes, R. 2007, AJ, 134, 1790
Morbidelli, A., Levison, H. F., Bottke, W. F., Dones, L., & Nesvorný, D. 2009, Icarus, 202, 310
Morbidelli, A., Brasser, R., Gomes, R., Levison, H. F., & Tsiganis, K. 2010, AJ, 140, 1391
Morbidelli, A., Marchi, S., & Bottke, W. F. 2012, LPI Cont. 1649, 53
Molnar, L. A., & Haegert, M. J. 2009, BAAS, 41, 2705
Nesvorný, D. 2010, EAR-A-VARGBDET-5-NESVORNYFAM-V1.0, NASA Planetary Data System
Nesvorný, D., & Vokrouhlický, D. 2006, AJ, 132, 1950
Nesvorný, D., Morbidelli, A., Vokrouhlický, D., Bottke, W. F., & Brož, M. 2002, Icarus, 157, 155
Nesvorný, D., Jedicke, R., Whiteley, R. J., & Ivezić, Ž. 2005, Icarus, 173, 132
Nesvorný, D., Vokrouhlický, D., & Morbidelli, A. 2007, AJ, 133, 1962
Nesvorný, D., Vokrouhlický, D., Morbidelli, A., & Bottke, W. F. 2009, Icarus, 200, 698
Neukum, G., Ivanov, B. A., & Hartmann, W. K. 2001, Space Sci. Rev., 96, 55
Norman, M. D., & Nemchin, A. A. 2012, LPI Cont., 1659, 1368
Novaković, B. 2010, MNRAS, 407, 1477
Novaković, B., Tsiganis, K., & Knežević, Z. 2010, Celest. Mech. Dyn. Astron., 107, 35
Novaković, B., Cellino, A., & Knežević, Z. 2011, Icarus, 216, 69
Parker, A., Ivezić, Ž., Jurić, M., et al. 2008, Icarus, 198, 138
Ryder, G., Koeberl, C., & Mojzsis, S. J. 2000, in Origin of the Earth and Moon, eds. R. M. Canup, & K. Righter (Tucson: University of Arizona Press), 475
Sheppard, S. S., & Trujillo, C. A. 2010, ApJ, 723, L233
Strom, R. G., Malhotra, R., Ito, T., Yoshida, F., & Kring, D. A. 2005, Science, 309, 1847
Swindle, T. D., Isachsen, C. E., Weirich, J. R., & Kring, D. A. 2009, Meteor. Planet. Sci., 44, 747
Tagle, R. 2005, LPI Cont., 36, 2008
Tanga, P., Cellino, A., Michel, P., et al. 1999, Icarus, 141, 65
Tedesco, E. F., Noah, P. V., Noah, M., & Price, S. D. 2002, AJ, 123, 1056
Tera, F., Papanastassiou, D. A., & Wasserburg, G. J. 1974, Earth Planet. Sci. Lett., 22, 1
Tsiganis, K., Gomes, R., Morbidelli, A., & Levison, H. F. 2005, Nature, 435, 459
Thomas, P. C., Binzel, R. P., Gaffey, M. J., et al. 1997, Science, 277, 1492
Vokrouhlický, D., & Nesvorný, D. 2011, AJ, 142, 26
Vokrouhlický, D., Brož, M., Bottke, W. F., Nesvorný, D., & Morbidelli, A. 2006, Icarus, 182, 118
Vokrouhlický, D., Nesvorný, D., & Levison, H. F. 2008, AJ, 136, 1463
Vokrouhlický, D., Nesvorný, D., Bottke, W. F., & Morbidelli, A. 2010, AJ, 139, 2148
Warner, B. D., Harris, A. W., Vokrouhlický, D., Nesvorný, D., & Bottke, W. F. 2009, Icarus, 204, 172
Weidenschilling, S. J. 2000, Space Sci. Rev., 92, 295
Zappalà, V., Bendjoya, Ph., Cellino, A., Farinella, P., & Froeschlé, C. 1995, Icarus, 116, 291

Pages 14 to 16 are available in the electronic edition of the journal at http://www.aanda.org

**Table 1.** A list of asteroid families and their physical parameters.

| Designation | | $v_{cutoff}$ m/s | $N$ | $p_V$ | Tax. | $D_{PB}$ km | $D_{Durda}$ km | LR/PB | $v_{esc}$ m/s | $q_1$ | $q_2$ | Age Gyr | Notes, references |
|---|---|---|---|---|---|---|---|---|---|---|---|---|---|
| 3 | Juno | 50 | 449 | 0.250 | S | 233 | ? | 0.999 | 139 | −4.9 | −3.2 | <0.7 | cratering, Nesvorný et al. (2005) |
| 4 | Vesta | 60 | 11 169 | 0.351w | V | 530 | 425! | 0.995 | 314 | −4.5 | −2.9 | 1.0 ± 0.25 | cratering, Marchi et al. (2012) |
| 8 | Flora | 60 | 5284 | 0.304w | S | 150c | 160 | 0.81–0.68 | 88 | −3.4 | −2.9 | 1.0 ± 0.5 | cut by $\nu_6$ resonance, LL chondrites |
| 10 | Hygiea | 70 | 3122 | 0.055 | C,B | 410 | 442 | 0.976–0.78 | 243 | −4.2 | −3.2 | 2.0 ± 1.0 | LHB? cratering |
| 15 | Eunomia | 50 | 2867 | 0.187 | S | 259 | 292 | 0.958–0.66 | 153 | −5.6 | −2.3 | 2.5 ± 0.5 | LHB? Michel et al. (2002) |
| 20 | Massalia | 40 | 2980 | 0.215 | S | 146 | 144 | 0.995 | 86 | −5.0 | −3.0 | 0.3 ± 0.1 | |
| 24 | Themis | 70 | 3581 | 0.066 | C | 268c | 380–430! | 0.43–0.09 | 158 | −2.7 | −2.4 | 2.5 ± 1.0 | LHB? |
| 44 | Nysa (Polana) | 60 | 9957 | 0.278w | S | 81c | ? | 0.65 | 48 | −6.9 | −2.6(0.5) | <1.5 | overlaps with the Polana family |
| 46 | Hestia | 65 | 95 | 0.053 | S | 124 | 153 | 0.992–0.53 | 74 | −3.3 | −2.0 | <0.2 | cratering, close to J3/1 resonance |
| 87 | Sylvia | 110 | 71 | 0.045 | C/X | 261 | 272 | 0.994–0.88 | 154 | −5.2 | −2.4 | 1.0–3.8 | LHB? cratering, Vokrouhlický et al. (2010) |
| 128 | Nemesis | 60 | 654 | 0.052 | C | 189 | 197 | 0.987–0.87 | 112 | −3.4 | −3.3 | 0.2 ± 0.1 | |
| 137 | Meliboea | 95 | 199 | 0.054 | C | 174c | 240–290! | 0.59–0.20 | 102 | −1.9 | −1.8 | <3.0 | old? |
| 142 | Polana (Nysa) | 60 | 3443 | 0.055w | C | 75 | ? | 0.42 | 45 | −7.0 | −3.6 | <1.5 | overlaps with Nysa |
| 145 | Adeona | 50 | 1161 | 0.065 | C | 171c | 185 | 0.69–0.54 | 101 | −5.2 | −2.8 | 0.7 ± 0.5 | cut by J5/2 resonance |
| 158 | Koronis | 50 | 4225 | 0.147 | S | 122c | 170-180 | 0.024–0.009 | 68 | −3.6(0.3) | −2.3 | 2.5 ± 1.0 | LHB? |
| 163 | Erigone | 60 | 1059 | 0.056 | C/X | 79 | 114 | 0.79–0.26 | 46 | ? | −3.6 | 0.3 ± 0.2 | |
| 170 | Maria | 80 | 3094 | 0.249w | S | 107c | 120-130 | 0.070–0.048 | 63 | −2.5(0.3) | −2.8 | 3.0 ± 1.0 | LHB? |
| 221 | Eos | 50 | 5976 | 0.130 | K | 208c | 381! | 0.13–0.020 | 123 | −3.5 | −2.1 | 1.3 ± 0.2 | |
| 283 | Emma | 75 | 345 | 0.050 | – | 152 | 185 | 0.92–0.51 | 90 | ? | −3.2 | <1.0 | satellite |
| 293 | Brasilia | 60 | 282 | 0.175w | C/X | 34 | ? | 0.020 | 20 | −1.4(0.5) | −3.7 | 0.05 ± 0.04 | (293) is interloper |
| 363 | Padua (Lydia) | 50 | 596 | 0.097 | C/X | 76 | 106 | 0.045–0.017 | 45 | −1.8 | −3.0 | 0.3 ± 0.2 | |
| 396 | Aeolia | 20 | 124 | 0.171 | C/X | 35 | 39 | 0.966–0.70 | 20 | ? | −4.3 | <0.1 | cratering |
| 410 | Chloris | 90 | 259 | 0.057 | C | 126c | 154 | 0.952–0.52 | 74 | ? | −2.1 | 0.7 ± 0.4 | |
| 490 | Veritas | – | – | – | C,P,D | – | 100–177 | – | – | – | – | 0.0083 ± 0.0005 | (490) is likely interloper (Michel et al. 2011) |
| 569 | Misa | 70 | 543 | 0.031 | C | 88c | 117 | 0.58–0.25 | 52 | −3.9 | −2.3 | 0.5 ± 0.2 | |
| 606 | Brangane | 30 | 81 | 0.102 | S | 37 | 46 | 0.92–0.48 | 22 | ? | −3.8 | 0.05 ± 0.04 | |
| 668 | Dora | 50 | 837 | 0.054 | C | 85 | 165! | 0.031–0.004 | 50 | −4.2 | −1.9 | 0.5 ± 0.2 | |
| 808 | Merxia | 50 | 549 | 0.227 | S | 37 | 121! | 0.66–0.018 | 22 | −2.7 | −3.4 | 0.3 ± 0.2 | |
| 832 | Karin | – | – | – | S | – | 40 | – | – | – | – | 0.0058 ± 0.0002 | |
| 845 | Naema | 30 | 173 | 0.081 | C | 77c | 81 | 0.35–0.30 | 46 | −5.2 | −2.9 | 0.1 ± 0.05 | |
| 847 | Agnia | 40 | 1077 | 0.177 | S | 39 | 61 | 0.38–0.10 | 23 | −2.8 | −3.1 | 0.2 ± 0.1 | |
| 1128 | Astrid | 50 | 265 | 0.079 | C | 43c | ? | 0.52 | 25 | −1.7 | −2.6 | 0.1 ± 0.05 | |
| 1272 | Gefion | 60 | 19 477 | 0.20 | S | 74c | 100–150! | 0.001–0.004 | 60 | −4.3 | −2.5 | 0.48 ± 0.05 | Nesvorný et al. (2009), L chondrites |
| 1400 | Tirela | 80 | 1001 | 0.070 | S | 86 | – | 0.12 | 86 | −4.2 | −3.4 | <1.0 | |
| 1658 | Innes | 70 | 621 | 0.246w | S | 27 | ? | 0.14 | 16 | −4.9 | −3.5 | <0.7 | (1644) Rafita is interloper |
| 1726 | Hoffmeister | 40 | 822 | 0.035 | C | 93c | 134 | 0.022–0.007 | 55 | −4.5 | −2.7 | 0.3 ± 0.2 | |
| 3556 | Lixiaohua | 60 | 439 | 0.044w | C/X | 62 | 220! | 0.029–0.001 | 35 | −6.1 | −3.3 | 0.15 ± 0.05 | Novaković et al. (2010) |
| 3815 | Konig | 60 | 177 | 0.044 | C | 33 | ? | 0.32 | 20 | ? | −3.0 | <0.1 | (1639) Bower is interloper |
| 4652 | Iannini | – | – | – | S | – | – | – | – | – | – | 0.005 ± 0.005 | |

**Notes.** There are the following columns: $v_{cutoff}$ is the selected cut–off velocity for the hierarchical clustering, $N$ the corresponding number of family members, $p_V$ the adopted value of the geometric albedo for family members which do not have measured diameters (from Tedesco et al. 2002 or Masiero et al. 2011, a letter "w" indicates it was necessary to use the WISE data to obtain median/mean albedo), taxonomic classification (according to the Sloan DSS MOC 4 colours, Parker et al. 2008), $D_{PB}$ parent body size, an additional "c" letter indicates that we prolonged the SFD slope down to zero $D$ (a typical uncertainty is 10%), $D_{Durda}$ PB size inferred from SPH simulations (Durda et al. 2007), an exclamation mark denotes a significant mismatch with $D_{PB}$, LR/PB the ratio of the volumes of the largest remnant to the parent body (an uncertainty corresponds to the last figure, a range is given if both $D_{PB}$ and $D_{Durda}$ are known), $v_{esc}$ the escape velocity, $q_1$ the slope of the SFD for larger $D$, $q_2$ the slope for smaller $D$ (a typical uncertainty of the slopes is 0.2, if not indicated otherwise), dynamical age including its uncertainty.

**Table 1.** continued.

| Designation | | $v_{cutoff}$ m/s | $N$ | $p_V$ | Tax. | $D_{PB}$ km | $D_{Durda}$ km | LR/PB | $v_{esc}$ m/s | $q_1$ | $q_2$ | Age Gyr | Notes, references |
|---|---|---|---|---|---|---|---|---|---|---|---|---|---|
| 9506 | Telramund | 40 | 146 | 0.217w | S | 22 | – | 0.05 | 13 | −3.9 | −3.7 | <0.5 | |
| 18 405 | 1993 $FY_{12}$ | 50 | 44 | 0.171w | C/X | 15 | – | 0.23 | 15 | −2.4 | −2.4 | <0.2 | cut by J5/2 resonance |
| 158 | $Koronis_{(2)}$ | – | – | – | S | 35 | – | – | – | – | – | 0.015 ± 0.005 | cratering, Molnar & Haegert (2009) |
| 298 | Baptistina | 50 | 1249 | 0.160w | C/X | 35c | – | 0.17 | 21 | −3.6 | −2.4 | <0.3 | overlaps with the Flora family |
| 434 | Hungaria | 200 | 4598 | 0.35 | E | 25 | – | 0.15 | 15 | −5.9 | −3.1 | 0.5 ± 0.2 | Warner et al. (2010) |
| 627 | Charis | 80 | 235 | 0.081 | S | >60 | – | 0.53 | 35 | ? | −3.4 | <1.0 | |
| 778 | Theobalda | 85 | 154 | 0.060 | C | 97c | – | 0.29 | 57 | ? | −2.9 | 0.007 ± 0.002 | cratering, Novaković (2010) |
| 302 | Clarissa | 30 | 75 | 0.054 | C | 39 | – | 0.96 | 23 | ? | −3.1 | <0.1 | cratering, Nesvorný (2010) |
| 656 | Beagle | 24 | 63 | 0.089 | C | 64 | – | 0.56 | 38 | −1.3 | −1.4 | <0.2 | |
| 752 | Sulamitis | 60 | 191 | 0.042 | C | 65 | – | 0.83 | 39 | −6.5 | −2.3 | <0.4 | |
| 1189 | Terentia | 50 | 18 | 0.070 | C | 56 | – | 0.990 | 33 | ? | −2.6? | <0.2 | cratering |
| 1892 | Lucienne | 100 | 57 | 0.223w | S | 14 | – | 0.71 | 8 | ? | −4.4 | <0.3 | |
| 7353 | Kazvia | 50 | 23 | 0.206w | S | 16 | – | 0.57 | 8 | ? | −1.8 | <0.1 | |
| 10 811 | Lau | 100 | 15 | 0.273w | S | 11 | – | 0.77 | 5 | ? | −2.8 | <0.1 | |
| 18 466 | 1995 $SU_{37}$ | 40 | 71 | 0.241w | S | 14 | – | 0.045 | 7 | ? | −5.0 | <0.3 | |
| 1270 | Datura | – | – | – | S | – | – | – | – | – | – | 0.00045–0.00060 | identified in osculating-element space, |
| 14 627 | Emilkowalski | – | – | – | C/X | – | – | – | – | – | – | 0.00019–0.00025 | Nesvorný & Vokrouhlický (2006) |
| 16 598 | 1992 $YC_2$ | – | – | – | S | – | – | – | – | – | – | 0.00005–0.00025 | |
| 21 509 | Lucascavin | – | – | – | S | – | – | – | – | – | – | 0.0003–0.0008 | |
| 2384 | Schulhof | – | – | – | S | – | – | – | – | – | – | 0.0007–0.0009 | Vokrouhlický & Nesvorný (2011) |
| 27 | Euterpe | 70 | 268 | 0.260w | S | 118c | – | 0.998 | 70 | −2.9 | −2.2 | <1.0 | cratering, Parker et al. (2008) |
| 375 | Ursula | 80 | 777 | 0.057w | C | 203c | 240–280 | 0.71–0.43 | 120 | −4.1 | −2.3 | <3.5 | old? |
| 1044 | Teutonia | 50 | 1950 | 0.343 | S | 27–120 | – | 0.17–0.98 | 16–71 | −3.5 | −3.9 | <0.5 | depends on (5) Astraea membership |
| 1296 | Andree | 60 | 401 | 0.290w | S | 17–74 | – | 0.010–0.95 | 10–43 | ? | −2.9(0.5) | <1.0 | depends on (79) Eurynome membership |
| 2007 | McCuskey | 34 | 236 | 0.06 | C | 29 | – | 0.41 | 17 | ? | −5.6 | <0.5 | overlaps with Nysa/Polana |
| 2085 | Henan | 54 | 946 | 0.200w | S | 27 | – | 0.13 | 16 | −4.2 | −3.2 | <1.0 | |
| 2262 | Mitidika | 83 | 410 | 0.064w | C | 49-79c | – | 0.037–0.81 | 26–46 | −4.5 | −2.2 | <1.0 | depends on (785) Zwetana membership, (2262) is interloper, overlaps with Juno |
| 2 | Pallas | 200 | 64 | 0.163 | B | 498c | – | 0.9996 | 295 | ? | −2.2 | <0.5 | high-$I$, Carruba (2010) |
| 25 | Phocaea | 160 | 1370 | 0.22 | S | 92 | – | 0.54 | 55 | −3.1 | −2.4 | <2.2 | old? high-$I/e$, cut by $\nu_6$ resonance, Carruba (2009) |
| 148 | Gallia | 150 | 57 | 0.169 | S | 98 | – | 0.058 | 58 | ? | −3.6 | <0.45 | high-$I$ |
| 480 | Hansa | 150 | 651 | 0.256 | S | 60 | – | 0.83 | 35 | −4.9 | −3.2 | <1.6 | high-$I$ |
| 686 | Gersuind | 130 | 178 | 0.146 | S | 52c | – | 0.48 | 40 | ? | −2.7 | <0.8 | high-$I$, Gil-Hutton (2006) |
| 945 | Barcelona | 110 | 129 | 0.248 | S | 28 | – | 0.77 | 16 | ? | −3.5 | <0.35 | high-$I$, Foglia & Masi (2004) |
| 1222 | Tina | 110 | 37 | 0.338 | S | 21 | – | 0.94 | 12 | ? | −4.1 | <0.15 | high-$I$ |
| 4203 | Brucato | – | – | – | – | – | – | – | – | – | – | <1.3 | in frequency space |
| 31 | Euphrosyne | 100 | 851 | 0.056 | C | 259 | – | 0.97 | 153 | −4.9 | −3.9 | <1.5 | cratering, high-$I$, Foglia & Massi (2004) |
| 702 | Alauda | 120 | 791 | 0.070 | B | 218c | 290-330! | 0.025 | 129 | −3.9 | −2.4 | <3.5 | old? high-$I$, cut by J2/1 resonance, satellite (Margot & Rojo 2007) |
| 107 | Camilla | ? | ? | 0.054 | – | >226 | ? | ? | ? | ? | ? | 3.8? | LHB? Cybele region, non-existent today, |
| 121 | Hermione | ? | ? | 0.058 | – | >209 | ? | ? | ? | ? | ? | 3.8? | LHB? Vokrouhlický et al. (2010) |

→ 138 ←

→ 139 ←

**Table 1.** continued.

| Designation | | $v_{cutoff}$ m/s | $N$ | $p_V$ | Tax. | $D_{PB}$ km | $D_{Durda}$ km | LR/PB | $v_{esc}$ m/s | $q_1$ | $q_2$ | Age Gyr | Notes, references |
|---|---|---|---|---|---|---|---|---|---|---|---|---|---|
| 1303 | Luthera | 100 | 142 | 0.043 | X | 92 | – | 0.81 | 54 | −3.9 | −2.7 | <0.5 | above (375) Ursula |
| 1547 | Nele | 20 | 57 | 0.311w | X | 19 | – | 0.85 | 11 | ? | −2.8(0.3) | <0.04 | close to (3) Juno |
| 2732 | Witt | 60 | 985 | 0.260w | S | 25 | – | 0.082 | 15 | −4.0(0.3) | −3.8 | <1.0 | only part with $\sin I > 0.099$, above (363) Padua |
| 81 | Terpsichore | 120 | 70 | 0.052 | C | 119 | – | 0.993 | 71 | ? | −4.4 | <0.5 | cratering, less-certain families in the "pristine zone" |
| 709 | Fringilla | 140 | 60 | 0.047 | X | 99c | 130-140 | 0.93–0.41 | 59 | −6.2 | −1.7 | <2.5 | old? |
| 918 | Itha | 140 | 63 | 0.23 | S | 38 | – | 0.16 | 22 | −2.7 | −1.5 | <1.5 | shallow SFD |
| 5567 | Durisen | 100 | 18 | 0.044w | X | 42 | – | 0.89 | 25 | ? | −1.7 | <0.5 | shallow SFD |
| 5614 | Yakovlev | 100 | 34 | 0.05 | C | 22 | – | 0.28 | 13 | ? | −3.2 | <0.2 | |
| 12 573 | 1999 $NJ_{53}$ | 40 | 13 | 0.190w | C | 15 | – | 0.13 | 9 | ? | −2.0(0.5) | <0.6 | incomplete SFD |
| 15 454 | 1998 $YB_3$ | 50 | 14 | 0.054w | C | 21 | – | 0.41 | 13 | ? | −1.6(0.3) | <0.5 | shallow SFD |
| 15 477 | 1999 $CG_1$ | 110 | 144 | 0.098w | S | 25 | – | 0.065 | 14 | ? | −4.6(0.5) | <1.5 | |
| 36 256 | 1999 $XT_{17}$ | 60 | 30 | 0.210w | S | 17 | – | 0.037 | 10 | ? | −1.4(0.5) | <0.3 | shallow SFD |

# References


Alexandersen, M., Gladman, B., Greenstreet, S., Kavelaars, J.J., Petit, J.M., Gwyn, S., 2013. A Uranian Trojan and the Frequency of Temporary Giant-Planet Co-Orbitals. Science 341, 994–997. doi:10.1126/science.1238072, arXiv:1303.5774.

Beaugé, C., Roig, F., 2001. A Semianalytical Model for the Motion of the Trojan Asteroids: Proper Elements and Families. Icarus 153, 391–415. doi:10.1006/icar.2001.6699.

Benavidez, P.G., Durda, D.D., Enke, B., Campo Bagatin, A., Richardson, D.C., Asphaug, E., Bottke, W.F., 2018. Impact simulation in the gravity regime: Exploring the effects of parent body size and internal structure. Icarus 304, 143–161. doi:10.1016/j.icarus.2017.05.030.

Benavidez, P.G., Durda, D.D., Enke, B.L., Bottke, W.F., Nesvorný, D., Richardson, D.C., Asphaug, E., Merline, W.J., 2012. A comparison between rubble-pile and monolithic targets in impact simulations: Application to asteroid satellites and family size distributions. Icarus 219, 57–76. doi:10.1016/j.icarus.2012.01.015.

Benz, W., 1990. Smooth Particle Hydrodynamics - a Review, in: Buchler, J.R. (Ed.), Numerical Modelling of Nonlinear Stellar Pulsations Problems and Prospects, p. 269.

Benz, W., Asphaug, E., 1994. Impact Simulations with Fracture. I. Method and Tests. Icarus 107, 98–116. doi:10.1006/icar.1994.1009.

Benz, W., Asphaug, E., 1999. Catastrophic Disruptions Revisited. Icarus 142, 5–20. doi:10.1006/icar.1999.6204, arXiv:astro-ph/9907117.

Bertotti, B., Farinella, P., Vokrouhlick, D., 2003. Physics of the Solar System — Dynamics and Evolution, Space Physics, and Spacetime Structure.. volume 293. doi:10.1007/978-94-010-0233-2.

Bottke, W.F., Brož, M., O'Brien, D.P., Campo Bagatin, A., Morbidelli, A., Marchi, S., 2015. The Collisional Evolution of the Main Asteroid Belt. pp. 701–724. doi:10.2458/azu_uapress_9780816532131-ch036.

Bowell, E., Virtanen, J., Muinonen, K., Boattini, A., 2002. Asteroid Orbit Computation. pp. 27–43.

Brasser, R., Morbidelli, A., Gomes, R., Tsiganis, K., Levison, H.F., 2009. Constructing the secular architecture of the solar system II: the terrestrial planets. Astron. Astrophys. 507, 1053–1065. doi:10.1051/0004-6361/200912878, arXiv:0909.1891.

Brož, M., 2021. Hydrodynamika v astronomii. Charles Univ., http://sirrah.troja.mff.cuni.cz/~mira/hydrodynamika/ .

Brož, M., Chrenko, O., Nesvorný, D., Dauphas, N., 2021. Early terrestrial planet formation by torque-driven convergent migration of planetary embryos. Nature Astronomy doi:10.1038/s41550-021-01383-3.

Brož, M., Morbidelli, A., Bottke, W.F., Rozehnal, J., Vokrouhlický, D., Nesvorný, D., 2013. Constraining the cometary flux through the asteroid belt during the late heavy bombardment. Astron. Astrophys. 551, A117. doi:10.1051/0004-6361/201219296, arXiv:1301.6221.

Brož, M., Rozehnal, J., 2011. Eurybates — the only asteroid family among Trojans? Mon. Not. R. Astron. Soc. 414, 565–574. doi:10.1111/j.1365-2966.2011.18420.x, arXiv:1109.1109.

Brož, M., Vokrouhlický, D., Morbidelli, A., Nesvorný, D., Bottke, W.F., 2011. Did the Hilda collisional family form during the late heavy bombardment? Mon. Not. R. Astron. Soc. 414, 2716–2727. doi:10.1111/j.1365-2966.2011.18587.x, arXiv:1109.1114.

Brown, M.E., Levison, H.F., Noll, K.S., Binzel, R., Buie, M.W., Grundy, W., Marchi, S., Olkin, C.B., Spencer, J., Statler, T.S., Weaver, H., 2021. The orbit and density of the Jupiter Trojan satellite system Eurybates-Queta. arXiv e-prints , arXiv:2106.02079arXiv:2106.02079.

Brown, M.E., Schemel, M., 2021. Colors of Jupiter Trojan Dynamical Families as Measured by the Zwicky Transient Facility. Research Notes of the American Astronomical Society 5, 42. doi:10.3847/2515-5172/abeb7d.

Carruba, V., Nesvorný, D., 2016. Constraints on the original ejection velocity fields of asteroid families. Mon. Not. R. Astron. Soc. 457, 1332–1338. doi:10.1093/mnras/stw043, arXiv:1602.04486.

Chrenko, O., Brož, M., Lambrechts, M., 2017. Eccentricity excitation and merging of planetary embryos heated by pebble accretion. Astron. Astrophys. 606, A114. doi:10.1051/0004-6361/201731033, arXiv:1706.06329.

Chrenko, O., Brož, M., Nesvorný, D., Tsiganis, K., Skoulidou, D.K., 2015. The origin of long-lived asteroids in the 2:1 mean-motion resonance with Jupiter. Mon. Not. R. Astron. Soc. 451, 2399–2416. doi:10.1093/mnras/stv1109, arXiv:1505.04329.

Christou, A.A., 2013. Orbital clustering of martian Trojans: An asteroid family in the inner Solar System? Icarus 224, 144–153. doi:10.1016/j.icarus.2013.02.013, arXiv:1303.0420.

Christou, A.A., Wiegert, P., 2012. A population of Main Belt Asteroids co-orbiting with Ceres and Vesta. Icarus 217, 27–42. doi:10.1016/j.icarus.2011.10.016, arXiv:1110.4810.

Cibulková, H., Brož, M., Benavidez, P.G., 2014. A six-part collisional model of the main asteroid belt. Icarus 241, 358–372. doi:10.1016/j.icarus.2014.07.016, arXiv:1407.6143.

Connors, M., Wiegert, P., Veillet, C., 2011. Earth's Trojan asteroid. Nature 475, 481–483. doi:10.1038/nature10233.

Cruikshank, D.P., Dalle Ore, C.M., Roush, T.L., Geballe, T.R., Owen, T.C., de Bergh, C., Cash, M.D., Hartmann, W.K., 2001. Constraints on the Composition of Trojan Asteroid 624 Hektor. Icarus 153, 348–360. doi:10.1006/icar.2001.6703.

Ćuk, M., Christou, A.A., Hamilton, D.P., 2015. Yarkovsky-driven spreading of the Eureka family of Mars Trojans. Icarus 252, 339–346. doi:10.1016/j.icarus.2015.02.009, arXiv:1412.1776.

de la Fuente Marcos, C., de la Fuente Marcos, R., 2014. Asteroid 2013 $ND_{15}$: Trojan companion to Venus, PHA to the Earth. Mon. Not. R. Astron. Soc. 439, 2970–2977. doi:10.1093/mnras/stu152, arXiv:1401.5013.

De Luise, F., Dotto, E., Fornasier, S., Barucci, M.A., Pinilla-Alonso, N., Perna, D., Marzari, F., 2010. A peculiar family of Jupiter Trojans: The Eurybates. Icarus 209, 586–590. doi:10.1016/j.icarus.2010.04.024, arXiv:1004.4180.

Delbo', M., Walsh, K., Bolin, B., Avdellidou, C., Morbidelli, A., 2017. Identification of a primordial asteroid family constrains the original planetesimal population. Science 357, 1026–1029. doi:10.1126/science.aam6036.

dell'Oro, A., PAolicchi, F., Marzari, P., Dotto, E., Vanzani, V., 1998. Trojan collision probability: a statistical approach. Astron. Astrophys. 339, 272–277.

Di Sisto, R.P., Ramos, X.S., Beaugé, C., 2014. Giga-year evolution of Jupiter Trojans and the asymmetry problem. Icarus 243, 287–295. doi:10.1016/j.icarus.2014.09.002, arXiv:1604.05331.

Dohnanyi, J.S., 1969. Collisional Model of Asteroids and Their Debris. J. Geophys. R. 74, 2531–2554. doi:10.1029/JB074i010p02531.

Dones, L., Weissman, P.R., Levison, H.F., Duncan, M.J., 2004. Oort cloud formation and dynamics. p. 153.

Durda, D.D., Bottke, W.F., Nesvorný, D., Enke, B.L., Merline, W.J., Asphaug, E., Richardson, D.C., 2007. Size-frequency distributions of fragments from SPH/ N-body simulations of asteroid impacts: Comparison with observed asteroid families. Icarus 186, 498–516. doi:10.1016/j.icarus.2006.09.013.

Durech, J., Sidorin, V., Kaasalainen, M., 2010. DAMIT: a database of asteroid models. Astron. Astrophys. 513, A46. doi:10.1051/0004-6361/200912693.

Eklund, H., Masset, F.S., 2017. Evolution of eccentricity and inclination of hot protoplanets embedded in radiative discs. Mon. Not. R. Astron. Soc. 469, 206–217. doi:10.1093/mnras/stx856, arXiv:1704.01931.

Emery, J.P., Burr, D.M., Cruikshank, D.P., 2011. Near-infrared Spectroscopy of Trojan Asteroids: Evidence for Two Compositional Groups. Astron. J. 141, 25. doi:10.1088/0004-6256/141/1/25, arXiv:1012.1284.

Emery, J.P., Cruikshank, D.P., Van Cleve, J., 2006. Thermal emission spectroscopy (5.2 38 $\mu$m) of three Trojan asteroids with the Spitzer Space Telescope: Detection of fine-grained silicates. Icarus 182, 496–512. doi:10.1016/j.icarus.2006.01.011.

Farinella, P., Froeschle, C., Gonczi, R., 1993. Meteorites from the Asteroid 6 Hebe. Celestial Mechanics and Dynamical Astronomy 56, 287–305. doi:10.1007/BF00699740.

Fernandez, J.A., Ip, W.H., 1984. Some dynamical aspects of the accretion of Uranus and Neptune: The exchange of orbital angular momentum with planetesimals. Icarus 58, 109–120. doi:10.1016/0019-1035(84)90101-5.

Fornasier, S., Dotto, E., Hainaut, O., Marzari, F., Boehnhardt, H., De Luise, F., Barucci, M.A., 2007. Visible spectroscopic and photometric survey of Jupiter Trojans: Final results on dynamical families. Icarus 190, 622–642. doi:10.1016/j.icarus.2007.03.033, arXiv:0704.0350.

Goldreich, P., Lithwick, Y., Sari, R., 2004. Final Stages of Planet Formation. Astrophys. J. 614, 497–507. doi:10.1086/423612, arXiv:astro-ph/0404240.

Gomes, R., Levison, H.F., Tsiganis, K., Morbidelli, A., 2005. Origin of the cataclysmic Late Heavy Bombardment period of the terrestrial planets. Nature 435, 466–469. doi:10.1038/nature03676.

Granvik, M., Vaubaillon, J., Jedicke, R., 2012. The population of natural Earth satellites. Icarus 218, 262–277. doi:10.1016/j.icarus.2011.12.003, arXiv:1112.3781.

Grav, T., Mainzer, A.K., Bauer, J., Masiero, J., Spahr, T., McMillan, R.S., Walker, R., Cutri, R., Wright, E., Eisenhardt, P.R.M., Blauvelt, E., DeBaun, E., Elsbury, D., Gautier, T., I., Gomillion, S., Hand, E., Wilkins, A., 2011. WISE/NEOWISE Observations of the Jovian Trojans: Preliminary Results. Astrophys. J. 742, 40. doi:10.1088/0004-637X/742/1/40, arXiv:1110.0280.

Grav, T., Mainzer, A.K., Bauer, J.M., Masiero, J.R., Nugent, C.R., 2012. WISE/NEOWISE Observations of the Jovian Trojan Population: Taxonomy. Astrophys. J. 759, 49. doi:10.1088/0004-637X/759/1/49, arXiv:1209.1549.

Harris, A.W., Boslough, M., Chapman, C.R., Drube, L., Michel, P., Harris, A.W., 2015. Asteroid Impacts and Modern Civilization: Can We Prevent a Catastrophe? pp. 835–854. doi:10.2458/azu_uapress_9780816532131-ch042.

Holt, T.R., Horner, J., Nesvorný, D., King, R., Popescu, M., Carter, B.D., Tylor, C.C.E., 2021. Astrocladistics of the Jovian Trojan Swarms. Mon. Not. R. Astron. Soc. 504, 1571–1608. doi:10.1093/mnras/stab894, arXiv:2103.10967.

Holt, T.R., Nesvorný, D., Horner, J., King, R., Marschall, R., Kamrowski, M., Carter, B., Brookshaw, L., Tylor, C., 2020a. Stability of Jovian Trojans and their collisional families. Mon. Not. R. Astron. Soc. 495, 4085–4097. doi:10.1093/mnras/staa1348, arXiv:2005.03635.

Holt, T.R., Vokrouhlický, D., Nesvorný, D., Brož, M., Horner, J., 2020b. A pair of Jovian Trojans at the L4 Lagrange point. Mon. Not. R. Astron. Soc. 499, 3630–3649. doi:10.1093/mnras/staa3064, arXiv:2009.06749.

Hou, X.Y., Scheeres, D.J., Liu, L., 2014. Saturn Trojans: a dynamical point of view. Mon. Not. R. Astron. Soc. 437, 1420–1433. doi:10.1093/mnras/stt1974.

Ivezic, Z., Juric, M., Lupton, R.H., Tabachnik, S., Quinn, T., 2002. Asteroids Observed by The Sloan Digital Sky Survey, in: Tyson, J.A., Wolff, S. (Eds.), Survey and Other Telescope Technologies and Discoveries, pp. 98–103. doi:10.1117/12.457304, arXiv:astro-ph/0208099.

Jiang, Y., Baoyin, H., Li, H., 2018. Orbital stability close to asteroid 624 Hektor using the polyhedral model. Advances in Space Research 61, 1371–1385. doi:10.1016/j.asr.2017.12.011, arXiv:1803.06781.

Jutzi, M., 2015. SPH calculations of asteroid disruptions: The role of pressure dependent failure models. Planet. Space Sci. 107, 3–9. doi:10.1016/j.pss.2014.09.012, arXiv:1502.01860.

Lagrange, J.L., 1772. Essai sur le problème des trois corps .

Laskar, J., Robutel, P., 2001. High order symplectic integrators for perturbed Hamiltonian systems. Celestial Mechanics and Dynamical Astronomy 80, 39–62. arXiv:astro-ph/0005074.

Levison, H.F., Bottke, W.F., Gounelle, M., Morbidelli, A., Nesvorný, D., Tsiganis, K., 2009. Contamination of the asteroid belt by primordial trans-Neptunian objects. Nature 460, 364–366. doi:10.1038/nature08094.

Levison, H.F., Duncan, M.J., 1994. The Long-Term Dynamical Behavior of Short-Period Comets. Icarus 108, 18–36. doi:10.1006/icar.1994.1039.

Levison, H.F., Lucy Science Team, 2016. Lucy: Surveying the Diversity of the Trojan Asteroids, the Fossils of Planet Formation, in: Lunar and Planetary Science Conference, p. 2061.

Li, R., Youdin, A.N., Simon, J.B., 2018. On the Numerical Robustness of the Streaming Instability: Particle Concentration and Gas Dynamics in Protoplanetary Disks. Astrophys. J. 862, 14. doi:10.3847/1538-4357/aaca99, arXiv:1803.03638.

Lin, H.W., Gerdes, D.W., Hamilton, S.J., Adams, F.C., Bernstein, G.M., Sako, M., Bernadinelli, P., Tucker, D., Allam, S., Becker, J.C., Khain, T., Markwardt, L., Franson, K., Abbott, T.M.C., Annis, J., Avila, S., Brooks, D., Carnero Rosell, A., Carrasco Kind, M., Cunha, C.E., D'Andrea, C.B., da Costa, L.N., De Vicente, J., Doel, P., Eifler, T.F., Flaugher, B., García-Bellido, J., Hollowood, D.L., Honscheid, K., James, D.J., Kuehn, K., Kuropatkin, N., Maia, M.A.G., Marshall, J.L., Miquel, R., Plazas, A.A., Romer, A.K., Sanchez, E., Scarpine, V., Sevilla-Noarbe, I., Smith, M., Smith, R.C., Soares-Santos, M., Sobreira, F., Suchyta, E., Tarle, G., Walker, A.R., Wester, W., 2019. Evidence for color dichotomy in the primordial Neptunian Trojan population. Icarus 321, 426–435. doi:10.1016/j.icarus.2018.12.006.

Lyra, W., Johansen, A., Klahr, H., Piskunov, N., 2009. Standing on the shoulders of giants. Trojan Earths and vortex trapping in low mass self-gravitating protoplanetary disks of gas and solids. Astron. Astrophys. 493, 1125–1139. doi:10.1051/0004-6361:200810797, arXiv:0810.3192.

Mainzer, A., Grav, T., Masiero, J., Hand, E., Bauer, J., Tholen, D., McMillan, R.S., Spahr, T., Cutri, R.M., Wright, E., Watkins, J., Mo, W., Maleszewski, C., 2011. NEOWISE Studies of Spectrophotometrically Classified Asteroids: Preliminary Results. Astrophys. J. 741, 90. doi:10.1088/0004-637X/741/2/90, arXiv:1109.6407.

Malhotra, R., 1995. The Origin of Pluto's Orbit: Implications for the Solar System Beyond Neptune. Astron. J. 110, 420. doi:10.1086/117532, arXiv:astro-ph/9504036.

Marchis, F., Durech, J., Castillo-Rogez, J., Vachier, F., Cuk, M., Berthier, J., Wong, M.H., Kalas, P., Duchene, G., van Dam, M.A., Hamanowa, H., Viikinkoski, M., 2014. The Puzzling Mutual Orbit of the Binary Trojan Asteroid (624) Hektor. Astrophys. J. Lett. 783, L37. doi:10.1088/2041-8205/783/2/L37, arXiv:1402.7336.

Marsset, M., Brož, M., Vernazza, P., Drouard, A., Castillo-Rogez, J., Hanuš, J., Viikinkoski, M., Rambaux, N., Carry, B., Jorda, L., Ševeček, P., Birlan, M., Marchis, F., Podlewska-Gaca, E., Asphaug, E., Bartczak, P., Berthier, J., Cipriani, F., Colas, F., Dudziński, G., Dumas, C., Durech, J., Ferrais, M., Fétick, R., Fusco, T., Jehin, E., Kaasalainen, M., Kryszczynska, A., Lamy, P., Le Coroller, H., Marciniak, A., Michalowski, T., Michel, P., Richardson, D.C., Santana-Ros, T., Tanga, P., Vachier, F., Vigan, A., Witasse, O., Yang, B., 2020. The violent collisional history of aqueously evolved (2) Pallas. Nature Astronomy 4, 569–576. doi:10.1038/s41550-019-1007-5.

Marzari, F., Scholl, H., 1998. Capture of Trojans by a Growing Proto-Jupiter. Icarus 131, 41–51. doi:10.1006/icar.1997.5841.

McDonald, I., Kerins, E., Poleski, R., Penny, M.T., Specht, D., Mao, S., Fouqué, P., Zhu, W., Zang, W., 2021. Kepler K2 Campaign 9 - I. Candidate short-duration events from the first space-based survey for planetary microlensing. Mon. Not. R. Astron. Soc. 505, 5584–5602. doi:10.1093/mnras/stab1377, arXiv:2107.02746.

McNeill, A., Erasmus, N., Trilling, D.E., Emery, J.P., Tonry, J.L., Denneau, L., Flewelling, H., Heinze, A., Stalder, B., Weiland, H.J., 2021. Comparison of the Physical Properties of the L4 and L5 Trojan Asteroids from ATLAS Data. Planet. Sci. J. 2, 6. doi:10.3847/PSJ/abcccd, arXiv:2101.04602.

Milani, A., Knežević, Z., Spoto, F., Cellino, A., Novaković, B., Tsirvoulis, G., 2017. On the ages of resonant, eroded and fossil asteroid families. Icarus 288, 240–264. doi:10.1016/j.icarus.2016.12.030, arXiv:1607.01998.

Monaghan, J.J., 1992. Smoothed particle hydrodynamics. Ann. Rev. Astron. Astrophys. 30, 543–574. doi:10.1146/annurev.aa.30.090192.002551.

Montesinos, M., Garrido-Deutelmoser, J., Olofsson, J., Giuppone, C.A., Cuadra, J., Bayo, A., Sucerquia, M., Cuello, N., 2020. Dust trapping around Lagrangian points in protoplanetary disks. Astron. Astrophys. 642, A224. doi:10.1051/0004-6361/202038758, arXiv:2009.10768.

Morbidelli, A., Bottke, W.F., Nesvorný, D., Levison, H.F., 2009. Asteroids were born big. Icarus 204, 558–573. doi:10.1016/j.icarus.2009.07.011, arXiv:0907.2512.

Morbidelli, A., Brasser, R., Gomes, R., Levison, H.F., Tsiganis, K., 2010. Evidence from the Asteroid Belt for a Violent Past Evolution of Jupiter's Orbit. Astron. J. 140, 1391–1401. doi:10.1088/0004-6256/140/5/1391, arXiv:1009.1521.

Morbidelli, A., Levison, H.F., Tsiganis, K., Gomes, R., 2005. Chaotic capture of Jupiter's Trojan asteroids in the early Solar System. Nature 435, 462–465. doi:10.1038/nature03540.

Morbidelli, A., Nesvorný, D., 2020. Kuiper belt: formation and evolution. pp. 25–59. doi:10.1016/B978-0-12-816490-7.00002-3.

Mróz, P., Poleski, R., Gould, A., Udalski, A., Sumi, T., Szymański, M.K., Soszyński, I., Pietrukowicz, P., Kozłowski, S., Skowron, J., Ulaczyk, K., OGLE Collaboration, Albrow, M.D., Chung, S.J., Han, C., Hwang, K.H., Jung, Y.K., Kim, H.W., Ryu, Y.H., Shin, I.G., Shvartzvald, Y., Yee, J.C., Zang, W., Cha, S.M., Kim, D.J., Kim, S.L., Lee, C.U., Lee, D.J., Lee, Y., Park, B.G., Pogge, R.W., KMT Collaboration, 2020. A Terrestrial-mass Rogue Planet Candidate Detected in the Shortest-timescale Microlensing Event. Astrophys. J. Lett. 903, L11. doi:10.3847/2041-8213/abbfad, arXiv:2009.12377.

Nesvorný, D., 2018. Dynamical Evolution of the Early Solar System. Ann. Rev. Astron. Astrophys. 56, 137–174. doi:10.1146/annurev-astro-081817-052028, arXiv:1807.06647.

Nesvorný, D., Brož, M., Carruba, V., 2015. Identification and Dynamical Properties of Asteroid Families. pp. 297–321. doi:10.2458/azu_uapress_9780816532131-ch016.

Nesvorný, D., Li, R., Youdin, A.N., Simon, J.B., Grundy, W.M., 2019. Trans-Neptunian binaries as evidence for planetesimal formation by the streaming instability. Nature Astronomy 3, 808–812. doi:10.1038/s41550-019-0806-z, arXiv:1906.11344.

Nesvorný, D., Morbidelli, A., 2012. Statistical Study of the Early Solar System's Instability with Four, Five, and Six Giant Planets. Astron. J. 144, 117. doi:10.1088/0004-6256/144/4/117, arXiv:1208.2957.

Nesvorny, D., Vokrouhlicky, D., Bottke, W.F., 2006. The Breakup of a Main-Belt Asteroid 450 Thousand Years Ago. Science 312, 1490. doi:10.1126/science.1126175.

Nesvorný, D., Vokrouhlický, D., Deienno, R., 2014. Capture of Irregular Satellites at Jupiter. Astrophys. J. 784, 22. doi:10.1088/0004-637X/784/1/22, arXiv:1401.0253.

Nesvorný, D., Vokrouhlický, D., Morbidelli, A., 2013. Capture of Trojans by Jumping Jupiter. Astrophys. J. 768, 45. doi:10.1088/0004-637X/768/1/45, arXiv:1303.2900.

Noll, K.S., Brown, M.E., Weaver, H.A., Grundy, W.M., Porter, S.B., Buie, M.W., Levison, H.F., Olkin, C., Spencer, J.R., Marchi, S., Statler, T.S., 2020. Detection of a Satellite of the Trojan Asteroid (3548) Eurybates—A Lucy Mission Target. Planet. Sci. J. 1, 44. doi:10.3847/PSJ/abac54, arXiv:2008.01858.

O'Brien, D.P., Morbidelli, A., 2008. The Collisional Evolution of Trojan Asteroids - A Possible Origin of the L4-L5 Asymmetry, in: Asteroids, Comets, Meteors 2008, p. 8367.

Park, R.S., Folkner, W.M., Williams, J.G., Boggs, D.H., 2021. The JPL Planetary and Lunar Ephemerides DE440 and DE441. Astron. J. 161, 105. doi:10.3847/1538-3881/abd414.

Parker, A., Ivezić, Ž., Jurić, M., Lupton, R., Sekora, M.D., Kowalski, A., 2008. The size distributions of asteroid families in the SDSS Moving Object Catalog 4. Icarus 198, 138–155. doi:10.1016/j.icarus.2008.07.002, arXiv:0807.3762.

Perna, D., Bott, N., Hromakina, T., Mazzotta Epifani, E., Dotto, E., Doressoundiram, A., 2018. Rotationally resolved spectroscopy of Jupiter Trojans (624) Hektor and (911) Agamemnon. Mon. Not. R. Astron. Soc. 475, 974–980. doi:10.1093/mnras/stx3341, arXiv:1712.08502.

Pirani, S., Johansen, A., Mustill, A.J., 2019. On the inclinations of the Jupiter Trojans. Astron. Astrophys. 631, A89. doi:10.1051/0004-6361/201936600, arXiv:1910.01507.

Quinn, T.R., Tremaine, S., Duncan, M., 1991. A Three Million Year Integration of the Earth's Orbit. Astron. J. 101, 2287. doi:10.1086/115850.

Richardson, D.C., Quinn, T., Stadel, J., Lake, G., 2000. Direct Large-Scale N-Body Simulations of Planetesimal Dynamics. Icarus 143, 45–59. doi:10.1006/icar.1999.6243.

Roig, F., Ribeiro, A.O., Gil-Hutton, R., 2008. Taxonomy of asteroid families among the Jupiter Trojans: comparison between spectroscopic data and the Sloan Digital Sky Survey colors. Astron. Astrophys. 483, 911–931. doi:10.1051/0004-6361:20079177, arXiv:0712.0046.

Rozehnal, J., Brož, M., Nesvorný, D., Durda, D.D., Walsh, K., Richardson, D.C., Asphaug, E., 2016. Hektor - an exceptional D-type family among Jovian Trojans. Mon. Not. R. Astron. Soc. 462, 2319–2332. doi:10.1093/mnras/stw1719, arXiv:1607.04677.

Ryan, E.L., Sharkey, B.N.L., Woodward, C.E., 2017. Trojan Asteroids in the Kepler Campaign 6 Field. Astron. J. 153, 116. doi:10.3847/1538-3881/153/3/116.

Ševeček, P., Brož, M., Jutzi, M., 2019. Impacts into rotating targets: angular momentum draining and efficient formation of synthetic families. Astron. Astrophys. 629, A122. doi:10.1051/0004-6361/201935690, arXiv:1908.03248.

Ševeček, P., Brož, M., Nesvorný, D., Enke, B., Durda, D., Walsh, K., Richardson, D.C., 2017. SPH/N-Body simulations of small ($D = 10\,\mathrm{km}$) asteroidal breakups and improved parametric relations for Monte-Carlo collisional models. Icarus 296, 239–256. doi:10.1016/j.icarus.2017.06.021, arXiv:1803.10666.

Sheppard, S.S., Trujillo, C.A., 2006. A Thick Cloud of Neptune Trojans and Their Colors. Science 313, 511–514. doi:10.1126/science.1127173.

Sheppard, S.S., Trujillo, C.A., 2010. The Size Distribution of the Neptune Trojans and the Missing Intermediate-sized Planetesimals. Astrophys. J. Lett. 723, L233–L237. doi:10.1088/2041-8205/723/2/L233, arXiv:1009.5990.

Sidlichovský, M., Nervorný, D., 1997. Frequency Modified Fourier Transform and its Application to Asteroids, in: Dvorak, R., Henrard, J. (Eds.), The Dynamical Behaviour of our Planetary System, p. 137.

Souza-Feliciano, A.C., De Prá, M., Pinilla-Alonso, N., Alvarez-Candal, A., Fernández-Valenzuela, E., De León, J., Binzel, R., Arcoverde, P., Rondón, E., Evangelista, M.S., 2020. Analysis in the visible range of NASA Lucy mission targets: Eurybates, Polymele, Orus and Donaldjohanson. Icarus 338, 113463. doi:10.1016/j.icarus.2019.113463, arXiv:1907.11451.

Sugiura, K., Kobayashi, H., Inutsuka, S., 2018. Toward understanding the origin of asteroid geometries. Variety in shapes produced by equal-mass impacts. Astron. Astrophys. 620, A167. doi:10.1051/0004-6361/201833227, arXiv:1804.11039.

Szabó, G.M., Ivezić, Ž., Jurić, M., Lupton, R., 2007. The properties of Jovian Trojan asteroids listed in SDSS Moving Object Catalogue 3. Mon. Not. R. Astron. Soc. 377, 1393–1406. doi:10.1111/j.1365-2966.2007.11687.x, arXiv:astro-ph/0703026.

Tillotson, J.H., 1962. Metallic Equations of State For Hypervelocity Impact.

Tsiganis, K., Gomes, R., Morbidelli, A., Levison, H.F., 2005. Origin of the orbital architecture of the giant planets of the Solar System. Nature 435, 459–461. doi:10.1038/nature03539.

Usui, F., Kuroda, D., Müller, T.G., Hasegawa, S., Ishiguro, M., Ootsubo, T., Ishihara, D., Kataza, H., Takita, S., Oyabu, S., Ueno, M., Matsuhara, H., Onaka, T., 2011. Asteroid Catalog Using Akari: AKARI/IRC Mid-Infrared Asteroid Survey. Publ. Astron. Soc. Japan 63, 1117–1138. doi:10.1093/pasj/63.5.1117.

Vernazza, P., Brož, M., Drouard, A., Hanuš, J., Viikinkoski, M., Marsset, M., Jorda, L., Fetick, R., Carry, B., Marchis, F., Birlan, M., Fusco, T., Santana-Ros, T., Podlewska-Gaca, E., Jehin, E., Ferrais, M., Bartczak, P., Dudziński, G., Berthier, J., Castillo-Rogez, J., Cipriani, F., Colas, F., Dumas, C., Ďurech, J., Kaasalainen, M., Kryszczynska, A., Lamy, P., Le Coroller, H., Marciniak, A., Michalowski, T., Michel, P., Pajuelo, M., Tanga, P., Vachier, F., Vigan, A., Warner, B., Witasse, O., Yang, B., Asphaug, E., Richardson, D.C., Ševeček, P., Gillon, M., Benkhaldoun, Z., 2018. The impact crater at the origin of the Julia family detected with VLT/SPHERE? Astron. Astrophys. 618, A154. doi:10.1051/0004-6361/201833477.

Vernazza, P., Castillo-Rogez, J., Beck, P., Emery, J., Brunetto, R., Delbo, M., Marsset, M., Marchis, F., Groussin, O., Zanda, B., Lamy, P., Jorda, L., Mousis, O., Delsanti, A., Djouadi, Z., Dionnet, Z., Borondics, F., Carry, B., 2017. Different Origins or Different Evolutions? Decoding the Spectral Diversity Among C-type Asteroids. Astron. J. 153, 72. doi:10.3847/1538-3881/153/2/72, arXiv:1701.06603.

Vinogradova, T.A., 2015. Identification of asteroid families in Trojans and Hildas. Mon. Not. R. Astron. Soc. 454, 2436–2440. doi:10.1093/mnras/stv2115.

Vokrouhlický, D., Nesvorný, D., Dones, L., 2019. Origin and Evolution of Long-period Comets. Astron. J. 157, 181. doi:10.3847/1538-3881/ab13aa, arXiv:1904.00728.

Wong, I., Brown, M.E., 2016. A Hypothesis for the Color Bimodality of Jupiter Trojans. Astron. J. 152, 90. doi:10.3847/0004-6256/152/4/90, arXiv:1607.04133.

Wong, I., Brown, M.E., 2017. The Color-Magnitude Distribution of Hilda Asteroids: Comparison with Jupiter Trojans. Astron. J. 153, 69. doi:10.3847/1538-3881/153/2/69, arXiv:1701.00367.

Wong, I., Brown, M.E., Emery, J.P., 2014. The Differing Magnitude Distributions of the Two Jupiter Trojan Color Populations. Astron. J. 148, 112. doi:10.1088/0004-6256/148/6/112, arXiv:1408.2485.

Zappala, V., Cellino, A., Farinella, P., Knezevic, Z., 1990. Asteroid Families. I. Identification by Hierarchical Clustering and Reliability Assessment. Astron. J. 100, 2030. doi:10.1086/115658.

Zhou, L., Zhou, L.Y., Dvorak, R., Li, J., 2020. Systematic survey of the dynamics of Uranus Trojans. Astron. Astrophys. 633, A153. doi:10.1051/0004-6361/201936332, arXiv:1912.10273.

# List of publications

**Hektor — an exceptional D-type family among Jovian Trojans**

Rozehnal, J.; Brož, M.; Nesvorný, D.; Durda, D. D.; Walsh, K.; Richardson, D. C.; Asphaug, E.

`https://ui.adsabs.harvard.edu/abs/2016MNRAS.462.2319R/abstract`

**Eurybates — the only asteroid family among Trojans?**

Brož, M. ; Rozehnal, J.

`https://ui.adsabs.harvard.edu/abs/2011MNRAS.414..565B/abstract`

**Constraining the cometary flux through the asteroid belt during the late heavy bombardment**

Brož, M.; Morbidelli, A.; Bottke, W. F.; Rozehnal, J.; Vokrouhlický, D.; Nesvorný, D.

`https://ui.adsabs.harvard.edu/abs/2013A%26A...551A.117B/abstract`

**Jovian Trojans: Orbital structures versus the WISE data**

Rozehnal, Jakub; Brož, Miroslav

In this work, we study the relation between orbital characteristics of Jovian Trojans and their albedos and diameters as measured by the WISE/NEOWISE mission (Grav et al. 2011, 2012). In our previous work (Brož & Rozehnal 2011), we concluded that there is only one collisional family with parent body size larger than 100 km among Trojans, namely the Eurybates. This finding was based on the analysis of the observed size distributions, colour data from the Sloan Digital Sky Survey, and simulations of orbital evolution. The WISE albedos serve as an independent source of information which allows us to verify our previous results. We also update our database of suitable resonant elements (i.e. the libration amplitude $D$, eccentricity $e$, inclination $I$) of Trojans and we look for new (to-be-discovered) clusters by the Hierarchical Clustering Method. Using the WISE diameters, we can construct more precise size-frequency distributions of Trojans in both the leading/trailing clouds which we compare to SFD of the cluster(s) mentioned above. We then prepare a collisional model (based on the Boulder code, Morbidelli et al. 2009). Initial conditions of our model are based on an assumption that the Trojans were captured from a destabilised transplanetary disc while Jupiter jumped during its close encounter with a Neptune-mass planet — the so-called "jump capture" (Nesvorný et al. 2013). Within the framework of this model we try to constrain the

age of the Eurybates family.

https://ui.adsabs.harvard.edu/abs/2013DPS....4511212R/abstract

**Long-term evolution of asteroid families among Jovian Trojans**

Rozehnal, Jakub; Brož, Miroslav

We updated the database of resonant elements (i.e. the libration amplitude $\Delta$, eccentricity $e$, inclination $I$) of Jupiter Trojans and we identified and verified clusters by both the Hierarchical Clustering Method and Monte Carlo simulations, which allow us to assess also the statistical significance of the asteroid families. Apart from the Eurybates family (Brož & Rozehnal 2011), we also found five clusters of potentially collisional origin — namely families around asteroids (20961) Arkesilaos, (624) Hektor and (9799) 1996 RJ in L4 cloud and (17492) Hippasos and (247341) in L5 cloud. As these clusters fulfill our criteria for collisional families (i.e. statistical significance, albedo homogeneity, steeper SFD than that of background), we tried to simulate their origin and consequential orbital evolution in different scenarios of planetary migration (e.g. Nesvorný et al. 2013). Using the WISE albedos and diameters (Grav et al. 2011, 2012), we constructed size-frequency distributions of Trojans in both the leading/trailing clouds which we compared to SFDs of the families. We then simulated the collisional evolution of the families (using the Boulder code, Morbidelli et al. 2009). The results show that the evolution of bodies larger than $D > 50\,\mathrm{km}$ is very slow and they exhibit only little evolution over the last 3.85 Gyr (i.e. post-LHB phase). Hence we can consider this part of the SFD as primordial. In the frame of this model, we also tried to constrain ages of the families. We also analyzed the dependence of the total number of catastrophic disruptions on the target diameter.

https://ui.adsabs.harvard.edu/abs/2014acm..conf..452R/abstract

**SPH simulations of high-speed collisions**

Rozehnal, Jakub; Brož, Miroslav

Our work is devoted to a comparison of: i) asteroid-asteroid collisions occurring at lower velocities (about 5 km/s in the Main Belt), and ii) mutual collisions of asteroids and cometary nuclei usually occurring at significantly higher relative velocities ($> 10\,\mathrm{km/s}$). We focus on differences in the propagation of the shock wave, ejection of the fragments and possible differences in the resulting size-frequency distributions of synthetic asteroid families. We also discuss scaling with respect to the "nominal" target diameter $D = 100\,\mathrm{km}$, projectile velocity 3 to 7 km/s, for which a number of simulations were done so far (Durda et al. 2007, Benavidez et al. 2012). In the latter case of asteroid-comet collisions, we simulate the impacts of brittle or pre-damaged impactors onto solid monolithic targets at high velocities, ranging from 10 to 15 km/s. The purpose of this numerical experiment is to better understand impact processes shaping the early Solar System, namely the primordial asteroid belt during during the (late) heavy bombardment (as a continuation of Broz et al. 2013).For all hydrodynamical simulations we use a smoothed-particle hydrodynamics method (SPH), namely the lagrangian SPH3D code (Benz & Asphaug 1994, 1995). The gravitational interactions between fragments (re-accumulation) is simulated with the Pkdgrav tree-code (Richardson et al. 2000).

https://ui.adsabs.harvard.edu/abs/2016DPS....4832912R/abstract

**Recent impact on (4709) Ennomos?**

Rozehnal, Jakub; Brož, Miroslav

In this work, we try to associate the albedo variations of the Trojan L5 asteroid (4709) Ennomos (Emery et al., 2016) with a relatively recent impact structure on its surface. Although the mean visual albedo of Trojans is generally very low ($p_V \simeq 0.07$, Grav et al., 2012), especially for asteroids with diameter $D > 50\,\mathrm{km}$, Fernández et al. (2003) reported unusually high albedo of (4709) Ennomos ($p_V \simeq 0.12$ to 0.18), which diameter is $D \simeq 80\,\mathrm{km}$. However, the albedo of (4709) Ennomos determined from the WISE data by Grav et al. (2012) is only $p_V \simeq 0.09$ and the same albedo derived from AKARI is about $p_V \simeq 0.08$ (Usui et al., 2011). One possible explanation for these discrepancies is that the albedo of (4709) Ennomos is strongly dependent on its rotational phase. Emery et al. (2016) reported a clear evidence of spectral slope variations of (4709) Ennomos with its rotation, what may also suggest an existence of a bright spot on its surface, caused e.g. by impact. As we reported the asteroid family associated with (4709) Ennomos in our previous works (e.g. Brož and Rozehnal, 2011, Rozehnal et al., 2016), we try to simulate the family origin by SPH simulations (Benz & Aspaugh, 1994). Because the albedo variations could be in principle used to estimate an approximate size of the impact structure (in the case of cratering event, what means $M_{\mathrm{LR}}/M_{\mathrm{PB}} > 0.5$) on the family parent body an hence an approximate size of the impactor, this is a unique chance to compare it with the results of the SPH simulations. In our work we also try to determine the age of the Ennomos family by simulating the dynamical evolution of our synthetic families in different impact geometries (with different $f$ and $\omega$).

https://ui.adsabs.harvard.edu/abs/2017DPS....4911041R/abstract